



HAL
open science

**Evolution du plateau continental externe de la Marge
Equatoriale Brésilienne depuis 4 Ma : impact des
sédiments silicoclastiques Amazoniens, des changements
eustatiques contrôlés par les paramètres orbitaux, de la
subsidence, et des courants océanographiques**

Lucas Tortarolo

► **To cite this version:**

Lucas Tortarolo. Evolution du plateau continental externe de la Marge Equatoriale Brésilienne depuis 4 Ma : impact des sédiments silicoclastiques Amazoniens, des changements eustatiques contrôlés par les paramètres orbitaux, de la subsidence, et des courants océanographiques. Geomorphology. Université de Bretagne occidentale - Brest; Universidade Federal Fluminense (Brésil), 2023. English. NNT : 2023BRES0058 . tel-04614728

HAL Id: tel-04614728

<https://theses.hal.science/tel-04614728>

Submitted on 17 Jun 2024

HAL is a multi-disciplinary open access archive for the deposit and dissemination of scientific research documents, whether they are published or not. The documents may come from teaching and research institutions in France or abroad, or from public or private research centers.

L'archive ouverte pluridisciplinaire **HAL**, est destinée au dépôt et à la diffusion de documents scientifiques de niveau recherche, publiés ou non, émanant des établissements d'enseignement et de recherche français ou étrangers, des laboratoires publics ou privés.

COLLEGE SCIENCES

DOCTORAL DE LA MER

BRETAGNE ET DU LITTORAL

UBO

Université de Bretagne Occidentale

uff Universidade Federal Fluminense

THESE DE DOCTORAT EN COTUTELLE INTERNATIONALE DE

L'UNIVERSITE DE BRETAGNE OCCIDENTALE

ECOLE DOCTORALE N° 598

Sciences de la Mer et du Littoral

Spécialité : *Géosciences marine*

ET

UNIVERSIDADE FEDERAL FLUMINENSE

ECOLE DOCTORALE

Doctoral Program in Ocean and Earth Dynamics

Spécialité : *Marine Geosciences*

Par

Lucas TORTAROLO

Shelf Edge Evolution of the Brazilian Equatorial Margin since 4 Ma: Impact of Amazonian Siliciclastic Sediments, Orbitally Controlled Sea-Level Changes, Subsidence, and Oceanographic Currents

Thèse présentée et soutenue à Brest, le 13 décembre 2023

Unité de recherche : Geo-Ocean

Rapporteurs avant soutenance :

Sébastien CASTELLTORT
Jean-Yves REYNAUD

Associate professor, Geneva University
Professor, Lille University

Composition du Jury :

Président du Jury : Jean-Yves REYNAUD
Examineurs : Ana Luiza ALBUQUERQUE
Daniel PRAEG
Sébastien CASTELLTORT


Professor, Lille University
Professor, Universidade Federal Fluminense
Research associate, Nice University
Associate professor, Geneva University

Dir. de thèse : Marina RABINEAU
Co-dir. de thèse : Christian GORINI
Cleverson Guizan SILVA

Research director, Bretagne Occidentale University
Professor, Sorbonne University
Professor, Universidade Federal Fluminense

Invité(s) : Slah BOULILA
Damien DO COUTO
Antonio Tadeu DOS REIS
André W. DROXLER

Associate professor, Sorbonne University
Associate professor, Sorbonne University
Professor, Universidade do Estado do Rio de Janeiro
Professor, Rice University



**Shelf Edge Evolution of the
Brazilian Equatorial Margin
since 4 Ma: Interplay of
Amazonian Siliciclastic
Sediments, Orbital forcing,
Sea-Level Dynamics,
Subsidence Patterns, and
Oceanic Current Influences**

Remerciements

Tout d'abord, un grand merci aux membres de mon jury, Jean-Yves Reynaud et Sébastien Castellort, pour avoir accepté d'évaluer et corriger mon manuscrit en plus de leur participation aux côtés de Ana Luiza Albuquerque et Daniel Praeg à ma soutenance.

Je souhaite ensuite remercier, tout spécialement, mes encadrants Antonio Tadeu Dos Reis, Slah Boulila et Damien Do Couto. Sans oublier Christian Gorini, je te remercie pour ton accueil à Paris et ton partage autant scientifique que personnel. Mais aussi Marina Rabineau, je te remercie et j'en profite pour remercier également Daniel Aslanian, pour votre soutien, les délicieux repas du mercredi et les opportunités que vous m'avez offerte tout au long de ma thèse. Ainsi que Cleverson Guizan Silva, je te remercie pour ton accueil chaleureux au Brésil.

Mes remerciements s'adressent aussi aux membres de mon CSI, pour leur suivi rigoureux et leurs conseils avisés : Linda Hinnov, Jean Loup Rubino, Sara Lafuerza et Germain Bayon. Je suis également reconnaissant envers ceux avec qui j'ai eu l'opportunité de collaborer, notamment André Droxler, Linda Hinnov, Jean Loup Rubino, Matthias Prange, Stephan Jorry, David Menier et Jean-Philippe Adam. Une mention spéciale à Daniel Praeg et Sébastien Migeon pour m'avoir permis de participer à la mission Amagas sur le Marion Dufresne. Ce fût pour moi une chance inouïe, de découvrir l'envers du décor mais aussi extrêmement enrichissante que ce soit techniquement ou humainement parlant.

Je remercie également les différentes équipes qui m'ont accueillies lors de mes nombreuses vadrouilles, pour avoir suivi l'avancée de mes travaux et avoir prodigué de précieux conseils. Tout d'abord, l'équipe ISTEP qui m'a réservé un très bon accueil malgré mes passages de dernière minute à la capitale, merci Dia, Sylvain, Camille, Goulwen, Guillaume, Julien et Thomas. Je remercie, bien sûr, toute l'équipe Geo-Ocean pour votre accueil malgré le Covid, et votre bienveillance des deux côtés du grillage. Je tiens également à remercier particulièrement Véronique et Margot pour votre soutien et votre aide à travers les multiples démarches administratives.

Merci infiniment à mes co-bureaux et collègues : Léa G., Théo, Pierre-Yves, Paul, Noémie, Juliette, Zoé, Edgar, Pedro, Amandine, Ophélie, Quentin, Suzanna, Joao, Ikenna, pour m'avoir soutenu dans la grisaille mais aussi pour tous ces bons moments passé ensemble, à rire, à jouer, à escalader ... Plus que des collègues aujourd'hui, devenu de précieux amis, auxquels s'ajoutent d'autres merveilleuses rencontres : Léa P., Pierre-Léo, Gaëlle, Audrey, Alexis, Justine, Nicolas, Fatemeh et Mathieu. Merci pour tout, sincèrement, votre soutien, votre

partage, et j'espère que nous aurons encore bien d'autres occasions de nous voir, peu importe où la vie nous aura mené.

Enfin, mes derniers remerciements vont à ma famille plus particulièrement à mes parents pour leur encouragement et l'intérêt qu'ils ont porté à tout ce que j'ai entrepris jusqu'à aujourd'hui. Merci également à ma tatie, mon oncle Yves et mon cousin Quentin, pour m'avoir accompagné et soutenu dans cette lointaine contrée bretonne. Merci à Lucile, Cyril, Fanny et Romain, pour m'avoir écouté parler de cailloux sans cesse ces dernières années. Finalement, je remercie Lyndsay, devenue ma femme durant cette aventure et qui en plus d'une aide psychologique précieuse a directement contribué à la réalisation de cette thèse en relisant et corrigeant moult fois mes travaux. Surtout merci pour ce magnifique cadeau que tu m'offres en fin de thèse et me permet de relativiser, j'ai hâte de découvrir notre futur « kiwi ».

Malgré ces longues lignes je suis certain d'oublier encore de nombreuses personnes, ce pourquoi je vous présente de sincères excuses et vous remercie de tout cœur de m'avoir épaulé d'une manière ou d'une autre.

Merci à vous tous pour cette merveilleuse aventure.

Table of contents

Chapter 1: Introduction	27
1.1. Amazonian margin, a natural laboratory for climate studies:	28
1.1.1. The continental shelf: a sensitive recorder of past sea-level changes.....	28
1.1.2. Utility of river inputs to record continental climate variation and pluviometry	29
1.1.3. Petroleum exploration along the Amazon margin.....	29
1.2. Thesis objectives: How the Amazon margin evolves during the last 4 Ma.....	30
1.2.1. Influences of climatic processes and events on the margin	31
1.2.2. Unveiling Paleoenvironmental Variations Along the Amazon Margin during the Plio-Quaternary Era	31
1.2.3. Evolution of Carbonate Sedimentation in a Silico-Clastic Dominated Environment	32
Chapter 2: Geological context and climatic forcings on the Amazon Continental Margin sedimentation	33
2.1. Earth's Orbital parameters	34
2.1.1. Historical overview of the main astronomical parameters and their impact on Earth's climate.....	34
2.1.2. Earth's orbital eccentricity cycles	36
2.1.3. Earth's obliquity cycles.....	37
2.1.4. Earth's precession cycles	37
2.1.5. Modelling and limitations of the astronomical parameters through geological time	39
2.2. Earth's climate during the Cenozoic:.....	40
2.2.1. Mechanisms influencing Earth climate: external (orbital) versus internal drivers .	40
2.2.2. The Northern Hemisphere Glaciation (NHG) and its intensification	40
2.2.3. The Mid-Pleistocene Transition and its impacts on glacial-interglacial cycles	44

2.2.4. The enigmatic Mid-Brunhes Transition	45
2.3. Opening of the Atlantic Ocean and creation of the Brazilian Equatorial Margin	47
2.3.1. Phase 1	47
2.3.2. Phase 2-3	47
2.3.3. Syn-rift Formation	50
2.3.4. Post-rift formation until the Amapá platform	51
2.4. Andean orogeny	54
2.4.1. The main stages of the orogeny	54
2.4.2. Evolution in drainage basins of northern South America	56
2.5. Shift in the Amazon margin sedimentation	60
2.5.1. The transcontinental Amazon event	60
2.5.2. Age of the Amapá platform burial	61
2.5.3. The Amazon deep-sea fan discovery and study	62
2.5.4. Age of the deep-sea fan initiation	63
2.5.5. Deposition of the silico-clastic series along the margin	63
2.5.6. The Great Amazon Reef System, from hypothesis to proof	66
2.6. Physical parameters influencing marine deposition along the Amazon Margin	68
2.6.1. Winds	68
2.6.2. Tides	69
2.6.3. Currents	69
2.6.4. River inputs	71
2.6.5. Climate	73
Chapter 3: Data and methods	75
3.1. Seismic data and methods	76
3.1.1. Seismic acquisition principle	76
3.1.2. Evolution of seismic from 2D to 3D	76
3.1.3. Seismic interpretation from line drawing to automatic picking	78
3.1.4. The seismic block, position and parameters	78

3.1.5. Seismic and Sequence stratigraphy principles	80
3.1.6. Paleoscan workflow	82
3.2. Boreholes data and methods	86
3.2.1. Principles of drilling and coring	86
3.2.2. Borehole data inventory	87
3.2.3. Wells acquired along the Amazon Margin	88
3.2.4. Cyclostratigraphy on borehole data	88
Chapter 4: Amazon Sedimentation Unveiled: Decoding the Shelf Edge Evolution of the Brazilian Equatorial Margin since the Pliocene	93
4.1. Introduction	95
4.2. Regional setting	97
4.3. Data and methods	101
4.3.1. 3D seismic and downhole datasets	101
4.3.2. Seismic sequence stratigraphic methods.....	101
4.3.3. Cyclostratigraphic methods of time-series analysis.....	103
4.4. Results	104
4.4.1. Dating the starts of the siliciclastic deposition	104
4.4.2. Stratigraphic sequences.....	105
4.4.3. Cyclostratigraphy	109
4.4.4. Comparison between seismic observations and cyclostratigraphy	113
4.5. Discussion.....	114
4.5.1. Cyclicity record in well and seismic data	114
4.5.2. The starts of siliciclastic deposition	116
4.5.3. Mega-sequences correlation to climate and sea-level changes.....	117
4.5.4. Subsidence: a vital factor for preservation.....	119
4.6. Conclusions	120
4.7. Supplementary contents.....	123
4.7.1. Data and methods:.....	123

4.7.2. Sequence and seismic stratigraphic methods	123
4.7.3. Identification and definition of seismic sequences	124
4.7.4. Supplementary Figures	129
4.8. Previous attempts and upcoming improvements	134
4.8.1. Age model based on intervals	134
4.8.2. HMM-Match	145
Chapter 5: Outer shelf 3D Geomorphological features in the Plio-Pleistocene of the Brazilian Equatorial Margin: depositional system driven by 405 kyr cyclicity.....	151
5.1. Introduction	153
5.2. Geologic and stratigraphic framework of the Equatorial Brazilian Margin and the Amazon River Mouth Basin.....	154
5.3. Data and methods	158
5.3.1. Seismic data	158
5.3.2. 3D seismic horizons creation	159
5.4. Results	160
5.4.1. 3D Geomorphologies along horizons 1 and 3.....	161
5.4.2. 3D Geomorphologies along horizon 2.....	164
5.4.3. 3D Geomorphologies along horizons 4 and 5.....	166
5.5. Interpretation and Discussion	170
5.5.1. Barrier-Lagoon environment.....	170
5.5.2. Strand Plain environment.....	172
5.5.3. Abrasion coastline environment.....	174
5.5.4. Shoreline record during exceptional lowstand.....	177
5.5.5. Change in the coastal current during Plio-Pleistocene Sea level falls	179
5.6. Conclusions	180
5.7. Supplementary contents.....	182
Chapter 6: Cyclic growth of the Amazon Reef System during the last 2.5 Ma.	187
6.1. The Amazon Reef System	189

6.2. Seismic sequence and ACM evolution	192
6.3. Development of the present-day Amazon Reef System	193
6.4 Previous development of Barrier Reef System.....	195
6.5. Initiation of carbonates development	198
6.6. Carbonates flourishing.....	199
6.7. Pleistocene cyclic growth	200
6.8. Hydrodynamical changes triggering carbonates development.....	201
6.9. Conclusions and perspectives	202
6.10. Supplementary contents.....	204
6.10.1. Introduction to the Super-interglacial stages.....	204
6.10.2. Data and methods.....	205
6.10.3. Supplementary figures	207
Chapter 7: General discussion and perspectives	209
7.1. Transition from Amapá carbonate to the siliciclastic sediment derived of the Amazon	210
7.2. Plio-Pleistocene climate impact on sediment architecture of the Amazon Continental Margin	213
7.3. Submarine landslides and canyons evolution along the ACM	218
7.4. North Brazil Current variation, hints from the seismic record of the ACM shelf edge	222
7.5. Long eccentricity parameter, major influence in global climate	228
7.6. Perspectives	231
References	235

Table of figures

Figure 2.1: Timeline of discovery of the main astronomical parameters impacting the Earth's climate. Ap means approximatively.....XX

Figure 2.2: From Imbrie, 1985: Variation in eccentricity, obliquity and precession over the past 800 ka and their combined effect on insolation. The obliquity scale is in degrees. The insolation scale is in standard deviation units.....XX

Figure 2.3: From Zachos et al., 2001: Global deep-sea oxygen records based on data compiled from more than 40 DSDP and ODP sites. The $\delta^{18}O$ temperature scale was computed for an ice-free ocean [$\sim 1.2/1000$ Standard Mean Ocean Water (SMOW)], and thus only applies to the time preceding the onset of large-scale glaciation on Antarctica (~ 35 Ma). The vertical bars provide a rough qualitative representation of ice volume in each hemisphere relative to the LGM, with the dashed bar representing periods of minimal ice coverage ($<50\%$), and the full bar representing close to maximum ice coverage ($>50\%$ of present). Some key tectonic and biotic events are listed as well.....XX

Figure 2.4: From Droxler et al. (2003): The benthic oxygen isotope record at ODP Site 849 from the eastern equatorial Pacific Ocean in 3839 m of water depth (Mix et al., 1995) can be used as a reliable proxy for ice volume and, therefore, climate and sea level changes for the last 5 My. Since the onset of major glaciations in the Northern Hemisphere about 3.0 to 2.7 Ma, the Earth climate evolution displays three main characteristics: (1) the gradual cooling of the Earth climate in the past 3.0 My, (2) the Earth climate cyclic fluctuations first at about 41 ky per cycle linked to the variations of the tilt of the Earth axis (or obliquity) and then at lower frequency of about 100 ky per cycle (or orbital eccentricity), and (3) the transition from glacial MIS 12 (the heaviest glacial values with MIS 16) to interglacial MIS 11, characterised by the first lightest values in the late Quaternary, therefore a unique glacial to interglacial transition due to its extreme amplitude.....XX

Figure 2.5: Brazilian Equatorial Margin extensional events according to Soares Júnior et al. (2008): (A) First Event from Early Triassic to Late Triassic, highlighted in purple; (B-E) Second Event from Berriasian to Aptian, highlighted in dark green and (F-G) Third Event during the Albian, highlighted in light green. Note that the rifting the process in the northern part of the Equatorial margin is attributed to extensional motions associated with normal faults, with no strike-slip faulting.....XX

Figure 2.6: From Cruz (2018): Simplified structural framework of the Offshore Amazon Basin based on an integrated analysis of seismic reflection and potential field data. Thin lines on the Araguari sub-

basin outer shelf-slope region represent faults recording gravity-driven deformation of the post-rift sedimentary succession, simplified from Perovano et al. (2009).....XX

Figure 2.7: From Cruz, 2018: Stratigraphic charts of the three sub-basins of the Offshore Amazon Basin.....XX

Figure 2.8: Inline 2300 revealing the different formation along the ACM and main biostratigraphic age.....XX

Figure 2.9: From Horton (2018): Maps of (A) tectonic framework, (B) topography, and (C) sedimentary basin configuration of South America. (A) Map of plate boundaries, Andean magmatic arc (including the northern, central, and southern volcanic zones), regions of flat slab subduction, modern stress orientations from earthquake focal mechanisms, eastern front of Andean fold-thrust belt, and key segments of the retroarc foreland basin system. Plate velocities are shown relative to stable South American plate. (B) DEM topographic map showing the Andes mountains and adjacent foreland region, including the Amazon, Parana, Orinoco, and Magdalena (Mag) river systems. (C) Map of Andean retroarc basins, showing isopach thicknesses (in km) of Cretaceous-Cenozoic basin fill, forebulge axis, and locations of 13 sites (8 foreland basins, 5 hinterland basins) considered in this synthesis.....XX

Figure 2.10: From Hoorn et al. (2010): Paleogeographic maps of the transition from “cratonic” (A and B) to “Andean”-dominated landscapes (C to F). (A) Amazonia once extended over most of northern South America. Breakup of the Pacific plates changed the geography and the Andes started uplifting. (B) The Andes continued to rise with the main drainage toward the northwest. (C) Mountain building in the Central and Northern Andes (~12 Ma) and wetland progradation into Western Amazonia. (D) Uplift of the Northern Andes restricted “pan-Amazonia” and facilitated allopatric speciation and extirpation [e.g., (21)]. (E) The megawetland disappeared and terra firme rainforests expanded; closing of Panama Isthmus and start of GABI. (F) Quaternary.....XX

Figure 2.11: From Albert et al. (2018): Principal landforms controlling basin connectivity in northern South America. Structural arches (dashed lines) of diverse geological origins partially bounding sedimentary basins. Sedimentary basins in orange draining to the Caribbean; in yellow to the Atlantic.....XX

Figure 2.12: From Cruz et al. (2019): A - Structural framework compiled from Schaller et al. (1971) and Perovano et al. (2009). Faults associated to gravity tectonics are compiled from Perovano et al. (2009) and Reis et al. (2010). B to E - Two-way travel time (s) maps of stratigraphic surfaces mapped in the work of Cruz (2018), coupled with bathymetric maps (m) of the present-day Amazon shelf. Paleoshelf edge positions defined from interpreted seismic data are shown as thick coloured lines. In B, note that the shelf edge position in the central region at ca. 24 Ma was nearly coincident with the most proximal gravity tectonic-related faults. Also note that the large embayment formed due to shelf-edge

retrogradation in the Central shelf was filled between ca. 8-3.7 Ma and only then was carbonate sedimentation completely suppressed on the NW shelf.....XX

Figure 2.13: From (Cruz et al., 2019): Graphs summarizing calculations of the non-eustatic accommodation space required for the deposition of each Neogene sedimentary unit on the Amazon shelf.....XX

Figure 2.14: Bathymetric map of the NW Equatorial Brazilian Margin, a thick blue arrow shows the North Brazilian Current (NBC). The extension of the Great Amazon Reef System calculated by Moura et al. (2016) Francini-Filho et al. (2018) and dos Santos Filho et al. (2022) is represented by superposed coloured area in light blue, dark blue and yellow respectively. The 3D seismic block studied is delimited by red geometry.....XX

Figure 2.15: From Dengler et al. (2004): Circulation in the western tropical Atlantic. Schematic representation of mean currents and eddy generation at the western boundary of the tropical Atlantic with warmwater pathways in red and North Atlantic Deep Water pathways in blue. Current branches indicated are the south equatorial current (SEC), the north Brazil current (NBC), the equatorial undercurrent (EUC), the north equatorial undercurrent (NEUC) merged with the north equatorial counter current (NECC) and the deep western boundary current (DWBC) with alternating zonal flows marked at the Equator. Depth contours are also shown.....XX

Figure 2.16: From Molleri et al. (2010): Examples of synthetic Sea Surface Salinity maps calculated from the empirical model for the following periods: (A) 25 January – 07 February 2004; (B) 17 – 31 June 2001; (C) 22 August – 04 September 2004; and (D) 21 September – 04 October 2003. The numbers in parentheses in each image indicate: (1) north westward dispersion of the Amazon River plume; (2) NECC transport of the Amazon River plume water into the Central Equatorial Atlantic Ocean; (3) NBC retroflexion; and (4) rings formed by this retroflexion.....XX

Figure 2.17: From Mason et al. (2019): Interpreted relationships between sea level, Andes-Amazon hydroclimate, and resultant changes in sediment production and transfer through fluvial network to deep-sea across glacial (A) and interglacial (B) phases. Arrows indicate direction of change in erosion rate in the Andes and the Amazon craton (up = increase in erosion, down = decrease).....XX

Figure 3.1: Comparison between 2D and 3D seismic lines. Both lines show exactly the same area.....XX

Figure 3.2: Map showing seismic reflection data and wells available from the Offshore Amazon Basin. Note that seismic profiles cover the entire region between the continental shelf-slope, where industry wells are located, and the distal Ceará Rise region, where ODP/DSDP scientific wells are located...XX

Figure 3.3: From Catuneanu (2006): Regional architecture of depositional systems, systems tracts, and stratigraphic surfaces. Systems tracts are defined by stratal stacking patterns and bounding surfaces,

with an inferred timing relative to the base-level curve at the shoreline. Abbreviations: e-FR—early forced regression; l-FR—late forced regression; e-T—early transgression; l-T—late transgression...XX

Figure 3.5: Paleoscan automatic faults interpretation workflow. Faults interpretation could be directly assessed from the seismic data, three steps are necessary, computation of a Variance seismic block associated with a 3D scan, fault thinning and finally the extraction and filtering.....XX

Figure 3.6: Model Grid creation workflow, the software uses seismic traces to create a grid. Each point of the grid is represented by a coloured dot. Vertical resolution could be determined using Peaks (red dot), Troughs (yellow dot) or Zero Crossings (blue dot) or an assemblage of them. Spatial resolution is defined by the distance between traces. Coloured lines around dot represent patch propagation used to form horizon.....XX

Figure 3.7: Paleoscan 3D Geo-Model workflow, the upper pair of pictures represent a 3D Geo-Model created without constraints while, the lower pair of pictures show the connected patches forming horizons in red used to constraint the Geo-Model visible on the right. The faults represented by black lines are not used to constraint the model as layers are still connected.....XX

Figure 3.8: From Weedon et al. (2004): Adding sinusoids with different wavelengths produces a time series with multiple frequency components. Power spectra are used to: (a) identify which frequency components are present (frequency = 1/wavelength); and (b) determine their relative amplitudes. In this case two sine waves of equal amplitude, but different wavelengths, have been added to produce the time series labelled “Sum”. The corresponding power spectrum has peaks that occur at frequencies corresponding to the component wavelengths. The peaks are equal in height because the components have the same amplitude. Note that it is impossible to tell from the spectrum whether the components are sine or cosine waves – in other words the spectrum is independent of the phase of the components.....XX

Figure 3.9: From Weedon et al. (2004): Adding three sine waves with different wavelengths and varying amplitudes produces a time series that looks extremely complicated. It is unlikely that mere visual inspection of the summed time series illustrated would allow one to recognize that just three frequency components are present, or to determine the wavelengths involved.....XX

Figure 4.1: Bathymetric map of the NW Equatorial Brazilian Margin along with the location of sites of the studied data. The 3D seismic block is shown with the sea floor topography. The North Brazilian Current (NBC) is indicated with a thick blue arrow (Note the current also sweeps the continental shelf, the arrow is only indicative). In the expanded view, three wells are displayed in green (well #1 and #2 inside the 3D block, and well #3 outside the 3D block); two inlines A and B in dark blue are interpreted in figures 4 and 5, in addition to two 2D seismic lines C and D (also shown) used to tie the well #3 with the 3D seismic block.....XX

Figure 4.2: Lithology and gamma ray (GR) data of Wells #1, #2 and #3, displaying their Plio-Pleistocene sections shown in these figures from left north (Well #1) to right south (Well #3). The purple interval at the beginning of the Plio-Pleistocene section, just above the top Amapá, in well #3 was dated by biostratigraphy at 3.7 to 4.1 Ma (Cruz et al., 2019). Some unusual changes in the GR values, due to technical issues such as the presence of casing or tool change, are noted in light grey along the wells.....XX

Figure 4.3: Seismic facies classification and architectural elements interpretation.....XX

Figure 4.4: Inlines A and B crossing respectively Wells #1 and #2 (See location in Figure 1). Lithology and GR data are shown along the wells. Black stars show the check shots position used for the time-depth relationship. The three intervals in orange, green, and yellow at the left side of the lower profiles, depicts the three interpreted mega-sequences (labelled MS-I to MS-III). In the interpreted profiles, along the wells, grey-shaded intervals noted S1 through S9 depicts the nine identified seismic sequences. Brown lines in the lower profiles (labelled SLi1 and SLi2) emphasize two Submarine Landslides scars and deposits. Light blue dots highlight potential shoreline position during lowest sea level. In the interpreted Inline B, labels FR1 through FR9 depicts the identified regressive prisms (Forced Regression 1 to 9) inside the last two seismic sequences.....XX

Figure 4.5: Cyclostratigraphic analysis of GR data of Well #1 (depths 168 to 1194 m KB, siliciclastic series). On the left-side panel: (A) Raw GR dataset extended to the seafloor; (B) Detrended GR data; (C) Filter on the 35 to 25 m (0.024 to 0.046) cycles potentially associated with the Earth’s short eccentricity; (D) Filter on the 11 m (0.065 to 0.097) cycles potentially associated with the Earth’s obliquity. The graph below presents the MTM analysis of the curve B with the interpreted orbital cyclicities using manual frequency ratio method. Red, green, yellow and black lines represent the 99%, 95%, 90% and median Robust AR(1) confidence levels respectively. The right-side panel present eCOCO results compared to the sedimentation rates obtained after a tuning on short eccentricity (curve C) and obliquity (curve D), respectively in purple and red.....XX

Figure 4.6: Cyclostratigraphic results of GR data of Well #1 (depths 168 to 1194 m KB, siliciclastic series). The upper panel shows; (A) global sea level variation from Miller et al. (2020); (B) the GR data of Well #1 in time after a tuning between the Earth’s short eccentricity minima and the minima of the filter on the 35 to 25 m frequencies; (C) the GR data of Well #1 in time after a tuning between the Earth’s obliquity minima and the minima of the filter on the 11 m frequency. Ages noted along the curves corresponds to seismic sequence boundaries and the potential eustatic lowstand associated. The lower panels present the Multi-Taper-Method of curves B and C (see corresponding colours), with the main astronomical cyclicities. Red, green, yellow and black lines represent the 99%, 95%, 90% and median Robust AR (1) confidence levels respectively.....XX

Figure 4.7: Sequence stratigraphy interpretation of the inlines A and B (see their location in Figure 1). The sea level curve of Miller et al. (2020) (raw data in dark blue and smoothed data in light blue) is shown on the right side of wells #1 and #2. The dashed white line represents the present-day sea level. The red and green triangles along Well #1 depicts the relative sea level variation interpreted through seismic observation. Red triangles represent regressions while the green ones transgressions. Estimated ages of seismic sequence (S1 to S9) boundaries (corresponding to the Transgressive Surface) are labelled on the left side of the inlines.....XX

Figure 5.1: Bathymetric map of the NW Equatorial Brazilian Margin presenting the data used in this study. The 3D seismic block is shown with the seafloor horizon. The North Brazilian Current (NBC) is represented with a thick blue arrow. In the zoom box, two wells are noted in green and two inlines interpreted in figures 2 are in blue.....XX

Figure 5.2: Sequence stratigraphy summary of the inline A (**Chapter 4**). Sequences S8 and S9 in the inline A are not detailed due to lack of data quality. Age of the seismic sequences (S1 to S9) boundaries (associated with the Transgressive Surface) are written on the left side of the inlines. Three Mega-Sequence (MS-I, MS-II and MS-III) encompass seismic sequences with geometrical similarities. Limits between each of this Mega-Sequence has been related to Earth climatic variation: NHG; intensification of Northern Hemisphere Glaciation at ~2.5 Ma and MPT; Mid-Pleistocene Transition at 1.2 to 0.7 Ma. The horizons presented in the next figures are localized along the Inline A with black dashed lines.....XX

Figure 5.3: Seismic horizon 1 which is part of a Highstand System tract visualised from above with in the left panel the seismic data treated with a Red-Green-Blue frequency filter and on the right side, the interpretation of the main morphologies observed. Some seismic lines (Xline or Inline) are presented along the figures.....XX

Figure 5.4: Seismic horizon 3 which is part of a Highstand System tract visualised from above with in the left panel the seismic data, in white positive amplitude and in black negative ones, on the right side, an interpretative scheme of the main morphologies is provided. Some seismic lines (Xline or Inline) are presented along the figures.....XX

Figure 5.5: Seismic horizon 2 which is part of a Falling Stage System tract visualised from above with in the left panel the seismic data treated with a Red-Green-Blue frequency filter and on the right side, the interpretation of the main morphologies observed. Some seismic lines (Xline or Inline) are presented along the figures.....XX

Figure 5.6: Seismic horizon 4 which is part of a Transgressive System tract visualised from above with in the left panel the seismic data, in white positive amplitude and in black negative ones, on the right

side, an interpretative scheme of the main morphologies is provided. Some seismic lines (Xline or Inline) are presented along the figures.....XX

Figure 5.7: Seismic horizon 5 which is part of a Transgressive System tract visualised from above with in the left panel the seismic data, in white positive amplitude and in black negative ones, on the right side, an interpretative scheme of the main morphologies is provided. Some seismic lines (Xline or Inline) are presented along the figures.....XX

Figure 5.8: Satellite picture (google Earth courtesy) of a potential analogue site in North Carolina, along the outer banks compared to the interpreted structures visualised in horizon 3.....XX

Figure 5.9: Satellite picture (google Earth courtesy) of a potential analogue site along the Rio de Janeiro state coastline in Brazil compared to the interpreted structures visible in Horizon 2.....XX

Figure 5.10: Satellite picture (google Earth courtesy) of a potential analogue site along the Rio Grande Do Norte State coast in Brazil compared to interpreted structures of the Horizon 4.....XX

Figure 5.11: Simplified drawing of the different deposit environment related to each different system tract.....XX

Figure 6.1: Bathymetric map of the Amazon Continental Margin, a thick blue arrow shows the North Brazilian Current (NBC). The extension of the Great Amazon Reef System calculated by Moura et al. (2016), Francini-Filho et al. (2018) and dos Santos Filho et al. (2022) is represented by superposed coloured areas in light blue, dark blue and yellow respectively. The 3D seismic block studied is delimited by red geometry. The graph below the map shows sea level variation from Miller et al. (2020; dark blue curve) during the last 4 Myr and its relationship with Earth Eccentricity (orange curve) parameters of 100 kyr and 405 kyr (red dashed curve is an extraction of the 405 kyr cyclicity only). Super-interglacials are indicated by orange ovals (Droxler and Jorry, 2021; Melles et al., 2012). Main climatic events time extends are presented by purple arrows. Lastly main trend in global climate and the subsequent main regressions are shown by a thick yellow arrow and light blue arrows respectively.....XX

Figure 6.2: 3D maps of the horizons 1 to 4 and the present-day sea floor. Colour gradients represent Z value in ms with shallow area in red and deepest part in purple. The red circled area along the present-day seafloor represents one of the dive sites depicted in Lavagnino et al. (2020) and Vale et al. (2022). Seismic lines showing cross-section geometries are visible below horizons. Two wells cross the seismic block and are highlighted on the 3D sea floor representation. The orientation of the pictures is highlighted by three arrows on the top right corner, yellow one points North, green one points East while the red one is vertical.....XX

Figure 6.3: Sequence stratigraphy from the **Chapter 4** adapted on an arbitrary line crossing most of the bioconstruction observed. Position of the line is shown on the map view of the seismic block on the top

left of the figure. Nine seismic sequences have been observed (S1 to S9). Boundaries of the seismic sequences (SU) correspond to the transgressive surface. Age of the seismic sequences (S1 to S9) are written on the left side of the line in dark green. Earth climatic variation: INHG; intensification of Northern Hemisphere Glaciation at ~2.6 Ma and MPT; Mid-Pleistocene Transition at 1.2 to 0.7 Ma could correspond to main changes in the sediments architecture and are associated with specific boundaries between seismic sequences S3 to S4 and S7 to S8 respectively. Purple dashed lines correspond to the horizons presented in the figure 2. SLi = Submarine Landslide; TST = Transgressive System Tract; FSST = Falling Stage System Tract; HST = Highstand System Tract; Cb = Carbonates.....XX

Figure 7.1: Z value along the Top Amapá horizon depicting a typical flat topped carbonate shelf. The outer shelf is highly deformed and affected by faults. The slope is very steep and shows gullies. The shelf is greatly affected by mega-sinkholes revealing emersion of the shelf at the end of the Amapá serie.....XX

Figure 7.2: 3D seismic viewer revealing the correlation used to propagate the biostratigraphic age from Well #3 to the seismic block through two 2D seismic lines named C and D. The small box in the bottom left shows the position of the different lines and wells compared to the seismic block position. The top of Amapá is eroded by a major canyon. The bottom part of the canyon is fulfilled by reflectors with onlapping terminations noted canyon infill in the figure. While the upper part shows easy to propagate and correlate sandy layers which are highlighted in yellow. The position of the samples used for biostratigraphy correspond to the first set of reflectors which covers the canyon and the adjacent shelf (purple dashed line).....XX

Figure 7.3: Isochore maps for the nine seismic sequences observed within the siliciclastic sedimentary series. Due to the substantial variability in sequence thickness, it was impractical to employ a consistent colour grading across all sequences; as a result, quantitative values are not presented in these maps. Black lines on the maps serve to delineate features indicative of submarine landslide scars.....XX

Figure 7.4: From Maslin et al. (2006): Comparison of the composite relative global sea level curves with the Milliman et al. (1975) theoretical model of changing morphology of the continental shelf and Amazon delta with lowering sea level. Red sea level curve is a composite of coral and Red Sea data and for comparison the blue curve is a composite coral and benthic oxygen isotope record. This study suggests that small changes in marine transgression or regression when sea level is below 50m can change the sediment supply to the Fan. This results in either channel floor aggradation or channel floor erosion and thus an avulsion event.....XX

Figure 7.5: Arbitrary line crossing the canyons along the slope in the seismic block. Erosion is less active in the southeastern part, whereas the northwestern part experiences high levels of erosion. Similarly, substantial infill occurs in the southeastern canyons, while almost no infill is evident in the

northwestern ones. Contrary to expectations related to the influence of the North Brazil Current (NBC), the canyons do not exhibit a north-westward deflection. Thick black line represents the basal erosive limit of canyons. Dashed black lines show stacked unit limits inside canyons.....XX

Figure 7.6: From He et al. (2013): Evolutionary model of the submarine canyons within a single canyon form. Three stages have been divided: erosion-dominated stage, erosion-deposition stage and deposition-dominated stage. ES: erosion surface; BL: basal lag; MTDs: mass transport deposition; LAPs, lateral accretion packages.....XX

Figure 7.7: Models of the meridional velocities at 100 m depth along the north-eastern part of South America for two climatic states: preindustrial and the Heinrich Event 1 using a global coupled model with 1 degree resolution (CCSM3). Positive value indicates a northward flow, while negative indicates a southward flow. The values are expressed in cm/s. Study area is represented by a red square. The thick black line indicates the present-day coastline. The thin black lines represent from the coast to the basin, 200, 2000, 3000 and 4000 m isobath respectively. NBC means North Brazil Current. It is clear that in the present-day configuration, the NBC deflect most of the sediment from the Amazon northward along the coastline of Brazil and the Guianas. While during Heinrich Event 1, the NBC is greatly reduced and is deflected around 3°N, while a southward flow affects the northern Brazilian coastline.....XX

Figure 7.8: From Nikiema et al. (2007): Surface salinity contour and surface velocity (m/s) after 200 h for north wind forcing. The tidal is introduced and the Amazon River discharges is (a, c) 230 000m³/s and (b, d) 90 000m³/s, and 11 000 m³/s for Para/Tocantins River: (a) and (b) during ebb; (c) and (d) during flood.....XX

Figure 7.9: From Roychowdhury, (2018): Schematic diagram showing that most “super-interglacials” are preceded by periods of extreme low eccentricity. (a) Variations in the eccentricity component of orbital forcing over the last 2.4 million years together with $\delta^{18}O$ values from the “LR04” benthic stack (Lisiecki and Raymo, 2005). (b) Variations in the eccentricity component shifted by 50 kyr together with $\delta^{18}O$ values showing how the low eccentricity periods match up with the “super-interglacials”. Periods of extremely low eccentricity are shaded in green, and the “super-interglacials” identified from the Lake El’gygytgyn record are shaded in red.

Figure S4.1: 3D seismic viewer revealing the correlation used to propagate the biostratigraphic age from Well #3 to the seismic block through two 2D seismic lines named C and D. The small box in the bottom left shows the position of the different lines and wells compared to the seismic block position. The top of Amapá is eroded by a major canyon avoiding an easy propagation. However, the bottom part of the canyon is fulfilled by reflectors with onlapping terminations noted canyon infill in the figure. While the upper part shows easy to propagate and correlate sandy layers which are highlighted in yellow. The position of the samples used for biostratigraphy correspond to the first set of reflectors which covers the canyon and the adjacent shelf (purple dashed line).....XX

Figure S4.2: Cyclostratigraphic analysis of GR data of the upper non-deformed interval of Well #2 (depths 120 to 596 m KB, upper siliciclastic series). On the left-side panel: (A) Raw GR dataset; (B) Detrended GR data; (C) Filter on the 32 m cycles potentially associated with the Earth’s short eccentricity; (D) Filter on the 12 m cycles potentially associated with the Earth’s obliquity. The graph below presents the MTM analysis of the curve (B) with the interpreted orbital cyclicities using manual frequency ratio method. The right-side panel present eCOCO results compared to the sedimentation rates obtained after a tuning on short eccentricity (curve (C)) and obliquity (curve (D)), respectively in purple and red.....XX

Figure S4.3: Cyclostratigraphic analysis of GR data of Well #3 (depths 132 to 1954 m KB, siliciclastic series). On the left-side panel: (A) Raw GR dataset extended to the seafloor; (B) Detrended and corrected GR data; (C) Filter on the 46 m cycles potentially associated with the Earth’s short eccentricity; (D) Filter on the 21 m cycles potentially associated with the Earth’s obliquity. The graph below presents the MTM analysis of the curve (B) with the interpreted orbital cyclicities using manual frequency ratio method. The right-side panel present eCOCO results compared to the sedimentation rates obtained after a tuning on short eccentricity (curve (C)) and obliquity (curve (D)), respectively in purple and red.....XX

Figure S4.4: Cyclostratigraphic results of GR data of Well #3 (depths 132 to 1954 m KB, siliciclastic series). The upper panel shows; (A) global sea level variation from Miller et al. (2020); (B) the GR data of Well #3 in time after a tuning between the Earth’s short eccentricity minima and the minima of the filter on the 46 m frequency; (C) the GR data of Well #3 in time after a tuning between the Earth’s obliquity minima and the minima of the filter on the 21 m frequency. Ages noted along the curves corresponds to potential seismic sequence boundaries. The lower panels present the Multi-Taper-Method of curves B and C (see corresponding colours), with the main astronomical cyclicities. Red, green, yellow and black lines represent the 99%, 95%, 90% and median Robust AR(1) confidence levels respectively.....XX

Figure S4.5: Cyclostratigraphic analysis of GR data of Well #1 (depths 242 to 1194 m, Plio-Pleistocene section). (A) Raw and detrended GR data along with the analysed stratigraphic intervals (labelled I1 through I9 from the oldest to the youngest). The filtered wavelength of the short eccentricity is also shown along with the detrended data. (B) 2π -MTM power spectra of the detrended stratigraphic intervals (mentioned by the color codes). Red, orange and blue stars on spectral peaks indicate possible short eccentricity, obliquity and precession related wavelengths. (C) The 100 kyr tuned GR data (blue: tuned to a pure 100 kyr sine curve, orange: the 100 kyr tuned GR curve is anchored to 405 kyr eccentricity cycle minima) along with the raw La2004 eccentricity data (yellow curve) and the filtered 405 kyr cycle band (light blue curve). The red-dashed curve depicts sedimentation rate inferred from the 405 kyr anchored curve. (D) 2π -MTM power spectra of the tuned GR data to a pure 100 kyr sine (in blue) and those retuned to 405 kyr cycle minima (in orange), along with the robust red noise levels (median, 90%, 95% and 99% confidence levels).....XX

Figure S4.6: COCO results for each interval of the Well #1 compared with the sedimentation rates obtain through manual frequency ratio methodology. The calculation of sedimentation rate through manual frequency ratio method is represented by the black boxes in each interval. The black stars highlight the most probable sedimentation rate obtain with the comparison with both methodologies and the number is in cm/kyr.....XX

Figure S4.7: Cyclostratigraphic analysis of GR data of Well #2 (depths 120 to 596 m, upper Plio-Pleistocene section). (A) Raw and detrended GR data along with the analysed stratigraphic intervals (labelled I6 through I9 from the oldest to the youngest). The filtered wavelength of the short eccentricity is also shown along with the detrended data. (B) 2π -MTM power spectra of the detrended stratigraphic intervals (mentioned by the color codes). Red, orange and blue stars on spectral peaks indicate possible short eccentricity, obliquity and precession related wavelengths. (C) The 100 kyr tuned GR data (blue: tuned to a pure 100 kyr sine curve, orange: the 100 kyr tuned GR curve is anchored to 405 kyr eccentricity cycle minima) along with the raw La2004 eccentricity data (yellow curve) and the filtered 405 kyr cycle band (light blue curve). The red-dashed curve depicts sedimentation rate inferred from the 405 kyr anchored curve. (D) 2π -MTM power spectra of the anchored GR data to 405 kyr cycle minima (in orange), along with the robust red noise levels (median, 90%, 95% and 99% confidence levels).....XX

Figure S4.8: COCO results for each interval of the Well #2 compared with the sedimentation rates obtain through manual frequency ratio methodology. The calculation of sedimentation rate through manual frequency ratio method is represented by the black boxes in each interval. The black stars highlight the most probable sedimentation rate obtain with the comparison with both methodologies and the number is in cm/kyr.....XX

Figure S4.9: Cyclostratigraphic analysis of GR data of Well #3 (depths 181 to 1954 m, Plio-Pleistocene section). (A) Raw and detrended GR data along with the analysed stratigraphic intervals (labelled I1

through I9 from the oldest to the youngest). The filtered wavelength of the short eccentricity is also shown along with the detrended data. (B) 2π -MTM power spectra of the detrended stratigraphic intervals (mentioned by the color codes). Red, orange and blue stars on spectral peaks indicate possible short eccentricity, obliquity and precession related wavelengths. (C) The 100 kyr tuned GR data (blue: tuned to a pure 100 kyr sine curve, orange: the 100 kyr tuned GR curve is anchored to 405 kyr eccentricity cycle minima) along with the raw La2004 eccentricity data (yellow curve) and the filtered 405 kyr cycle band (light blue curve). The red-dashed curve depicts sedimentation rate inferred from the 405 kyr anchored curve. (D) 2π -MTM power spectra of the anchored GR data to 405 kyr cycle minima (in orange), along with the robust red noise levels (median, 90%, 95% and 99% confidence levels).....XX

Figure S4.10: COCO results for each interval of the Well #3 compared with the sedimentation rates obtain through manual frequency ratio methodology. The calculation of sedimentation rate through manual frequency ratio method is represented by the black boxes in each interval. The black stars highlight the most probable sedimentation rate obtain with the comparison with both methodologies and the number is in cm/kyr.....XX

Figure S4.11: Results of the “eCOCO” method for the three wells along with sedimentation rates inferred from the 100 kyr tuned GR data (stair-like white curves). Pearson correlation coefficient, and Null hypothesis H0 for non-orbital forcing estimated by the evolutive eCOCO approach. Sedimentation rate step is fixed at 0.2 cm/kyr. The used astronomical solution is from Laskar 2004 model (Laskar et al., 2004) with a middle age of the data at 2.0 Ma for wells #1 and #3, and 1.0 Ma for Well #2. The sliding window is fixed at 100, 150 and 200 m for wells #1, #2 and #3 respectively. A step of 1 m is fixed for the three wells.....XX

Figure S4.12: HMM-Match: Well #1 was correlated with the sea-level curve from Miller et al. (2020) spanning from 0.3 to 3.7 Myr. The starting age of the gamma-ray (GR) dataset from Well #1 was determined based on the mean sedimentation rate along the well. The upper age limit of the series was inferred from the projected biostratigraphic age data of Well #3. Both curves were normalized to zero. The first graph presents the sequences before alignment while the second graph present the results of the HMM-Match alignment.....XX

Figure S4.13: HMM-Match uncertainties. The 7 iterations of Run 3 attempted to minimize the adjustments between the Well #1 and sea level for the alignment (Match). The iterative procedure gives information about time assignments where multiple test alignments have high probability, which leads to greater uncertainty. In this case, the maximum uncertainty is +30 kyr at 1 Ma; otherwise, uncertainties are extremely low, on average around + 2 to 3 kyr.....XX

Figure S4.14: Adjustments of initial time scale assigned to Well #1 relative to the sea level time scale. A value of 1 indicates no adjustment; values greater than 1 indicate squeezing of Well #1 initial time scale; values less than 1 indicate stretching was required.....XX

Figure S4.15: 2pi MTM spectrum of different set of data. The first graph presents MTM of Well #1 assigned to time span of sea level target before HMM-Match. The second graph presents MTM of Well #1 after the HMM-Match. The third graph presents the MTM of Miller’s Sea level curve (2020) between 0.3 to 3.7 Myr.....XX

Figure S5.1: From Goslin and Clemmensen (2017): Schematic illustration of transgressive and regressive coastal barrier systems. Storm-wave induced markers are: A-Beach ridges, B-Storm scarps, C-Washover features. Coastal barrier sub-environments are: 1-Beach-ridge succession (strandplain); 2-Back-barrier lagoonal saltmarsh; 3-Brackish coastal mire; 4-Freshwater coastal lake, 5-Tidal inlet & flood/Ebb delta sedimentary features, 6-Beach berms, 7-Swash bars, 8-Shoreface, 9-Mainland/bedrock.....XX

Figure S5.2: From Hein et al. (2013): Schematic six-stage evolutionary model of Pinheira (not to scale). Boxes on the left are all map views; righthand boxes are three-dimensional cross-sections of sections of the strandplain (locations shown as horizontal black bars in map views). Note the multiple changes in scale of transect side views throughout the progression as indicated by the black line in map views. (A) 6 to 5 ka: Sea-level highstand at Pinheira. Waves crash on the bedrock that forms the landward side of Pinheira while fine sediment, derived from the nearby Made and Massiambu River systems, is deposited in the nearshore zone. (B) 5 to 3.3 ka: Early progradation in the form of a normal regression. A large offshore sediment supply allows for the development of shallow offshore-dipping beds. As sea-level fall begins, the system transitions into steeper-dipping, offlapping beds typical of forced regression. (C) >3.3 ka: Onshore migration of a large quantity of sand as multiple intertidal bars due to perturbation in the rate or direction of sea-level change. (D) ca 3.3 ka: Slowly rising or stable sea-level allows for vertical accretion of sediments on top of bars, forming subaerial barriers, separated by multiple inlets, and backed by a shallow lagoon. The lagoon drains through a 250 m wide inlet in the barrier and probably is also connected to both the Madre and Massiambu drainage systems. Either a small rise in sea-level or a storm event results in overwash and the deposition of a washover unit in the backbarrier. (E) <3.3 ka: Sea-level fall reinitiates shoreline progradation. The seaward side of the barrier transitions into a progradational beach ridge/foredune ridge plain. The central inlet is filled with shoreface and/or foreshore sands and then closes as a result of falling sea-level and reduction in tidal prism. The lagoon begins closing and filling with both fine sand and marsh; drainage is primarily to the north. (F) ca 1 ka: Late stage progradation. The northernmost reaches of the lagoon continue to drain out through a small tributary to the Massiambu River. The remainder of the lagoon transitions into a lowland fresh water marsh. The palaeo-barrier has since been covered by an aeolian dune that nucleated upon the high-profile barrier feature.....XX

Figure S5.3: From Cattaneo and Steel (2002): (A) Transgressive part of the transgression– regression diagram of Curry (1964). (B) Revised version of the diagram. Depositional regime w (as defined by Thorne and Swift, 1991) is expressed as the accommodation– supply ratio (A/S). See text for discussion.....XX

Figure S5.4: From Claudino-Sales et al. (2018): Illustration of the dynamics and evolution of headland-beach dune systems.....XX

Figures S6.1: Figure S6.1: Map of the present-day outer shelf seafloor presenting the Carbonate barrier reef feature and the terraces. The outer shelf map is an extraction from the full seismic block (bottom right). The terraces have been extracted through filtering of points along a dip/depth graph (top right).....XX

Extended abstract

In this PhD thesis, three interconnected studies investigate the stratigraphic and geomorphological evolution of the Brazilian Equatorial Margin, focusing on the Amazon siliciclastic sediment succession. With limited geochronological data available, including a single biostratigraphic age at the base of the series suggesting an age range of 3.7-4.1 Myr for the initial sediments deposited by the Amazon River, this research fills critical knowledge gaps.

We established an age model based on cyclostratigraphy and sequence stratigraphy to explore the Plio-Pleistocene archives. By employing 3D seismic block analysis and Gamma-Ray borehole data, this study identifies nine seismic sequences dating back to 3.7-4.1 Ma, corresponding to long 405-kyr eccentricity cycles. These sequences primarily result from sea-level dynamics over the last 4 million years, providing insights into significant milestones in Earth's Quaternary climate, such as the intensification of Northern Hemisphere Glaciations and the Mid-Pleistocene Transition, manifesting as notable geometrical changes in sedimentary architecture.

Next, we employed high-resolution 3D seismic horizons analysis to examine geomorphological changes in the outer shelf since 3.7-4.1 Ma. The area reveals a succession of coastline morphologies, including lagoonal environments, strand plains, and cliffs. These are shaped by sea-level fluctuations and sediment supply from the Amazon River or its absence. The study finds that the north-westward flow of the North Brazil Current and its occasional deflections have a significant impact on sediment deposition and preservation. Furthermore, it underscores the significance of 405 kyr eustatic changes as a contributing factor to these coastal transformations.

Lastly, we focused on the Great Amazon Reef System (GARS), an intriguing deep-reef ecosystem recently uncovered along the Amazon Continental Margin. This investigation unveils remarkable structures on the contemporary seabed characterized by their rapid build-up, reminiscent of shallow reefs. Furthermore, it highlights that these build-ups are not isolated phenomena but are integral components of a cyclic pattern, occurring over 405-kyr intervals, in the development of the reef system. This cyclic pattern is notably influenced by Northern Hemisphere Glaciation and the corresponding sea-level fluctuations. The study also suggests that the growth of the reef is likely facilitated by reduced turbidity along the shelf edge, particularly during the initial phases of deglacial sea-level rises.

This thesis demonstrates the effectiveness of a multi-faceted approach that integrates seismic stratigraphy, 3D seismic geomorphology, and cyclostratigraphy in unravelling the intricate interplay among subsidence, sediment supply, sea-level fluctuations, and oceanic currents. These findings significantly enhance our comprehension of the stratigraphic and geomorphic evolution of a south Atlantic passive continental margin. This margin's sedimentary history has been remarkably preserved through continuous subsidence processes over time.

Résumé étendu

Dans cette thèse, trois études interconnectées examinent l'évolution stratigraphique et géomorphologique de la marge équatoriale brésilienne, en se concentrant sur les sédiments siliciclastiques de l'Amazonie. Avec un manque de données géochronologiques et une seule datation biostratigraphique suggérant un âge de 3,7 à 4,1 millions d'années pour les sédiments initialement déposés par le fleuve Amazone dans la zone d'étude, cette recherche vise à combler des lacunes majeures. Un modèle d'âge a été développé grâce à la cyclostratigraphie, basé sur des données de Gamma-Ray le long de 3 puits et la stratigraphie séquentielle, basé sur des données de sismique 3D. Cette étude a permis d'identifier neuf séquences sismiques au cours des derniers 4 Ma, correspondant à des cycles de longue excentricité de 405 000 ans. Ces séquences reflètent principalement les changements du niveau de la mer sur les 4 derniers millions d'années, enregistrant des étapes-clés du climat terrestre durant le quaternaire, telles que l'intensification des glaciations de l'hémisphère nord et la transition du milieu du Pléistocène, se manifestant par des changements géométriques dans l'architecture sédimentaire.

La création et l'analyse d'horizons sismiques 3D ont ensuite permis de révéler des changements géomorphologiques sur le plateau continental externe durant le Plio-Pleistocène. La zone présente une variété de morphologies côtières, allant des environnements lagunaires aux cordons littoraux progradants et aux falaises. Ces environnements sont influencés par les fluctuations du niveau de la mer et les apports sédimentaire de l'Amazonie. De plus, le courant Nord Brésilien, en longeant les côtes vers le nord-ouest, joue un rôle significatif dans la dynamique de dépôt et de préservation des sédiments. Les changements eustatiques de 405 000 ans ont été identifiés comme un facteur déterminant de ces transformations côtières.

Enfin, nous avons étudié le Grand Système de Récifs de l'Amazonie (GARS), un écosystème de récifs profonds nouvellement découvert. Cette partie de l'étude révèle des structures remarquables sur le fond marin actuel, qui se sont développées durant le début de la transgression qui fait suite au dernier maximum glaciaire. Ces structures ne sont pas isolées mais sont récurrentes depuis les derniers 2.5 Ma. Ce développement n'est possible que grâce à un changement dans les courants le long de la marge qui lors d'épisode glaciaire important redirige les sédiments Amazoniens vers le bassin profond.

Cette thèse démontre l'efficacité d'une approche multidisciplinaire qui intègre la stratigraphie sismique, la géomorphologie 3D et la cyclostratigraphie pour élucider les interactions complexes entre la subsidence, les apports sédimentaires, les fluctuations du niveau de la mer et les courants océaniques. Ces découvertes améliorent considérablement notre compréhension de l'évolution stratigraphique et morphologique d'une marge continentale passive de l'Atlantique Sud.



Chapter 1: Introduction

The foundation of this PhD project was initially built upon the expectations arising from the oceanographic cruise IODP 387. However, our research trajectory shifted as we redirected our focus towards existing data, which, fortuitously, is abundant along the Brazilian Equatorial Margin. This wealth of data has been collected through extensive exploration efforts by numerous oil and gas companies. Within the same research team that supervises this project, other studies have leveraged this dataset to delve into the margin's basement and its history of opening (Cruz, 2018), as well as the evolution of older post-rift successions (Boulila et al., 2020; Cruz et al., 2019). Additionally, extensive research has been conducted on the incidence of landslides along the deep-sea fan and slope (Le Bouteiller et al., 2019; Silva et al., 2016; Souza et al., 2020), and the recent history, covering less than 0.5 million years, has been thoroughly investigated through piston core analyses (Horn, 1997; Mason et al., 2019; Nace et al., 2014; Rühlemann et al., 2001). Nevertheless, a significant knowledge gap persists in our understanding of the Brazilian Equatorial Margin, particularly its evolution since the initial influx of sediments derived from the Andes. Therefore, our research endeavours are strategically centred on this crucial interval. This period offers a unique window of opportunity due to distinct conditions, including substantial subsidence and sedimentation rates, coupled with minimal erosion along the outer shelf. As we explore this interval, we aim to document various driving forces and gain valuable insights into global climatic changes and events.

1.1. Amazonian margin, a natural laboratory for climate studies:

1.1.1. The continental shelf: a sensitive recorder of past sea-level changes

The continental shelf is characterised by its gently sloping and shallow seabed with water depth ranging from 0 to 200 meters, but it increases rapidly along the slope, marking the outer boundary of the continental shelf. The coast forms the inner edge of the continental shelf. The relatively shallow bathymetry of the continental shelf is the result of its tectonic nature, as it represents the transitional zone between continental and oceanic crusts (Smith and Sandwell, 1997). This tectonic history has left the shelf with a generally low altitude and minimal relief, rendering it susceptible to submergence during periods of rising sea levels. Consequently, the continental shelf becomes a highly sensitive area for monitoring fluctuations in sea level, thus making it a vital area for researching historical sea-level changes. Various studies focus on different eustatic markers to reconstruct past sea-level variations. For instance, analysing lithological characteristics of sediment cores and studying geophysical parameters, such as Gamma Ray (GR) data, can provide valuable information on the position of paleo-coastlines

and paleo-bathymetry. Additionally, modern bathymetric data is utilized to investigate geomorphic features dating back to previous low sea levels, helping to determine both the position and depth of ancient coastlines.

1.1.2. Utility of river inputs to record continental climate variation and pluviometry

In our study, the presence of the Amazon River is of paramount significance for understanding continental climate variation. The river brings a crucial flux of sediments from the continent, leading to an accelerated rate of sedimentation within our study area. This heightened sedimentation rate significantly enhances the resolution of our research conducted along the continental shelf. Moreover, the nature of these sediment inputs is a treasure trove of information. It offers valuable insights into their origin, reflecting the climatic conditions on the continent, and it also reveals variations in erosion rates over time

When the influx of sediment inputs reaches a certain threshold, it triggers subsidence of the continental shelf, effectively creating space for the deposition of new sediments. This subsidence mechanism plays a pivotal role in preserving the sedimentary record over time. Conversely, when the subsidence rate of the continental shelf is insufficient, during periods of global sea-level drop, a significant portion of the previously deposited marine sediments from higher sea levels may erode away.

As a result, only a limited number of coastal margins manage to retain a complete record of sediment sequences. Our study recognizes the crucial role that river inputs along these margins play in providing an abundance of additional information and ensuring better sediment preservation over time. This preservation allows us to delve deeper into the intricate story of continental climate variation.

1.1.3. Petroleum exploration along the Amazon margin

Since the late 1960s, Petrobras, a government-owned Brazilian company, has been actively engaged in exploration activities along the Amazonian margin. This extensive exploration effort persisted for nearly two decades and resulted in the acquisition of a vast dataset consisting of thousands of 2D seismic profiles that span the entire margin, stretching over 1000 kilometres from the state of Rio Grande Do Norte to the state of Amapá. The focus of this oil exploration wasn't limited to the continental shelf alone; it extended into the slope and deep-sea fan of the Amazon. Over the course of this exploration campaign, close to a hundred exploration wells

were drilled across various environments, with water depths ranging from a few tens of meters to well over a thousand meters. The economic significance of the region prompted the Brazilian government to offer multiple zones along the margin for sale.

As of the present day, there are 47 blocks designated for "permanent offer" by the National Petroleum Agency (ANP) along the Equatorial Margin. Additionally, an additional 157 blocks are currently under consideration to be auctioned off in the future. In a noteworthy development in 2013, Petrobras sold six blocks to major international oil companies Total (40%) and BP (30%) during an auction orchestrated by the National Petroleum Agency. Notably, most of these blocks were entirely covered by 3D seismic data, reflecting the industry's commitment to advanced exploration techniques and technologies in this strategically important region.

1.2. Thesis objectives: How the Amazon margin evolves during the last 4 Ma

This thesis is part of an ongoing collaborative project jointly between the University of Sorbonne in Paris, the University of Western Brittany in Brest, and two Brazilian universities: the Federal Fluminense University (UFF) and the State University of Rio de Janeiro (UERJ). Several previous theses and master's projects have explored this region using a dataset similar to the one employed in this thesis. This research builds upon the work of Alberto Cruz, whose thesis was completed and defended in 2018. Cruz conducted a comprehensive study of the basin on a larger scale, with a primary focus on the structural aspects, including the evolution of synrift faults and their impact on the current geometry of the basin. Additionally, he examined the post-rift series, particularly the Amapá carbonate series. Cruz's work made significant contributions to addressing the challenges related to the lack of biostratigraphic data along the plateau. His research facilitated the correlation of several wells and improved dating within the plateau and during the deposition of the Amapá series.

To advance this research, the focus of this thesis has shifted towards investigating the relatively recent silico-clastic series that have accumulated on the Amapá platform since the Amazon River connected to the Andes. This connection has resulted in a significantly increased sediment volume entering the basin. However, these series currently lack adequate dating.

These sediments, primarily composed of silico-clastic materials, have not been subject to thorough study or sampling during the drilling of exploration wells, mainly because they lack economic interest. Consequently, a critical knowledge gap exists regarding their age and geological history, which this thesis aims to address.

To enhance our comprehension of silico-clastic sedimentation along the Amazon margin, we have chosen to focus our analysis on a 3D seismic block owned by the CGG company, located 400 kilometres north of the mouth of the Amazon River. In pursuit of this objective, we have identified several key research goals, which are detailed in the following paragraphs.

1.2.1. Influences of climatic processes and events on the margin

The Amazon margin, being ideally situated, serves as a critical recorder of changes impacting both the oceanic and continental domains. Its unique position between the sea and the land raises fundamental questions about the dominant processes influencing sediment deposition along the margin. A multitude of factors come into play, including climate variations that significantly affect sea levels, shifting the coastline and influencing sediment distribution across the plateau. Additionally, Andean orogenesis plays a crucial role by influencing the rate of Andes uplift and, consequently, the erosion rate, leading to variations in sedimentation within the basin. Moreover, gravity tectonics can also have a profound impact by modifying the available space for sediments on the upper part of the slope and within the plateau.

To better distinguish the individual impact of climate, a comprehensive study encompassing both cyclostratigraphy and sequence stratigraphy was undertaken. This approach allowed for the precise dating of sediments and facilitated the observation of potential correlations between significant alterations in sediment geometry and climatic fluctuations, as well as other relevant factors (as detailed in **Chapter 4**).

1.2.2. Unveiling Paleoenvironmental Variations Along the Amazon Margin during the Plio-Quaternary Era

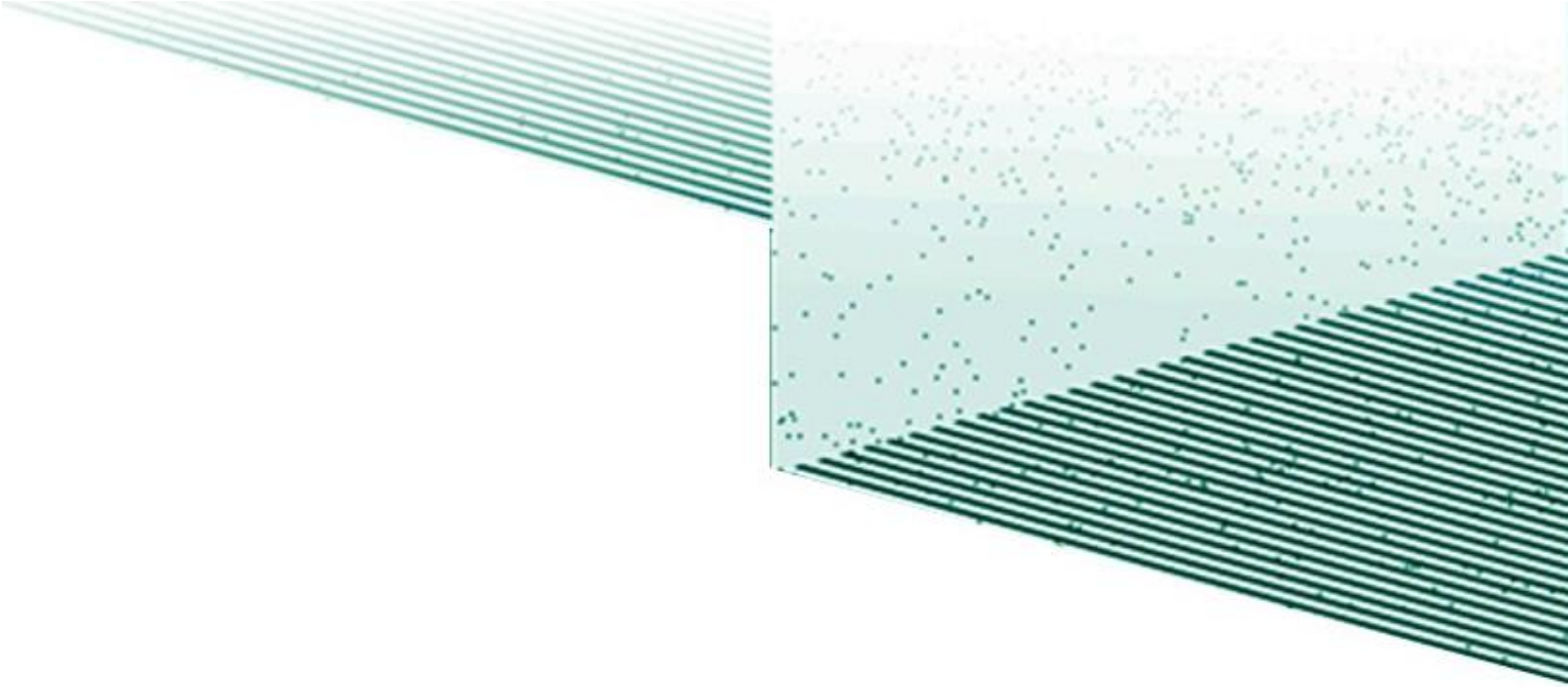
During the initial phase of this thesis, our examination of the 3D seismic block uncovered striking geomorphological features. Consequently, we made the decision to delve deeper into the study of paleoenvironmental variations along the Amazon Margin, with a particular focus on the Plio-Quaternary period. The high-quality data provided us with detailed imaging of the geomorphology of the silico-clastic layers, allowing for a comprehensive analysis. Through the integration of previously obtained age data and the examination of sedimentary assemblages linked to sea-level fluctuations, we have successfully established meaningful connections between the observed geomorphological features and the past climate changes that have left their mark on our planet. These findings are extensively discussed in **Chapter 5**, shedding light

on the intricate relationship between the Earth's dynamic climate and the evolving landscapes of the Amazon Margin.

1.2.3. Evolution of Carbonate Sedimentation in a Silico-Clastic Dominated Environment

Our exploration of the 3D seismic block, incorporating both vertical seismic lines and seismic horizons, has unveiled a surprising revelation—the presence of extensive carbonate structures. Remarkably, these structures are significantly larger and more complex than what initial expectations dictated, especially considering the prevailing conditions that influence the continental shelf of the Amazon margin.

At present, the Amazon plume, carrying a heavy load of clay, redirected northwards by the North Brazilian Current, which flows along the Brazilian and Guyanese coasts, extends even to the Caribbean Sea. Consequently, the waters along the margin exhibit remarkable turbidity, significantly impacting organisms that rely on solar energy for growth. This led to the long-held belief that carbonate formation would be improbable under such circumstances. However, during the drilling of the first wells along the margin, carbonates were unexpectedly encountered within the predominantly silico-clastic series of Plio-Quaternary age. It wasn't until 2016, when, an oceanographic mission equipped with a submarine ventured to explore the outer shelf of the Amazon, that the presence of extensive, still-active carbonate structures was definitively revealed. The geomorphological features associated with the development of these carbonates, as observed within the 3D seismic block, now offer invaluable insights into the timing of their existence and how they have evolved over geological time scales. These findings are comprehensively discussed in **Chapter 6**, shedding light on the enigmatic history of carbonate structures within the turbid waters of the Amazon Margin.



**Chapter 2: Geological
context and climatic forcings
on the Amazon Continental
Margin sedimentation**

In this chapter, we examine the diverse set of forcings and events that have influenced, and continue to influence, the Amazon Continental Margin. These range from broad Earth-system forcings with a quick historical overview of the astronomical parameter to specific geological events that have led to the creation and development of the passive margin, and extend to present-day physical oceanographic influences.

2.1. Earth's Orbital parameters

2.1.1. Historical overview of the main astronomical parameters and their impact on Earth's climate

From prehistoric times, the study of astronomy is evident through the worship of celestial bodies. The famous Stonehenge (Newall and Atkinson, 1956) in the United Kingdom stands as one of the most well-known examples of such customs closely linked to the stars. Additionally, numerous other artifacts, like the ritual golden cones interpreted as headgear for solar cult priests, and the Goseck Circle (Bertemes et al., 2007), known as the oldest solar observatory, further emphasize the significance of observing and studying the stars (*Figure 2.1*).

In antiquity, astronomy played a pivotal role not only in religious cults but also as a science. During this time, Babylonian astronomers noticed variations in the positions of stars when observing the sky on the same day of the year and at the same hour, without fully understanding the underlying cause. Subsequently, the Greeks were the first to separate astronomy as a scientific pursuit from its associations with religious practices. This led to a remarkable advancement in astronomy. During this period a Greek astronomer named Hipparchus hypothesized that the Earth's axis direction changes gradually by more than one degree per century by comparing representations of the sky made a century earlier with his own observations (*Figure 2.1*). This observation, previously made by the Babylonians, is now known as the precession of the equinoxes, one of the key orbital parameters influencing Earth's climate. Pytheas, another Greek astronomer, observed the inclination of the Earth's axis with respect to the ecliptic plane (*Figure 2.1*). By measuring the length of shadows during the summer solstice, he deduced that the sun was not aligned with the equator on that day. Later, he directly witnessed this inclination during his journey above the Arctic Circle, describing the phenomenon of the midnight sun during the summer solstice, a direct consequence of Earth's axial tilt. Eratosthenes also demonstrated this phenomenon (*Figure 2.1*). It was not until the early 17th century, with the invention of the first telescope and its refinement by Galileo and

Kepler, that the last of the three major orbital parameters influencing Earth's climate could be observed. Johannes Kepler, based on his observations of the orbit of Mars, discovered the eccentricity of the orbits of planets, publishing his findings in his book "Astronomia nova" (1609) (*Figure 2.1*).

However, it would take several centuries before a connection was established between Earth's orbital parameters and climate. The idea that variations in orbital parameters are responsible for significant changes in Earth's past climate emerged primarily in the mid-19th century. It was first essential to demonstrate the presence and recurrence of glaciations on Earth. In 1824, the Norwegian, Jens Esmark, suggested that variations in Earth's orbit cause climate changes (*Figure 2.1*). The Swiss geologist Louis Agassiz, in 1837, recognized that glaciations were the cause of moraines and erratic blocks found in various locations in the Alps, Scotland, and Scandinavia, echoing his Norwegian colleague (*Figure 2.1*). A few years later, the French mathematician Adh mar (in "R volutions de la Mer: D luges p riodiques," private publication, Paris, 1842) proposed that Earth's orbital variations could be responsible for climatic changes and glacial cycles (*Figure 2.1*). Adh mar's idea, though deemed absurd by his contemporaries, strongly influenced the later work of Croll (1875), who developed the first detailed astronomical theory of paleoclimates (*Figure 2.1*). Croll's theory made a major breakthrough by demonstrating the modulation of precession by variations in eccentricity. Although he also suggested that changes in obliquity could play a role, he was unable to estimate them. The interest in astronomical theories of climates experienced a resurgence with the work of the Serbian mathematician Milutin Milankovitch between 1920 and 1941 (*Figure 2.1*). Utilizing increasingly improved astronomical solutions, Milankovitch calculated the summer insolation at the top of the atmosphere for different latitudes, considering variations in Earth's eccentricity, precession, and obliquity. Nevertheless, similar to Croll's theory, Milankovitch's prediction of alternating glacial periods, regardless of continental distribution and more detailed climate considerations related to oceanic and atmospheric circulation, was met with scepticism from many climatologists and geologists. Over time, the combination of contributions and improvements from astronomical solutions, particularly from the Paris Observatory (Le Verrier, 1856, as the precursor), along with geological and geochemical data from the 1950s onwards, gradually allowed for testing and validating the idea of astronomical influence on climate variability. In 1976, Jim Hays and his colleagues demonstrated for the first time the presence of Milankovitch cycles (eccentricity, obliquity, and precession) in the variation of continental glacier volume over the past 500,000 years (Hays et al., 1976; *Figure 2.1*).

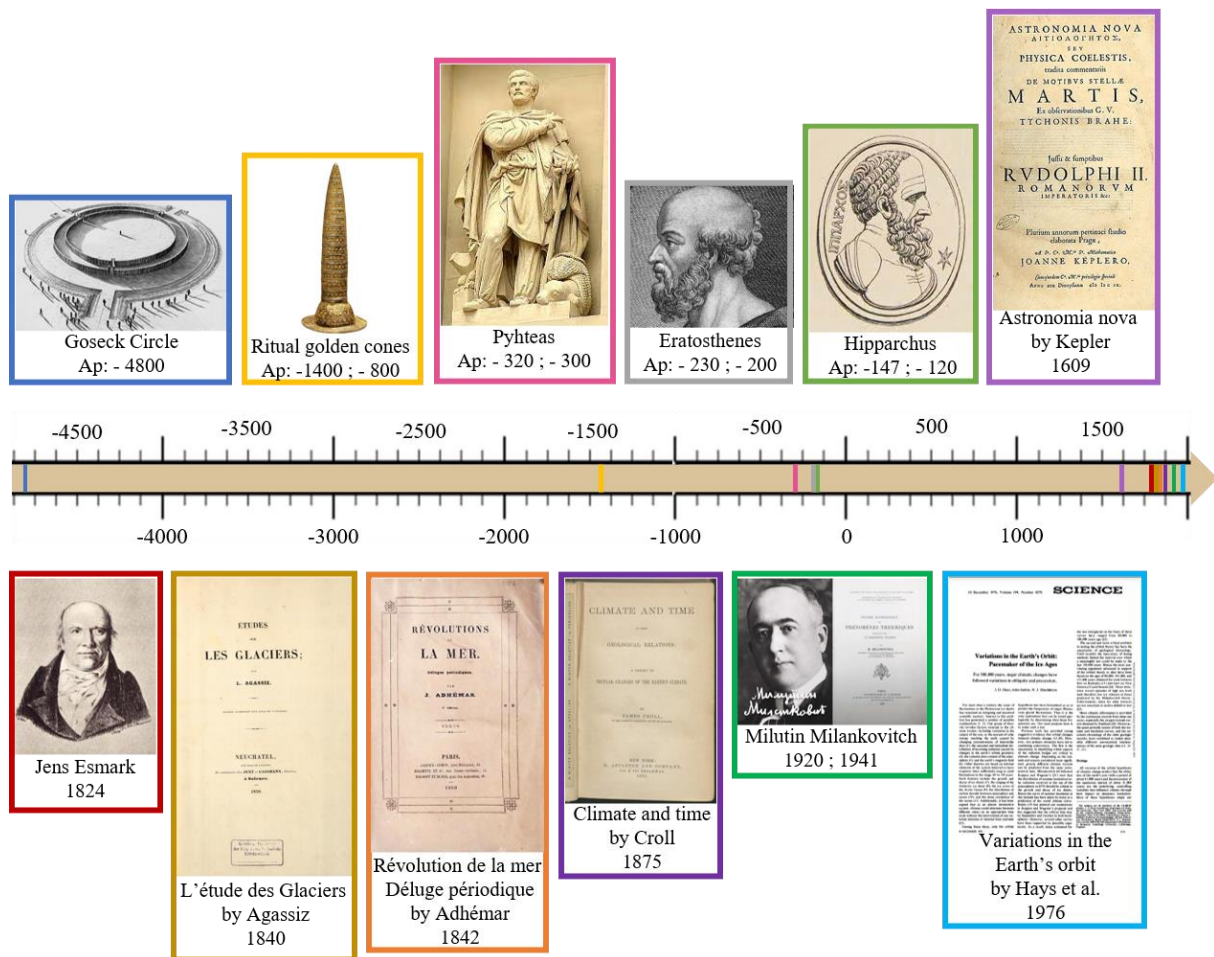


Figure 2.1: Timeline of discovery of the main astronomical parameters impacting the Earth's climate. Ap means approximately.

2.1.2. Earth's orbital eccentricity cycles

The eccentricity of an orbit is a measure of the difference between a hypothetical perfectly circular orbit and the actual orbit of a celestial body (*Figure 2.2*). Eccentricity is expressed in dimensionless values. This variation in a planet's orbit is caused by the gravitational forces of other celestial bodies nearby, which slightly alter its trajectory. The eccentricity of Earth's orbit ranges from a nearly circular trajectory (~ 0) to a more elliptical orbit (~ 0.06). The multitude of celestial bodies influencing Earth's trajectory results in quasi-periodic variations in Earth's eccentricity (Laskar et al., 2011, 2004). The main cycles of Earth's eccentricity variations occur at approximately 95,000, 125,000, and 405,000 years (*Figure 2.2*). The 405,000-year eccentricity component, which is called the “long” eccentricity cycle, is with the largest amplitude, and is considered to be the most stable among all of Earth's orbital eccentricity cycles (Laskar et al., 2004). It is therefore used to astronomically calibrate the Cenozoic and

Mesozoic time scales (Hinnov, 2013). However, many other cycles exist. In 2015, a study demonstrated the presence of a 9-million-year cycle in Earth's orbit, potentially associated with interaction with the planet Mars (Martinez and Dera, 2015).

Eccentricity significantly influences Earth's climate, particularly when Earth's eccentricity is at its maximum (0.058) and the planet is at its closest point to the Sun in its trajectory. During this time, our planet can receive up to 26% more energy compared to the energy received at its farthest point from the Sun. Unlike other parameters, the effect of eccentricity is uniform across the globe, independent of latitude (Berger and Loutre, 1994).

2.1.3. Earth's obliquity cycles

Obliquity refers to the angle between the rotational axis of a celestial body and a perpendicular axis to the plane of its orbit, passing through the centre of the body (*Figure 2.2*). This parameter is influenced by the gravitational interactions between a planet and other celestial bodies in its vicinity. Earth's obliquity varies between 21.8° and 24.4° over a 41,000-year period (*Figure 2.2*). At present, Earth's obliquity is gradually decreasing and currently stands at 23.44° , reaching its lowest value in approximately 10,000 years. The positioning of the tropics is directly linked to the obliquity parameter, as they represent the latitudes intersecting the plane of Earth's orbit during the summer solstice in each hemisphere. Similarly, the polar circle is affected by Earth's inclination, representing the part of the poles illuminated for at least a full day during the summer solstice and experiencing no sunlight for a complete day during the winter solstice. The polar circle shifts in latitude with changes in obliquity. Earth's obliquity plays a crucial role in determining the seasons. For instance, the summer solstice in the Northern Hemisphere occurs when the North Pole is most inclined toward the Sun. The influence of Earth's distance from the Sun is relatively minor compared to obliquity when it comes to the solar energy received, resulting in the possibility of the summer solstice coinciding with the time when Earth is farthest from the Sun. Notably, the obliquity parameter significantly affects higher latitudes, intensifying the distinction between seasons with colder winters and hotter summers (Berger and Loutre, 1994).

2.1.4. Earth's precession cycles

Precession is the term used to describe the variation in the direction of the rotational axis of a celestial body (*Figure 2.2*). The precession of Earth's spin axis is particularly influenced by the gravitational forces of the Sun and the Moon (Murray and Dermott, 1999). Its present

periodicity also called the precession constant is about 25,800 years (Laskar et al., 2004). However, the astronomical precession that controls Earth's climate, called the climatic precession, arises from the combination of the precession constant and the precession of perihelion. The precession of perihelion is related to the variation of the eccentricity, which depends on the motion of the other planets. That's why the climatic precession is modulated by the eccentricity. If the eccentricity is zero, i.e., the orbit of the Earth follows a circle, the effect of the precession of the equinoxes is also zero. Earth's climatic precession is characterised by two main cycles of approximately 19,000 and 23,000 years (Hays et al., 1976). The effect of precession on Earth's climate depends on the orientation of the rotational axis with respect to Earth's orbit. If the axis is tilted toward the Sun (with the North Pole closest to the Sun) during Earth's approach to its perihelion (the point in its orbit closest to the star), the summer in the Northern Hemisphere will be particularly warm, while the winter in the Southern Hemisphere will be mild (*Figure 2.2*). Conversely, when Earth moves towards its aphelion (the point in its orbit farthest from the star), the Northern Hemisphere will experience a harsh winter, and the Southern Hemisphere will have a milder summer (Berger and Loutre, 1994). As a result, seasons will be more pronounced in one hemisphere and less so in the other. The effect of precession is distinct and significant depending on the hemisphere being considered.

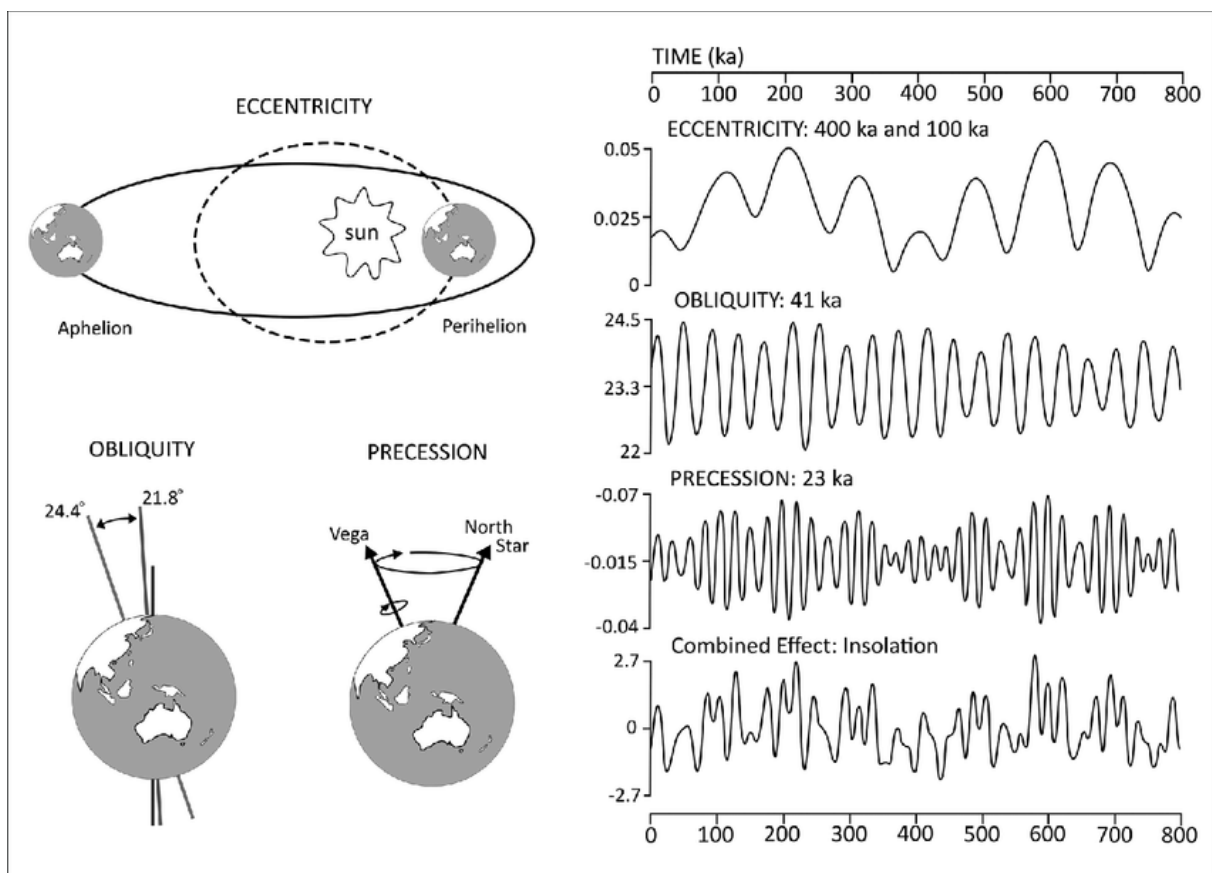


Figure 2.2: From Imbrie, 1985: Variation in eccentricity, obliquity and precession over the past 800 ka and their combined effect on insolation. The obliquity scale is in degrees. The insolation scale is in standard deviation units.

2.1.5. Modelling and limitations of the astronomical parameters through geological time

Since the significance of Earth's orbital parameters on climate has been established, some researchers have been dedicated to reconstructing past astronomical cycles (Williams, 1993). The initial models that reconstruct the motions of celestial bodies and their implications on Milankovitch parameters were solely based on physical theories and short-term astronomical observations. These models are then used in the analysis of sedimentary successions through a discipline known as cyclostratigraphy. By associating cyclic variations in the sedimentary record (lithology, sediment colour, rock chemical and physical properties, etc) with orbital cyclicities, this approach provides a mean to measure relative ages of the sedimentary series (astrochronology) and insights into how Earth's past climate responded to orbitally forced insolation. However, these numerical models do have certain limitations; for instance, even a minor variation of one meter in the initial position of a planet within the model can result in significant differences among the analysed astronomical solutions after approximately ten million years (Laskar, 1999).

Advancements in various astronomical models have given rise to multiple astronomical solutions: Quinn91, La93, Varadi03, La04, La10 (Laskar et al., 2011, 2004, 1993; Quinn et al., 1991; Varadi et al., 2003). Nonetheless, modelling the motion of celestial bodies beyond 65 million years remains a challenge (Laskar et al., 2011). To enhance these models, the data acquired can no longer be based solely on astronomical observations. Geological insights now complement the improvement of the models. Cyclostratigraphy, for example, provides the duration of Milankovitch cycles, which are then utilized to calibrate the models on very long timescales (Charbonnier et al., 2023; Westerhold et al., 2015; Zeebe and Lourens, 2022, 2019).

2.2. Earth's climate during the Cenozoic:

2.2.1. Mechanisms influencing Earth climate: external (orbital) versus internal drivers

Various processes influence Earth's climate, and some of them are external to the Earth system as the Astronomical parameters discussed in previous chapters. However, many other factors also play a crucial role in shaping Earth's climate on different timescales. For example, the movement of tectonic plates causes shifts in continental positions, significantly impacting climate over tens to hundreds of millions of years (Boulila et al., 2018; Hay, 1996). The formation of mountain ranges leads to increased erosion and dramatic changes in wind patterns, influencing climate over tens of millions of years. Earth's volcanic activity can cause climate variations spanning several million years down to just a few years (Nikolov and Petrov, 2014). Additionally, the amount of CO₂ in the atmosphere plays a significant role in climate dynamics over timescales ranging from millions to hundreds of years (Kump et al., 2000). Other factors, such as cosmic rays and solar activity, have shorter-term effects, spanning up to several thousand years at most. Some of these parameters create feedback loops, triggering chain reactions. One such example is the albedo effect, where ice and snow reflect light, reducing solar energy received on Earth, which in turn promotes further ice growth, leading to a snowball effect. In contrast, external parameters like orbital cycles do not create feedback loops; they are entirely independent of Earth's climate system and can cause shifts between glacial and interglacial phases over periods of hundreds to tens of thousands of years (Berger and Loutre, 1994).

2.2.2. The Northern Hemisphere Glaciation (NHG) and its intensification

Early evidence of Northern Hemisphere glaciation, represented by isolated glaciers and small ice caps reaching Greenland or Svalbard's coastlines, has been discovered through glaciogenic microstructures on Palaeocene quartz sand grains (Immonen, 2013), as well as in Ice-Rafted Debris (IRD) records from the middle Eocene (45 Ma) in the Arctic Ocean (Moran et al., 2006), and from the middle Eocene (44 Ma) to early Oligocene (38–30 Ma) in the Greenland Sea (Eldrett et al., 2007). However, it was only during the middle to late Miocene and Pliocene that small-scale glaciations in the Arctic region became more frequent (e.g., Knies and Gaina, 2008), and the late Pliocene marked the transition from local to extensive regional-scale glaciations in

the Northern Hemisphere (Bailey et al., 2013; De Schepper et al., 2014; Kleiven et al., 2002) (*Figure 2.3*).

While the first major glaciation in the southern hemisphere occurred around 35 million years ago, the earliest recorded of major glaciation in the Northern Hemisphere is dated between 15 and 6 million years ago during the late Miocene (e.g., ODP Leg 151, 1994; (Eldrett et al., 2007; Herbert et al., 2016; Jansen and Sjøholm, 1991; Maslin et al., 1995; Moran et al., 2006) (*Figure 2.3*). This period saw a significant build-up of ice on Southern Greenland, but the process gained more momentum around 3.5-3 million years ago when the Greenland ice sheet expanded to include Northern Greenland (*Figure 2.4*). Evidence reviewed in (Maslin et al., 1998) suggests that the initiation of large-scale Northern Hemisphere glaciation was the culmination of a longer-term, high-latitude cooling (Maslin et al., 1998, 1996, 1995; Raymo, 1994).

The progressive spread of ice-sheets through the northernmost latitudes occurred during episodes that seemed to have come on relatively suddenly, at least when considering a timescale of several million years (Jakob et al., 2020). Stepwise episodes of widespread increase in iceberg activity, indicated by grit dropped to the sea floor by melting bergs, and corresponding falls in sea level indicating ice buildup on land surfaces, occurred at various intervals, including 2.74 Ma (corresponding to rapid glaciation of the Eurasian Arctic and Northeast Asia), 2.70 Ma (glaciation of Alaska), and major glaciation of the North American continent at 2.54 Ma (Schackleton et al., 1995) (*Figure 2.4*). However, the step-like nature of the ice rafting records may conceal a more gradual process of ice build-up inland, as indicated by the progressive $\delta^{18}\text{O}$ enrichment of deep-sea (benthic) isotope records (Schackleton et al., 1995). The ice-rafting records only indicate when continental ice sheets were mature enough to spill over the landmass onto adjacent oceans, and the events may not have been as sudden as they appear.

Numerous gradual processes, spanning millions of years, are believed to have played a crucial role in setting the stage for Northern Hemisphere glaciation (Maslin et al., 1996; Maslin et al., 1998). Tectonic changes, including the uplift of the Himalayan-Tibetan Plateau (Raymo, 1994; Raymo and Ruddiman, 1992; Ruddiman and Raymo, 1988; Zhisheng et al., 2001), the deepening of the Bering Strait (Brierley and Fedorov, 2016; Haywood et al., 2016; Marinovich and Gladenkov, 1999), and/or the formation of the Greenland-Scotland ridge (Uenzelmann-Neben and Gruetzner, 2018), as well as the emergence of the Panama Isthmus (Haug and Tiedemann, 1998; Jaramillo et al., 2018; O’Dea et al., 2016), have been proposed as significant factors (Brierley and Fedorov, 2016; Raymo, 1994). However, these processes alone seem too

gradual to fully account for the rapid onset of Northern Hemisphere glaciation, particularly during the periods of rapid ice growth indicated by ice-rafting events.

In an attempt to explain the apparent abruptness of ice sheet evidence in each region, Maslin et al. (1998, 1996) suggest that tectonic changes may have gradually brought the global climate to a critical threshold. At this point, relatively rapid variations in the Earth's orbital parameters (and thus insolation) triggered extensive Northern Hemisphere glaciation. This theory is supported by computer simulations of the ice-and-climate system, indicating that it is possible to build up Northern Hemisphere ice sheets within a relatively brief 200,000 years, around 2.75 to 2.55 million years ago, by altering only the seasonal solar radiation pattern controlled by orbital parameters (Maslin et al., 1998). Nevertheless, it is important to exercise caution due to the relative simplicity of the model and the approximation of certain factors, such as neglecting the differences in continental arrangement between the Pliocene and the present.

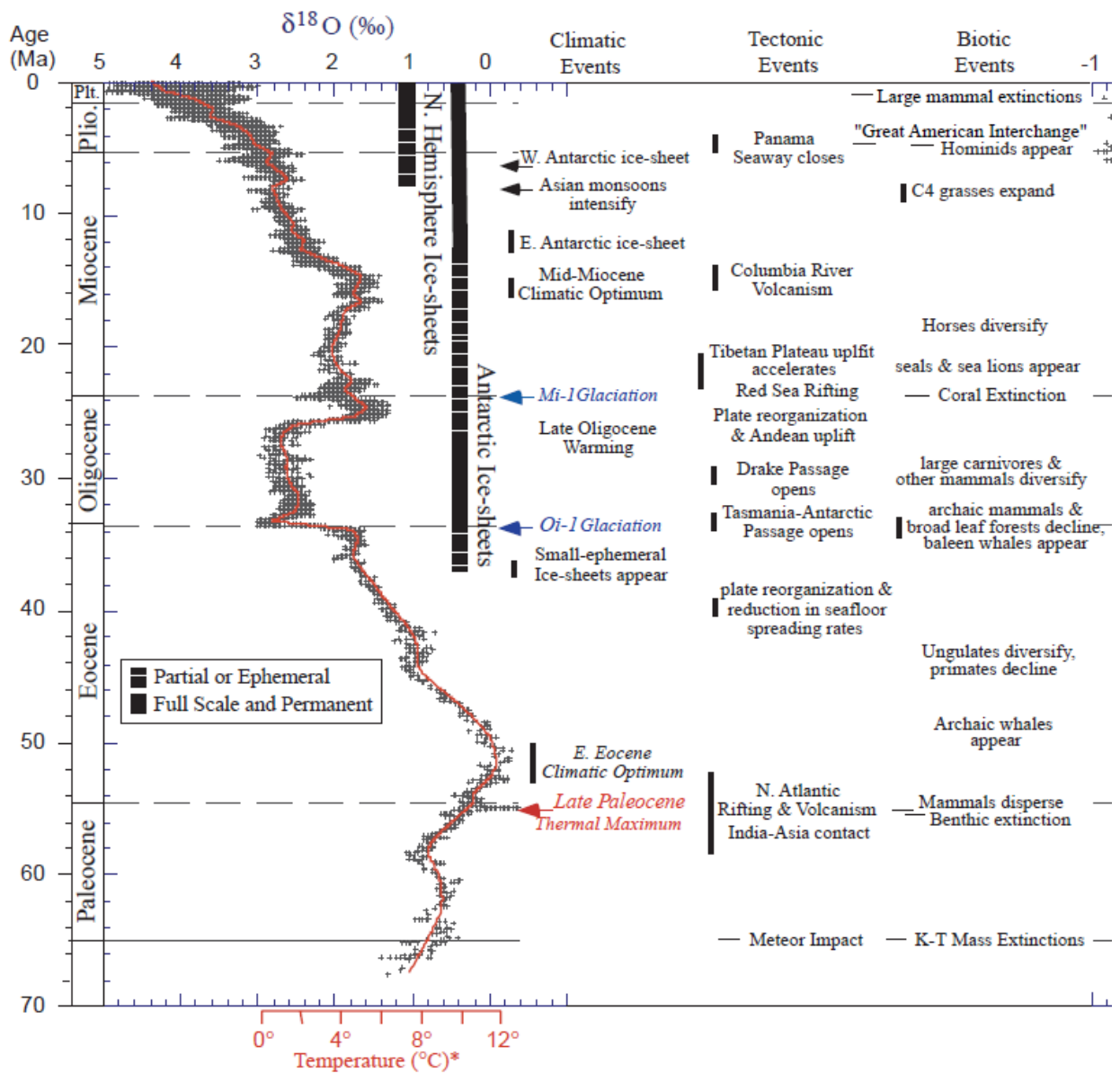


Figure 2.3: From Zachos et al., 2001: Global deep-sea oxygen records based on data compiled from more than 40 DSDP and ODP sites. The $\delta^{18}\text{O}$ temperature scale was computed for an ice-free ocean [$\sim 1.2/1000$ Standard Mean Ocean Water (SMOW)], and thus only applies to the time preceding the onset of large-scale glaciation on Antarctica (~ 35 Ma). The vertical bars provide a rough qualitative representation of ice volume in each hemisphere relative to the LGM, with the dashed bar representing periods of minimal ice coverage ($<50\%$), and the full bar representing close to maximum ice coverage ($>50\%$ of present). Some key tectonic and biotic events are listed as well.

2.2.3. The Mid-Pleistocene Transition and its impacts on glacial-interglacial cycles

The Mid-Pleistocene Transition (MPT) represents a significant shift in Earth's climate system. Early Pleistocene glacial-interglacial (G-IG) cycles were primarily paced by approximately 40,000-year obliquity cycles. However, after the MPT, G-IG cycles gradually intensified to reach cycles of 100,000-year. It is still unclear if this cyclicity is related to the eccentricity parameter or if it is the effect of multiple obliquity cycles (Berends et al., 2021). The precession also plays an important role either by a combination with eccentricity or obliquity. The longer G-IG cycles exhibit an asymmetric pattern with gradual glacial growth and abrupt terminations. These changes led to longer, colder, and dustier Late Pleistocene ice ages, characterised by larger continental ice sheets and lower global sea levels (Chalk et al., 2017; Head and Gibbard, 2015, 2005).

The MPT occurred without any notable changes in orbital forcing, indicating an internal shift within the climate system rather than an external influence. During the early Pleistocene, subtle signs of this transition appeared, such as the saw-tooth asymmetry in glacial cycles, which became more pronounced over time. Around 1.4 million years ago, there was a significant decrease in the relative durations of interglacials, and the glacial cycles ceased to be modulated only by obliquity forcing, marking a major transition in climate dynamics (Lisiecki and Raymo, 2007, 2005).

Between 1.25 and 1.2 million years ago, low-frequency variability emerged, along with increased power in the 70-kyr band and long-term global ice-volume increase (Head et al., 2008). During this period, various adjustments occurred in the climate system, including the intensification of the tropical Pacific Ocean and atmospheric circulation, evolution of the Asian monsoon system, cooling and expansion of subarctic and polar water masses, cooling in upwelling systems and the deep Atlantic Ocean, and changes to the thermohaline circulation (McClymont et al., 2013 and references therein).

The progression of the MPT can be seen in the wavelet analysis of the LR04 stack, with low-frequency variability gaining power at around 1000–900 thousand years ago and intensifying around 700–650 thousand years ago. The transition from 41 kyr G-IG cycles to 100 kyr is considered complete by approximately 700 thousand years ago, as supported by various studies (e.g. Clark et al., 2006), or at different points like 640 thousand years ago (Hodell et al., 2008) or 420 thousand years ago (Billups et al., 2006).

2.2.4. The enigmatic Mid-Brunhes Transition

Starting around 430,000 years ago (Marine Isotope Stage 11; *Figure 2.4*), interglacial periods have experienced higher temperatures (Jouzel et al., 2007a) and increased concentrations of atmospheric CO₂ (Lüthi et al., 2008a) compared to earlier interglacial periods within the last 800,000 years. Deep-sea foraminiferal $\delta^{18}\text{O}$ records have also confirmed the transition to higher-amplitude interglacial periods, indicating reduced ice volume and/or warmer deep-ocean temperatures (Lisiecki and Raymo, 2005).

Originally labelled as a singular Mid-Brunhes Event, the change in interglacial amplitude was later redefined by Yin (2013) as the Mid-Brunhes Transition (MBT), denoting a shift between two distinct climate states. The change from low-amplitude to high-amplitude 100,000-year variability around 430,000 years ago coincides with a period of reduced eccentricity and precession variations. Similar orbital conditions occurred before and after the MBT, but no comparable response was observed, suggesting that the MBT was due to an internal change within the climate system (Barth et al., 2018). Several mechanisms have been proposed to explain the MBT, including a latitudinal shift in the position of the Southern Hemisphere westerlies leading to increased upwelling of respired carbon in the post-MBT Southern Ocean (Kemp et al., 2010). Another proposed mechanism involves changes in Antarctic Bottom Water formation due to insolation-induced feedbacks on sea ice and surface water density (Yin, 2013).

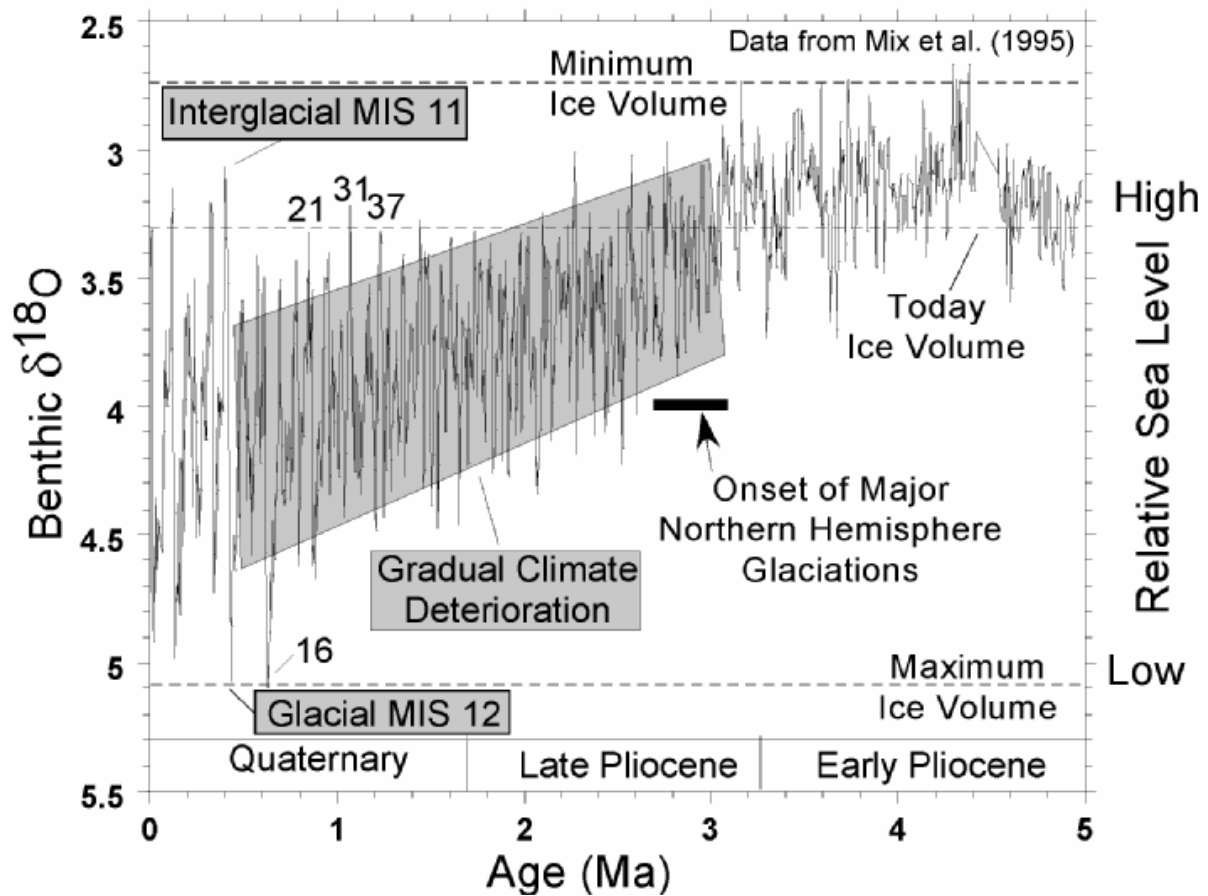


Figure 2.4: From Droxler et al. (2003): The benthic oxygen isotope record at ODP Site 849 from the eastern equatorial Pacific Ocean in 3839 m of water depth (Mix et al., 1995) can be used as a reliable proxy for ice volume and, therefore, climate and sea level changes for the last 5 My. Since the onset of major glaciations in the Northern Hemisphere about 3.0 to 2.7 Ma, the Earth climate evolution displays three main characteristics: (1) the gradual cooling of the Earth climate in the past 3.0 My, (2) the Earth climate cyclic fluctuations first at about 41 ky per cycle linked to the variations of the tilt of the Earth axis (or obliquity) and then at lower frequency of about 100 ky per cycle (or orbital eccentricity), and (3) the transition from glacial MIS 12 (the heaviest glacial values with MIS 16) to interglacial MIS 11, characterised by the first lightest values in the late Quaternary, therefore a unique glacial to interglacial transition due to its extreme amplitude.

2.3. Opening of the Atlantic Ocean and creation of the Brazilian Equatorial Margin

The Brazilian Equatorial passive margin is the result of the opening of the Atlantic Ocean. Evidence for the age and geographical extent of the rifting process can be found in sediment accumulation along the margin. In the following sections, we offer a review of the primary phases of this opening.

2.3.1. Phase 1

The Offshore Amazon Basin began accumulating sediments in the Late Triassic-Early Jurassic period (235-194 Ma), during which it underwent deformation due to the Central Atlantic opening (Figueiredo et al., 2007) (*Figure 2.5*). However, the precise impact of this event on the Offshore Amazon Basin remains uncertain. While some authors propose that the region became a relatively calm sag basin during the Late Triassic-Early Jurassic (Figueiredo et al., 2007), others suggest that a branch of the Central Atlantic rift influenced the area (Soares Júnior et al., 2011, 2008). According to the latter group, this rift branch was initially active but got abandoned near the Triassic-Jurassic transition, only to reactivate during the Early Cretaceous (Soares Júnior et al., 2011, 2008) (*Figure 2.5*). Soares Júnior et al. (2008) termed this potential early aborted rift as the "First event" within a three-phase model describing the Equatorial Atlantic's opening.

2.3.2. Phase 2-3

The most significant rifting occurred in the Offshore Amazon Basin during the Early Cretaceous, coinciding with the breakup of South America and Africa and the creation of the Equatorial Atlantic Ocean (De Matos et al., 2000; Figueiredo et al., 2007; Soares Júnior et al., 2008). This rifting involved extensional and transform movements that resulted in complex marginal sedimentary basins along the Equatorial Atlantic Margin (*Figure 2.5*). These basins exhibited various subsidence phases and structural styles (De Matos et al., 2000; Soares Júnior et al., 2008). Soares Júnior et al. (2011, 2008) divided the Early Cretaceous rifting into two events (Second and Third events). According to them, during the Berriasian to the Aptian, the Equatorial Atlantic's initial opening marked the second rifting event (*Figure 2.5*). This phase reactivated, expanded, and extended the Late Triassic-Early Jurassic grabens from the First Event, connecting the northern Offshore Amazon Basin's rift system (Cassiporé Graben) with

the newly formed Marajó Basin in the south (*Figure 2.5*). Subsequently, a Third Event (Albian) created a rift system characterised by a sequence of normal faults propagating from SE to NW along the Equatorial Margin, eventually leading to continental breakup (*Figure 2.5*). Soares Júnior et al. (2011, 2008) assert that after this third event, by the end of the Albian, oceanic crust began to form in the Offshore Amazon Basin. Although the model of two Cretaceous rifting events by Soares Júnior et al. (2011, 2008) aligns with the geodynamic Equatorial Atlantic model proposed by Basile et al. (2005). According to the latter authors, the opening of the Equatorial Atlantic was dominated by divergent motions until the late Aptian. However, Basile et al. (2005) states that from late Aptian deformation began to take place along intra-continental transform faults leading to oceanic crust accretion during the latest Albian, thus differing from the exclusively divergent rifting model proposed by Soares Júnior et al. (2011, 2008) for the Amazon margin. Nonetheless, Basile et al. (2005) also categorises most of the Offshore Amazon Basin and the conjugate African basin in Liberia as divergent margin segments.

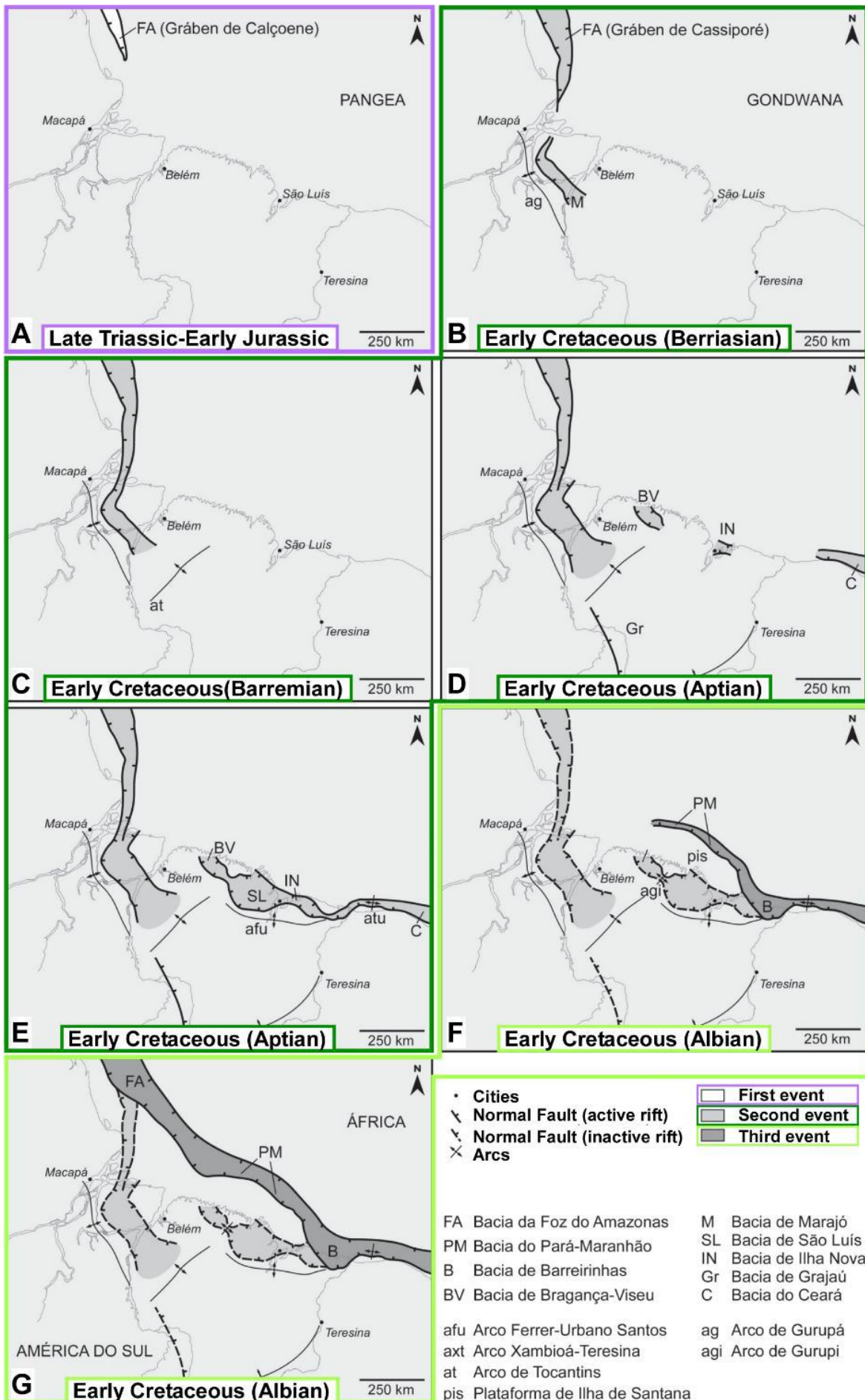


Figure 2.5: Brazilian Equatorial Margin extensional events according to Soares Júnior et al. (2008): (A) First Event from Early Triassic to Late Triassic, highlighted in purple; (B-E) Second Event from Berriasian to Aptian, highlighted in dark green and (F-G) Third Event during the Albian, highlighted in light green. Note that the rifting process in the northern part of the Equatorial margin is attributed to extensional motions associated with normal faults, with no strike-slip faulting.

2.3.3. Syn-rift Formation

Study based on gravity and magnetic anomalies with seismically imaged basement and syn-rift structures, reveals three distinct structural regions along the Amazon margin (Cruz, 2018) (*Figure 2.6*). These regions align approximately with areas displaying varying Neogene geodynamics-associated post-rift stratigraphic architectures as described by Cruz et al. (2019). These regions are believed to correspond to distinct sub-basins: the Cassiporé sub-basin, the Araguari sub-basin, and the Machadinho sub-basin, situated from NW to SE respectively (*Figure 2.6*). These sub-basins' unique features are thought to mirror the intricate rifting processes on the Amazon margin, which led to a diverse structural framework significantly influencing sediment deposition from syn-rift to post-rift periods. The syn-rift megasequence formed mainly during the Early Cretaceous, concurrent with the Equatorial Atlantic Ocean's opening. This megasequence predominantly comprises the Cassiporé Formation's regressive siliciclastic deposits (including fluvial-deltaic and lacustrine intercalated shales and fine sandstones) and the Codó Formation's transgressive shales and calcilutites (Brandão and Feijó, 1994; Figueiredo et al., 2007). These formations were laid down within structural lows (grabens and half grabens) and attain a maximum estimated thickness of 7 km (Brandão and Feijó, 1994; Figueiredo et al., 2007).

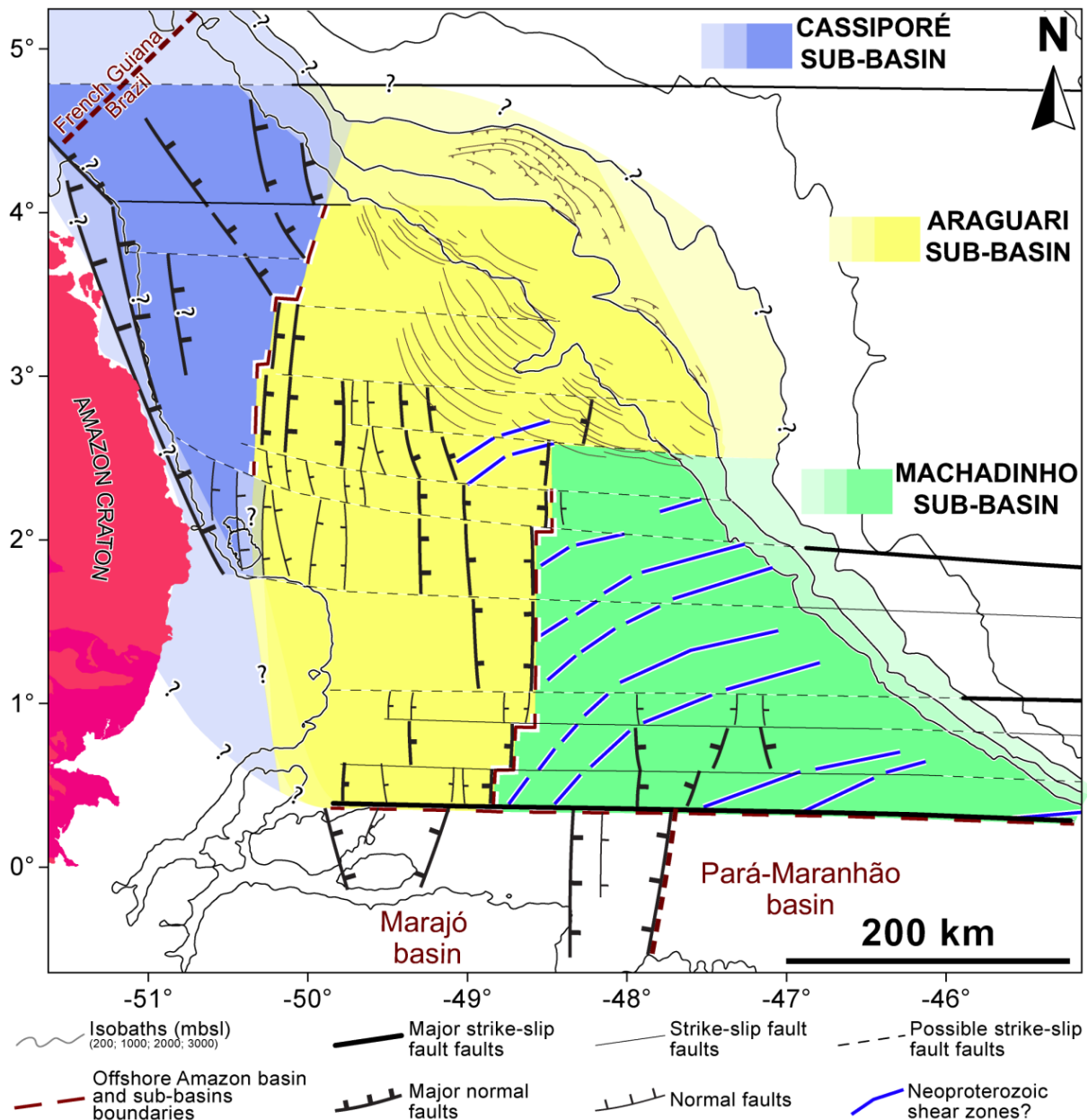


Figure 2.6: From Cruz (2018): Simplified structural framework of the Offshore Amazon Basin based on an integrated analysis of seismic reflection and potential field data. Thin lines on the Araguari sub-basin outer shelf-slope region represent faults recording gravity-driven deformation of the post-rift sedimentary succession, simplified from Perovano et al. (2009).

2.3.4. Post-rift formation until the Amapá platform

Figueiredo et al. (2007) indicates that post-rift megasequence deposition commenced towards the late Albian (around 102 Ma), marked by the Limoeiro Formation's onset, reflecting the beginning of open marine sedimentation (Figure 2.7). Originally characterised by Schaller et

al. (1971), the Limoeiro Formation constitutes interbedded sandy and muddy sediments that extend beyond basin structural lows but attain their greatest thickness within them (*Figure 2.7*). The Limoeiro Formation's maximum thickness is estimated at 2.5 km (Brandão and Feijó, 1994). Brandão and Feijó (1994) describe varying deposition conditions ranging from fluvial to bathyal, encompassing diverse depositional environments. The deposition of the Limoeiro Formation ends during the Early Paleocene (Danian) (*Figure 2.7*).

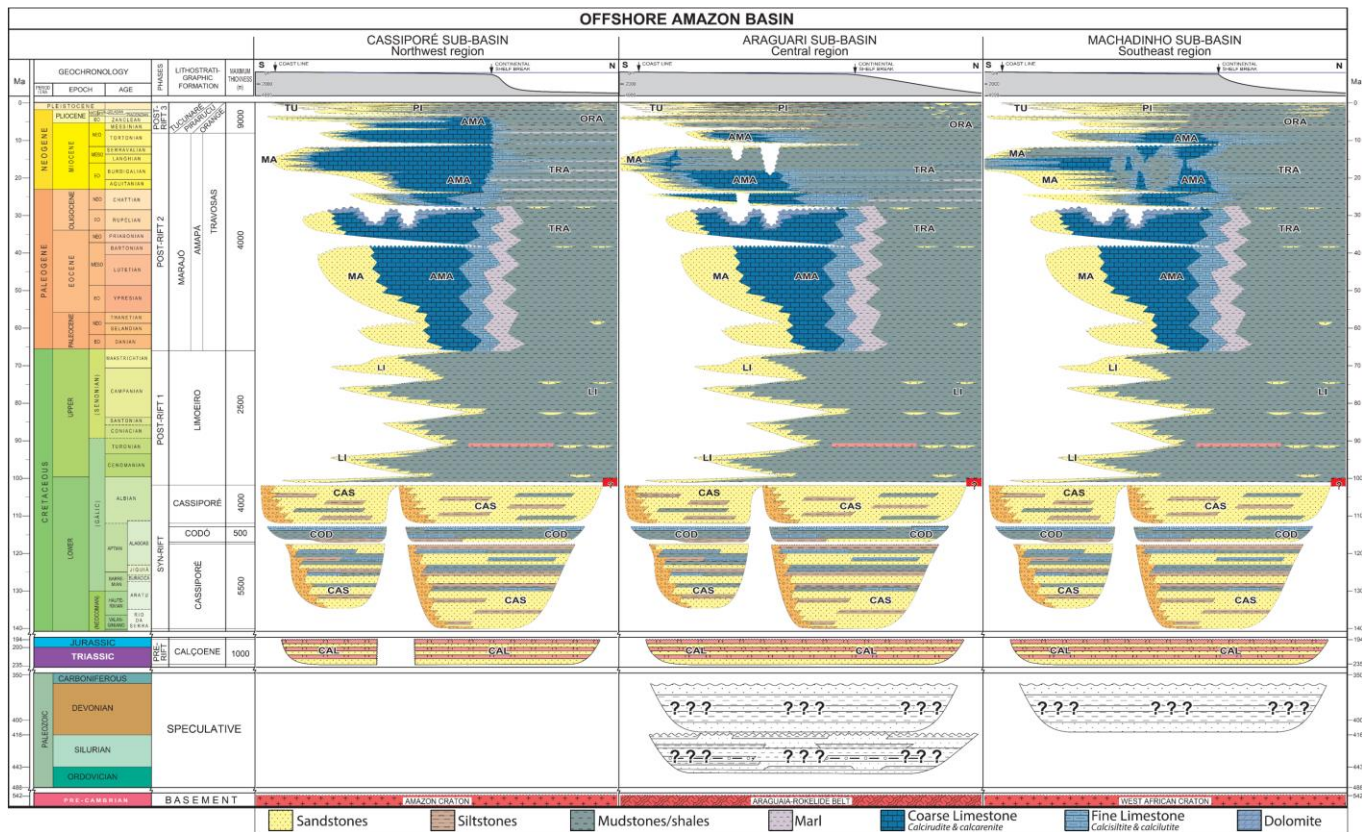


Figure 2.7: From Cruz, 2018: Stratigraphic charts of the three sub-basins of the Offshore Amazon Basin.

Figueiredo et al. (2007) propose that the second post-rift megasequence was deposited from the Late Paleocene to the Middle Miocene (*Figure 2.7*). During this phase, Brandão and Feijó (1994) identify three coeval formations: the proximal Marajó Formation (comprising siliciclastic sediments), the laterally extensive Amapá Formation (consisting of shelfal carbonates), and the distal Travosas Formation (dominated by muddy sediments across the slope and deep basin).

As per Carozzi (1981), the Amapá Formation likely represents a significant coralgal-foraminiferal platform, mainly formed through substantial bioaccumulation of red algae and large foraminifers. The Amapá Formation's carbonate evolution is described by Carozzi (1981)

and Wolff and Carozzi (1984) in terms of four major depositional cycles (*Figure 2.7*), punctuated by widespread subaerial exposure:

- Cycle I: Paleocene to Early Eocene, reflecting the establishment of a mixed carbonate-siliciclastic platform featuring a broad lagoonal environment, oolitic shoals, and intermittent foraminifer banks surrounded by mechanically reworked calcarenites. This cycle lacks red algae deposits and the outer shelf is predominantly composed of nummulitid banks.

- Cycle II: Middle Eocene, indicating the expansion of carbonate-dominated environments and the development of a wide belt of large foraminifer and red algae banks, along with their reworked calcarenites. The widening belt leads to a narrower lagoon landward and promotes the seaward progradation of outer shelf bank deposits over the previous cycle's slope deposits. Proximal fan delta and lagoonal shale conditions remain restricted behind the carbonate platform during this deposition.

- Cycle III: Late Eocene to Late Oligocene, showcasing the stabilization and further expansion of carbonate-dominated environments. However, during this cycle, a series of canyons/troughs partially filled with olistoliths and shales start to cut through banks/atolls in the central shelf.

- Cycle IV: Early to Middle Miocene, recording the "destruction" of the carbonate shelf. The previous large foraminifer belt vanishes, replaced by outer shelf red algae banks. Increased shelf breaching leads to canyons forming on the central shelf, and the previous lagoonal environment shifts to open marine conditions.

Numerous studies have proposed that the Offshore Amazon Basin's shelfal carbonate sedimentation ceased due to significant influxes of terrigenous sediments (*Figure 2.8*) around the transition from the Middle to Late Miocene (Brandão and Feijó, 1994; Carozzi, 1981; Figueiredo et al., 2007; Schaller et al., 1971). This influx of terrigenous material is attributed to the initiation of a transcontinental Amazon River. Nevertheless, the cause of such a terrigenous influx into the basin and the timing of this event have sparked debates.

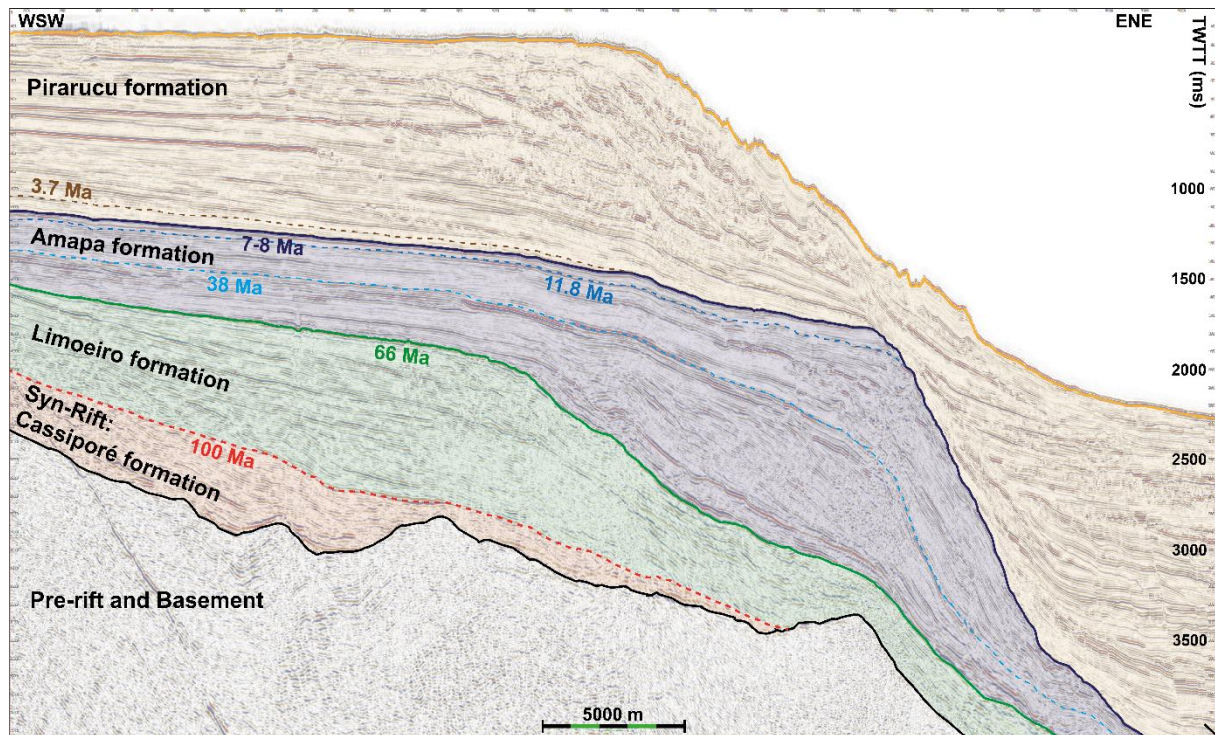


Figure 2.8: Inline 2300 revealing the different formation along the ACM and main biostratigraphic age.

2.4. Andean orogeny

2.4.1. The main stages of the orogeny

The Andean orogeny, a complex geological event ongoing for approximately 150 million years, has primarily sculpted the Andes Mountains along the western margin of South America (James and Sacks, 1999; Sempere et al., 1990). Originating in the Late Jurassic period, this orogenic system was initiated by the subduction of the Nazca Plate beneath the South American Plate. It has encompassed a series of intricate deformation events, volcanic activities, and metamorphic transformations, significantly influencing both the northern and central segments of the Andes (Bayona et al., 2008; Mora et al., 2010).

Following its inception during the Jurassic to Early Cretaceous periods, the continental margin underwent substantial deformation. Concurrently, the development of magmatic arcs and the accumulation of sediments in the forearc and back-arc basins facilitated the formation of fold-thrust belts (Charrier et al., 2007). Subsequently, from the Late Cretaceous to the Paleogene, the collision of various terranes with the South American continental margin resulted in intense crustal shortening and thickening (Cobbold et al., 2007). This compression

gave rise to the uplift of the Western Cordillera, thereby laying the groundwork for modern Andean topography (Mpodozis and Ramos, 1990) (*Figure 2.9*).

Deformation in the northern and central Andes has been generally episodic, characterized by brief, intense pulses of contraction, interspersed with periods of tectonic quiescence or extensional collapse (Noble et al., 1990). Following a prolonged period of relative tectonic inactivity during the Late Oligocene and earliest Miocene (Noble et al., 1990), the Central Andes experienced two distinct phases of compressional deformation. According to Steinmann et al. (1999), a major compressional event around 18 Ma affected the Ecuadorian Andes, while Noble et al. (1990) and Wise et al. (2008) dated the Quechua I tectonic event in the Peruvian Andes to approximately 19 Ma and 17 Ma, respectively. Steinmann et al. (1999) also documented a later phase of regional compressive deformation in the Ecuadorian Andes between 9.5 and 6 Ma, with peak activity occurring from 9 to 8 Ma. Wise et al. (2008) assigned an age of around 8.7 Ma to the Quechua II compressive event in the Peruvian Andes.

Concurrently, significant transitions in the Nazca plate's subduction direction and dipping angle under the Ecuadorian-Peruvian Andes occurred. Rousse et al. (2002) reported that around 8 Ma, strata in the Peruvian Andes experienced rapid uplift and substantial rotation when subduction possibly “froze and the entirety of Nazca–South American plate convergence was accommodated by shortening in the continent”. Around 7 Ma, the Nazca-South American convergence system transitioned from steep slab subduction under the Peruvian Andes to a low-angle flat slab subduction (Espurt et al., 2008). This suggests that northern South America underwent a critical juncture in its geodynamic history around 8-7 Ma, potentially altering the region's geodynamic behaviour.

In the Quaternary period, the modern Andes have continued to evolve through ongoing tectonic processes such as earthquakes, volcanic eruptions, and glacial erosion (*Figure 2.9*). Recent studies aim to elucidate the intricate relationships among tectonics, climate, and surface processes in shaping the present landscape (Ehlers and Poulsen, 2009; Montgomery et al., 2001).

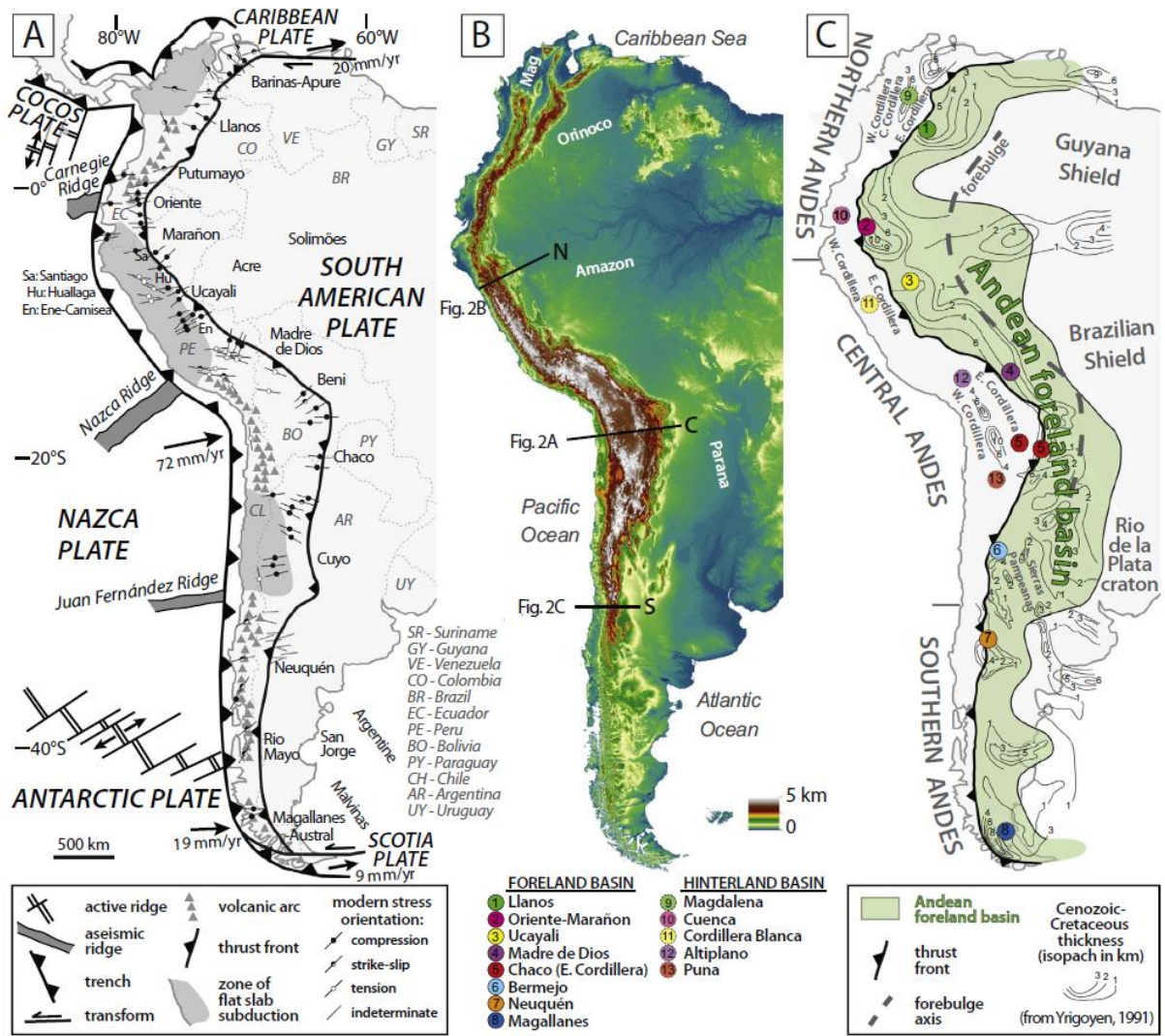


Figure 2.9: From Horton (2018): Maps of (A) tectonic framework, (B) topography, and (C) sedimentary basin configuration of South America. (A) Map of plate boundaries, Andean magmatic arc (including the northern, central, and southern volcanic zones), regions of flat slab subduction, modern stress orientations from earthquake focal mechanisms, eastern front of Andean fold-thrust belt, and key segments of the retroarc foreland basin system. Plate velocities are shown relative to stable South American plate. (B) DEM topographic map showing the Andes mountains and adjacent foreland region, including the Amazon, Parana, Orinoco, and Magdalena (Mag) river systems. (C) Map of Andean retroarc basins, showing isopach thicknesses (in km) of Cretaceous-Cenozoic basin fill, forebulge axis, and locations of 13 sites (8 foreland basins, 5 hinterland basins) considered in this synthesis.

2.4.2. Evolution in drainage basins of northern South America

The Amazon drainage basin represents a region of high heterogeneity, where geological history, landscape, climate, soils, and biota have evolved in concert with large-scale subduction processes stemming from the Nazca-South America convergence system (Roddaz et al.,

2005a). From the Oligocene to early Miocene (approximately 30-20 Ma), uplift of the Andes significantly influenced drainage systems in northern South America, primarily due to the subduction of the Nazca Plate beneath the South American Plate (Garziona et al., 2008; Hoorn et al., 2010). This uplift resulted in the reorganization of major fluvial systems, such as the Amazon and Orinoco, which were initially westward-draining but later reoriented to their current eastward and northward flow patterns, respectively (Latrubesse et al., 2010) (Figure 2.10).

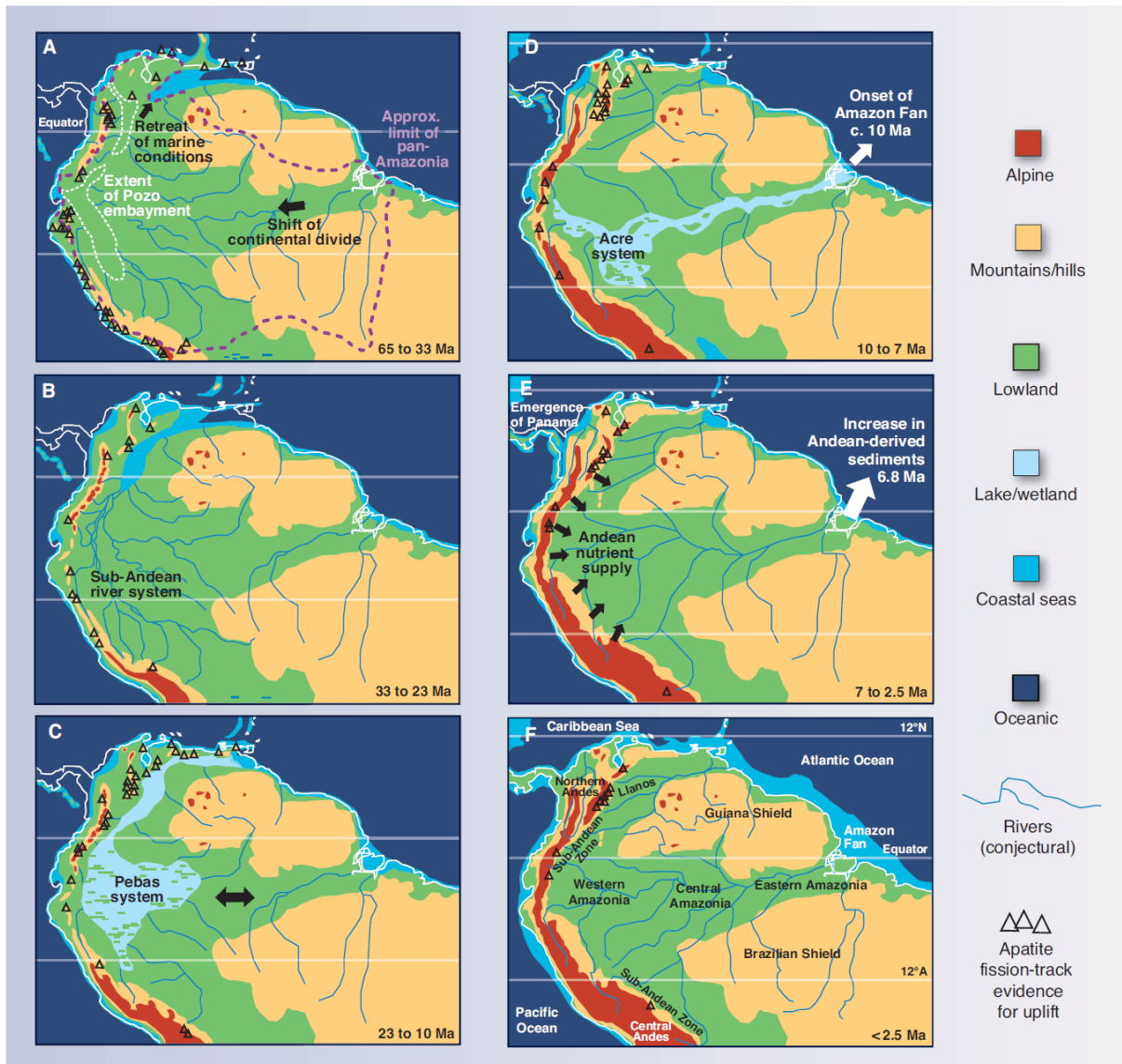


Figure 2.10: From Hoorn et al. (2010): Paleogeographic maps of the transition from “cratonic” (A and B) to “Andean”-dominated landscapes (C to F). (A) Amazonia once extended over most of northern South America. Breakup of the Pacific plates changed the geography and the Andes started uplifting. (B) The Andes continued to rise with the main drainage toward the northwest. (C) Mountain building in the Central and Northern Andes (~12 Ma) and wetland progradation into Western Amazonia. (D) Uplift

of the Northern Andes restricted “pan-Amazonia” and facilitated allopatric speciation and extirpation [e.g., (21)]. (E) The megawetland disappeared and terra firme rainforests expanded; closing of Panama Isthmus and start of GABI. (F) Quaternary.

Consensus exists that until at least the Late Miocene, the Purus Arc, a subsurface structural high in central Amazonia, acted as a barrier separating two drainage systems: a western system extending from the Andean range to the Caribbean and an eastern Proto-Amazon River draining the Guiana and Brazilian cratonic shields toward the Atlantic Ocean (Campbell et al., 2006; Figueiredo et al., 2009; Latrubesse et al., 2010). During the Early Miocene (from ~23 Myr bp), an inland fluvio-lacustrine/marginally marine Amazonian system partially flooded northwest South America, with regional drainage mainly directed northward toward the Caribbean (Hoorn, 1993; Hoorn et al., 1995; Räsänen et al., 1995; Vonhof et al., 2003). By the Late Miocene (10.5–5.3 Ma), a complex system of rivers, deltas, and estuaries had evolved along the onshore Amazon basin, flowing toward the Atlantic Ocean, a development supported by sediment provenance, paleo-transport direction, and biostratigraphic studies (Hoorn, 1993; Hoorn et al., 1995; Räsänen et al., 1995; Roddaz et al., 2005a) (*Figure 2.10*).

Mora et al. (2010) suggest that the Late Miocene transition from a filled to an overfilled Amazonian foreland, followed by the Late Miocene-Pliocene uplift of the Vaupés Swell, led to the permanent separation of the Orinoco and Amazon drainage basins. Any remaining Amazonian-Caribbean connection was definitively severed by the Late Miocene (Hoorn et al., 1995), and the Amazon River reached its present configuration from the Plio-Pleistocene onward (Figueiredo et al., 2009; Hoorn et al., 1995).

During the Early and Middle Miocene, a restricted eastward-flowing Paleo-Amazon River likely drained to the Atlantic coast (Figueiredo et al., 2009) (*Figure 2.10*). Stratigraphic data suggest that the Purus arch (*Figure 2.11*) limited this fluvial system westward, separating the Solimões and Amazonas basins and confining the Amazonian mega-wetland to the west and the Paleo-Amazon River to the east. Major Miocene changes in drainage patterns and the formation of the Amazon River are attributed to uplift in the northwest Andes (Marshall and Lundberg, 1996; Roddaz et al., 2006, 2005a, 2005b). This uplift caused flexural subsidence in the foreland basins, redirecting a significant portion of northwest Amazon basin drainage along the northward-flowing Paleo-Orinoco and Magdalena rivers to the east (Hoorn et al., 1995). Landscape evolution has also been linked to Early Tertiary to Holocene intraplate tectonics, which include subsidence linked to a low-rate extension contributing to a structural low (Costa

et al., 2001). Additionally, the Late Miocene (~11 Myr bp) is marked by a significant sea-level drop, contributing to the disappearance of the Amazonian mega-wetland (Haq et al., 1987; Hoorn et al., 1996).

Shephard et al. (2010) propose that the formation of the modern Amazon River was largely driven by mantle-convection-driven subsidence and uplift of the western regions of South America. Subsidence of approximately 10-20 m/Myr in eastern South America, due to its movement over sinking slab material in the lower mantle, facilitated the river's formation. Paleo-geographic reconstructions indicate significant uplift in the west and subsidence in the central and eastern basins from 14 Myr bp to the present, with up to 400 m of subsidence occurring at the Amazon's mouth between 60 Myr bp and the present.

Around the Pliocene to Pleistocene boundary (approximately 5-2 Ma), the closure of the Isthmus of Panama precipitated significant oceanographic and climatic changes, affecting the hydrological balance of northern South America (O'Dea et al., 2016). This closure also impacted sediment supply and fluvial architecture across the region (Sepulchre et al., 2014).

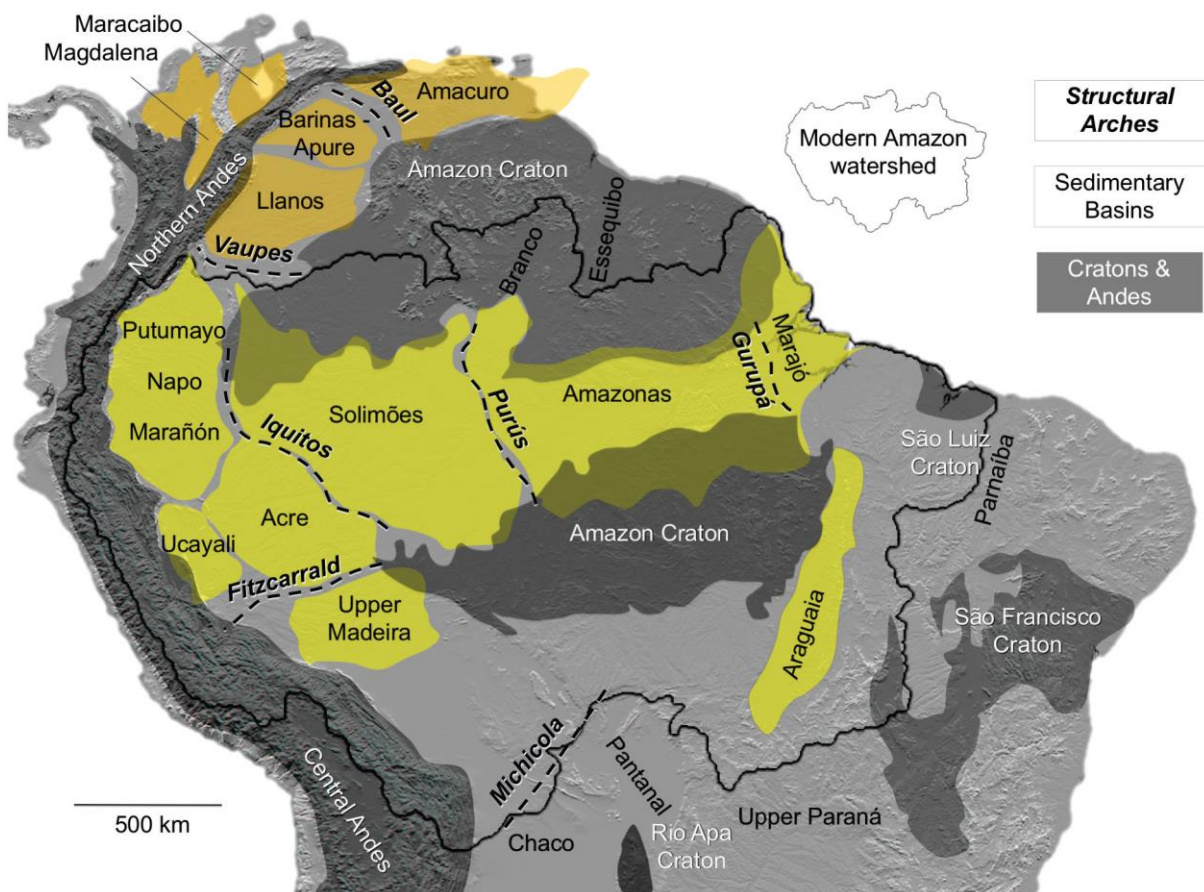


Figure 2.11: From Albert et al. (2018): Principal landforms controlling basin connectivity in northern South America. Structural arches (dashed lines) of diverse geological origins partially bounding sedimentary basins. Sedimentary basins in orange draining to the Caribbean; in yellow to the Atlantic.

Note the Guiana Shield is composed mostly of the northern Amazon Craton, the Brazilian Shield by the southern Amazon craton, and the Atlantic Shield by the São Luís, São Francisco, Luís Alves and Río de la Plata cratons, all overlaid in parts with Palaeozoic sedimentary formations.

2.5. Shift in the Amazon margin sedimentation

2.5.1. The transcontinental Amazon event

The Amazon River, with a drainage basin covering 5.8 million km² and an average water discharge of 6,642 km³/year, serves as the world's largest river (Dai and Trenberth, 2002; Roddaz et al., 2005a). Its geological history, particularly the evolution from an intracratonic drainage system to a transcontinental river, remains an area of active debate. Until the Late Miocene, the Purus Arc, a structural high in central Amazonia, acted as a barrier between two distinct drainage systems: a western system flowing from the Andean range to the Caribbean, and an eastern Proto-Amazon River flowing to the Atlantic Ocean (Campbell et al., 2006; Figueiredo et al., 2009; Latrubesse et al., 2010). These two drainage systems eventually merged into the single transcontinental Amazon River, extending from the Andean range to the Atlantic Ocean. However, consensus on when and how this inversion occurred is lacking.

One of the primary challenges in understanding this history is the limited access to the modern Amazon drainage basin. The dense rainforest restricts most outcrop investigation, allowing research only on a few river banks and road cuts (Latrubesse et al., 2010; Nogueira et al., 2013). Sparse well and borehole data acquired for oil exploration in the western Amazonian basins also prove to be less than ideal for academic research (Hoorn, 1994; Latrubesse et al., 2010; Soares et al., 2017). Furthermore, inconsistent naming conventions and different approaches to sedimentary formations across national borders in the western Amazon complicate regional geological understanding.

Some of the earliest estimates for the transcontinentalization of the Amazon river were based on studies of the Offshore Amazon Basin, where evidence of Miocene onset was identified (Carozzi, 1981; Figueiredo et al., 2007; Hoorn et al., 2010; Schaller et al., 1971). However, these initial estimates have been revised over time. Carozzi (1981) suggested an early Middle Miocene onset, whereas Hoorn et al. (2017) later proposed a Late Miocene age between 9.4-9 Ma, a difference of at least 4.4 Ma.

Recent onshore studies have challenged the Miocene assumption, suggesting that the transcontinental Amazon River may be younger (Campbell et al., 2006; Latrubesse et al., 2010;

Nogueira et al., 2013; Ribas et al., 2012; Rossetti et al., 2015). For example, Latrubesse et al. (2010) argued for a connection between western and eastern fluvial systems no earlier than ~5 Ma, leading to a regional integration of the Amazon fluvial system in the early Pliocene. Conversely, Campbell et al. (2006) proposed a lacustrine environment dominating the western Amazon until the earliest Quaternary (~2.5 Ma), when eastward flow began. Disagreements and alternative explanations further add complexity to understanding this transformative phase in the Amazon's history.

The Amazon's connection with Andean orogeny during the Late Miocene has also been considered (Damuth and Kumar, 1975; Figueiredo et al., 2009; Hoorn et al., 2017, 1995; Silva et al., 1999). However, the correlation between Andean orogenic phases and events in the Offshore Amazon basin is fraught with uncertainty. Varied methodologies and study areas have led to different estimated ages for Andean orogenic phases, with an overall agreement on the timing of intense orogeny after 10 Ma, including significant phases around 9-8 Ma and 6-5 Ma (Bermudez et al., 2011; Garzzone et al., 2008; Hungerbühler et al., 2002; Rouse et al., 2002; Steinmann et al., 1999).

2.5.2. Age of the Amapá platform burial

In the offshore Amazon basin, the cessation of carbonate sedimentation on the Amapá platform has been a subject of debate and continuous revision. Initial studies positioned this event within the middle Miocene, a time frame established through research by Schaller et al. (1971) and Carozzi (1981). However, more nuanced interpretations emerged with studies by Brandão and Feijó (1994) and Wolff and Carozzi (1984), proposing a cessation at the boundary between the middle and late Miocene.

A critical advancement came with Silva et al. (1999), who were the first to pinpoint a specific age of 10 Ma for the top of the carbonate platform. Subsequent research based on calcareous nannofossil zonations further refined this age, with Figueiredo et al. (2009) estimating between 11.8 and 11.3 Ma. Campbell (2010) challenged this, leading to a revision to 10.5 Ma by Figueiredo et al. (2010). In a more comprehensive study, Gorini et al. (2014) found variations across the basin, dating the end of sedimentation between 9.5 and 8.3 Ma on the Central shelf, with younger dates on the NW shelf. Finally, Cruz et al. (2019) proposed that terrigenous sediments prograded across the entire NW shelf, leading to the cessation of carbonate production on the Amazon continental shelf, only after the central embayment was completely infilled by Amazonian sediments at around 3.7 Ma.

The nature of the transition from carbonate to terrigenous sedimentation in the Offshore Amazon Basin remains under dispute. Carozzi (1981) interpreted the top of the carbonate platform as being marked by a large transgression due to sea-level rise, whereas Figueiredo et al. (2009) associated it with a “regional unconformity” connected to the Serravallian/Tortonian eustatic fall as highlighted by Haq et al. (1987). More recently, Gorini et al. (2014) used seismic and well data to demonstrate that the carbonates are overlain by shelf clinoforms, suggesting the carbonate-siliciclastic boundary is a flooding surface.

2.5.3. The Amazon deep-sea fan discovery and study

The continental slope beyond the shelf is characterised by the lobate form of the Amazon fan, a significant sedimentary depocenter reflecting a rise in siliciclastic influx since the late Miocene (Silva et al., 1999).

The discovery and understanding of deep-sea fans and turbidity currents have evolved significantly over time, driven by advances in technology and scientific exploration. The concept of turbidity currents was initially inspired by observations of 'flysch' deposits in the Alpine region, where sediment-laden water flowed down the continental slope and deposited materials on the deep ocean floor. However, the dynamics and mechanisms of turbidity currents were not fully understood during the early 20th century (Mutti et al., 2009; Shanmugam, 2016).

In the mid-20th century, advancements in oceanography and seafloor mapping allowed scientists to study the ocean floor in more detail. Direct observations of deep-sea fans and turbidity currents were made using submersibles and sonar technology, and submarine canyons were identified as potential pathways for turbidity currents to reach the deep ocean.

The late 20th century saw significant progress with the advent of deep-sea drilling and coring techniques. Sediment samples from deep sea fans became accessible, providing valuable insights into the depositional processes and sedimentary structures associated with turbidity currents.

The Amazon deep-sea fan came into focus during geological and geophysical surveys conducted by the oil industry in the late 1970s and early 1980s. Seismic data revealed the presence of a massive submarine sedimentary fan system in the Amazon basin, stretching over almost 400 km along the slope to depths of more than 4000 m (Damuth et al., 1983; Damuth and Kumar, 1975; Kuehl et al., 1986; Milliman et al., 1975).

In 1994, the Ocean Drilling Program's expedition (ODP leg 155) significantly increased data on the Amazon fan region. Researchers studied sediment cores and conducted detailed analyses of sediment transport, sedimentation rates, and composition, providing valuable

insights into the fan system's dynamics and evolution (Flood et al., 1995; Haberle, 1999; M. Maslin et al., 1998).

Since then, numerous studies have looked into the formation and functioning of the Amazon deep-sea fan. In 2023, the French vessel Marion Dufresne embarked on the Amagas-Amaryllis mission, focusing on two primary topics: gas hydrates and their potential impact on submarine landslides if destabilized, and paleoclimate reconstruction along the equatorial margin. This recent expedition offered valuable data for furthering our knowledge of the deep-sea fan's complex features.

2.5.4. Age of the deep-sea fan initiation

Historically, the initiation of Amazon fan deposition has been linked to the suppression of carbonate sedimentation on the shelf (Figueiredo et al., 2009, 2007; Schaller et al., 1971; Silva et al., 1999).

Early research on the Amazon fan's inception can be traced back to the studies by Damuth and Kumar (1975) and Damuth et al. (1983). Through an extrapolation of the latest Quaternary sedimentation rates obtained from core samples, these studies proposed an initiation between 16.5 and 8 Ma during the middle to late Miocene. This broad range was later narrowed down through correlation techniques involving well data and seismic profiles.

Silva et al. (1999), alongside Figueiredo et al. (2009, 2007), used these correlations to propose more constrained ages between 11.8 and 10.5 Ma for the base of the Amazon fan. This methodology allowed for a more refined understanding of the stratigraphy and sedimentological characteristics of the fan.

However, further refinement came with Hoorn et al. (2017), who used planktonic calcareous nannofossil zonation in a single well, calibrated to the international time scale of Gradstein et al. (2012). This approach provided an even more specific age range of 9.4 to 9 Ma for the base of the fan. Hoorn et al.'s findings also led to an intriguing hypothesis that the Amazon fan could post-date the cessation of shelfal carbonate sedimentation by 1 to 1.5 Myr.

2.5.5. Deposition of the silico-clastic series along the margin

The characteristics of the third post-rift megasequence in the Offshore Amazon Basin are distinct from the coeval units in other basins of the Brazilian Equatorial Margin, such as the Pará-Maranhão, Barreirinhas, Ceará, and Potiguar basins. In these other basins, tectonic stability coupled with a low terrigenous sediment supply allowed the continued deposition of

shelfal carbonates up to the Recent period. Conversely, in the Offshore Amazon Basin, carbonate production was interrupted during the Late Miocene by a substantial influx of terrigenous sediments, leading to the burial of the existing carbonate platform and the subsequent development of the Amazon Fan on the slope and abyssal plain (Cruz et al., 2019; Figueiredo et al., 2007) (*Figure 2.12*).

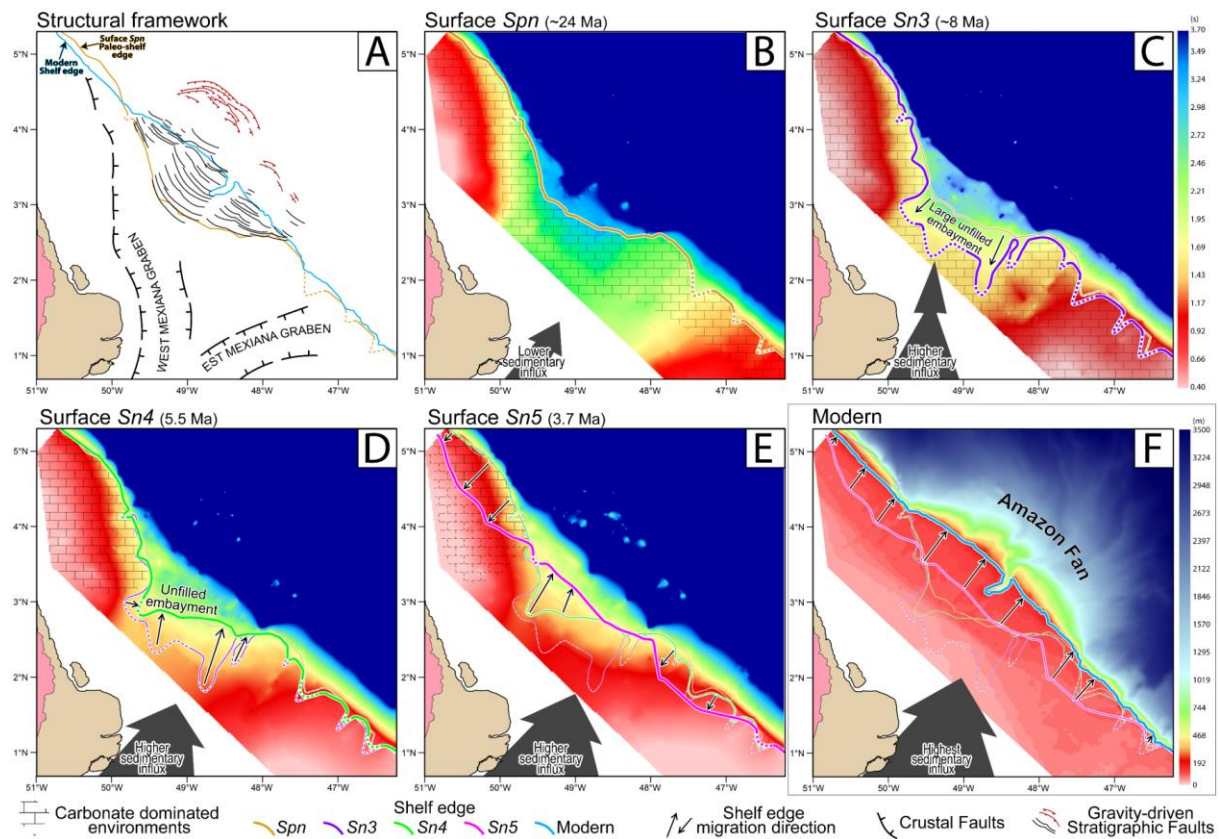


Figure 2.12: From Cruz et al. (2019): A - Structural framework compiled from Schaller et al. (1971) and Perovano et al. (2009). Faults associated to gravity tectonics are compiled from Perovano et al. (2009) and Reis et al. (2010). B to E - Two-way travel time (s) maps of stratigraphic surfaces mapped in the work of Cruz (2018), coupled with bathymetric maps (m) of the present-day Amazon shelf. Paleoshelf edge positions defined from interpreted seismic data are shown as thick coloured lines. In B, note that the shelf edge position in the central region at ca. 24 Ma was nearly coincident with the most proximal gravity tectonic-related faults. Also note that the large embayment formed due to shelf-edge retrogradation in the Central shelf was filled between ca. 8-3.7 Ma and only then was carbonate sedimentation completely suppressed on the NW shelf.

This sedimentary influx shaped the uppermost megasequence, comprising the formations of the Pará Group, which include the proximal Tucunaré Formation characterised by coarse to fine sands, the laterally continuous Pirarucu Formation composed mainly of fine

sands and muddy sediments, and the Orange Formation, distinguished by distal muddy sediments with interspersed layers of fine sands deposited by turbidity currents (Figueiredo et al., 2007).

Silva et al. (1999) portrayed the third post-rift megasequence as a fluvial deltaic-continental slope progradational prism with variable thickness—up to 9 km thick in the northwest part of the Amazon Fan, and around 1.2 km thick elsewhere in the basin. These authors also revealed that the Offshore Amazon Basin experienced significant flexural isostatic subsidence as a result of the sedimentary load of the Amazon Fan (*Figure 2.13*). This finding aligns with the flexural subsidence models developed by Driscoll and Karner (1994), who discovered that the load of the Amazon Fan induced subsidence of up to 2.3 km beneath the primary depocenter and a corresponding peripheral bulge, leading to an onshore uplift of as much as 50 meters. Additionally, Driscoll and Karner (1994) hypothesized that the flexural subsidence prompted by the load of the Amazon Fan could have created roughly 200-300 meters of accommodation space near the present-day coastline since the Middle Miocene.

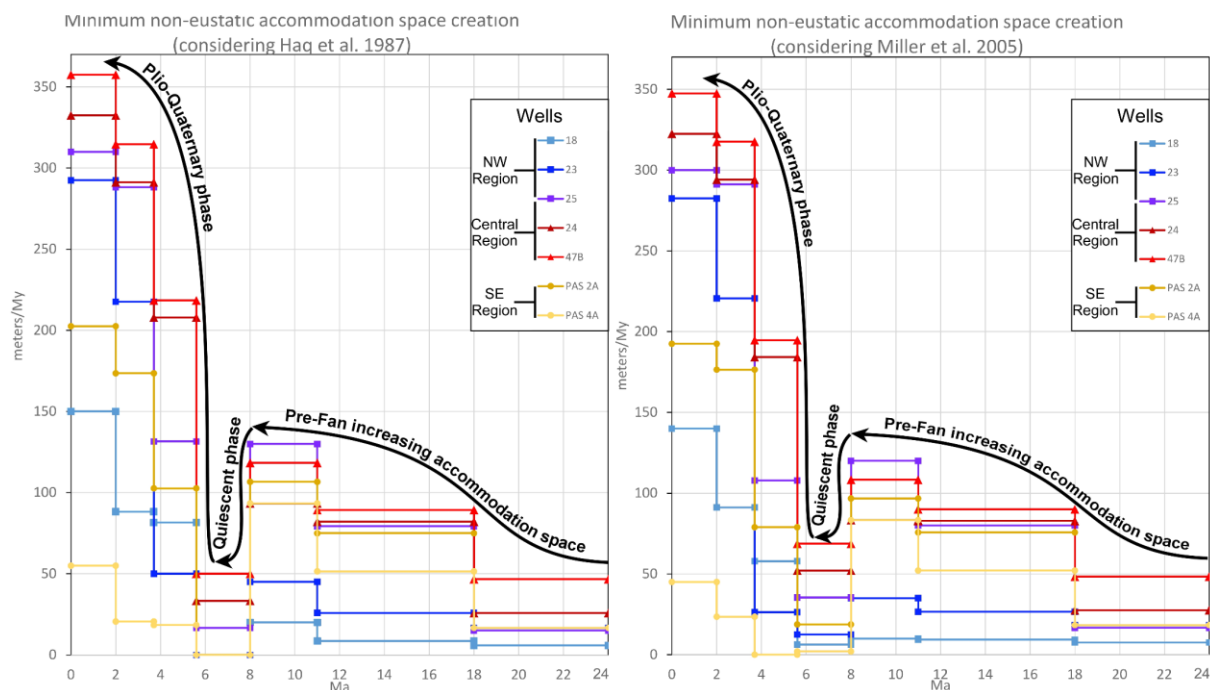


Figure 2.13: From (Cruz et al., 2019): Graphs summarizing calculations of the non-eustatic accommodation space required for the deposition of each Neogene sedimentary unit on the Amazon shelf.

2.5.6. The Great Amazon Reef System, from hypothesis to proof

The existence of a carbonate reef structure along the Amazon Continental Margin (ACM) was initially hypothesized in the 1970s by Kempf (1970) and Milliman et al. (1975). This idea gained support from observations of reef-associated fish and sponges made by Collette and Rützler (1977) and Moura et al. (1999). Finally, Moura et al. (2016) published crucial findings from a significant campaign that unveiled the composition and extent of the so-called "Amazon extensive reef system" (*Figure 2.14*). This discovery challenged conventional perceptions, as it revealed the possibility of carbonate development despite the challenging conditions posed by the large amount of sediment carried by the Amazon River (with an annual suspended-sediment load of $1.2 \cdot 10^9$ tons, Meade et al., 1985). This reef system is currently active, and numerous studies have documented a diverse array of reef-associated living organisms along the entire margin at depths ranging from 70 to 220 m (Banha et al., 2022; De Mahiques et al., 2019; Francini-Filho et al., 2018; Vale et al., 2022, 2018) (*Figure 2.14*). This reef system primarily consists of black corals, sponges, and red algae (De Mahiques et al., 2019; Francini-Filho et al., 2018; Moura et al., 2016; Vale et al., 2022, 2018).

Since the revelation of the Amazon Reef System in the past decade, there has been a noticeable decrease in oil exploration and exploitation activities along the ACM, sparking debates regarding the size and age of the reef. Moura et al. (2016) initially proposed an extension of over 9,500 km² for the Amazon Reef System (*Figure 2.14*). Subsequently, Francini-Filho et al. (2018) significantly increased the estimated living reef area by a factor of five, suggesting a size of 56,000 km² for the Amazon Reef System (*Figure 2.14*). In contrast, dos Santos Filho et al. (2022), relying on bathymetric, surface sediments, and 2D seismic reflection data, conducted a revision of the extension, ultimately reducing the size of the reef system to 13,478 km² (*Figure 2.14*).

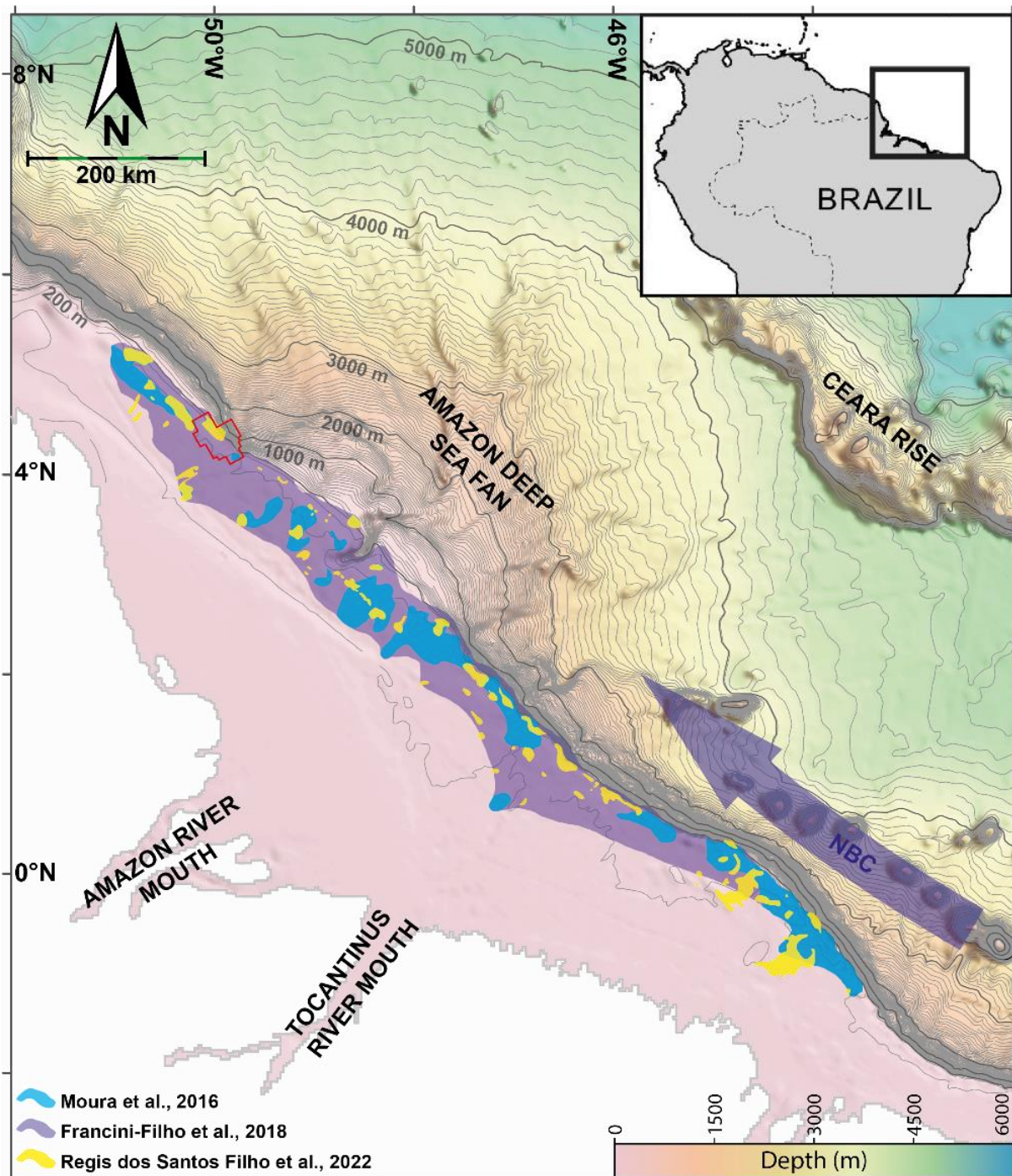


Figure 2.14: Bathymetric map of the NW Equatorial Brazilian Margin, a thick blue arrow shows the North Brazilian Current (NBC). The extension of the Great Amazon Reef System calculated by Moura et al. (2016) Francini-Filho et al. (2018) and dos Santos Filho et al. (2022) is represented by superposed coloured area in light blue, dark blue and yellow respectively. The 3D seismic block studied is delimited by red geometry.

2.6. Physical parameters influencing marine deposition along the Amazon Margin

Equatorial continental shelves are very dynamic regions, as they are affected by distinct forcings. These include wind, tides, river input, surface waves, western boundary currents, and large-scale ocean circulation (Aguiar et al., 2022; Lentz and Fewings, 2012; Nittrouer and Wright, 1994; Parra et al., 2016). The Brazilian Equatorial Shelf is subject to these energetic forcings, such as resonant semidiurnal macrotides, significant buoyancy flux from the Amazon River, northeasterly and southeasterly trade winds, and intense flow along the continental margin associated with the North Brazilian Current. These forces play a crucial role in the dispersion of the Amazon freshwater discharge and its associated suspended sediment (Muller-Karger et al., 1988; Nikiema et al., 2007). Moreover, the Brazilian Equatorial Shelf, with its unique features, plays a significant role on Earth; its circulation is a major component in the interhemispheric exchange of freshwater (Stramma et al., 2003), as well as heat, and energy (Dengler et al., 2004; Johns et al., 2003), thereby exerting a substantial influence on global ocean circulation.

2.6.1. Winds

Trade winds are a prominent feature of intertropical atmospheric circulation, forming the surface portion of the Hadley cells. These winds are characterised by a flow directed from the tropics to the equator in both hemispheres, culminating in the formation of the Intertropical Convergence Zone (ITCZ). The ITCZ's position fluctuates seasonally in response to variations in Sea Surface Temperature (SST). During the boreal winter, an increase in SST in the South Atlantic causes the ITCZ to shift southward. Conversely, during the boreal summer, the ITCZ moves northward (Adam et al., 2016; Ruggiero, 2008; Schneider et al., 2014). This seasonality in the ITCZ leads to changes in the wind pattern over the Brazilian Equatorial Shelf. During the boreal winter and spring, winds tend to blow preferentially from the northeast, while southeasterly winds are prevalent during the boreal summer and fall. These shifts in wind dynamics subsequently influence the circulation and distribution of upper ocean parameters (Aguiar et al., 2022).

2.6.2. Tides

Tides along the Brazilian Equatorial Shelf are primarily driven by deep ocean tides (Geyer et al., 1996). The semidiurnal tidal components (M2, S2, and N2), are generally recognized as dominant in the equatorial Atlantic Ocean (Nittrouer and DeMaster, 1996), and they exhibit strong fortnightly modulations, such as spring and neap tides. The Amazon Continental Shelf's response to these semidiurnal ocean forces is highly intricate, owing to both the Amazon mouth's geography and the shelf bathymetries. Specifically, the M2 tidal wave propagates perpendicular to the coast, influencing the Amazon and Tocantins rivers, as well as the Amazon River mouth and the Amazon Continental Shelf between latitudes 1° N and 4° N. Within this region, the M2 wave achieves its maximum amplitude at the point where the shelf width is at its greatest, thereby creating quasi-resonant conditions (Geyer et al., 1996). A study by Beardsley et al. (1995) revealed that the M2 component plays a critical role in the Amazon Continental Shelf circulation, accounting for approximately 70% of tidal variability. This force induces potent currents, which can reach 2 m/s during spring tides, and elevations with amplitudes surpassing 1.5 m near the coast. Additionally, the M2 amplitude has been observed to increase to 1.75 m at around 2° N (Fontes et al., 2008). In contrast, the lunar diurnal constituent of tides in the ACS, primarily represented by K1 and O1 components, have markedly smaller amplitudes, generally ranging from 0.06 to 0.08 m over the shelf (Aguiar et al., 2022).

2.6.3. Currents

The surface circulation in the ocean region adjacent to the Brazilian Equatorial Shelf (BES) is dominated by the North Brazil Current (NBC) (*Figure 2.15*). The NBC is responsible for the transport of heat and water mass across the equator. The NBC is a well-established western boundary currents formed by the bifurcation of the South Equatorial Current (SEC), and it exhibits seasonal variability (Johns et al., 1990; Richardson and Walsh, 1986; Silva et al., 1999). NBC velocities can exceed 1 m/s, as observed in previous studies (Flagg et al., 1986; Geyer et al., 1996; Geyer and Kineke, 1995). According to Johns et al. (1998), the NBC ranges from a maximum transport of 35 Sv in July and August to a minimum of 13 Sv in April and May in the upper 300 m at 4°S. This current feeds the equatorial countercurrent system and exports surface waters from the South Atlantic into the North Atlantic (Johns et al., 1998; Stramma et al., 2003).

The NBC is intermittent at the surface. Flowing off the BES, it can take two paths: it flows northwestward or retroflects eastward, feeding the North Equatorial Counter Currents (NECC; see *Figure 2.15*). Retroflexion occurs with greater magnitude in the boreal summer and fall, weakening in winter, and may even disappear in spring (Garraffo et al., 2003; Johns et al., 1998). The NBC retroflexion system comprises retroflexions at different times, latitudes, and depths, as well as eddies shed along the western boundary (Richardson et al., 1994). These retroflexions contribute to the transport of the Equatorial Undercurrent (EUC) and the North Equatorial Countercurrent (NECC) (Bourles et al., 1999; Goes et al., 2005; Schott et al., 1995; Stramma and Schott, 1999).

Regarding the vertical structure of the BES circulation, the NBC core is shallow (20 m) and found over the shelf in May. In November, however, the core is observed off the shelf break and becomes deeper (100 m). Just north of the Amazon River mouth (2°N), a well-mixed region extends over the shelf to about 120 km in both May and November, followed by a 10 m deep plume, which reaches 220 km and 200 km in May and November, respectively. South of the river mouth (1°S), the mixing zone and the plume are observed only in May. In the retroflexion region (5°N), the freshwater core is close to the coast in May, while it is more advected eastward by the NBC retroflexion in November (Aguiar et al., 2022). The results of Aguiar et al. (2022) showed that the NBC exhibited the strongest flow when all forcings, including winds, tides, and river discharge, were included in the simulation. Thus, these factors work in concert with NBC dynamics (Aguiar et al., 2022).

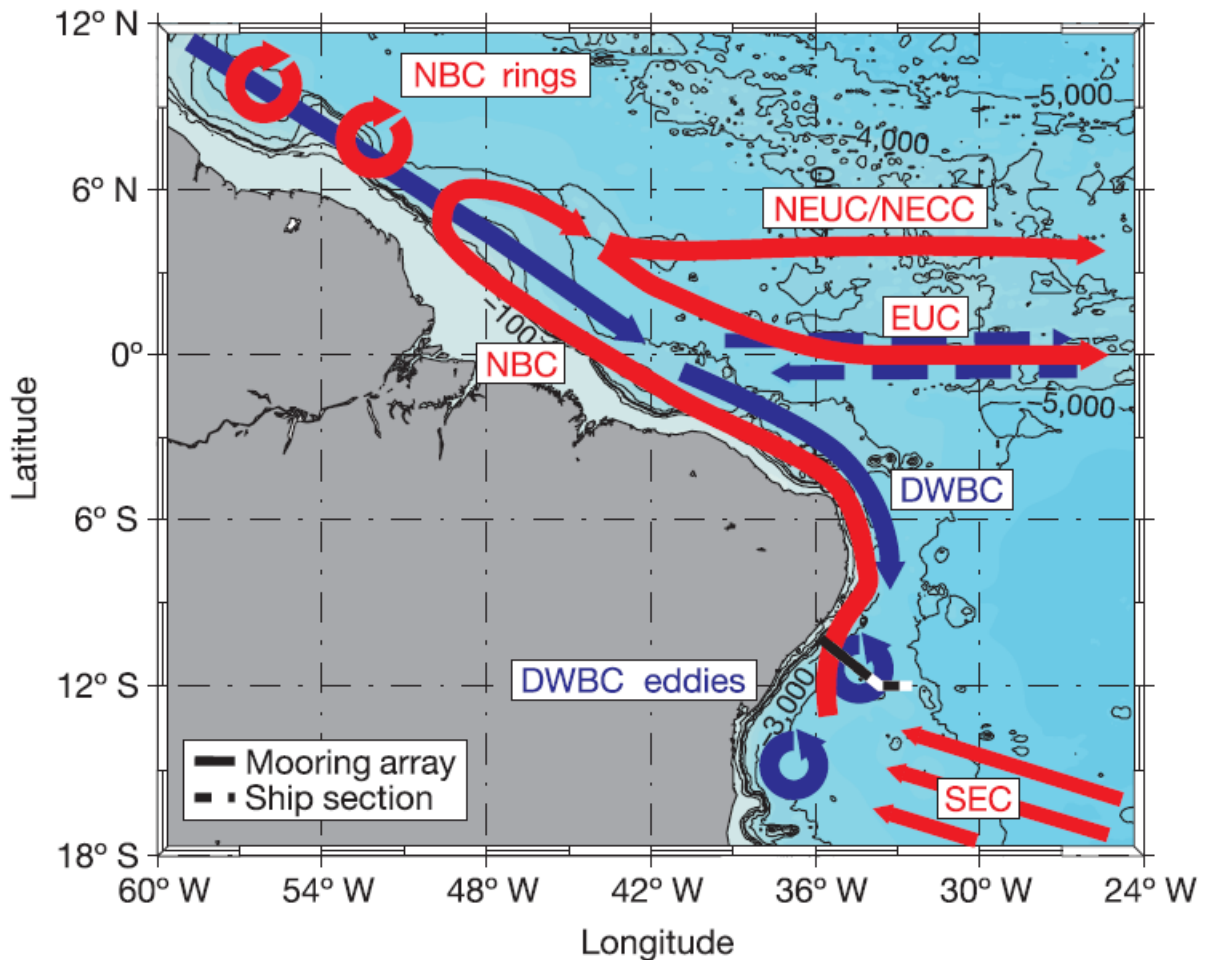


Figure 2.15: From Dengler et al. (2004): Circulation in the western tropical Atlantic. Schematic representation of mean currents and eddy generation at the western boundary of the tropical Atlantic with warmwater pathways in red and North Atlantic Deep Water pathways in blue. Current branches indicated are the south equatorial current (SEC), the north Brazil current (NBC), the equatorial undercurrent (EUC), the north equatorial undercurrent (NEUC) merged with the north equatorial counter current (NECC) and the deep western boundary current (DWBC) with alternating zonal flows marked at the Equator. Depth contours are also shown.

2.6.4. River inputs

The Amazon drainage basin represents $6.1 \times 10^6 \text{ km}^2$, and the Amazon River discharges $1.7 \times 10^5 \text{ m}^3/\text{s}$ into the Equatorial Atlantic Ocean (Dagg et al., 2004; Dai and Trenberth, 2002; Milliman and Meade, 1983; Wright and Nittrouer, 1995). The maximum flow ($2.2 \times 10^5 \text{ m}^3/\text{s}$) occurs in May, while the minimum flow (on average $10^5 \text{ m}^3/\text{s}$) occurs in November (Richey et al., 1986). This plume influences the salinity distribution hundreds of kilometers along the coast

(Lentz, 1995). The freshwater plume forms after a mixing zone and maintains most of its characteristics even as it enters the open ocean (*Figure 2.16*).

Moller et al. (2010) investigated the space-time variability of the Amazon River plume using satellite data from 2000 to 2004. They found that the freshwater plume (waters with a salinity lower than 34) is transported by the North Equatorial Countercurrent (NECC) in the Equatorial Atlantic Ocean, between approximately 5°N and 10°N, during September and October. In contrast, the plume remains confined to the coast during other months. From August through October, typically 70% of the Amazon plume is deflected eastward in the NECC along the NBC retroflection (Lentz, 1995). This pattern is correlated with the regional wind field. Indeed, during the boreal winter and spring, the Brazilian Equatorial Shelf is influenced by northeasterly trade winds, with a strong component towards the coast, resulting in a net alongshore transport to the northwest in the northern hemisphere. Conversely, during the boreal summer and fall, southeasterly trade winds blow with a component parallel to the coast, leading to a net cross-shore transport to the northeast (Ruggiero, 2008).

According to Geyer et al. (1996), the Amazon plume is the top layer of brackish water, typically less than 10 m thick, extending over the outer shelf and off the front zone. This plume flows through various areas of the shelf, each possessing distinct hydrological and dynamic characteristics.

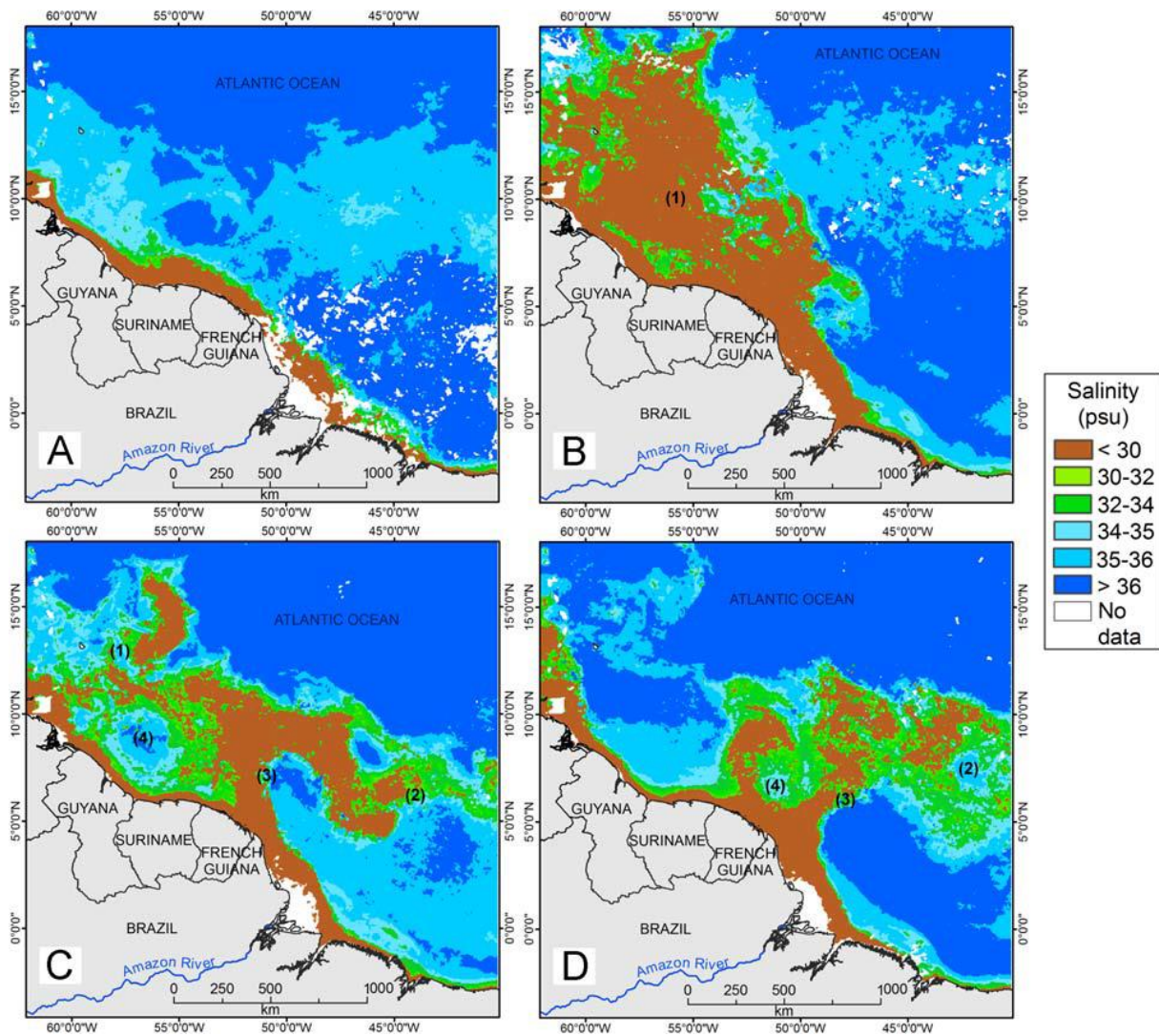


Figure 2.16: From Molleri et al. (2010): Examples of synthetic Sea Surface Salinity maps calculated from the empirical model for the following periods: (A) 25 January – 07 February 2004; (B) 17 – 31 June 2001; (C) 22 August – 04 September 2004; and (D) 21 September – 04 October 2003. The numbers in parentheses in each image indicate: (1) north westward dispersion of the Amazon River plume; (2) NECC transport of the Amazon River plume water into the Central Equatorial Atlantic Ocean; (3) NBC retroflection; and (4) rings formed by this retroflection.

2.6.5. Climate

Numerous studies have examined the consequences of climate change on Amazon deposits. These studies reveal that during the Last Glacial Maximum (LGM) or Marine Isotope Stage 2 (MIS 2), there was increased precipitation in the Andes (Baker and Fritz, 2015; Harris and Mix, 1999; Mason et al., 2019) and a migration of the coastline towards the basin (Figure 2.17). This migration results in variations in base level which allow a more efficient transfer of the Amazon

sediments across the South American continent to the deep sea. This was potentially facilitated by South America hydroclimate anti-phasing: enhanced precipitation and erosion of the central Andes during glacial maxima, while increased aridity in much of the Amazon Basin led to decreased weathering and erosion rates. Enhanced Andean sediment loads in the Amazon River during glacial lowstands would have coincided with incision and increased channel gradients along the lower 1200 km of the Amazon River (Mason et al., 2019). Similar configurations have been observed during Marine Isotopic Stage 6 (MIS 6), suggesting that these variations in sediment provenance, sedimentation rates, and the position of the depocenter are valid for each glacial cycle of the Pleistocene (Mason et al., 2019). These observations align with studies on the morphology of the deep-sea fan (Lopez, 2001; Maslin et al., 2006), which indicate that the development of submarine channel systems occurs primarily during glacial phases, while interglacial phases witness the covering of channels by hemipelagic sediments. Palynological studies (Hoorn, 1997; Hoorn et al., 2017) support these findings by revealing increased concentrations of pollen from species residing at high altitudes in the Andes during glacial periods compared to interglacial periods. However, these studies are limited to the past few hundred thousand years.

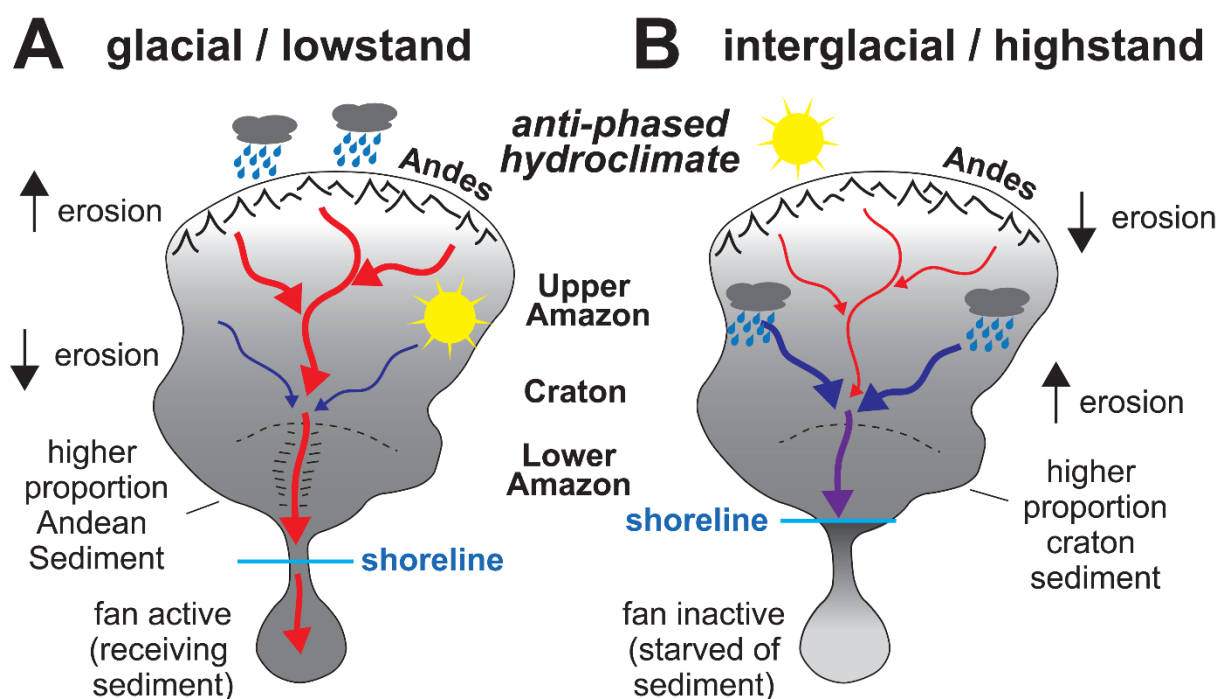
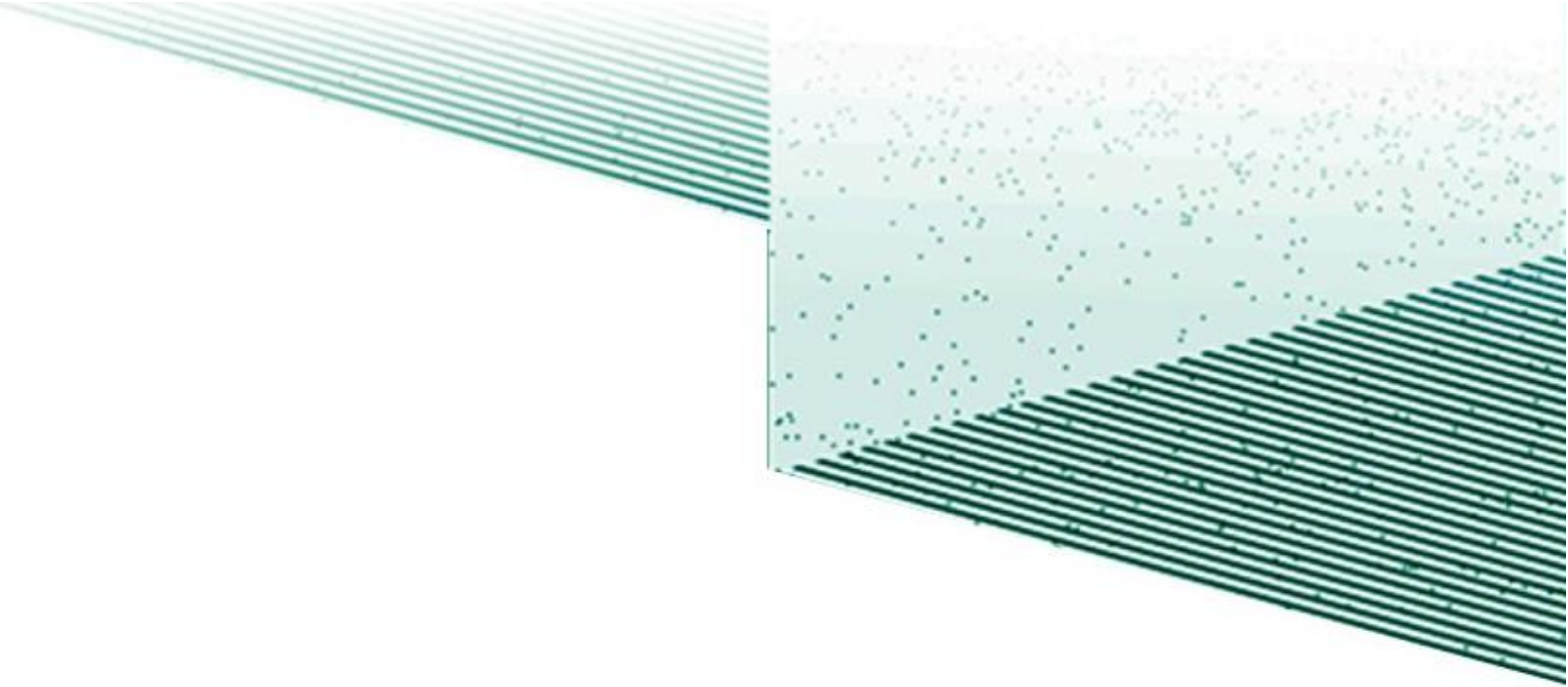


Figure 2.17: From Mason et al. (2019): Interpreted relationships between sea level, Andes-Amazon hydroclimate, and resultant changes in sediment production and transfer through fluvial network to deep-sea across glacial (A) and interglacial (B) phases. Arrows indicate direction of change in erosion rate in the Andes and the Amazon craton (up = increase in erosion, down = decrease).



Chapter 3: Data and methods

3.1. Seismic data and methods

3.1.1. Seismic acquisition principle

Seismic acquisition is a comprehensive and multifaceted technique utilized to explore the Earth's subsurface layers. This investigation begins with the generation of seismic waves, through impulsive sources like explosives or non-impulsive sources like vibratory mechanisms, known as vibroseis trucks (Sheriff and Geldart, 1995). The specific frequency and energy of these seismic waves are adjusted based on the target's depth and resolution (Yilmaz, 2001). The frequency and energy of the seismic waves are chosen based on the depth and resolution of the target. Lower frequencies can penetrate deeper but offer lower resolution, while higher frequencies provide finer resolution but might not penetrate as deep.

As the seismic waves travel through the Earth, they interact with various geological layers; experiencing changes in speed and direction depending on the properties of the material, they encounter (Telford et al., 1990). When the waves reach a boundary between two layers with contrasting acoustic impedances, a portion of the energy is reflected back to the surface (Sheriff and Geldart, 1995).

The detection of these reflected seismic waves is performed using geophones on land or hydrophones in water, converting ground motion or pressure changes into electrical signals (Yilmaz, 2001). The organization of these detectors is often carefully configured to ensure that signals from various depths are accurately captured (Sheriff and Geldart, 1995).

The raw data must undergo extensive processing to derive a coherent image of the subsurface. This includes preprocessing to correct known biases, migration to reposition seismic events accurately, filtering to enhance the signal-to-noise ratio, and stacking to fortify the true signal (Yilmaz, 2001). Velocity analysis is a vital step, providing information about the speed of seismic waves through different subsurface layers, crucial for translating travel times into accurate depth measurements (Sheriff and Geldart, 1995).

In conclusion, seismic acquisition is a complex yet invaluable method for exploring the subsurface, utilized across various scientific and engineering fields. Its methodologies continue to evolve, thanks to technological advancements and computational innovations (Yilmaz, 2001).

3.1.2. Evolution of seismic from 2D to 3D

The origins of seismic acquisition can be traced back to the early 20th century. Initially developed for geological and mining exploration, 2D seismic acquisition used dynamite or

other impulsive energy sources to generate seismic waves, capturing the reflections with a linear array of geophones (Sheriff and Geldart, 1995). Over time, the technique was adapted for both land and marine environments. On land, the geophones would be placed in straight lines across the terrain, while at sea; hydrophones were towed in a straight line behind a survey vessel. While offering valuable insights into subsurface structures, 2D seismic acquisition provided only a limited, cross-sectional view of the Earth's subsurface along the survey line (Telford et al., 1990).

The first 3D seismic survey was shot over a field in Texas in 1967. Since then, there has been an increasingly rapid expansion in the application of this technology (Bakker, 2002). The development of 3D seismic acquisition from this 2D foundation greatly influenced how geophysicists visualize and interpret the Earth's subsurface. One of the most striking differences between 2D and 3D seismic acquisition lies in their spatial coverage. While 2D acquisition provided a cross-sectional view, 3D seismic acquisition arranges detectors in a grid pattern, encompassing a significantly larger area and leading to a volumetric representation of the subsurface.

The increased size and complexity of 3D seismic acquisition have made it particularly suitable for marine environments. Offshore, specialized vessels equipped to handle large arrays of hydrophones, known as "streamers" or "flutes," enable coverage of large areas (Cordson et al., 2000). These streamers can be kilometers long, containing thousands of individual hydrophones, a scale challenging to achieve on land.

The transition from 2D to 3D seismic has not been without challenges, demanding significant investment in equipment, computational resources, and expertise. However, the depth and breadth of insight gleaned from 3D data have justified these challenges, particularly for complex geological structures (Cartwright and Huuse, 2005) (*Figure 3.1*).

Finally, the development of 3D seismic has laid the groundwork for 4D seismic or time-lapse seismic. By repeatedly conducting 3D surveys over the same area at different times, it's possible to observe changes in the subsurface over time (Lumley, 2001). This ability to track temporal changes represents an evolution of seismic acquisition, demonstrating how the shift from 2D to 3D has expanded our capabilities in spatial terms and opened new dimensions in understanding dynamic subsurface processes.

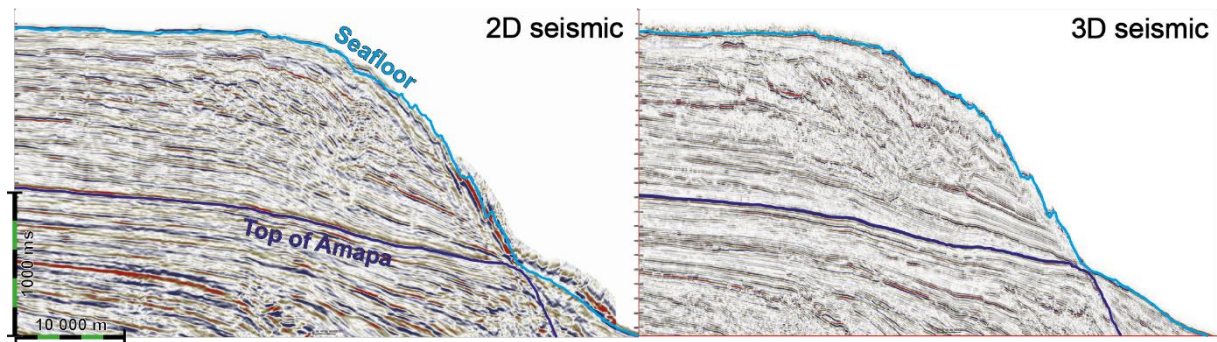


Figure 3.1: Comparison between 2D and 3D seismic lines. Both lines show exactly the same area.

3.1.3. Seismic interpretation from line drawing to automatic picking

In the early years, geoscientists would delineate subsurface structures manually using paper sections, a process that demanded substantial time and effort. With the advent of computer technology and digital processing during the latter half of the 20th century, seismic data interpretation was revolutionized, allowing specialized software to facilitate more precise and efficient mapping of subsurface geological features. This technological advancement gave rise to semi-automatic picking methods. Although algorithms generated initial interpretations, human experts are still needed for validation and refinement. While this method provided a quicker way to process 2D seismic data, its true power was realized in the interpretation of 3D data. The manual interpretation of 3D data is limited by the constraints of 2D viewing windows, such as seismic lines or time slices. In contrast, automatic picking considers all nearby information in 3D, enabling better and finer picking. More recent breakthroughs in machine learning and artificial intelligence have opened doors to fully automatic horizons picking, which can quickly analyse vast seismic datasets with minimal human intervention. This progression not only signifies a remarkable reduction in time and effort but also ensures more consistent and objective interpretations. Such innovations contribute to an enhanced and comprehensive understanding of the Earth's subsurface. However, it remains essential to carefully refine and verify the results produced by the software.

3.1.4. The seismic block, position and parameters

The 3D seismic block used in this thesis was acquired by Compagnie Générale de Géophysique (CGG) in 2008. This block is located along the outer shelf of the Equatorial Brazilian Margin, to the north of the Amazon Canyon (*Figure 3.2*). Covering an approximate area of 1700 km², the seismic block measures around 60 km in length and 40 km in width. It has been migrated from the time to the depth domain. However, this migration is not sufficient for the purpose of

the thesis. The seismic block was initially acquired for petroleum exploration, with target series more than one kilometer deep. As a result, the block was processed to enhance deep reflectors, compromising the resolution and the time-depth model near the subsurface. Therefore, the 3D Pre-Stack Time Migration (PSTM) survey was employed, featuring a grid spacing of 25 meters, encompassing 2387 Inlines and 1733 Xlines. The data has a sampling interval of 4 ms, and the full-stack signal exhibits a dominant frequency of 37 Hz. This provides a vertical resolution of 10-20 m for velocities ranging from 1500 to 3000 m/s.

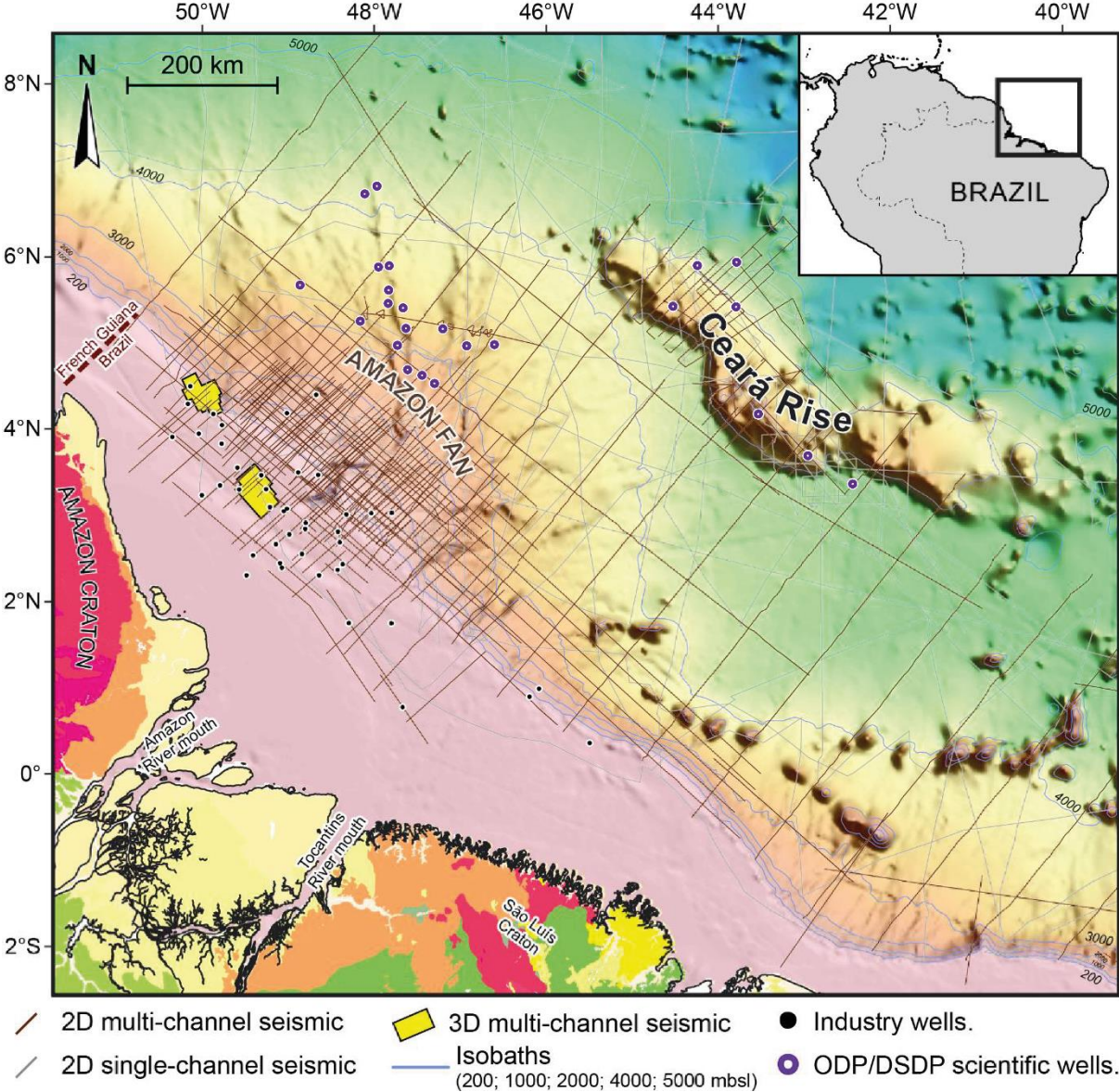


Figure 3.2: Map showing seismic reflection data and wells available from the Offshore Amazon Basin. Note that seismic profiles cover the entire region between the continental shelf-slope, where industry wells are located, and the distal Ceará Rise region, where ODP/DSDP scientific wells are located.

3.1.5. Seismic and Sequence stratigraphy principles

Initially, a seismic interpretation approach was employed on the seismic block, focusing on the recognition and mapping of seismic facies as described by (Mitchum et al., 1977) (**Chapter 4**). The methodology adopted in this study centers on identifying seismic patterns based on the following parameters: (1) the character of the reflectors, including amplitude, continuity, lateral correlation, scattering, and frequency; (2) the bathymetric expression or morphology of the reflectors; (3) the configuration of the reflectors, whether subparallel/parallel, even/wavy, divergent, disrupted, chaotic, lenticular, or shingled; and (4) the terminations of the reflectors, such as downlap, onlap, offlap, and toplap/truncation.

Subsequently, a sequence stratigraphy analysis was conducted (**Chapter 4**). Sequence stratigraphy is a branch of geology that plays a crucial role in understanding the geological evolution of sedimentary basins. This approach facilitates the interpretation of depositional systems, tectonic history, and paleogeography. Initially developed in the mid-20th century, the concept has since been refined (Mitchum et al., 1977; Posamentier and Vail, 1988; Vail et al., 1977).

The primary aim of sequence stratigraphy is to correlate and predict sedimentary strata packages, utilizing the concept of sequences which are stratigraphic units bounded by unconformities or their correlative conformities. Seismic sequence stratigraphy, building on these foundational principles, employs seismic data to further the understanding of depositional history and goes beyond surface observation by probing beneath the Earth's surface (Van Wagoner et al., 1988).

Unconformities are critical to this methodology as they represent breaks in the geologic record indicative of erosion or non-deposition, providing clues about the history and shifts in geological conditions (Payton, 1977). In seismic sequence stratigraphy, these unconformities are significant for dividing the sequences into different system tracts, which carry distinct geological meanings.

Three primary system tracts are generally recognized: Lowstand Systems Tract (LST), which corresponds to falling relative sea levels; Transgressive Systems Tract (TST), reflecting the rise of relative sea levels; and Highstand Systems Tract (HST), associated with the highest relative sea levels (Catuneanu, 2006; Posamentier and Vail, 1988; Posamentier and Allen, 1999). In addition, at the beginning of the 1990s, a new system tract was added: the Falling Stage Systems Tract (FSST) (Ainsworth, 1994, 1992, 1991; Hunt and Tucker, 1992; Hunt, 1992). The Falling Stage Systems Tract represents a critical phase within sequence stratigraphy,

reflecting the period of sediment deposition during falling relative sea levels, but prior to reaching the lowest level. This concept was introduced to capture the transitional phase between highstand and lowstand conditions, offering a more nuanced understanding of depositional sequences (Catuneanu et al., 2009). Each tract aids in interpreting various aspects of geological history, such as tectonic setting, paleoclimate, and sea-level fluctuations (*Figure 3.3*).

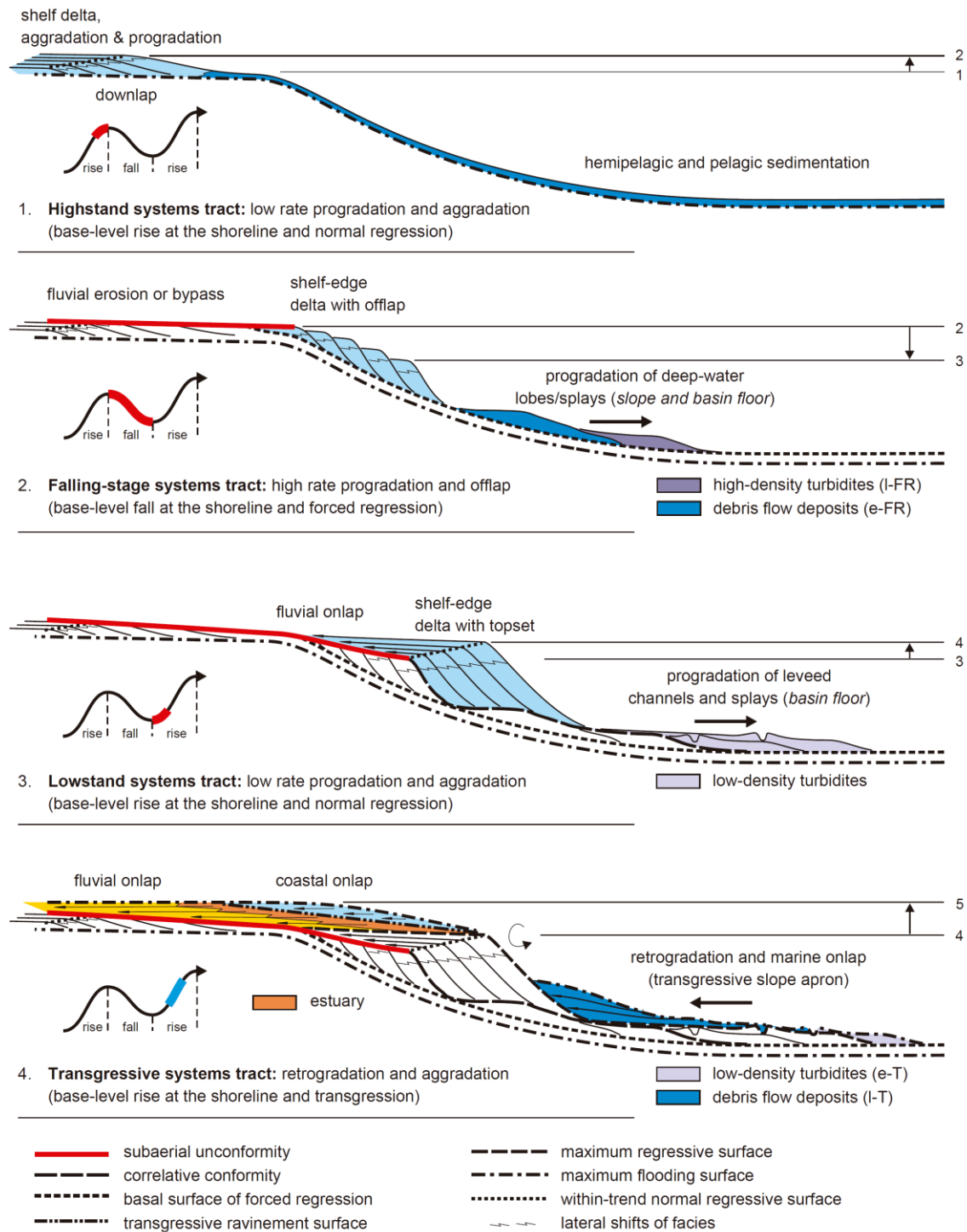


Figure 3.3: From Catuneanu (2006): Regional architecture of depositional systems, systems tracts, and stratigraphic surfaces. Systems tracts are defined by stratal stacking patterns and bounding surfaces, with an inferred timing relative to the base-level curve at the shoreline. Abbreviations: e-FR—early forced regression; l-FR—late forced regression; e-T—early transgression; l-T—late transgression.

3.1.6. Paleoscan workflow

PaleoScan is a specialized software allowing loading and interpreting 3D seismic data. Its main differences compared to other software like Opendtect (DGBES) or Petrel (Schlumberger) lie in the automation of various processes that are typically time-consuming (Figure 3.4). Indeed, Paleoscan allows for a simple and straightforward automatic picking of horizons and faults along an entire seismic block or only part of it. The fault sets generated are also used to avoid incorrect correlations during horizon picking due to fault offset (Figure 3.5).

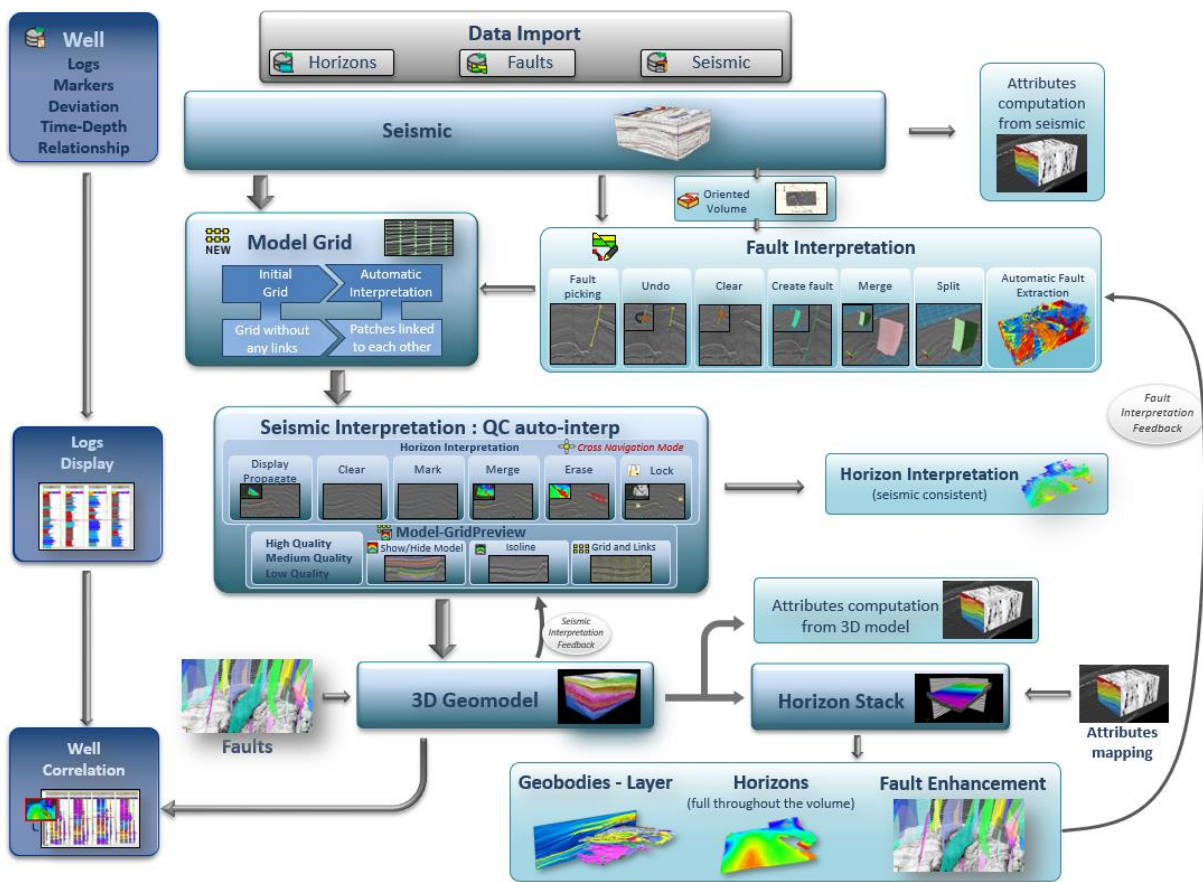


Figure 3.4: Synthesis diagram of the different steps used in the Paleoscan 3D seismic interpretation workflow. The main objective of the workflow is to build a 3D Geomodel, to do that, the first step consists in fault interpretation to better constraint the next step which is the model grid creation. The most important part is the manual refinement of the model grid to obtain the best 3D Geomodel possible. After this step, the computation of the Geomodel allows us to create different objects as horizons, horizons stacks, layers.

3-step workflow:

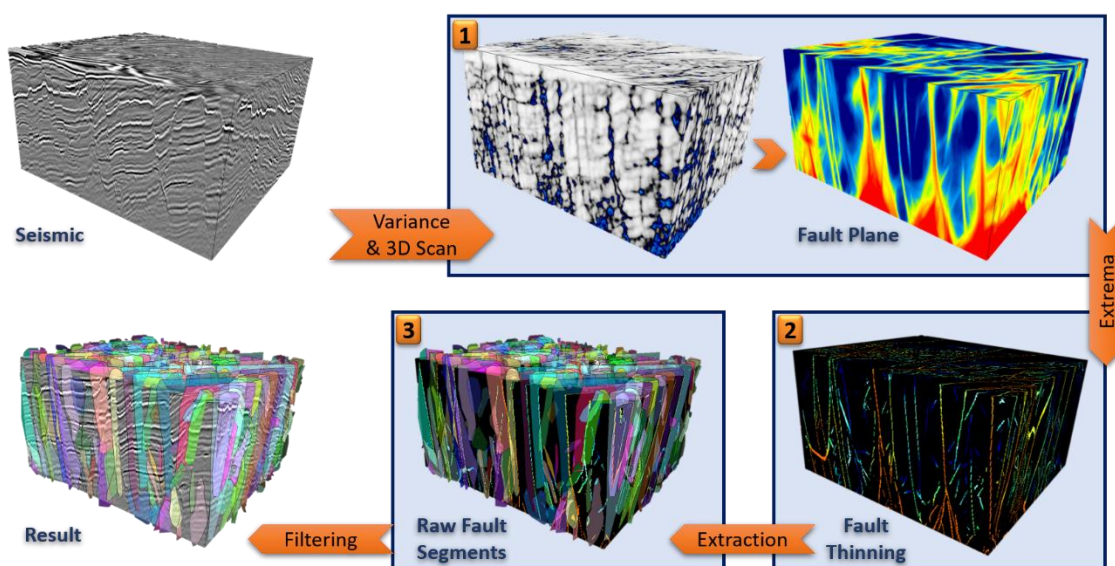
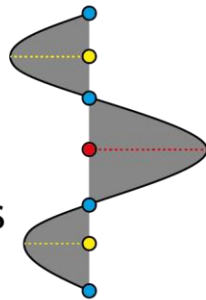


Figure 3.5: Paleoscan automatic faults interpretation workflow. Faults interpretation could be directly assessed from the seismic data, three steps are necessary, computation of a Variance seismic block associated with a 3D scan, fault thinning and finally the extraction and filtering.

PaleoScan's new horizon-picking feature also provides an innovative and more effective methodology to explore 3D seismic blocks (Gupta et al., 2008; Lutome et al., 2022; Paumard et al., 2018). Specifically, Paleoscan offers a full-volume, semi-automatic, seismic interpretation using advanced algorithms-based methods to autotrack simultaneously horizons throughout the seismic volume and compute geological models. This approach constitutes a revolution in seismic interpretation as this method permits to fully appreciate the three dimensionality of the data by comparing several horizons in parallel and potentially providing more accurate solutions than classic manual picking (Paumard et al., 2018). Manual picking achieved through extraction of 2D sections around closed loops such that the beginning and end are coincident is a commonly used-process known as loop tying but it is time-consuming and have a very low resolution (Lomask and Guitton, 2007). The model-grid created with Paleoscan is calculated by establishing links between elementary horizon patches which are based on signal amplitude of neighbouring traces throughout the 3D data (Figure 3.6). The model-grid can subsequently be used to create a 3D Geo-model (Figure 3.7). From the 3D Geo-model, it is possible to automatically extract horizons, the software correlates nearby points if they share common parameters, such as positive high-amplitude reflection. This automated computation however needs a careful checking from the interpreter in order to help the software in tectonically complicated areas or poorly resolved seismic.

Vertical Resolution:

- Peaks
- Troughs
- Zero Crossings



Spatial Resolution: σ

- Trace spacing:
- e.g. every 3, 5, 7 traces

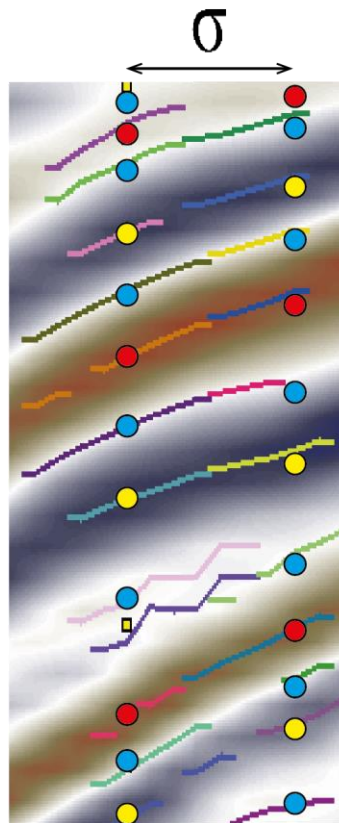


Figure 3.6: Model Grid creation workflow, the software uses seismic traces to create a grid. Each point of the grid is represented by a coloured dot. Vertical resolution could be determined using Peaks (red dot), Troughs (yellow dot) or Zero Crossings (blue dot) or an assemblage of them. Spatial resolution is defined by the distance between traces. Coloured lines around dot represent patch propagation used to form horizon.

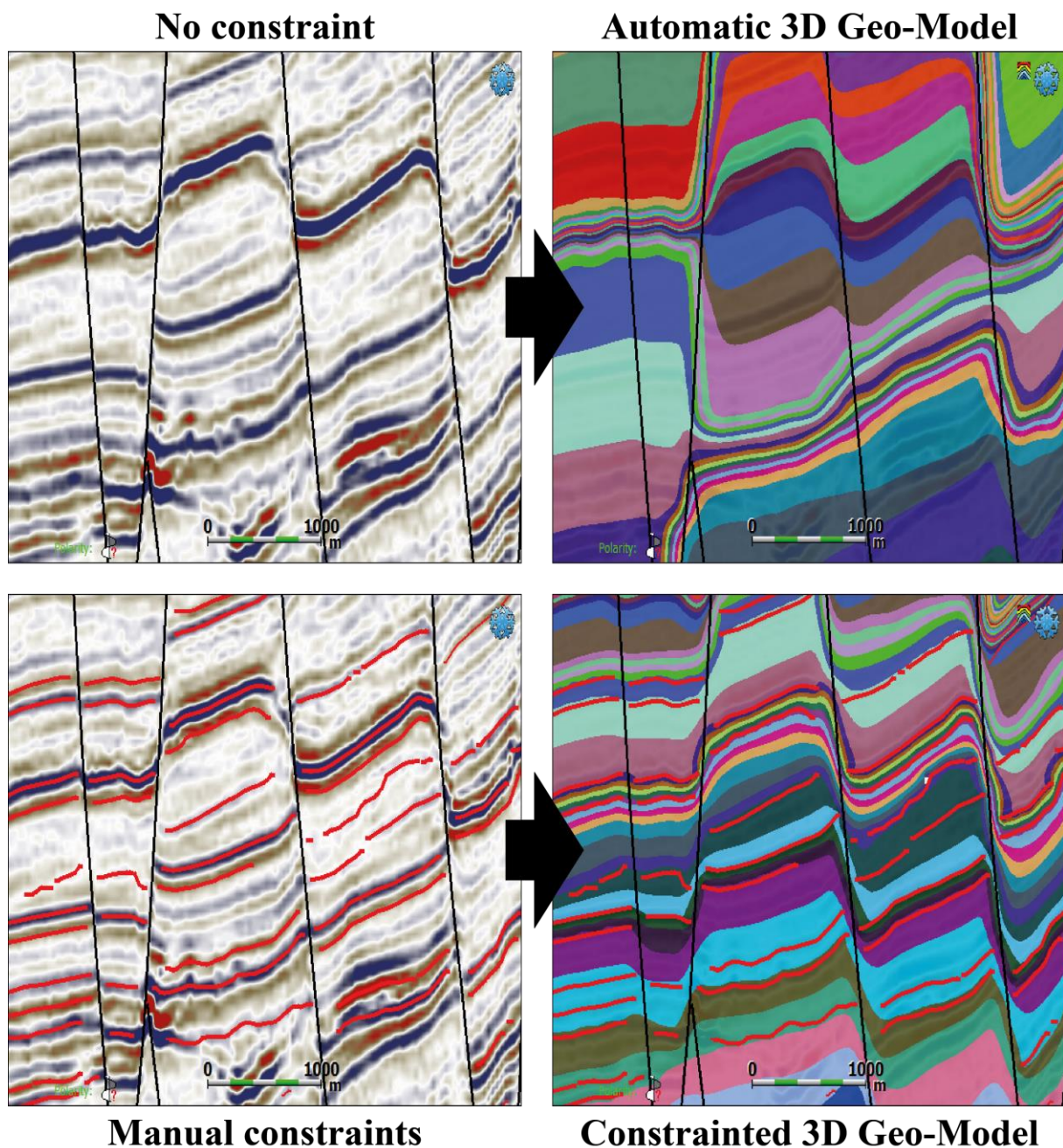


Figure 3.7: Paleoscan 3D Geo-Model workflow, the upper pair of pictures represent a 3D Geo-Model created without constraints while, the lower pair of pictures show the connected patches forming horizons in red used to constraint the Geo-Model visible on the right. The faults represented by black lines are not used to constraint the model as layers are still connected.

Finally, set of horizons (i.e. horizon stack) can be extracted from the 3D Geo-model. Thanks to the high-resolution of the interpretation and its full propagation in 3D, the user can scroll up and down through the horizon stacks to conduct stratigraphic and structural analysis. Horizon stacks are highly valuable for better understanding and interpreting a 3D seismic block, as they allow imaging of the block by examining each reflector's geometry. This replaces the old-fashioned timeslice viewer. Paleoscan also offers real-time visualisation of various

attributes (as Root Mean Square Amplitude or Dip Attributes) on both the 2D lines and the horizon stacks, which significantly aids in the interpretation of the seismic block. However, refinement and checks are still mandatory, and some corrections are always necessary to obtain an accurate horizon stack that allows 3D seismic interpretation.

In this work, 300 horizons were generated along the siliciclastic Plio-Pleistocene series. These horizons were initially used to correlate observations from one well to another (**Chapter 4**) but also to observe geomorphologies and their correlation with sequence stratigraphy (**Chapter 5**). Ultimately, the horizons revealed the evolution of carbonate structures along the margin (**Chapter 6**).

3.2. Boreholes data and methods

3.2.1. Principles of drilling and coring

In academic geosciences, drilling and coring are indispensable techniques used to investigate the subsurface, each with distinct purposes and capabilities. While drilling allows for reaching deeper structures, it is considered a destructive method. Coring, on the other hand, involves extracting undisturbed samples known as cores from ice or rocks. The depth attainable by gravity or piston cores is significantly constrained compared to drilling. The longest core obtained using this technique is around seventy meters and was acquired with the Marion Dufresne's Calypso-core tool in soft offshore sediments. In contrast, onshore coring rarely reaches such depths due to harder lithology. Drilling can easily attain several hundred meters and up to several kilometers, as demonstrated by the Kola Superdeep Borehole, a scientific drilling project of the Soviet Union that reached a depth of 12,262 meters (Popov et al., 1999).

Coring within a borehole is also possible, enabling the extraction of representative core samples for detailed examination. These samples provide unparalleled insights into lithology, mineralogy, and sedimentary structures at greater depths than gravity or piston cores, thereby shedding light on processes such as climate change and tectonics in older rocks. In contrast, drilling aims for a broader exploration of subsurface formations and quaternary sediments, utilizing sophisticated offshore vessels equipped with dynamic positioning systems or onshore truck-mounted rigs.

Given the requirement for precise retrieval of intact samples, coring often takes longer than drilling. For instance, a coring operation to reach 30 meters depth might require several hours, whereas drilling to a similar depth could be accomplished more quickly. However, drilling is a larger operation that requires much more equipment. It is also substantially more

expensive and is therefore mainly utilized by private companies. In the academic domain, the International Ocean Discovery Program allows scientists to drill for scientific purposes. In sum, the differences between drilling and coring are evident in their respective methodologies, outcomes, depth limitations, time requirements, and applicability across different environments. Coring, with its focus on retrieving pristine samples, plays a crucial role in nuanced subsurface investigations, while drilling facilitates a more comprehensive view of geological formations. Together, these techniques contribute to expanding our understanding of the Earth's subsurface and fostering new avenues of scientific exploration (Lisiecki and Raymo, 2005).

3.2.2. Borehole data inventory

Borehole data acquired during the drilling process encompass a wide range of measurements that inform various scientific and industrial objectives. These data often include information such as temperature, pressure, fluid content, resistivity, and sonic velocities, among others, within the geological formations being drilled.

Temperature and pressure measurements are essential in understanding the subsurface conditions and can reveal information about the geothermal gradient and formation pressures. Fluid content analysis helps in identifying the presence and types of liquids or gases, such as water, oil, or natural gas, within the formations. Resistivity measurements are utilized to distinguish between different rock types and their saturation levels with fluids. Sonic velocities, through the recording of sound waves, provide insights into rock's elastic properties and structure, which are valuable in characterizing the subsurface's geological features. Density logs, measure the bulk density of the subsurface formations. By sending a gamma-ray source into the borehole and detecting the scattered gamma rays, the density of the material surrounding the borehole can be deduced. These logs yield insights into the porosity and mineral composition of the rocks. Gamma-ray data are collected by measuring the natural gamma radiation emitted from subsurface formations. This radiation primarily emanates from radioactive isotopes of potassium, uranium, and thorium present in the rocks. Gamma-ray logs are valuable in differentiating between various rock types, particularly in distinguishing shale from non-shale formations.

Collectively, the data obtained from borehole drilling contribute to a comprehensive and multifaceted perspective on subsurface formations, yielding valuable insights that advance both scientific knowledge and practical applications in various fields.

3.2.3. Wells acquired along the Amazon Margin

More than 40 exploration wells have been acquired along the Brazilian Equatorial Margin, primarily by oil and gas companies between the early 1970s and the late 1980s (*Figure 3.2*). Most of these industrial wells are located on the shelf, with only a few on the slope and the Amazon fan. Some wells have reached depths of almost 5000 meters. These exploration wells mainly targeted the Amapá and Limoeiro Formations, and as a result, most of the geophysical data were acquired only within these intervals. Consequently, the siliciclastic Plio-Pleistocene series is largely devoid of geophysical data, except for Gamma-Ray data, which were acquired in all wells along the Plio-Pleistocene series. Lithological descriptions are available, but within the Plio-Pleistocene series, these descriptions are sparse and often lack precision. Detailed chronostratigraphic data, based on micropaleontological findings, are available from four exploratory wells (Cruz et al., 2019).

Additionally, two Ocean Drilling Program (ODP) legs explored the nearby region of the Brazilian Equatorial Margin in 1994. The first one, ODP Leg 154, focused on the Ceara Rise, an aseismic rise located 800 km from the coast, in front of the Amazon River Mouth (Curry et al., 1995). The second ODP leg, Leg 155, explored the Amazon Deep Sea fan but only drilled the superficial series. The deepest well acquired during ODP Leg 155 extends 433.80 meters in length and is located at a water depth of 3586 meters (Flood et al., 1995).

3.2.4. Cyclostratigraphy on borehole data

Cyclostratigraphy is a subfield of stratigraphy that deals with the identification and investigation of repetitive, cyclic variations within sedimentary successions. These cyclic variations often result from environmental changes driven by astronomical forcing factors, such as Earth's orbital parameters (Berger, 1984; Hinnov, 2013). By analyzing these cycles, cyclostratigraphy helps in interpreting climatic and environmental changes over geological timescales.

The concept of cyclostratigraphy emerged in the latter half of the 20th century, with significant advancements made since the 1980s (Weedon et al., 2004). Scientists began recognizing the significance of astronomical cycles in sedimentary records (Berger, 1984; Hays et al., 1976), and the development of numerical tools and analytical methods has allowed for more sophisticated analysis (Hilgen et al., 2015; Weedon et al., 2004). Cyclostratigraphy is based on the notion that a signal comprises a sum of various wavelengths (*Figures 3.8 and 3.9*).

Cyclostratigraphy's primary utility lies in its ability to correlate sedimentary sequences across vast distances and in various environments (Strasser et al., 2006). By recognizing and measuring cycles, it allows for the development of highly refined time scales (Boulila et al., 2020). It can also aid in understanding the depositional environment and climatic changes by revealing how sedimentation rates and patterns have evolved through time (Hinnov, 2013).

Cyclical or periodic processes in Earth's history extend across a broad spectrum, ranging from twice-daily tidal cycles to plate-tectonic movements that recur over tens of millions of years (House, 1995). Among these, the cycles most often utilized in cyclostratigraphy are the Milankovitch cycles, caused by perturbations in the Earth's orbit and changes in the inclination of its axis (Hays et al., 1976).

Cyclostratigraphy employs astronomical cycles of known durations as a temporal framework (Berger et al., 1989). The fundamental prerequisite for this approach is the identification of patterns in the sedimentary record that can be confidently linked to astronomical cycles. These patterns often manifest as repetitive sedimentary, biological, and/or geochemical changes, serving as proxies for cyclical processes within the geosphere-hydrosphere-biosphere-atmosphere system, influenced by orbitally induced changes in solar radiation (Laskar et al., 2004). To seek these patterns, detailed examination of the studied sections or cores is essential, and they must be as complete as possible.

Numerous studies have affirmed that orbital cycles are recorded within sedimentary rocks and can be employed to refine the timing of Earth's history (Weedon et al., 2004). Typically, two methods are synergistically used to attain reliable results:

- Independent Time Control: This method constrains the time frame for the cyclostratigraphical study through direct radiometric age dating or via biostratigraphy, chemostratigraphy, magnetostratigraphy, and/or sequence stratigraphy, all calibrated to radiometric age dates (Gradstein et al., 2012). Even with substantial error margins, an approximate duration of a sedimentary cycle can be gleaned, forming the basis for further exploration.
- Analysis of Hierarchical Stacking Patterns: In studying Phanerozoic sediments, it is often assumed that the precession of the equinoxes corresponds to 20 kyr, and the short and long eccentricity cycles to 100 and 405 kyr, respectively. This correspondence yields a 1:5:20 ratio for analyzing the stratigraphic record. For obliquity, and to a lesser extent also for precession, the periodicity has to be selected based on the geological age of the studied sediments.

Testing the anticipated ratios between orbital periodicities often involves time-series analysis. The success of such analysis hinges on the judicious selection of measured parameters and sampling density (Fischer et al., 2004; Weedon et al., 2004). Stratigraphic gaps must be identified and factored into the study.

In cyclostratigraphy, converting the initial depth-domain record into the time domain using age calibration points is a critical aspect of time-series analysis. These points may originate from radiometrically dated ash layers, bio-events, or magnetostratigraphic calibration to the geomagnetic polarity time scale (Hinnov, 2000). Several techniques, such as Fourier analyses, wavelet analysis, or neural-net-aided detection, can detect orbital periodicities (Brescia et al., 1996; Hinnov, 2000; Preto et al., 2004; Weedon and Jenkyns, 1999; Zühlke, 2004). Notably, Fourier spectral analysis decomposes a time series into sinusoids with defined frequencies, amplitudes, and phases. The outcome is typically represented in a frequency-domain spectrum. This understanding of frequency dependence may unlock vital insights into underlying natural phenomena (Strasser et al., 2006).

Upon identifying a Milankovitch signal in the stratigraphic record and associating sedimentary, biological, or geochemical cycles with specific orbital cycles, the astronomical forcing of climate change can be reconstructed. Furthermore, for more recent stratigraphic records, astronomical time scales can be derived by tuning the orbitally controlled proxy cycles to astronomical target curves based on Solar System solutions (Laskar et al., 2011, 2004; Weedon and Jenkyns, 1999). These time scales offer unparalleled accuracy and resolution.

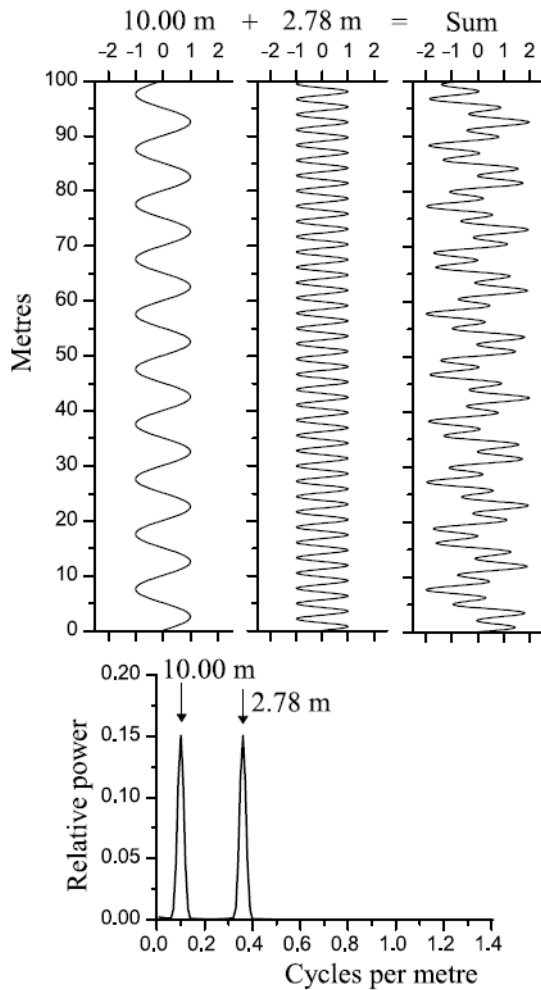


Figure 3.8: From Weedon et al. (2004): Adding sinusoids with different wavelengths produces a time series with multiple frequency components. Power spectra are used to: (a) identify which frequency components are present (frequency = $1/\text{wavelength}$); and (b) determine their relative amplitudes. In this case two sine waves of equal amplitude, but different wavelengths, have been added to produce the time series labelled “Sum”. The corresponding power spectrum has peaks that occur at frequencies corresponding to the component wavelengths. The peaks are equal in height because the components have the same amplitude. Note that it is impossible to tell from the spectrum whether the components are sine or cosine waves – in other words the spectrum is independent of the phase of the components.

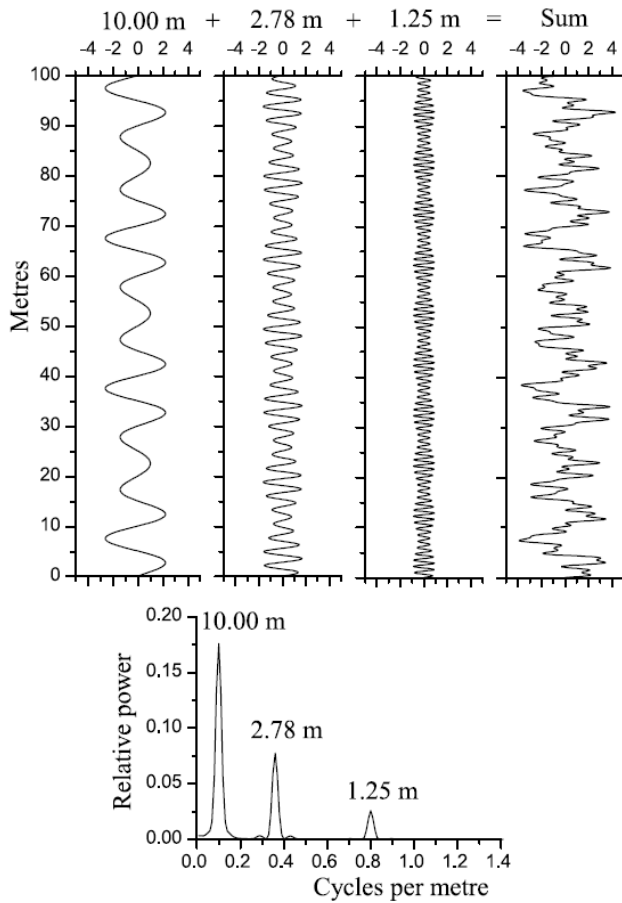
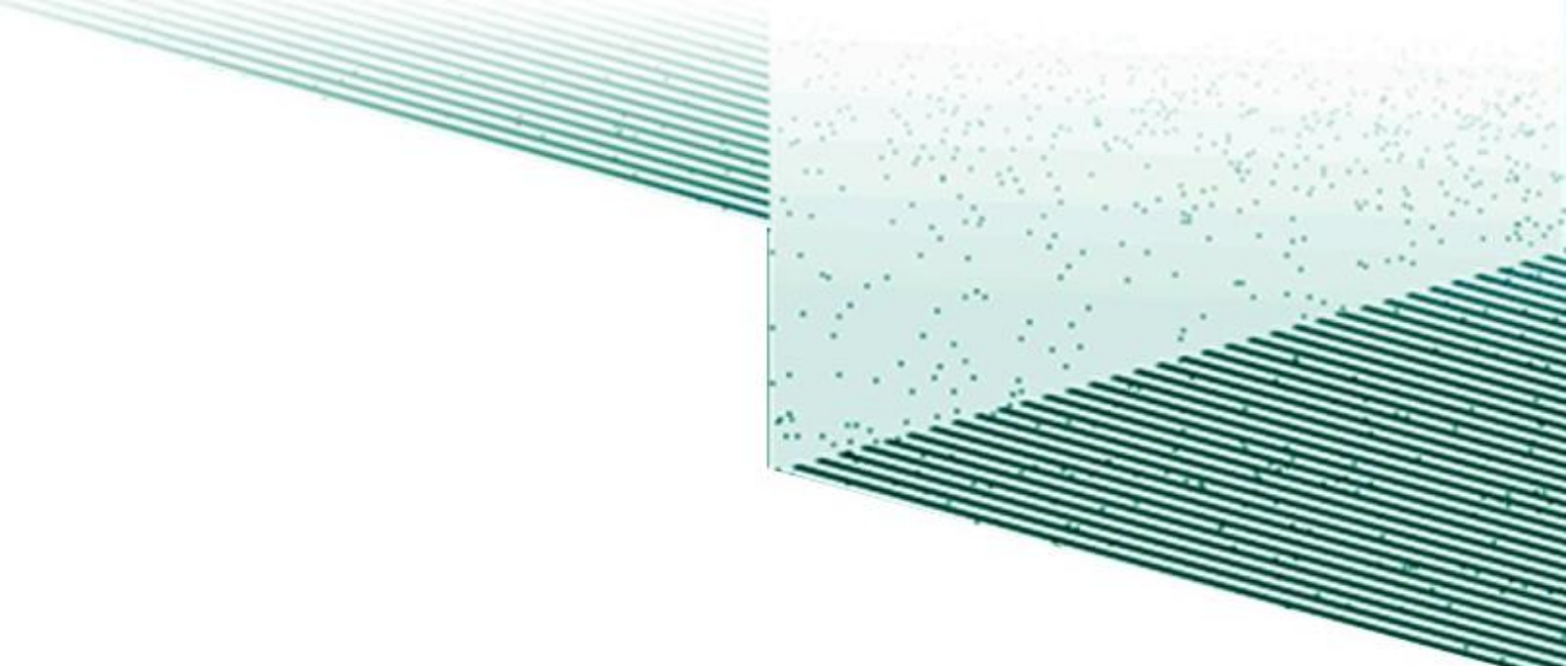


Figure 3.9: From Weedon et al. (2004): Adding three sine waves with different wavelengths and varying amplitudes produces a time series that looks extremely complicated. It is unlikely that mere visual inspection of the summed time series illustrated would allow one to recognize that just three frequency components are present, or to determine the wavelengths involved.



Chapter 4: Amazon
Sedimentation Unveiled:
Decoding the Shelf Edge
Evolution of the Brazilian
Equatorial Margin since the
Pliocene

Amazon Sedimentation Unveiled: Decoding the Shelf Edge Evolution of the Brazilian Equatorial Margin since the Pliocene

Submitted to *Global and Planetary Changes*, this manuscript was initially rejected but the editor has offered an opportunity for resubmission following major revisions. Presented here is the revised version.

Lucas Tortarolo^{a,b,f}, Marina Rabineau^a, Slah Boulila^b, Christian Gorini^b, Linda Hinnov, Damien Do Couto^b, Antonio Tadeu Dos Reis^c, André W. Droxler^d, Daniel Praeg, Alberto Machado Cruz^e, Cleverton Guizan Silva^f

^a Laboratoire Geo-Ocean, Institut Universitaire Européen de la Mer, UBO, UBS, IFREMER, CNRS, UMR6538, Rue Dumont d'Urville, 29280 Plouzané, France

^b Institut des Sciences de la Terre Paris (ISTEP), Sorbonne Université, CNRS, UMR 7193, 4 Pl. Jussieu, 75005 Paris, France

^c Departamento de Oceanografia Geologica, Universidade do Estado do Rio de Janeiro, Rua São Francisco Xavier, 524, Rio de Janeiro, RJ, Brazil

^d Department of Earth, Environmental and Planetary Sciences, Rice University, 6100 Main St., Houston, TX 77005, USA

^e Beicip-Franlab, Rua da Assembléia, 10 - Centro, Rio de Janeiro - RJ, 20011-901, Brazil

^f Departamento de Geologia e Geofísica, Universidade Federal Fluminense, Av. Gal. Milton Tavares de Souza, Campus da Praia Vermelha, Boa Viagem, Niterói, RJ, Brazil

corresponding author: lucas.toratorolo@univ-brest.fr

Abstract

The Brazilian Equatorial Margin is a setting where the stratigraphic architecture of the continental margin is strongly influenced by sediment supply from the Amazon River, but where the Plio-Pleistocene succession lacks geochronological data. This study examines a shelf-edge area of the Brazilian Equatorial margin when siliciclastic deposition, around 4 Ma, starts, above the well-known Amapá carbonate platform. The study employs a coupled approach of sequence stratigraphic analysis of a 3D seismic block, and cyclostratigraphic analysis of gamma-ray (GR) log data from three exploration wells. We identify nine main seismic sequences from the start of siliciclastic deposition, which is dated at 3.7-4.1 Ma from the only biostratigraphic age available at the base of the serie. As a first approximation, each sequence therefore likely corresponds to a long 405-kyr eccentricity cycle. Internal characteristics of the seismic sequences support their grouping into three major depositional mega-sequences (MS-I to MS-III). The correlation between orbital cycles and seismic sequence

is supported by a cyclostratigraphic age-model based on spectral analyses of GR data and tuned on obliquity cycles, which allow us to propose ages for each sequence. Our results suggest that the primary driver of changes in stratal architecture observed along the Brazilian Equatorial shelf edge during the last 4.0 My is the well-established long-term increase in the amplitude of sea-level fluctuations. Mega-sequence boundaries likely reflect major steps in the Earth's Quaternary climate at 2.4 and 0.8 Ma, specifically overall cooling that led to the intensification of Northern Hemisphere Glaciations (iNHG) and the Mid-Pleistocene Transition (MPT). A further significant change in shelf edge architecture at around 0.4 Ma corresponds to a change from mostly prograding patterns since 0.8 Ma to mostly aggrading ones during the last 405 kyr. This shift in the depositional system is likely related to the prominent high amplitude sea-level rise characterizing the long-lasting Marine Isotopic Stage 11. We conclude that changes in the Brazilian Equatorial shelf edge geometry over the last 4.0 Myr were likely paced by orbitally forced climate which affect sea-level changes and sediments supply from the Amazon at the 405 kyr and 100 kyr Earth orbital eccentricity cycles. Major changes observed in geometries are being correlated with main global climatic events. This nice preservation of high-resolution cycles is due to high total subsidence rates (~300 m/Myr) most probably related to the loading effect of the Amazon deep-sea fan.

Keywords: Brazilian Equatorial Margin, Offshore Amazon Basin, Plio-Pleistocene, cyclostratigraphy, seismic and sequence stratigraphy, astro-climate.

4.1. Introduction

The Amazon River plays a significant role in Earth's hydrologic budget, contributing to 20% of global fluvial input to the oceans (Dai and Trenberth, 2002). Covering 35.5% of the South American continental surface, the Amazonian hydrographic basin is the world's largest drainage basin (Milliman, 2001; Nittrouer et al., 1986), and contains the Amazonian Forest and ecosystem, which serve as vital indicators of Earth's climate (Malhi et al., 2008). The Amazon River further acts as a biological barrier on land and at sea due to its prominent sediment plume of low salinity (< 35) and high concentrations of suspended material and nutrients that spreads for thousands of kilometres over the North Brazilian Continental Shelf and adjacent open waters (Giachini Tosetto et al., 2022). As a result, the intricate relationship between climate, its effects on the supply of water and sediment along the Amazon River, and the record of this in the stratigraphic succession of the adjacent continental margin concerns a broad scientific community, including geoscientists, oceanographers, and biologists.

The stratigraphic succession of the Amazon continental margin records a variety of climate change aspects, including but not limited to cyclic sea-level fluctuations and precipitation variations which influence sediment supply over time. Previous research based on 2D seismic and cores analysis by Damuth and Kumar (1975) underscored the dominance of sea-level variations in shaping the Amazon offshore sedimentary system. During sea level highstands, sedimentary deposits primarily accumulate nearshore, while suspended sediments are transported by longshore currents, partially accumulating along the northern Brazilian coastline or reaching the French Guiana shelf and beyond (Eisma and van der Marel, 1971; Jacobs and Ewing, 1969; Milliman et al., 1975). Milliman et al. (1975) proposed that the subaqueous delta, comprising a mud wedge, mainly expands during sea levels ranging from -20 to -80 meters below the present-day level. Ultimately, as sea level decreases and reaches the shelf edge, terrigenous sediments from the Amazon are intercepted by the Amazon Canyon, bypassing the outer shelf and accumulating directly on the well-developed Amazon deep-sea fan along the Brazilian margin's slope (Damuth et al., 1983; Damuth and Kumar, 1975).

Gaining a deeper comprehension of the impact of sea level fluctuations and the broader influence of climate has been the central theme of numerous studies (Behling et al., 2000; Crivellari et al., 2018; Hoorn, 1997; Nace et al., 2014; Rühlemann et al., 2001; Zhang et al., 2015). Notably, orbital parameters exert a distinct influence on global climate, particularly the dominant effect of eccentricity during the last million year. This influence extends to the Amazon drainage basin and margin. As highlighted by Mason et al. (2019), the last two glacial stages were characterized by increased precipitation in the Andean Mountains, accompanied by drier conditions in the Amazon Basin. However, our understanding of the impact of climate change on sediment accumulation over longer time spans remains less clear due to limited data availability and quality near the Amazon River mouth. Due to high offshore sedimentation rates, piston cores from the Amazon shelf and upper slope provide information on sediments younger than 100-405 kyrs (Behling et al., 2000; Crivellari et al., 2018; Hoorn, 1997; Nace et al., 2014; Rühlemann et al., 2001; Zhang et al., 2015). Although more than 40 exploration wells have been drilled on the Amazon shelf, they typically target deeper sedimentary formations and contain limited information on the Plio-Quaternary succession. Gamma-ray and other log data from upper well sections offer insight into lithologies, but only a few studies have focused on chronostratigraphic analyses of the Plio-Pleistocene (e.g. (Cruz et al., 2019; Cruz, 2018; Figueiredo et al., 2009, 2007; Gorini et al., 2014). Cruz et al. (2019) established a geochronological framework for the Neogene succession on the Amazon margin using biostratigraphic data available from three wells. Biostratigraphic data for the Plio-Pleistocene

succession are otherwise scarce, resulting in an insufficiently defined chronology and evolution of continental margin architecture during this period.

This study examines the Plio-Pleistocene stratigraphy of a part of the Amazon margin, using a 3D seismic block and log data from three nearby wells. Our approach involves two distinct methods. On one hand, utilizing gamma-ray logs, we develop cyclostratigraphy to identify dominant cycles and establish an age model for the shelf edge sedimentary succession. In parallel, the analysis of the 3D seismic block, within a sequence stratigraphic framework, permits the integration of shelf edge architecture evolution over time. Finally, the aim of our study is to test the recognition and impact of climate cyclicities in the record of sediments, their effect on sediment architecture and propose a more detail chronostratigraphic framework.

4.2. Regional setting

The Brazilian Equatorial Margin (*Figure 4.1*) formed during the opening of the Equatorial Atlantic Ocean, in two phases: an early phase in the Triassic-Jurassic period (225-145 Ma) leading to the opening of the Central Atlantic Ocean, and a later phase associated with continental rifting during the Early Cretaceous (~120–105 Ma) (Darros de Matos, 2000). Open-marine deposition began around the Albian with the clastics Limoeiro Formation (approximately 102 Ma) and persisted until the Palaeocene Figueiredo et al. (2007). From the late Palaeocene (around 59 Ma) to the late Miocene, the basin was dominated by mixed carbonate-siliciclastic shelf sediments (Marajo and Amapá Formations) (Figueiredo et al., 2007). From the late Miocene onward, increasing clastic sediment influx led to the burial of the carbonate platform (Gorini et al., 2014), resulting in the formation of the present-day Offshore Amazon Basin including continental shelf deposition and the Amazon Fan laying on the slope and abyssal plain. The events triggering the transition from carbonates to silico-clastic sedimentation remain a subject of ongoing debate (Campbell, 2010; Cruz et al., 2019; Figueiredo et al., 2010, 2009; Gorini et al., 2014).

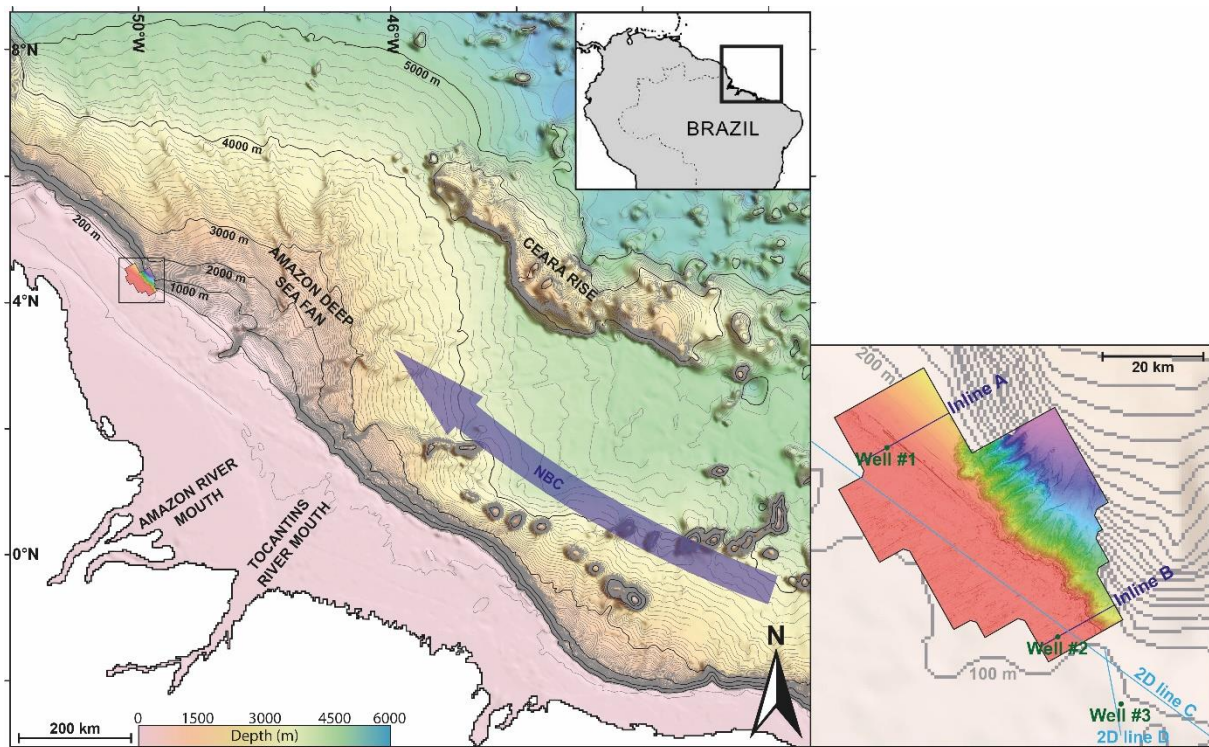


Figure 4.1: Bathymetric map of the NW Equatorial Brazilian Margin along with the location of sites of the studied data. The 3D seismic block is shown with the sea floor topography. The North Brazilian Current (NBC) is indicated with a thick blue arrow (Note the current also sweeps the continental shelf, the arrow is only indicative). In the expanded view, three wells are displayed in green (well #1 and #2 inside the 3D block, and well #3 outside the 3D block); two inlines A and B in dark blue are interpreted in figures 4 and 5, in addition to two 2D seismic lines C and D (also shown) used to tie the well #3 with the 3D seismic block.

Various studies of the stratal architecture of the Offshore Amazon Basin have proposed a Late Miocene age for the cessation of carbonate sedimentation, marked by the top of the Amapá Formation, linked to an increase in siliciclastic sediments due to the initiation of the transcontinental Amazon River (Brandão and Feijó, 1994; Campbell, 2010; Carozzi, 1981; Figueiredo et al., 2010, 2009; Silva et al., 1999; Wolff and Carozzi, 1984). However, recent research suggests that carbonate sedimentation persisted in the Offshore Amazon Basin well after the Late Miocene (Cruz et al., 2019; Gorini et al., 2014). In particular, Cruz et al. (2019) used calcareous nannofossil zonation in well data to re-evaluate the study of Figueiredo et al. (2009), taking into account the variability in the cessation of carbonate deposition proposed by Gorini et al. (2014). This led to the establishment of a Late Miocene age (8 million years) for the cessation of carbonate sedimentation in the southern part of the Brazilian Equatorial shelf, versus an Early Pliocene age (3.7-4.1 Myrs, Figure 4.2) in the northern sector of the basin (near well #3).

The Offshore Amazon Basin lies in the northwestern portion of the Brazilian Equatorial Margin (*Figure 4.1*) and encompasses an area of approximately 360,000 km² (Silva et al., 1998). The basin corresponds to a depocenter in front of the Amazon River Mouth, containing up to 9 km of siliciclastic sediments. Between 8 to 3.7 million years, most of the clastic sediments were trapped in a paleo-embayment in front of the Amazon River mouth (Cruz et al., 2019). Following the embayment's completion, sediment progradation commenced, primarily toward the northeast due to the influence of the North Brazilian Current (NBC), which continues to impact the Amazon plume and facilitate sediment migration toward the northern part of the margin (Gensac et al., 2016; Hu et al., 2004). During periods of falling sea levels, the slope and basin experience significant influence from Amazon-derived sediments deposited into the Amazon deep-sea fan via the Amazon Canyon (Flood et al., 1995; Maslin et al., 2006). In proximity to the canyon, the deep-sea fan expands to around 380 km in width and extends to the abyssal plain at depths reaching approximately 4850 m (Damuth and Kumar, 1975). The thickness of sediment within the Amazon fan (reaching up to 9 km) has prompted isostatic subsidence and lithospheric flexural deformation beneath the fan and surrounding regions, including the outer shelf (Cruz, 2018; N. W. Driscoll and Karner, 1994; Rodger et al., 2006; Silva et al., 1998).

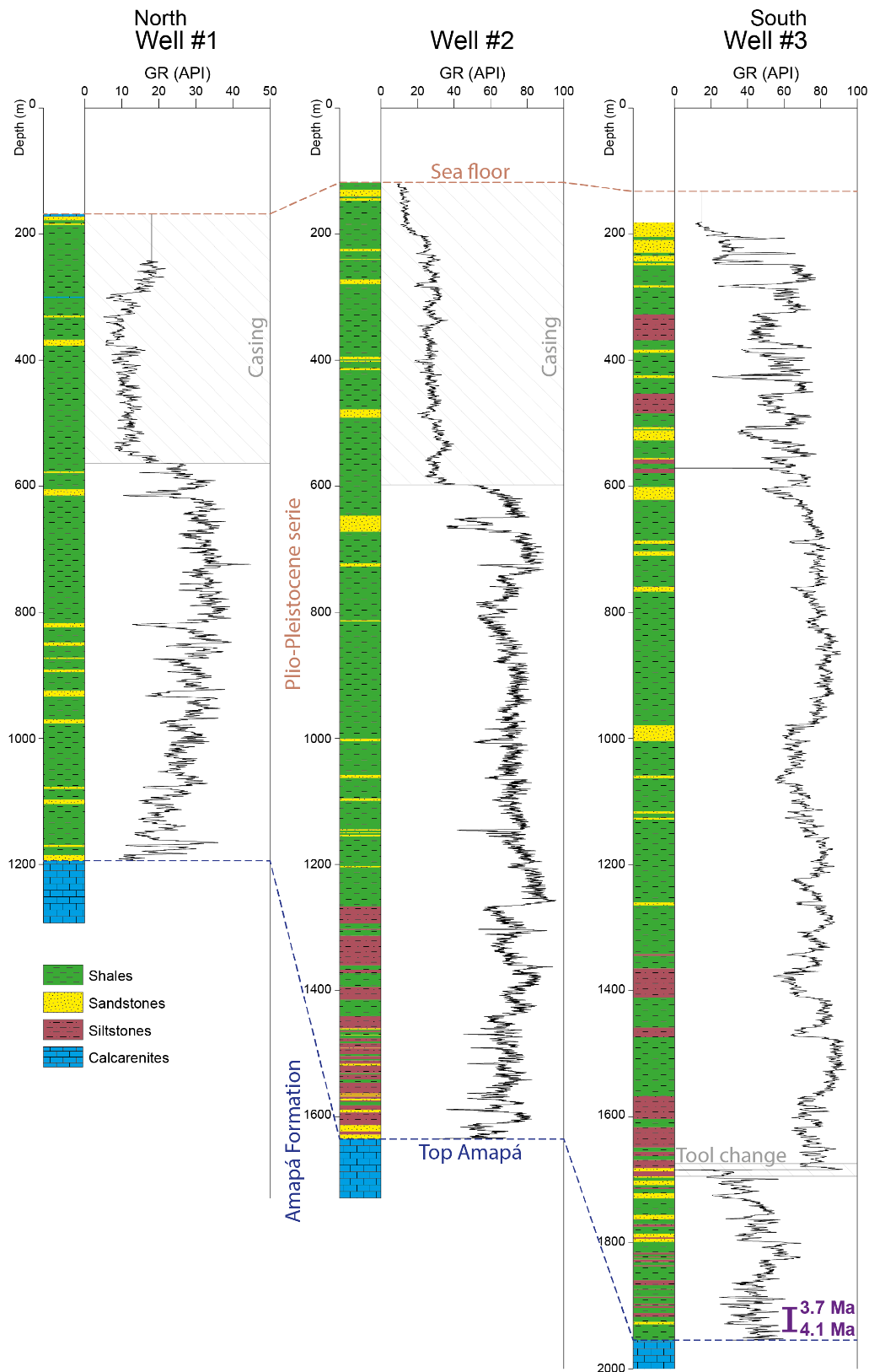


Figure 4.2: Lithology and gamma ray (GR) data of Wells #1, #2 and #3, displaying their Plio-Pleistocene sections shown in these figures from left north (Well #1) to right south (Well #3). The purple interval at the beginning of the Plio-Pleistocene section, just above the top Amapá, in well #3 was dated by biostratigraphy at 3.7 to 4.1 Ma (Cruz et al., 2019). Some unusual changes in the GR values, due to technical issues such as the presence of casing or tool change, are noted in light grey along the wells.

4.3. Data and methods

4.3.1. 3D seismic and downhole datasets

This study uses a 3D seismic block up to 60 km long and 40 km wide, covering an approximate area of 1700 km² (*Figure 4.1*). The block features a grid spacing of 25 meters, encompassing 2387 inlines and 1733 crosslines. The seismic volume was processed using a standard sequence that included pre-stack time migration (PSTM). The data has a vertical sampling interval of 4 ms, and the full-stack signal exhibits a dominant frequency of 37 Hz, offering a vertical resolution of 10-20 m for velocities from 1500 to 3000 m/s.

Downhole data were used from three wells situated within or near the 3D seismic block (*Figure 4.1*), which span the entire Plio-Pleistocene series (*Figure 4.2*). The wells, labelled as APS_44, APS_29, and APS_45B, are referred to as Wells #1, #2, and #3, respectively. Wells #1 and #2 lie within the 3D seismic block, Well #3 lies <20 km outside the 3D seismic block (*Figure 4.1*). Gamma-ray (GR) log data have a vertical resolution of 15-20 cm; values are presented in API (American Petroleum Institute) units. GR logs are available from seafloor in Well #2, and below depths of 75 m and 49 m in Wells #1 and #3, respectively. Significant shifts in GR values around 560 m in Well #1 and 600 m in Well #2 are associated with the presence of casings in the upper intervals rather than lithological variations. Lithological descriptions thanks to mud sampling analysis are available for the Plio-Pleistocene series in wells #1, #2, and #3, however the sampling rates is between 3 to 5 meters and does not provide good representation of the lithological changes. In Well #3, a biostratigraphic age based on the Last Occurrence (LO) of calcareous nannofossils, *Sphenolithus Neoabies* (LO: 3.7-3.92 Ma), is observed at 1910 m, along with the First Occurrence (FO) of *Discoaster tamalis* (FO: 3.92-4.13 Ma) at 1940 m. This biostratigraphic data point as been correlated from the well to the 3D seismic dataset (*Figure S4.1*).

4.3.2. Seismic sequence stratigraphic methods

A standard seismic analysis approach (Mitchum and Vail, 1977) was used for the 3D seismic data based on the recognition of reflection termination such as onlap, erosional truncations, seismic facies/configuration and vertical stacking patterns. This method led to the creation of a seismic facies and architectural element catalogue (*Figure 4.3*).

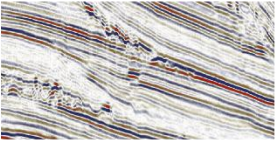
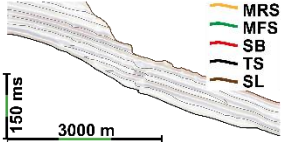
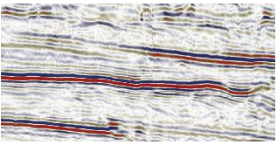
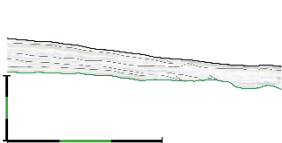
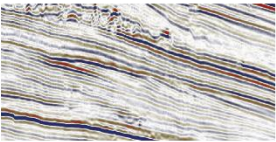
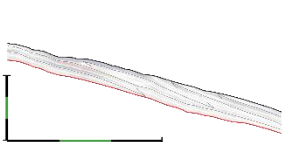
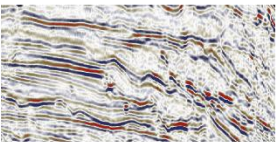
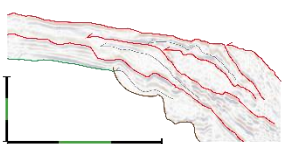
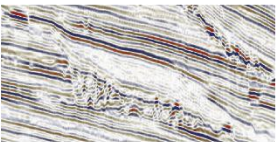

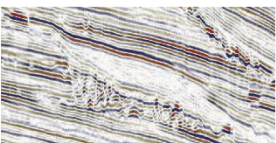

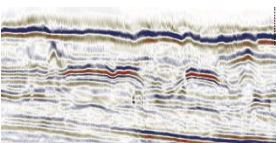
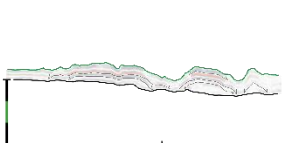
Seismic data	Seismic interpretation	Description	Interpretation
		SF1: Mostly aggrading, continuous, sub-parallel, medium amplitude reflectors with onlap	SF1: Transgressive System Tract (TST)
		SF2: Prograding and aggrading continuous, convergent, medium amplitude reflectors with downlap	SF2: Highstand System Tract (HST)
		SF3: Only prograding, continuous, low amplitude reflectors with offlap and downlap	SF3: Falling Stage System Tract (FSST) along the outer shelf
		SF4: Mostly prograding, continuous, medium to low amplitude reflectors with high inclination, offlap and downlap	SF4: Falling Stage System Tract (FSST) and/or Lowstand System Tract (LST: if there is aggrading pattern) located on the slope
		SF5: Mostly prograding and slightly aggrading, low amplitude reflectors with onlap and downlap	SF5: Lowstand System Tract (LST) located on the slope
		SF6: Chaotic, discontinuous, medium amplitude reflectors	SF6: Submarine Landslide (SL)
		SF7: High amplitude reflectors with build-up geometries	SF7: Transgressive carbonates

Figure 4.3: Seismic facies classification and architectural elements interpretation.

In addition to the seismic analysis, a sequence stratigraphy model has been developed (Figure 4.4). Each of the observed facies is interpreted in terms of system tracts, following the stratigraphic sequence definition put forth by Catuneanu (2019, 2006) and Catuneanu et al. (2011, 2009). According to this definition, a stratigraphic sequence consists of a succession of strata deposited during a complete cycle of change in accommodation space or sediment supply. Accommodation, representing the relative volume available for sediments at a given time, is primarily influenced by two mechanisms: eustatic fluctuations and subsidence (Catuneanu et al., 2011). This definition is particularly evident in the shelf to upper slope areas with relatively shallow environments. In deeper settings, such as the lower slope and deep basin, the effects of hydrodynamics and currents must be considered more carefully, as they could generate significant deposits such as turbidites or contourites.

Consequently, a sequence is composed of various system tracts, each corresponding to different stages in the variation of the ratio between accommodation rate and sediment supply (A/S ratio). We used the Depositional Sequence IV, introduced by Hunt and Tucker (1992) and Helland-Hansen and Gjelberg (1994) to define each system tract. According to this model, a complete sequence cycle comprises four distinct system tracts: The Transgressive System Tract (TST), The Highstand System Tract (HST), The Falling Stage System Tract (FSST), and the Lowstand System Tract (LST).

Moreover, since progradation typically takes place as a continuous depositional process from Highstand to Lowstand conditions, identifying and correlating the Sequence Boundaries (SBs), limiting the FSST to the LST, on a regional scale can be challenging. As a result, we prefer to use the reflectors corresponding to the Transgressive Surface (TS) as markers for sequence boundaries.

In pursuit of a comprehensive understanding of the study area's evolution, the interpretation and analysis of stratigraphic sequences were conducted using specialized 3D seismic interpretation software, PALEOSCAN (<https://www.eliis-geo.com>).

4.3.3. Cyclostratigraphic methods of time-series analysis

We used GR data as a proxy of sea level fluctuations. In prior studies, GR well log data has effectively served as an indirect paleoclimatic proxy for characterizing orbitally-driven continental and marine sediments (e.g., Ruffell and Worden, 1999; Weedon et al., 2004; Wu et al., 2013).

The workflow starts by extending the GR signal in Well #1 and #3 to the seafloor to add a geochronological anchor of 0 kyr or 20 kyr if we consider the sea floor as an erosive surface resulting of the last glacial maximum. Afterward, we detrend the GR dataset using the weighted-average lowess method (Cleveland, 1979) to mitigate abrupt changes resulting from acquisition issues like tool changes and cased intervals as well as to eliminate long-wavelength components that could minimize the amplitude of higher frequencies. Subsequently, we use multi-taper method (MTM) spectral analysis to seek sedimentary cyclicities within GR data (Thomson, 1982). The manual frequency ratio method; such as the 5:2:1 relationship among short eccentricity (~100 kyr), the obliquity component (~41 kyr), and precession (~20 kyr); aids in identifying potential astronomical cyclicities. We used a Gaussian filter to detect and highlight recorded astronomical cycles (Paillard et al., 1996). Two filters are made on each well, on the potential short eccentricity and obliquity, which are the most prominent astronomical cycle in our datasets. We then construct age model for the Well #1 and #3 by

aligning the minima of the different filter with minima of Earth's short eccentricity and obliquity. Well #2 cross in the lower siliciclastic series, a highly deformed area, therefore the GR dataset of Well #2 is not suitable to build an age model (*Figure 4.4*). As well #1 and #3 do not start at the sea floor, we use Lastly, we compare our age model with the outcomes of the "eCOCO" method. The "eCOCO" tool is based on the COrrrelation COefficient method (Li et al., 2019) and allow to study sedimentation rate evolution across datasets. The COCO technique, inspired by the average spectral misfit (ASM) method of Meyers and Sageman (2007), is an automatic frequency ratio method. It estimates the correlation coefficient between the power spectra of an astronomical target signal and paleoclimate proxy series across a range of tested sedimentation rates. Similar to ASM, a null hypothesis of no astronomical forcing is assessed through Monte Carlo simulation. Prior to validating our results. The age models obtained are compared with the only available biostratigraphic data from Well #3 (Cruz et al., 2019). The analysis steps were performed using Acycle v2.0 software (Li et al., 2019).

4.4. Results

4.4.1. Dating the starts of the siliciclastic deposition

A prominent and continuous high-amplitude reflector (*Figure 4.4*) marks the top of the Amapá Formation. In the wells, this reflector corresponds to a lithological change from sand-sized carbonates to fine-grained siliciclastic sediments. Notably, this horizon covers nearly the entire surface of the seismic block. Additionally, a second thick, continuous, high-amplitude reflector represents the seafloor, defining the top of the Plio-Pleistocene series.

As explained in the Data and Methods section, only one biostratigraphic age spanning 3.7-4.1 Ma is available at the base of siliciclastic deposition studied in well #3 (*Figure 4.2*). This well is just outside our 3D block, but we followed the position of the biostratigraphic point from well #3 along seismic reflexion of a 2D seismic line crossing the well #3 towards our 3D seismic block (see *Figure S4.1*). The correlation falls just above the Amapá carbonate platform and in the first reflections of the siliciclastic sediment in Well #2 (*Figure S4.1*). Therefore, we suggest an age of around 4 Ma for the start of post Amapá siliciclastic sediments deposition in our study area.

4.4.2. Stratigraphic sequences

4.4.2.1. *Seismic facies and associated sedimentary architecture*

We identified seven seismic facies (SF1 to SF7, *Figure 4.3*) through an analysis of the geometry, terminations, and impedance of seismic reflectors, and provided an interpretation in terms of depositional architecture.

- SF1 consists of stacked horizontal and parallel reflectors with high amplitude and good lateral continuity (corresponding to a high impedance contrast between beds). SF1 overlaps other seismic facies, displaying onlapping terminations. SF1 is capped by a distinct prograding clinoform surface (base of the HST), therefore it corresponds to a Transgressive System Tract (TST).

- SF2 comprises seismic reflectors of medium amplitude and low lateral continuity, with mostly sub-horizontal and sub-parallel reflectors. Sigmoidal to oblique reflections corresponding to basinward prograding foresets allow clear differentiation of this seismic unit from the TST. This seismic facies is linked to a Highstand System Tract (HST).

- SF3 is characterized by clinoforms (oblique) towards the basin of low to medium amplitude reflectors with steep angles. Reflectors are toplapping and outward building into the basin, exhibiting downlaps at the base of the seismic unit. This facies displays progradation only with a clear downward shift of toplaps that links it to the Falling Stage System Tract (FSST).

- SF4 is defined by inclined reflectors of medium to low amplitude with steep angles, and is topped by one or two high-amplitude reflectors. Reflectors show progradation, while a minor aggradational component is visible in some parts. This seismic facies is hence linked to a Falling Stage System Tract (FSST) or/and a Lowstand System Tract (LST) on the slope, contingent on the presence or absence of aggradation.

- SF5 is marked by very low amplitude reflectors that prograde and aggrade. This facies exhibits onlap and downlap terminations and is associated with the Lowstand System Tract (LST) or early Transgressive System Tract (TST).

- SF6 features discontinuous and deformed reflectors of medium to high amplitude. Due to its internal geometry and position along Submarine Landslide scar (SLi), it is linked to mass transport deposits.

- SF7 is characterized by high amplitude and low-frequency reflectors, sometimes presenting a lateral shift in polarity. This seismic facies is also associated with topographic high

features. The combination of these characteristics suggests the occurrence of carbonate build-ups.

4.4.2.2. Lithologies and general settings

Within the wells, the Pliocene-Pleistocene series is primarily composed of shales, accounting for approximately 90% of the drilled lithologies, with sandstone being the second most abundant lithology (*Figure 4.2*). Some siltstones are also observed in the lower part of the series, closer to the Amazon River mouth (Wells #2 and #3; *Figure 4.2*). Finally, calcarenites constitute around 1% of the recovered sediments.

The thickness of the Plio-Pleistocene series varies based on the distance from the Amazon River mouth. It is thicker in the southern part of the seismic block, reaching 1822 m at Well #3, and 1514 m at Well #2, while it decreases to 1026 m at Well #1 in the northern part of the seismic block. The primary morphology of the Plio-Pleistocene series features slightly tilted reflectors prograding towards the North-East (*Figure 4.4*).

4.4.2.3. Seismic sequences and their organization into mega-sequences

Stratigraphic interpretation of the 3D seismic data allowed the identification of nine seismic sequences (S1 to S9, *Figure 4.4*) defined as a succession of strata deposited during a complete cycle of change in accommodation space or sediment supply and identified by the succession of various system tracts, each corresponding to different stages in the variation of the ratio between accommodation rate and sediment supply (A/S ratio). The TS is used as sequence boundary and is defined by the change from mostly prograding to mostly aggrading condition. The surface is characterized by extensive retrogradational stacking patterns showing numerous onlap terminations. Based on common characteristics, the nine seismic sequences were grouped into three different mega-sequences, referred to as MS-I, MS-II, and MS-III. Extensive descriptions of each seismic sequence are available in supplementary material.

MS-I comprises seismic sequences S1, S2, and S3 which encompass the lower part of the Plio-Pleistocene series, with a thickness of 374 m below 820 m in Well #1 (*Figure 4.4*). Transgressive System Tracts (TSTs) are not clearly identified within S1 to S3, as the onlap terminations that typically define these seismic sequences are not discernible in this mega-sequence. Nevertheless, thick high impedance reflectors cover the top of the underlying regressive pattern. Sometimes, these intervals appear notably thicker toward the continent with apparent onlap. These reflectors were thus identified as TSTs, and the higher impedance contrast may be linked to sand deposits (*Figure 4.2*, Well #1). Highstand System Tracts (HSTs) and Falling Stage System Tracts (FSSTs) within S1 to S3 exhibit reflectors with low steepness. Furthermore, the foresets of the clinoforms within S1 to S3 are well-developed and can extend

over tens of kilometers in length. Erosion within S1 to S3 remains limited (*Figure 4.4*). Notably, the thicknesses of S1 to S3 exhibit a clear decrease over time in Well #1 (*Figure 4.4*) due to important progradation.

MS-II comprises seismic sequences S4 to S7, which measure 366 m in thickness in Well #1 (*Figure 4.4*). These seismic sequences share common features, including increased TST thicknesses compared to MS-I. In MS-II, within S4 to S7, the TSTs are characterized by stacked sub-parallel reflectors with onlapping terminations, displaying a thick aggrading pattern. Internal reflectors within clinoforms show a notable increase in steepness and a reduction in bottomset extension relative to MS-I. The most significant change from MS-I is extensive erosion observed in MS-II (*Figure 4.4*). S4 to S7 are significantly affected by erosion, both on the outer shelf and on the slope. Submarine landslides along the slope have removed substantial sediment volumes, while on the outer shelf, the Transgressive Surface (TS) is marked by erosive unconformities.

MS-III comprises seismic sequences S8 and S9 and measures only 286 m in thickness in Well #1 (*Figure 4.4*). MS-III is distinguished by a shift of sediment accumulation into the slope area, leading to a substantial increase in progradation rates. On the slope, sub-seismic cycles are evident, corresponding to nine smaller-scale Falling Stage System Tracts (FSSTs) (referred to as FR1 to FR9 in *Figure 4.4*). These sub-cycles are only observed within S8 and S9. Consequently, S8 and S9 have been classified under a separate mega-sequence. Their morphologies and distribution notably differ from the seven main FSSTs observed in MS-I and MS-II. The nine FSSTs can be categorized into two groups. The first five regressions (FR1 to FR5) only exhibit progradations with a shift toward the basin (*Figure 4.4*). Conversely, the four younger regressions (FR6 to FR9), situated at the top of the Plio-Pleistocene series, display a distinct high aggradation pattern. Their geometries vary markedly from the south to the north, featuring very steep reflectors along Inline B (*Figure 4.4*) and low-angle reflectors along Inline A (*Figure 4.4*). MS-III is also distinctive for the emergence and development of steep canyons along the slope and the abundance of carbonate build-ups (SF7; *Figure 4.3*).

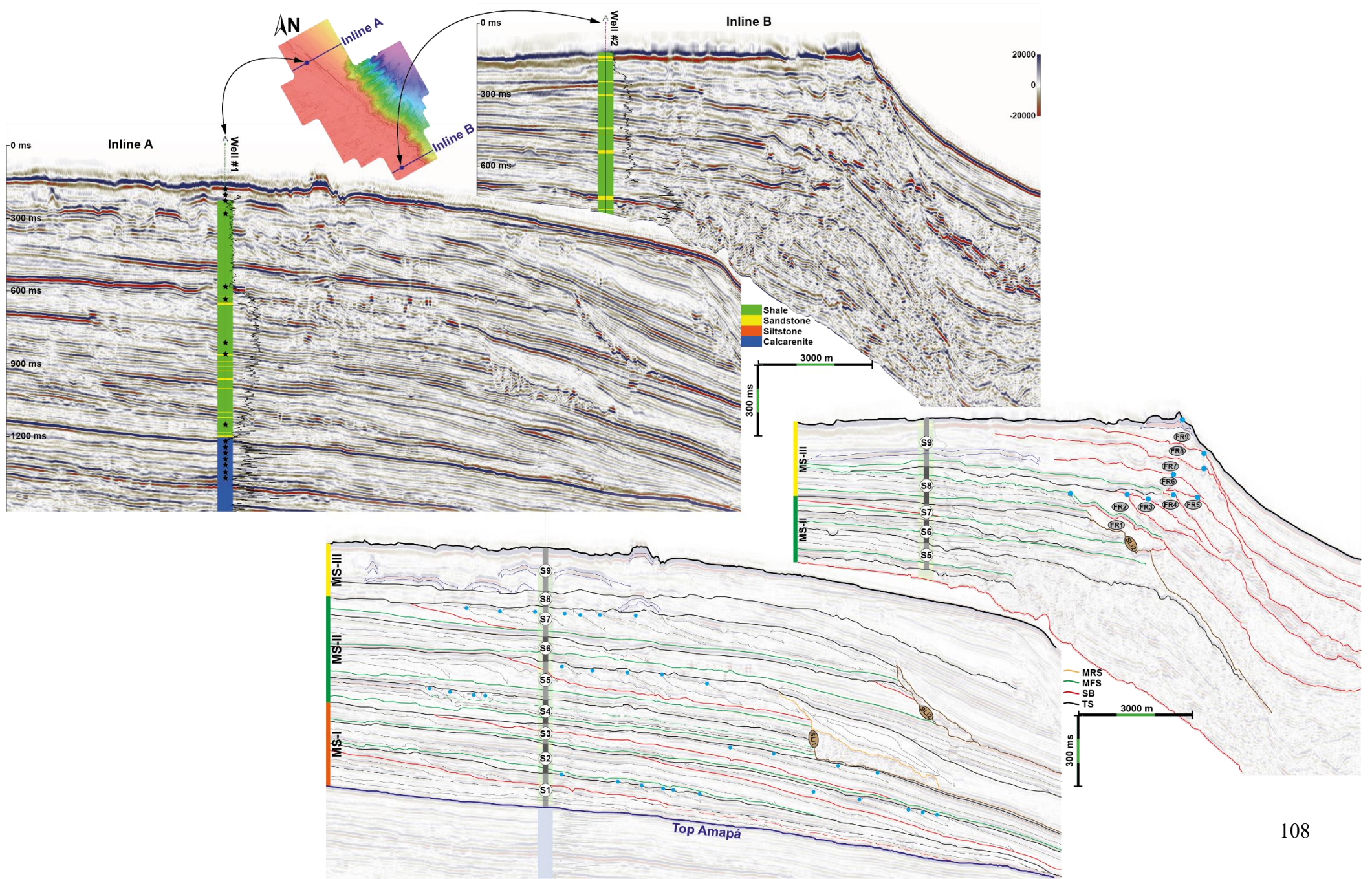


Figure 4.4: Inlines A and B crossing respectively Wells #1 and #2 (See location in Figure 1). Lithology and GR data are shown along the wells. Black stars show the check shots position used for the time-depth relationship. The three intervals in orange, green, and yellow at the left side of the lower profiles, depicts the three interpreted mega-sequences (labelled MS-I to MS-III). In the interpreted profiles, along the wells, grey-shaded intervals noted S1 through S9 depicts the nine identified seismic sequences. Brown lines in the lower profiles (labelled SLi1 and SLi2) emphasize two Submarine Landslides scars and deposits. Light blue dots highlight potential shoreline position during lowest sea level. In the interpreted Inline B, labels FR1 through FR9 depicts the identified regressive prisms (Forced Regression 1 to 9) inside the last two seismic sequences.

4.4.3. Cyclostratigraphy

In this chapter, figures from only Well #1 are shown; figures from the other wells can be found in the supplementary section.

The Multi-Taper Method (MTM) spectral analysis reveals numerous frequencies within the Gamma-Ray (GR) dataset (*Figure 4.5*). Through manual frequency ratio analysis, we identified three sets of frequencies in each well that align with Earth's short eccentricity (97-128 kyr), obliquity (41 kyr), and precession (19-23 kyr). In Well #1, these frequencies correspond to cycles of 35 m and 25 m for short eccentricity, 11 m for obliquity, and 6 m for precession. In Well #2, cycles of 32 m are associated with short eccentricity, 12 m with obliquity, and 6 m with precession (*Figure S4.2*). Lastly, in Well #3, cycles of 46 m correspond to short eccentricity, 21 m to obliquity, and 11 m to precession (*Figure S4.3*). The increase in cycle length from north to south, from Well #1 to Well #3, aligns with an increase in sediment thickness and input closer to the mouth of the Amazon River. Broad bandpass filters have been applied to the potential Earth's short eccentricity and obliquity frequencies for each well (*Figure 4.5*). Although Earth's long eccentricity cycle is not strongly expressed in the dataset, it appears to correspond to wavelengths of 132 m in Well #2 and 172 m in Well #3 (*Figures S4.2 and S4.3*).

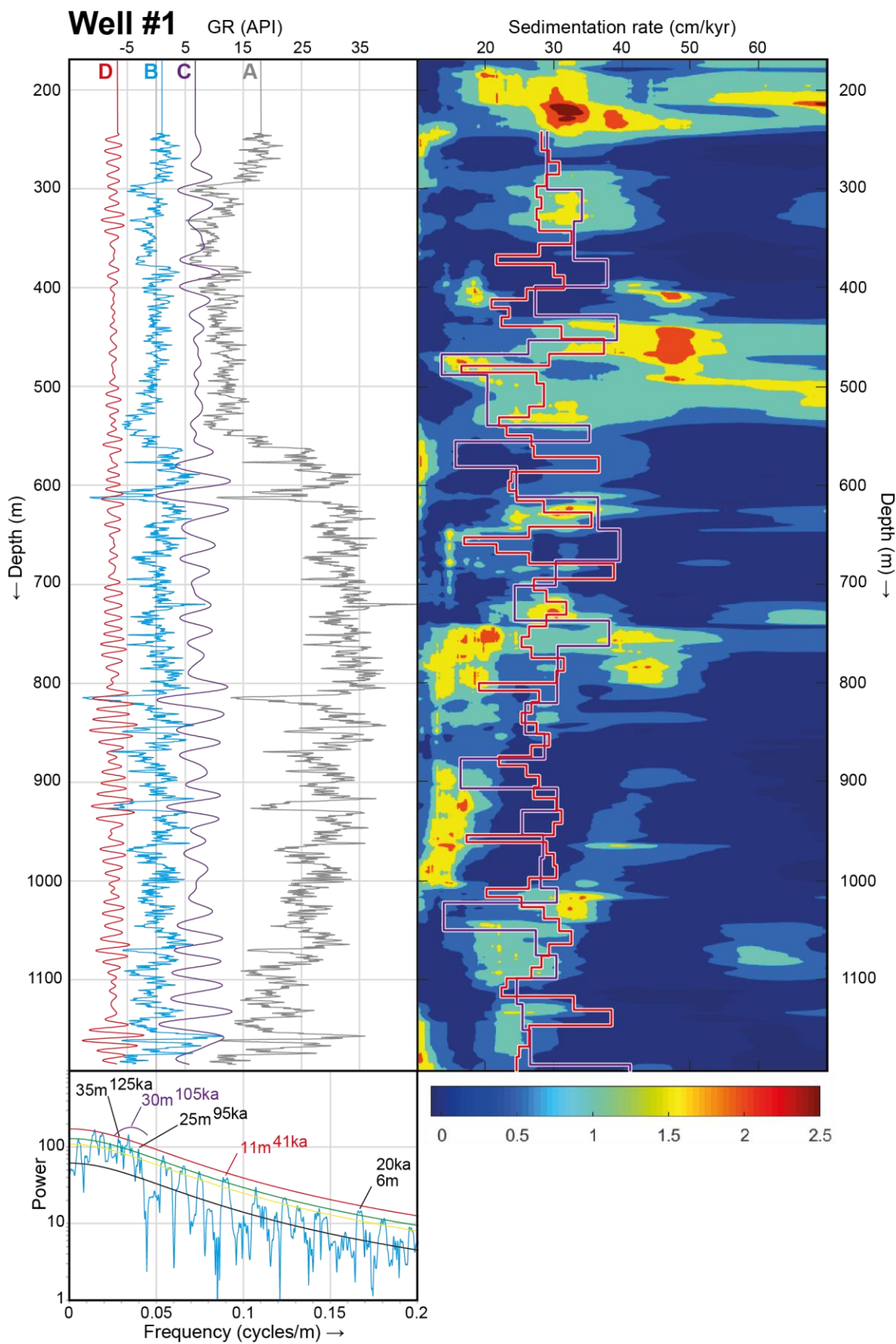


Figure 4.5: Cyclostratigraphic analysis of GR data of Well #1 (depths 168 to 1194 m KB, siliciclastic series). On the left-side panel: (A) Raw GR dataset extended to the seafloor; (B) Detrended GR data;

(C) Filter on the 35 to 25 m (0.024 to 0.046) cycles potentially associated with the Earth's short eccentricity; (D) Filter on the 11 m (0.065 to 0.097) cycles potentially associated with the Earth's obliquity. The graph below presents the MTM analysis of the curve B with the interpreted orbital cyclicities using manual frequency ratio method. Red, green, yellow and black lines represent the 99%, 95%, 90% and median Robust AR(1) confidence levels respectively. The right-side panel present eCOCO results compared to the sedimentation rates obtained after a tuning on short eccentricity (curve C) and obliquity (curve D), respectively in purple and red.

Two independent age models were constructed for Wells #1 and #3 based on the minima of Earth's short eccentricity and obliquity, as illustrated in *Figure 4.6*. These age models are anchored on the closest minima of short eccentricity or obliquity, around 250 kyr for Well #1 and 100 kyr for Well #3 (*Figure S4.4*). These anchoring points are determined using the median sedimentation rate along each well and correspond to the start of the Gamma-Ray (GR) acquisition in time.

In Well #1, the median sedimentation rate is calculated as 1194 m - 168 m divided by either 3.7 Ma or 4.1 Ma, yielding sedimentation rates of either 277 m/Myr or 250 m/Myr. The GR acquisition in this well commences at a depth of 242 m, which is 74 m below the seafloor. Based on the calculated sedimentation rate, this depth corresponds to an age range of 267-296 kyr.

In Well #3, the median sedimentation rate is obtained by dividing (1954 m - 132 m) by either 3.7 Ma or 4.1 Ma, resulting in sedimentation rates of 444-492 m/Myr. The GR acquisition starts at a depth of 180 m, 48 m below the seafloor, and thus corresponds to an age range of 108-97 kyr.

The age models for Well #1 indicate a base for the siliciclastic series at 3688 kyr when tuned on Earth's short eccentricity, and at 3692 kyr when tuned on Earth's obliquity (*Figure 4.6*). Ages of each seismic unit limit are also available in the *Figure 4.6*. These findings are consistent with the global sea-level curve proposed by Miller et al. (2020), in which global sea level lowstands corresponds to seismic sequence boundaries, associated with transgressive surfaces, marking the shift from regressive to transgressive conditions. For Well #3, the age models suggest a base for the siliciclastic series at 3960 kyr and 3981 kyr when based on short eccentricity and obliquity, respectively (*Figure S4.4*). Significant declines in Gamma-Ray (GR) values are likewise correlated with major lowstands in the global sea level curve (Miller et al., 2020). Due to the suboptimal quality of the available 2D seismic lines, the limits of seismic sequences could not be accurately extended to Well #3. Nonetheless, it is postulated that significant drops in the GR dataset of Well #3 are in close alignment with those in Wells #1

and #2. These significant drops have been correlated with seismic sequence boundaries thanks to the time-depth relationship.

Each of the age models allows for the calculation of variations in sedimentation rates along the well bore. These calculated sedimentation rates were compared with rates determined using the eCOCO tool. The sedimentation rates inferred from both the age models and the eCOCO tool exhibit high variability. Along Well #1, sedimentation rates range from less than 15 cm/kyr to up to 40 cm/kyr (*Figure 4.5*). Similar ranges of variability are observed for Wells #2 and #3, with rates varying from 18 to 45 cm/kyr and 25 to 65 cm/kyr, respectively (*Figures S4.2 and S4.3*). This high variability in sedimentation rates accounts for the multiple frequency peaks observed in the Multi-Taper Method (MTM) spectral analysis (*Figure 4.5*). The MTM analysis also reveal a stronger short eccentricity component compared to the obliquity power (*Figure 4.6 and Figure S4.4*).

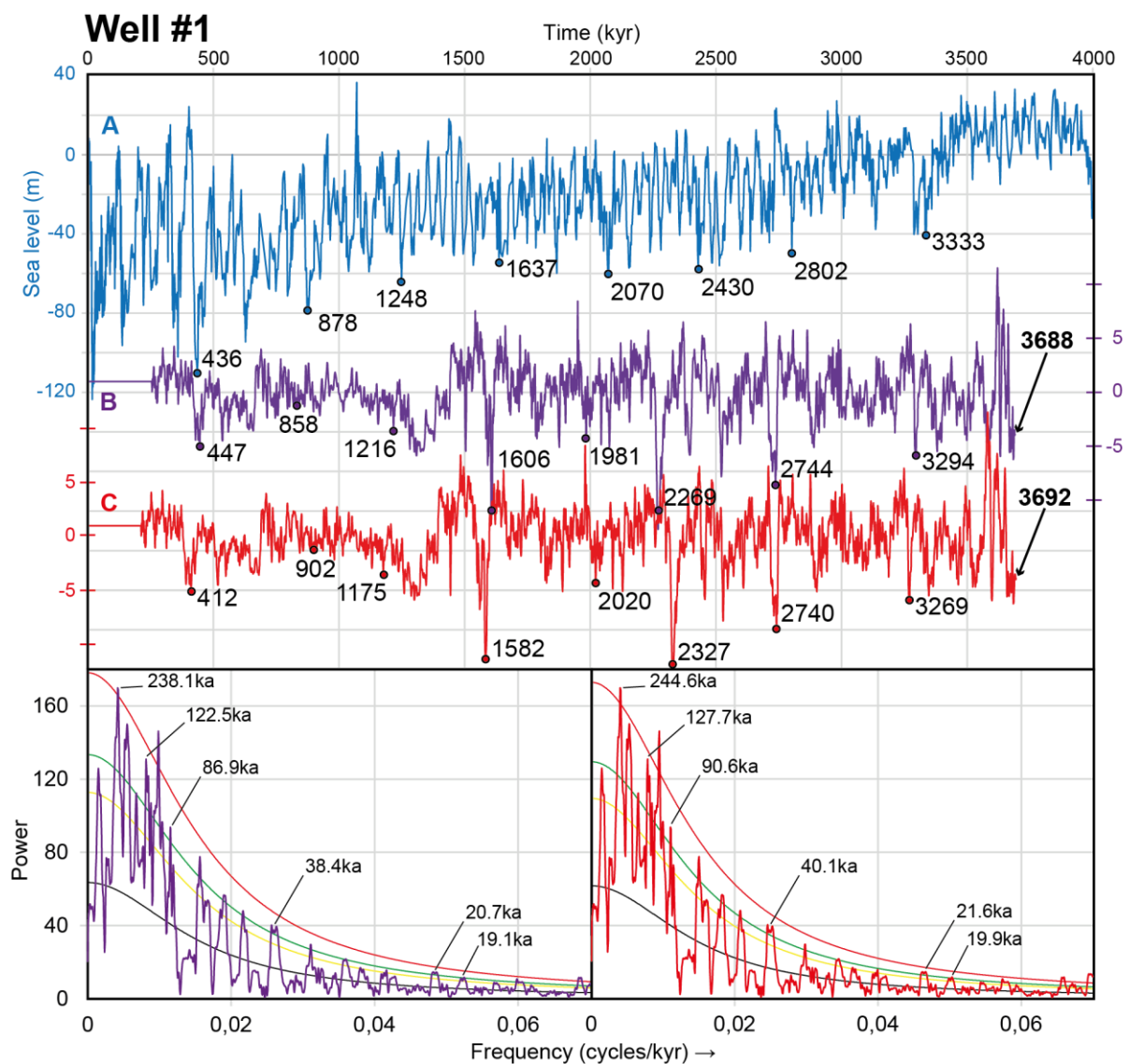


Figure 4.6: Cyclostratigraphic results of GR data of Well #1 (depths 168 to 1194 m KB, siliciclastic series). The upper panel shows; (A) global sea level variation from Miller et al. (2020); (B) the GR data of Well #1 in time after a tuning between the Earth's short eccentricity minima and the minima of the filter on the 35 to 25 m frequencies; (C) the GR data of Well #1 in time after a tuning between the Earth's obliquity minima and the minima of the filter on the 11 m frequency. Ages noted along the curves corresponds to seismic sequence boundaries and the potential eustatic lowstand associated. The lower panels present the Multi-Taper-Method of curves B and C (see corresponding colours), with the main astronomical cyclicities. Red, green, yellow and black lines represent the 99%, 95%, 90% and median Robust AR (1) confidence levels respectively.

4.4.4. Comparison between seismic observations and cyclostratigraphy

As a first approximation, we can assume that each seismic sequence has developed over the same amount of time and corresponds to the same cyclicity response. Thus, we divide the duration of the siliciclastic series in the study area (given by biostratigraphy: 3.7-4.1 Ma) by the number of seismic sequences observed. We obtain a duration of 411-456 ka for each of the seismic sequences (9 sequences/3.7-4.1 Ma; *Figure 4.4*). This approximation is also consistent with the observation of 4 to 5 short eccentricity cycles (97 to 128 kyr) obtained in the cyclostratigraphy study within each major seismic sequence (*Figure 4.5*) and the presence of long eccentricity cycle (405 kyr) in Wells #2 and #3 (*Figures S4.2 and S4.3*). Therefore, we conclude that long eccentricity (405 kyr) is the main orbital parameter influencing the sediment architecture on the Amazon continental margin as observed on our seismic data.

Within seismic sequences S8 and S9, nine smaller scale sequences are observed (FR1 to FR9 in *Figure 4.4*). The seismic sequences (S1 to S9) being associated with long eccentricity cycles (405 kyr), the time interval during which the S8 and S9 form is estimated at ~810 kyr. This gives us a duration for each of the nine higher resolution sequence deposition of (810 kyr divided by 9) ~90 kyr. We can also use the age obtained through cyclostratigraphy for the base of Sequence S8 inside the Well #1: 858-902 ka (*Figure 4.5*) and inside the Well #3: 901-1005 ka (*Figure S4.4*) to calculate the cyclicity of these smaller scale sequences. We obtain two ages of: (Well #1: 858 or 902/9) ~95.3 or 100 kyr and (Well #3: 901 or 1005/9) ~100 or 112 kyr. This cyclicity is also clearly visible along the Well #3. Indeed, nine cycles identified as short eccentricity (97-128 kyr) influence the GR data, the amplitude of the GR signal along these cycles is more important compared to the rest of the signal (*Figure S4.4*).

4.5. Discussion

4.5.1. Cyclicity record in well and seismic data

Our results highlight the impact of Milankovitch cycles on the nature and architecture of sediments in the offshore Amazon Basin. The results of our cyclostratigraphic analysis isolate three major peaks related to eccentricity (97-128 kyr), obliquity (41 kyr) and precession (19-23 kyr). Furthermore, seismic sequences are correlated to the leading 405 kyr eccentricity term (*Figure 4.6*).

Previous studies of the sedimentary architecture of continental margins using seismic and well data have proposed a correlation between depositional sequences and the 405 kyr orbital eccentricity cycles (e.g., (Chima et al., 2020; Gorini et al., 2014). On the Amazon margin, Gorini et al. (2014) proposed that the 405 kyr cycle drove the deposition of clastic sequences overlying the Amapá carbonate platform from 2.4 Ma on the area. The improved astronomical age model proposed in our study indicate that the outbuilding of the shelf due to deposition of Amazon-derived clastics began earlier, at 3.7 Ma (*Figure 4.7*).

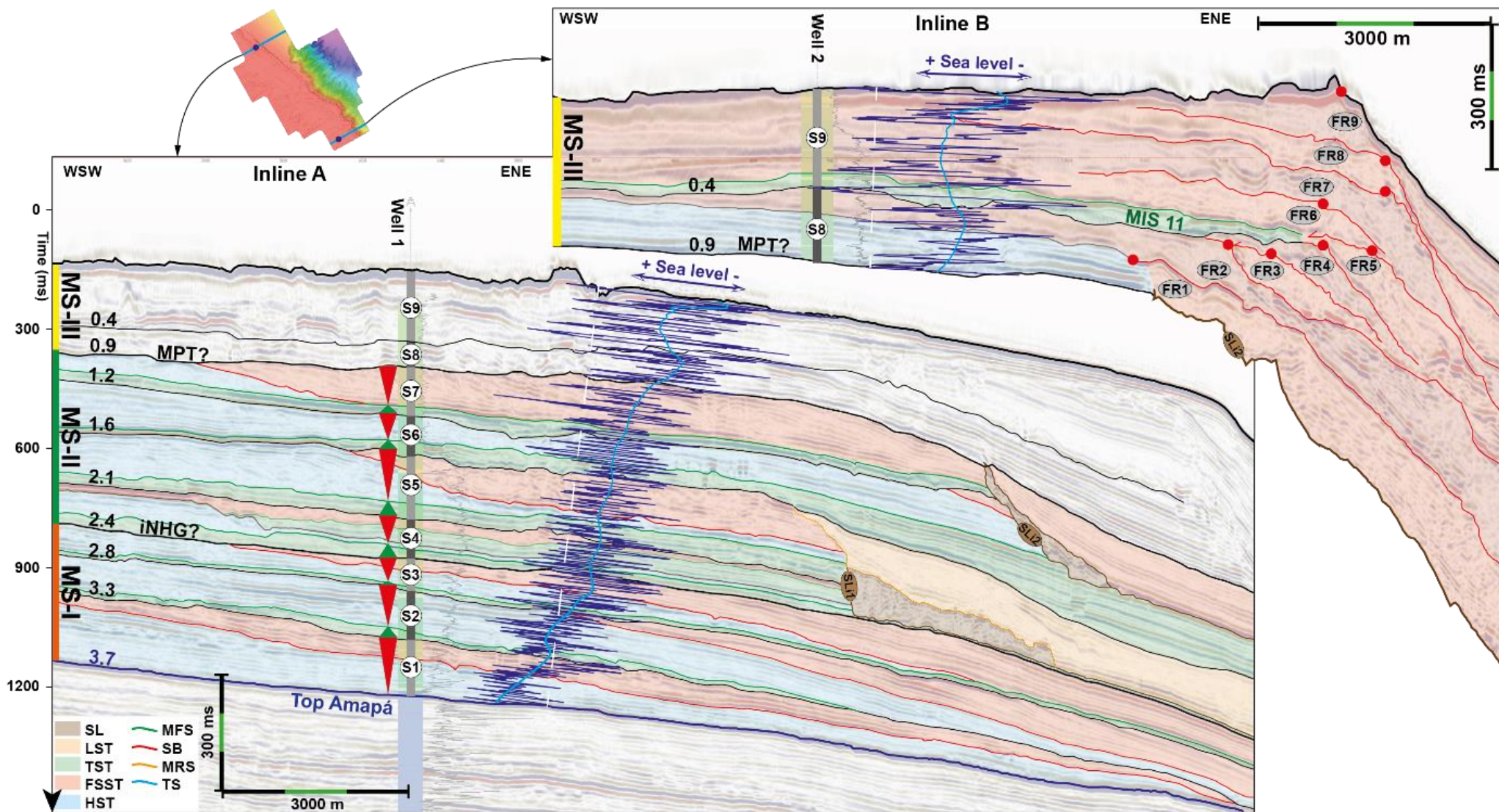


Figure 4.7: Sequence stratigraphy interpretation of the inlines A and B (see their location in Figure 1). The sea level curve of Miller et al. (2020) (raw data in dark blue and smoothed data in light blue) is shown on the right side of wells #1 and #2. The dashed white line represents the present-day sea level. The red and green triangles along Well #1 depicts the relative sea level variation interpreted through seismic observation. Red triangles represent regressions while the green ones transgressions. Estimated ages of seismic sequence (S1 to S9) boundaries (corresponding to the Transgressive Surface) are labelled on the left side of the inlines.

In the two youngest seismic sequences (S8 and S9, *Figure 4.7*), a cyclicity of 100 kyr is proposed and explains the presence of 9 Falling Stage System Tracts or forced regression (FR1 to FR9; *Figure 4.7*). These forced regressions in the late Quaternary are well known features in many places in the world (e.g. Lobo and Ridente, 2014; Rabineau et al., 2006, 2005; Ridente et al., 2009 in Mediterranean case studies or Anderson and Fillon, 2004 in Gulf of Mexico). In Well #3, this cyclicity is apparent in the GR records, and its greater preservation could be explained by the position of the well closer to the main depocenter of the Amazon deep-sea fan (*Figure 4.1*). Indeed, the flexural deformation of the lithosphere associated to the deep-sea fan loading can be recognized by changes in the rate of subsidence in the adjacent areas and an increased accommodation space favourable to the aggradation and preservation of shelf-edge deltas (Cruz, 2018; Neal W. Driscoll and Karner, 1994; Rodger et al., 2006; Silva et al., 1999).

Our study also indicates that lithological variation along the offshore Amazon Basin is mainly influenced by short eccentricity (97-128 kyr) as depicted by the MTM analysis (*Figure 4.6*). This contrasts with the widely accepted idea that obliquity is the main parameter influencing the Earth's climate prior to the Mid-Pleistocene Transition (0.7-1.2 Ma) (Raymo et al., 1997). This difference could be explained by the location of the study area close to the equator, a latitude more sensitive to precession-eccentricity forcing (Berger and Loutre, 1994). So, astronomically driven climate is the dominant parameter influencing the sedimentation pattern in the study area, whereas the flexural subsidence likely remains the main factor preserving the higher frequency climatic variations recorded in the deltaic sequences of the Amazon margin (Cruz, 2018; *Figure 4.7*).

4.5.2. The starts of siliciclastic deposition

Mega-sequence MS-I is bounded at its base by the transition from Amapá carbonate sediment to clastic sediments from the Amazon River, we date this transition to 3.7 Ma based on cyclostratigraphy along Well #1 (*Figures 4.6*). Further south in Well #3, the basal age of the

Plio-Pleistocene series shows an earlier age of 4 Ma (*Figure S4.4*). These diachronous ages are consistent with the work of Cruz et al. (2019), who showed that the age of carbonates demise decreased northward across the offshore Amazon Basin, with a longer carbonate growth towards the north (and therefore a younger age of cessation). This result is also consistent with the observation of NE migration clinoforms by Gorini et al. (2014), which cover the Amapá carbonate platform. This is consistent with our results revealing a 10m layer of sandy sediments covering the last occurrence of Amapá carbonates (*Figure 4.2*). This sandy unit is covered by a Highstand System Tract (HST), consisting of muddy bottomsets of delta-scale subaqueous clinoforms downlapping the previous surface (*Figure 4.7*).

4.5.3. Mega-sequences correlation to climate and sea-level changes

Here, we suggest to correlate changes observed in seismic geometries and dated by cyclostratigraphy, with trends of now well recognised global sea level curves (Miller et al., 2020).

Within MS-I, the first identified Falling Stage System Tract (FSST) inside the seismic sequence S1 is probably associated with a climatic change between 3.5 to 3.3 Ma and a global sea level fall (Mammoth 2 event or MIS M2; (De Schepper et al., 2013). During the Sequence 1 (S1) deposition, the main sea level fall, is fast with high amplitude (60 m in 100 kyr; Miller et al., 2020). During this time span, FSST observations reveal clear migration of the coastline towards the basin with a large (marine) erosional surface at its base. Seismic Sequence 2 (S2) corresponds to a period of relatively high sea level defined by the development of a HST that last from 3.3 to 3.0 Ma based on the cyclostratigraphic age model. This time interval matches with the timing of the Mid-Pliocene warm period, ranging from 3.264 to 3.025 Ma (Dowsett and Caballero Gill, 2010; Haywood et al., 2009). This interval is recorded as a thick aggrading and prograding Highstand System Tract (HST) inside S2 (*Figure 4.7*). This warm period is followed by a cooling event and a long period of sea level fall (from 3.0 to 2.8 Ma; Miller et al., 2020) with shorter amplitude compared to S1 (50 m in 200 kyr: speed of 25 m/100 kyr, Miller et al., 2020) and could explain the difference of geometries recorded in the sequence with a basinward shift of the S2 FSST (and less erosion at its base and top). The third FSST inside S3 corresponds to a global sea level fall standing from 2.75 Ma to 2.51 Ma with an amplitude of almost 80 m (Miller et al., 2020). Even if it represents the biggest sea level fall in terms of height, it is also the longest in duration (320 kyr), thus implying a very low rate of sea level fall. This explains the well-developed FSST, with a larger volume of sediments than in the previous two FSST.

MS-II is delimited at its base by a drastic change in the shape of FSSTs, and the preservation of thicker TST. In addition, well developed erosional truncations as well as giant submarine landslides scars have been recorded. The transition from MS-I to MS-II is dated at 2.4 Ma according to cyclostratigraphy which could be related to the intensification of Northern Hemisphere Glaciation (iNHG) occurring between 3.0 to 2.5 Ma (Bartoli et al., 2005; Kleiven et al., 2002; M. A. Maslin et al., 1998; Wohlfarth et al., 2008). The thicknesses and volumes of the FSST and TST are greater during MS-II than MS-I which might be correlated to higher sedimentation rates. The increased sedimentation rates may be due to enhanced erosion since the iNHG, due to enhanced Andean glaciation and variation in precipitation on the Amazon drainage basin during colder glacial stages (Harris and Mix, 1999; Mason et al., 2019). This change is also observed in pollen data (at 2.6 Ma) (transition between zone C to D described by Hoorn et al., 2017) which reflects an increase in the sedimentation rates and the development of open vegetation in the high Andes from 2.6 to 0.8 Ma. During MS-II (2.4 to 0.9 Ma), Transgressive System Tracts (TST) are more developed and we correlated the first two with sea level rise events from 2.5 to 2.2 Ma (MIS 95-91, Lisiecki and Raymo, 2005) and from 1.64 to 1.44 Ma (MIS 57-47, Lisiecki and Raymo, 2005). The last Transgressive System Tract observed in S7 is probably associated with MIS 31 (1.07 Ma, Lisiecki and Raymo, 2005). These sea level rise events are considered as super interglacials stages by Melles et al., (2012). Other studies prove the impact of these super interglacials on geological records with increased carbonate productivity (Droxler and Jorry, 2021, 2013).

Two main Submarine Landslide (SLi) scars are also observed in the MS-II interval of the Plio-Pleistocene series. The triggering mechanisms of megaslides on passive continental margins can be multifaceted and may include various pre-conditioning factors (Garziglia et al., 2008; Urlaub et al., 2013; Vanneste et al., 2013). In the study area, submarine landslides seem to have been instigated by significant sea level falls. Indeed, the scars affect the Falling Stage System Tract and are also covered by the Lowstand System Tract, indicating that the landslides occurred during a relative sea level fall and before reaching the relative minimum sea level. SLi1 is dated, thanks to the age model, between 2.1 to 1.6 Ma, while SLi2 is dated between 1.2 to 0.9 Ma. The age of SLi1 coincides with horizon H, as noted by Reis et al. (2016). Horizon H (1.8 Ma) has been used to date AM2-AM6 mass transport deposits, all of which occurred during the mid to late Pleistocene along the slope of the Amazon deep-sea fan (Reis et al., 2016).

During MS-III (0.9 to present-day), the shape of the FSST changes drastically as well as their location along the passive margin (*Figure 4.7*). This could be explained by the variation of the dominant orbital parameter on the climate. Indeed, after the MPT, the Earth is dominated

by 97-128 kyr cyclicity and sea level variation has increased drastically (Berger and Loutre, 1994; Chalk et al., 2017; Clark et al., 2006; Pias and Moore, 1981; Willeit et al., 2019). This leads to shorter seismic sequences associated with short eccentricity cycles, in contrast to the 405 kyr cycles observed previously. The successive decline in sea level related to glacial stages led to high variation of the coastline position which results in regressive prisms along the slope (forced regression). Indeed, the available space for sediments is considerably reduced on the outer shelf during strong sea level falls and the sediments migrate towards the slope. During the S8 seismic sequence, the FSSTs mainly prograde and the aggradation remains very low (*Figure 4.7*). However, during seismic sequence S9, aggradation overcomes progradation. This correlates with the Mid-Brunhes transition, which shows over the last 405 kyr, interglacial stages with warmer temperatures (Jouzel et al., 2007a) and higher concentrations of atmospheric CO₂ (Lüthi et al., 2008) and an overall increase in the mean sea level (Barth et al., 2018; Mitsui and Boers, 2022). This association between FSST and the short eccentricity (97-128 kyr) after the Mid-Pleistocene Transition has also been observed in other deltas (Lafosse et al., 2018; Rabineau et al., 2006). These FSSTs are also accompanied by an increase in erosive patterns. Indeed, during low sea levels, the shoreline reaches the outer shelf and most of the shelf is then exposed to aerial erosion. During transgression, patch reef extensively grew around the outer shelf on top of the shelf edge deltas (forced regressions). During the transition between S8 to S9 sequences, we observed an increase in carbonate production, we associate this with the MIS 11 event at 0.45 Ma (Droxler and Jorry, 2021).

4.5.4. Subsidence: a vital factor for preservation

The observation of 97-128 kyr short eccentricity cycles as well as the record of obliquity and precession parameters in our dataset reveals the good preservation of the sedimentary deposits on the north-western Brazilian Equatorial margin. Indeed, most stratigraphic sequences seem to be preserved with limited seismic evidence of erosion. Such high preservation is only possible through subsidence. Two types of subsidence affect the Brazilian equatorial margin (Bott, 1992): thermal subsidence due to post-rift (<100 Ma) cooling; and sediment loading by the Amazon fan since 8 Ma, which can be 10 times higher.

We can calculate this total subsidence rate around Well#1 with simple approximations. If we consider that the top of Amapa formation is at 0m water-depth, as well as the top of S9 at MIS2 (20 ka). We measure a thickness of sediment deposition of 1090 ms TWTT, which corresponds to about 1090 m, considering an average velocity within the sediments of 2000m/s. Therefore, we obtain an average total subsidence rate of: 1090m deposited in (3.7 – 0.02) =

~300 m/Myr. This value is rather high, but has been observed on other margins in the world (e.g. in the Mediterranean Sea: Rabineau et al., 2014) and is, in fact, a pre-conditioning factor for the record of Pliocene and Quaternary high resolution sequences on the shelf. The same calculation on Well#3 leads to an average subsidence rate of: $1822\text{m}/4\text{ Ma} = \sim 450\text{m/Myr}$. Note that Well #2, which is in between, well #1 and well#3 shows an intermediate subsidence rate of $\sim 375\text{m/Myr}$. Therefore, the variations between the northern and southern geometries can be explained by differential subsidence rate. The southern part of the seismic block being closer to the Amazon deep sea fan, is more impacted by sediment loading. The relative sea level rise (or increase in water depth) is faster in the southern part due to the additional subsidence and absolute sea level rise. As a result, the transgressive system tract reaches the inner shelf faster and less sediment associated with transgression is deposited on the outer shelf. This might explain the difference in thickness of the transgressive system tract, greater in the north end tip of our seismic block, compared to the south. Seismic sequences S8 and S9 reveal an opposite pattern with steeper reflectors at the southern edge of the seismic block. However, this is due to the presence at the base of the S8 sequence of a submarine landslide, which changes the shape of the slope. At the southern edge of the seismic block, the landslide washed away an important volume of sediment along the slope. The steepness of the slope increases due to this event, forcing sediments to settle in higher water depths on the upper slope. While at the northern part, the submarine landslide removed a smaller volume of sediments creating a less steep slope, the sediments infilling this area show more continuous reflectors with smaller dips.

4.6. Conclusions

This study provides new information on the possible effects of climate variations on the architecture of Plio-Quaternary sedimentary deposits along the Brazilian Equatorial Margin influenced by terrigenous inputs. A 3D seismic sequence stratigraphic study reveals the margin to include 3 mega-sequences and 9 seismic sequences, deposited during the last 3.7-4.1 Ma based on biostratigraphic data from wells. A cyclostratigraphic analysis of gamma ray data in 3 wells yields an age model in which the seismic sequences correspond to the 405 kyr eccentricity cycle. The first mega-sequence (MS-I) is dated between 4.0 to 2.4 Ma and its characteristics are interpreted to record sea level variations of low amplitude ($\sim 40\text{ m}$) preceding the intensification of Northern Hemisphere Glaciation. The second mega-sequence (MS-II) is dated to 2.4-0.9 Ma and is characterized by the development of major erosive surfaces and an increase in the slope of clinoform forests. This change in the overall geometry of the shelf is potentially due to an increase in the amplitude of sea level variations coupled with an

intensification of the erosion rate within the Amazon basin. The third mega-sequence (MS-III) is dated to 0.9-0 Ma and is characterised by nine lowstand prisms, of which the oldest five are prograding, while the youngest four become aggrading. The age model allowed us to ascribe these prisms to a cyclicity of 100 kyr matching the short eccentricity (97-128 kyr). The abundance of lowstand packages is related to a change in the orbital forcing regime at the Mid-Pleistocene Transition. Moreover, ~405 kyr ago during MIS 12-11 transition, the average temperature of the Earth increased, raising the average sea level and allowing the lowstand prisms observed in the seismic record to become aggrading. Correlation with the absolute sea level curve indicates that the 9 prisms within MS-III correspond to glacial-interglacial cycles and correlate with MIS 6, 8, 10, 12, 14, 16, 18, 20 and 22. In summary, the sedimentary architecture of the North-western Brazilian Equatorial Margin records significant changes in its overall geometry at 2.4 Ma, 0.9 Ma and 0.4 Ma due to the intensification of Northern Hemisphere Glaciation, the Mid Pleistocene Transition and the Mid-Brunhes Transition, respectively. The nice record and preservation of these climate-related sequences is due to a significant total subsidence rate in the area of ~300m/Ma on the outer shelf. We related this important subsidence rate to the loading effect of the Amazon deep-sea fan.

Declaration of interests

The authors declare that they have no known competing financial interests or personal relationships that could have appeared to influence the work reported in this paper.

Acknowledgments

This work was supported by the “Region Bretagne” as well as ISblue project: Interdisciplinary graduate School for the blue planet (ANR-17-EURE-0015) and co-funded by a grant from the French government under the program "Investissements d'Avenir" embedded in France 2030. This project was supported by the Region Bretagne and UMR6538 Geo-Ocean joint Unit (CNRS, Univ Brest, Ifremer, Univ. Bretagne Sud). Lucas Tortarolo is a PhD student at “Université de Bretagne Occidentale (UBO, Univ Brest)” and Sorbonne University (SU) in France, and is in joint supervision with “Universidade Federal Fluminense (UFF)” in Brazil. This project is also a collaboration with the “Faculdade de Oceanografia” (UERJ) located in Brazil. Antonio Tadeu dos Reis also thanks “CNPq” and “FAPERJ” for the research grants

(process #309779/2021-9 and process #200.427/2023, respectively). Cleverson Guizan Silva acknowledges “CNPq” for the research grant 311589/2022-7. Slah Boulila was supported by the French Agence Nationale de la Recherche (ANR-19-CE31-0002 AstroMeso), and the European Research Council (ERC) under the European Union’s Horizon 2020 Research and Innovation Program (Advanced Grant AstroGeo-885250).

This work employed Artificial Intelligence to correct and enhance the writing. The following prompt was utilized for this purpose: "Proofread my writing. Fix grammar and spelling mistakes. And make suggestions that will improve the clarity of my writing".

4.7. Supplementary contents

4.7.1. Data and methods:

The cyclostratigraphic method is based on gamma ray (GR) well-log data. GR variations in geological formations are connected to the concentrations of radioactive atomic nuclei, mostly uranium, thorium and potassium, which in general are higher in shale and clay intervals than sandy sediments, and very low in limestones. Therefore, GR logs are a good proxy for lithological variations in a siliciclastic and mixed siliciclastic-carbonate sedimentary environments. In shelf settings, sediment sorting is mostly related to variations in ocean energy, which to a first approximation decrease seaward. Thus, GR well log data can provide a reliable proxy of distance from the shore during sea-level variations (Merkel, 1979). GR well log data has already been used as an indirect paleoclimatic proxy to characterize orbitally-driven sea level variation (e.g. Ruffell and Worden, 1999; Weedon et al., 2004; Wu et al., 2013).

To correlate well logs to seismic data in the time domain, downhole check-shots were used and an additional statistical wavelet was created on Paleoscan Software. A more accurate deterministic wavelet could not be generated due to the lack of geophysical well log data from the Plio-Pleistocene succession. The time-depth relationship therefore has an uncertainty estimated at 30 m, except for certain lithological transitions, e.g., from Amapá carbonates to overlying siliciclastics, which are well defined in both the well and seismic data.

4.7.2. Sequence and seismic stratigraphic methods

Catuneanu et al. (2011) redefined a sequence as "a succession of strata deposited during a full cycle of changes in accommodation or sediment supply." In this study, we adopted this definition, using the terms "sequence" or "seismic sequence."

Below, additional information regarding system tracts and their boundaries is presented:

The Transgressive Surface (TS) corresponds to the transition from a coastline shifting toward the basin to a coastline migrating toward the continent. The Maximum Flooding Surface (MFS) represents the top boundary of the Transgressive System Tract (TST) and is characterized by a shift in the migration of the coastline from the coast towards the basin, opposite to the TS.

The Highstand System Tract (HST) is initiated by normal regression when sea-level rise decelerates, and sediment starts to prograde due to a decrease in the A/S ratio. Although the global sea level is still rising, the coastline migrates basinwards due to the dominant role of

sediment influx. The upper limit of the HST is defined by the Sequence Boundary (SB). The SB consists of a subaerial erosive surface that develops as sea level falls and the coastline starts to migrate towards the basin, although the foresets of the HST can still remain under submarine conditions.

The Falling Stage System Tract (FSST) wedge shows only a series of downward progradations due to the dominant role of eustatic sea-level fall.

The Lowstand System Tract (LST) continues to develop even after eustatic sea level starts to rise. As long as sediment supplies remain greater than accommodation, the shoreline continues to migrate basinwards. When accommodation overcomes the rate of sediment supply, the shoreline starts to move towards the coastline, which marks the Transgressive Surface.

To distinguish each package, four important factors were considered during seismic facies interpretation (*Figure 4.3*):

- Morphology of the horizons (erosion, steepness, extent, position)
- Stratal terminations (Onlap, Offlap, Toplap, and Downlap)
- The offlap break position (topset edge), when preserved
- Stacking patterns of successive sedimentary units

To obtain horizons instead of time slices, a geo-model was built in the specialized 3D seismic interpretation software, PALEOSCAN (<https://www.eliis-geo.com>), with an automatic tracking of reflections, conversion to horizons, and stratigraphic organization. A manual interpretation of the main horizons was conducted to check, refine, and update the geo-model. In this case study, throughout the Plio-Pleistocene series, 300 seismic horizons were generated and correlated between wells inside the seismic block. Furthermore, the identification and extent of the main limits of our seismic sequences across the entire study area were based on those multiple horizons.

4.7.3. Identification and definition of seismic sequences

Nine seismic sequences were identified through seismic interpretation (S1 to S9, *Figure 4.4*). Each seismic sequence was interpreted as a full cycle of depositional system tracts by analysing their respective seismic architecture (*Figure 4.4*). In addition, when the identification of depositional systems tract could also be achieved all together by analyses of wireline log motifs and cyclostratigraphy (*Figures 4.5 and 4.6*), we can define with more confidence a sequential stratigraphy for the Pliocene-Pleistocene Amazon shelf. For instance, we can observe an

excellent correlation between Transgressive Surface (TS), drops in GR values and lithological transitions from shale to sandstone. It should be noted that TST are not well developed along the area and LST are absent on the shelf. During lowstands, much of the sediments of the Amazon are probably directly funnelled to the deep-sea fan, therefore, bypassing the outer shelf and are not transported by the longshore current to our study area. This implies that the Sequence Boundary (SB), the Transgressive Surface (TS), and the Maximum Flooding Surface (MFS) are either a common horizon or a small seismic interval in some part of the seismic block.

Sequence S1 displays a thickness of 140 ms TWTT in Well #1 (*Figure 4.4*). Deposition of S1 starts on top of a high amplitude reflector associated with carbonate lithology. This reflector marks the transition from the Amapá Fm to the Plio-Pleistocene siliciclastic series. On top of this reflector, the first sediments part of the sequence S1 begins to downlap the area, lithological log reveals that these siliciclastic sediments are sandstone (*Figure 4.2*). Above these sands, the lower part of S1 seismic sequence shows very low amplitude and poorly continuous reflectors with downlapping character, able to build outward and upward into the available space, with very low slope angles. This seismic facies; SF2 (*Figure 4.3*), is associated with fine-grained sediments on the logs and is interpreted as prodeltaic units of a HST. Two or three reflectors at the end of the HST present toplapping terminations with only progradational behaviour (SF3; *Figure 4.3*); it seems to be part of a distal FSST with a very small thickness (30 ms TWTT at its thickest part). Above this depositional system tract, the S1 sequence presents moderate to high amplitude reflectors with a rapid increase of steepness and a better continuity of the reflectors. Its base is erosive (red line inside the S1 on *Figure 4.4*). This unit is interpreted as a SF3 (*Figure 4.3*) and thus corresponds to a FSST with a rapid shift of the sedimentation towards the basin. However, this FSST begins at a proximal position compared to the two or three reflectors below showing similar seismic facies. It is possible to separate, therefore, this Sequence S1 in two different seismic sequences, yet we interpret the small interval as a sub-sequence related to a smaller scale cyclicity.

Sequence S2 displays a thickness of 120 ms TWTT in Well #1 (*Figure 4.4*). S2 consists mainly of a thick aggradational sedimentary interval, which downlap the top of the S1 FSST. Low to medium amplitude reflectors are observed in Sequence S2, and are interpreted as a SF2 (*Figure 4.3*), which corresponds to a HST composed of shales (*Figure 4.2*). On top of this HST, clinofolds associated with SF3 (*Figure 4.3*) with only progradational behaviour reveal the presence of a FSST (*Figure 4.4*). Compared to the FSST of sequence S1, this FSST begins at a distal position and the offlap break position (blue circle in *Figure 4.4*) is closer to the slope.

Sequence S3 displays a thickness of 100 ms TWTT in Well #1 (*Figure 4.4*). Contrary to the previous sequence, a high amplitude reflector covers the previous S2 FSST. This reflector is associated with SF1 (*Figure 4.3*) and represents a small transgressive interval. Prograding and aggrading reflectors associated with HST (SF2; *Figure 4.3*), overlay the transgressive interval. Clinoforms with only progradational behaviour begins to cover the HST (SF3; *Figure 4.3*). Compared to the same transition inside sequence S2, the transition from HST to FSST occurs at a proximal point, the offlap break position shows the same proximal migration (*Figure 4.4*). Foresets of the FSST present elongated shapes that extend towards the shelf and reach the slope (*Figure 4.4*).

Sequence S4 displays a thickness of 100 ms TWTT in Well #1 (*Figure 4.4*). At first sight, S4 is mostly composed of stacked sub-parallel reflectors (SF1; *Figure 4.3*) reaching a thickness of 75 ms TWTT in Well #1 (*Figure 4.4*). On top of this TST, an interval presents progradational clinoforms (SF4; *Figure 4.3*) and is associated with a small FSST (30 ms TWTT thick at its thickest part along the Inline 1, FSST inside S1, S2 and S3 reach thickness of 50 to 100 ms TWTT). However, at a finer scale, S4 is composed at its base by three stacked reflectors of high amplitude, which covers the FSST inside sequence S3. This set of sub-parallel reflectors correspond to a thick transgressive interval (SF1; *Figure 4.3*). Above, on the proximal part of the inline 1 (*Figure 4.4*), packages of aggrading and oblique reflectors compose a small HST (SF2; *Figure 4.3*). However, the HST is highly eroded (see orange line corresponding to a Transgressive Surface, inside S4 in the *Figure 4.4*), the erosive boundary cut through almost the entirety of the HST leaving a gap of 70 ms TWTT of sediments on the most distal part of the outer shelf. The Transgressive Surface (TS), which corresponds to the erosional unconformity, reveals two different reflector amplitude domains. Indeed, the proximal part displays a flat reflector of high amplitude, while the distal part exhibits a highly eroded unconformity with low amplitude reflection. The gap created by this erosion is filled by reflectors of low to medium amplitude with onlap termination toward the coast with sub-parallel and continuous nature (SF1; *Figure 4.3*). S4 could be separated, therefore, in two different seismic sequences but we decided due to its size to interpret the small HST package in the proximal part of the seismic block as a sub-sequence associated with a smaller scale cyclicity.

Sequence S5 displays thickness of 170 ms TWTT in Well #1 (*Figure 4.4*). S5 starts with three reflectors corresponding to a SF1 (*Figure 4.3*) and are characteristics of a TST. The following reflectors show low amplitude associated with intense progradation and low aggradation (SF2; *Figure 4.3*). The angle of foresets is particularly high (compared to the same feature in the older sequences) while the bottomsets extension is limited (*Figure 4.4*). It is

difficult to identify the point at which aggradation ceases, and the system tract gradually evolve from a HST to a FSST. Finally, FSST progrades through high angle clinofolds along the outer shelf (SF3'; *Figure 4.3*). The thickness of the FSST is more constant along the outer shelf in this sequence compared to the FSST inside S1, S2 and S3. Closer to the slope, a scar from a submarine landslide affects the foresets of FSST clinofolds but is also buried under the foresets of newly generated clinofolds part of the same FSST inside S5. On the slope, chaotic reflectors (SF5, see *Figure 4.3*) are visible and correspond to displaced sediments remaining at the foot of the landslide scar. These chaotic reflectors are covered by clinofolds of very low amplitude with mostly prograding nature. However, the aggrading nature of some reflectors could indicate that these clinofolds are part of a LST (SF4; *Figure 4.3*), which is younger than the Submarine Landslide 1 (SL1, *Figure 4.4*).

Sequence S6 displays thickness of 90 ms TWTT in Well #1 (*Figure 4.4*). Transition between Sequence S5 and S6 reveals a highly erosive unconformity that is topped on the slope by sub-parallel reflectors of medium to high amplitude, which correspond to a TST (SF1; *Figure 4.3*) (*Figure 4.4*). This TST is the thickest transgressive package observed in the seismic block during the deposition of the Plio-Pleistocene series. It reaches a thickness of more than 100 ms TWTT along the Inline A at its thickest area. The TST is also at a very distal part of the seismic block, which implies a prior important relative sea-level fall. Along the Inline B (*Figure 4.4*), multiple landslides and deformation affect the slope domain, and therefore the TST reflectors. Above this system tract, reflectors of medium amplitude downlap the previous reflectors and prograde towards the basin with an important aggradational behaviour (SF2; *Figure 4.3*). Finally, aggradation ceases and only prograding reflectors are visible near the slope (*Figure 4.4*). Along the inline B (*Figure 4.4*), the erosive unconformity delimiting the S6 and S7 has eroded the most distal part of the regressive cortege, so, the S6 FSST is not visible.

Sequence S7 displays a thickness of 120 ms TWTT in Well #1 (*Figure 4.4*). The first reflectors associated with S7 are based on an erosive unconformity (Orange line at the interface of S6 and S7 in *Figure 4.4*). A set of reflectors of high amplitude, associated with SF1, covers this unconformity, and are, therefore, part of a TST. Above the TST, clinofolds prograde towards the basin, most of the clinofolds are only prograding and are related to SF3 (*Figure 4.3*) and are part of a FSST. Only bottomsets of the previous HST appear inside the seismic block possibly due to its position closer to the continent. Close to the slope, a Submarine Landslide scar cut the end of the FSST. This second Submarine Landslide (SL2) shows the same pattern as the one observed in SL1. Stacked reflectors of low amplitude also cover it,

which could be associated with a LST. However, the lack of data towards the basin prevents a clear identification.

Sequence S8 displays a thickness of 70 ms TWTT in Well #1 (*Figure 4.4*). Along the slope, the thickness of S8 increases drastically. Along the Inline A (*Figure 4.4*), only clinoforms with extended bottomsets cover the slope. The Inline B (*Figure 4.4*), reveals more precise patterns, five intervals with clear progradation topped by a high amplitude reflector are identified as SF4 (*Figure 4.3*) and correspond to FSST/LST (FR 1 to FR 5 in the *Figure 4.4*) developed on the slope. These regressive systems are at a smaller scale compared to the FSST observed during the previous seismic sequence; indeed, FSST/LST only extend along the slope on stretch of one or two kilometres in width, whereas the previous FSST can extend along the entire width of the all the outer shelf for five to ten kilometres. On the outer shelf, data quality declines and most of the reflectors have poor continuity. However, some area along Inline A reveal a clear stacking of high amplitude reflectors along a stretch as wide as one kilometre. It is associated with SF7 (*Figure 4.3*) and are related to carbonate build-up.

Sequence S9 displays a thickness of 180 ms TWTT in Well #1 (*Figure 4.4*). On the outer shelf along the Inline A (*Figure 4.4*), reflectors of high amplitude highlight topographic features which are associated with SF7 (*Figure 4.3*) and are characteristic of carbonated build-ups during TST. Poor data quality prevents more detailed interpretation of this area. However, along slope in the Inline B, four intervals: FR 6 to FR 9 (*Figure 4.4*) which show aggradation and progradation, are topped by high amplitude reflector and correspond to SF4 (*Figure 4.3*). These intervals correspond to FSST and LST of smaller scale compared to the ones observed in the Sequences S1 to S7. Finally, the sea floor reveals topographic highs along the outer shelf which could be associated with SF7 (*Figure 4.3*).

4.7.4. Supplementary Figures

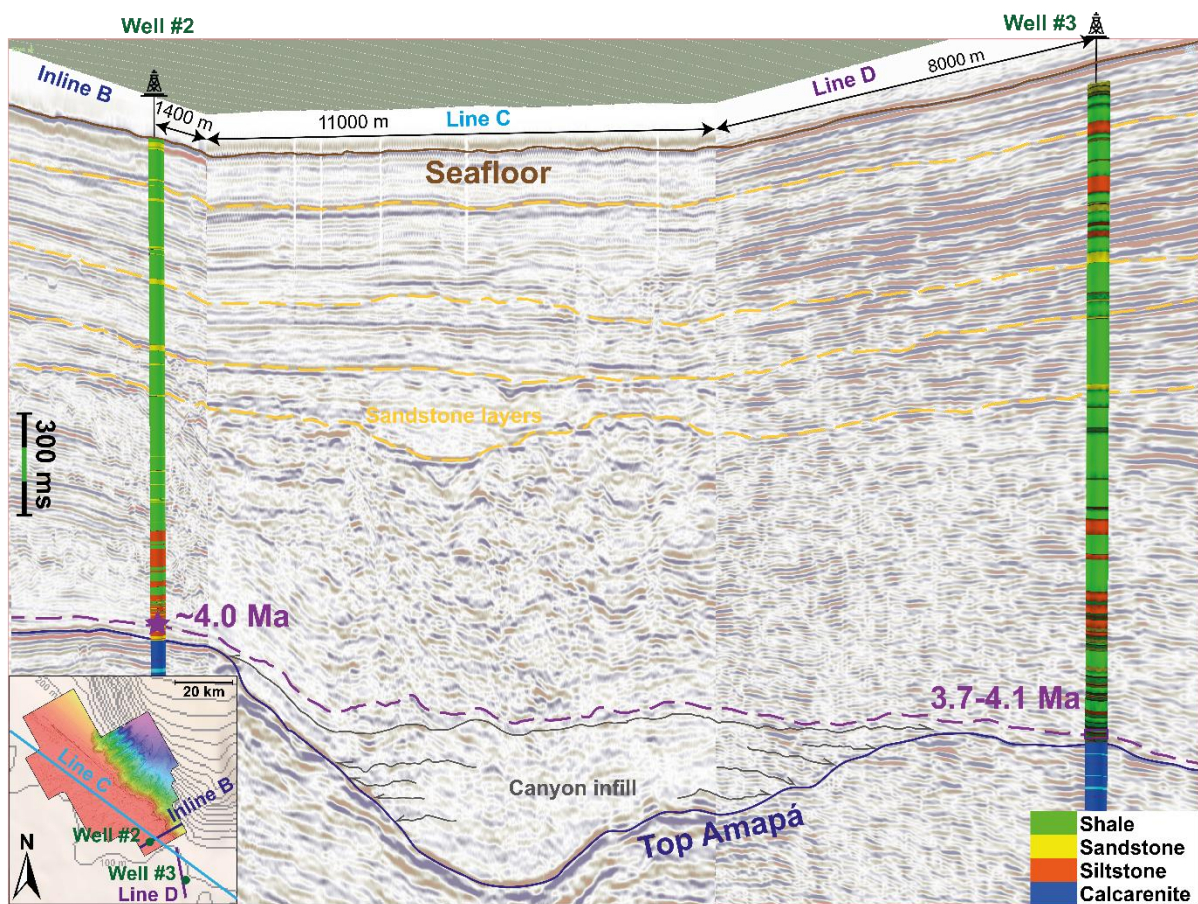


Figure S4.1: 3D seismic viewer revealing the correlation used to propagate the biostratigraphic age from Well #3 to the seismic block through two 2D seismic lines named C and D. The small box in the bottom left shows the position of the different lines and wells compared to the seismic block position. The top of Amapá is eroded by a major canyon avoiding an easy propagation. However, the bottom part of the canyon is fulfilled by reflectors with onlapping terminations noted canyon infill in the figure. While the upper part shows easy to propagate and correlate sandy layers which are highlighted in yellow. The position of the samples used for biostratigraphy correspond to the first set of reflectors which covers the canyon and the adjacent shelf (purple dashed line).

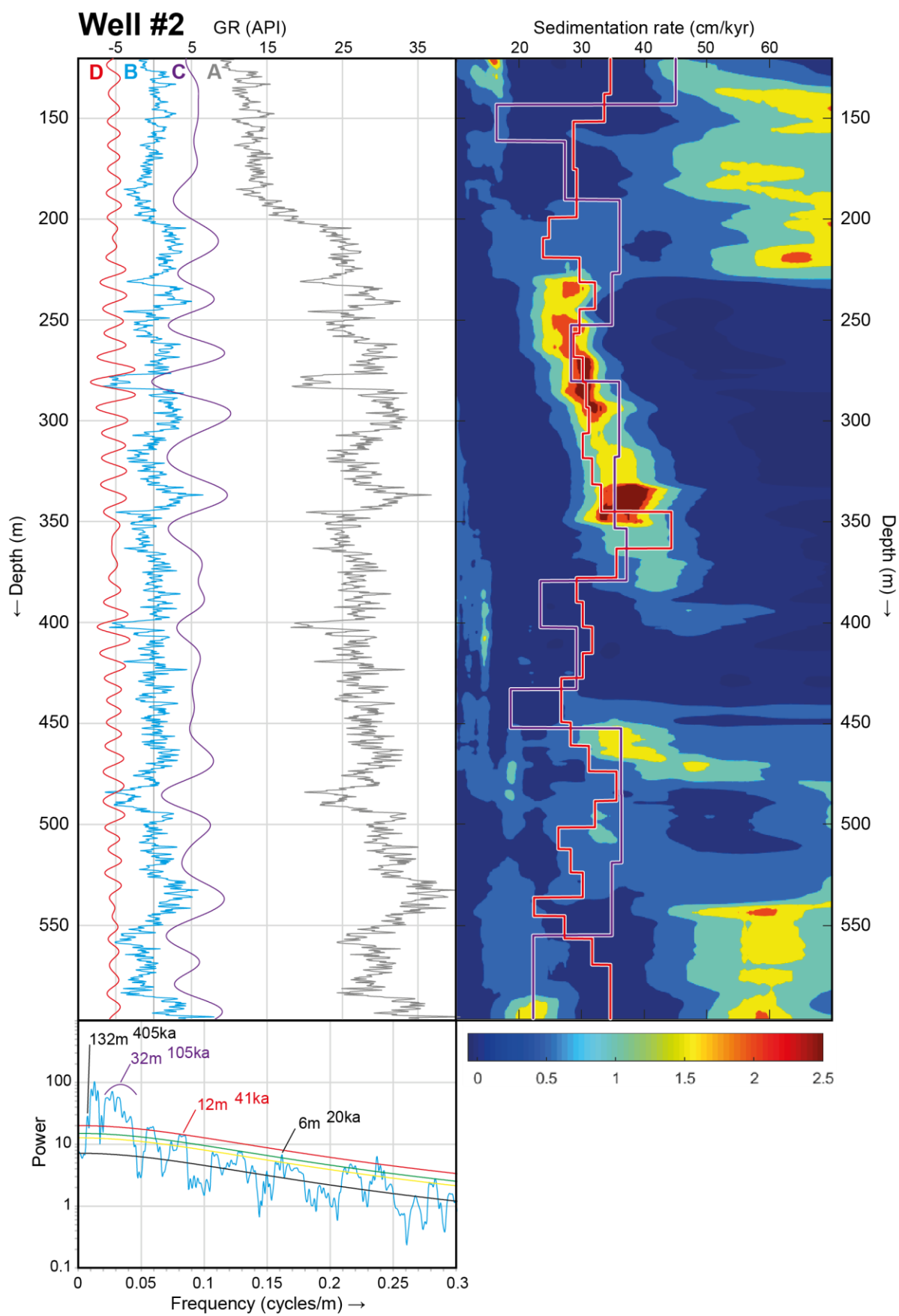


Figure S4.2: Cyclostratigraphic analysis of GR data of the upper non-deformed interval of Well #2 (depths 120 to 596 m KB, upper siliciclastic series). On the left-side panel: (A) Raw GR dataset; (B) Detrended GR data; (C) Filter on the 32 m cycles potentially associated with the Earth's short eccentricity; (D) Filter on the 12 m cycles potentially associated with the Earth's obliquity. The graph below presents the MTM analysis of the curve (B) with the interpreted orbital cyclicities using manual frequency ratio method. The right-side panel present eCOCO results compared to the sedimentation rates obtained after a tuning on short eccentricity (curve (C)) and obliquity (curve (D)), respectively in purple and red.

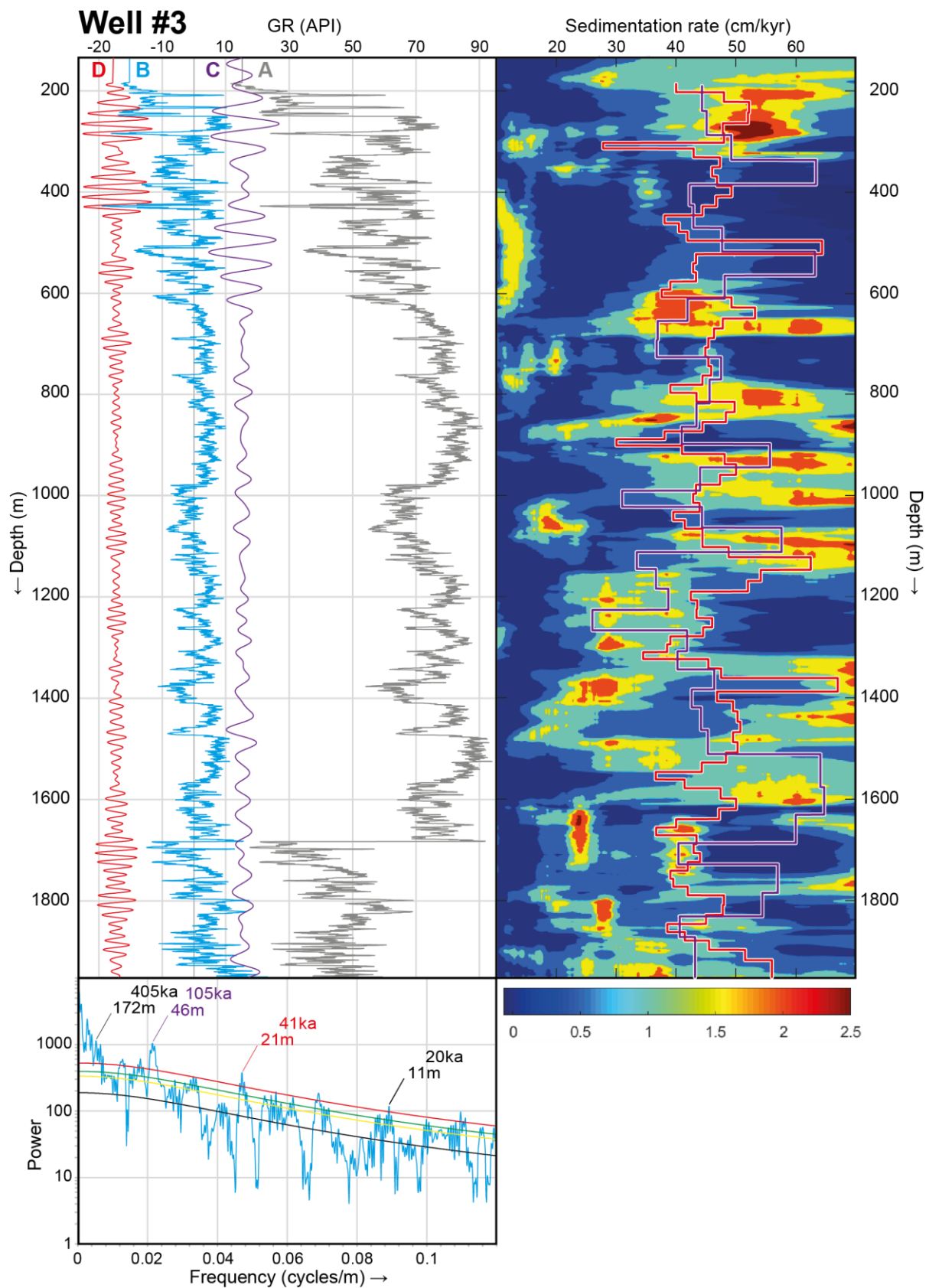


Figure S4.3: Cyclostratigraphic analysis of GR data of Well #3 (depths 132 to 1954 m KB, siliciclastic series). On the left-side panel: (A) Raw GR dataset extended to the seafloor; (B) Detrended and corrected GR data; (C) Filter on the 46 m cycles potentially associated with the Earth's short eccentricity; (D) Filter on the 21 m cycles potentially associated with the Earth's obliquity. The graph

below presents the MTM analysis of the curve (B) with the interpreted orbital cyclicities using manual frequency ratio method. The right-side panel present *eCOCO* results compared to the sedimentation rates obtained after a tuning on short eccentricity (curve (C)) and obliquity (curve (D)), respectively in purple and red.

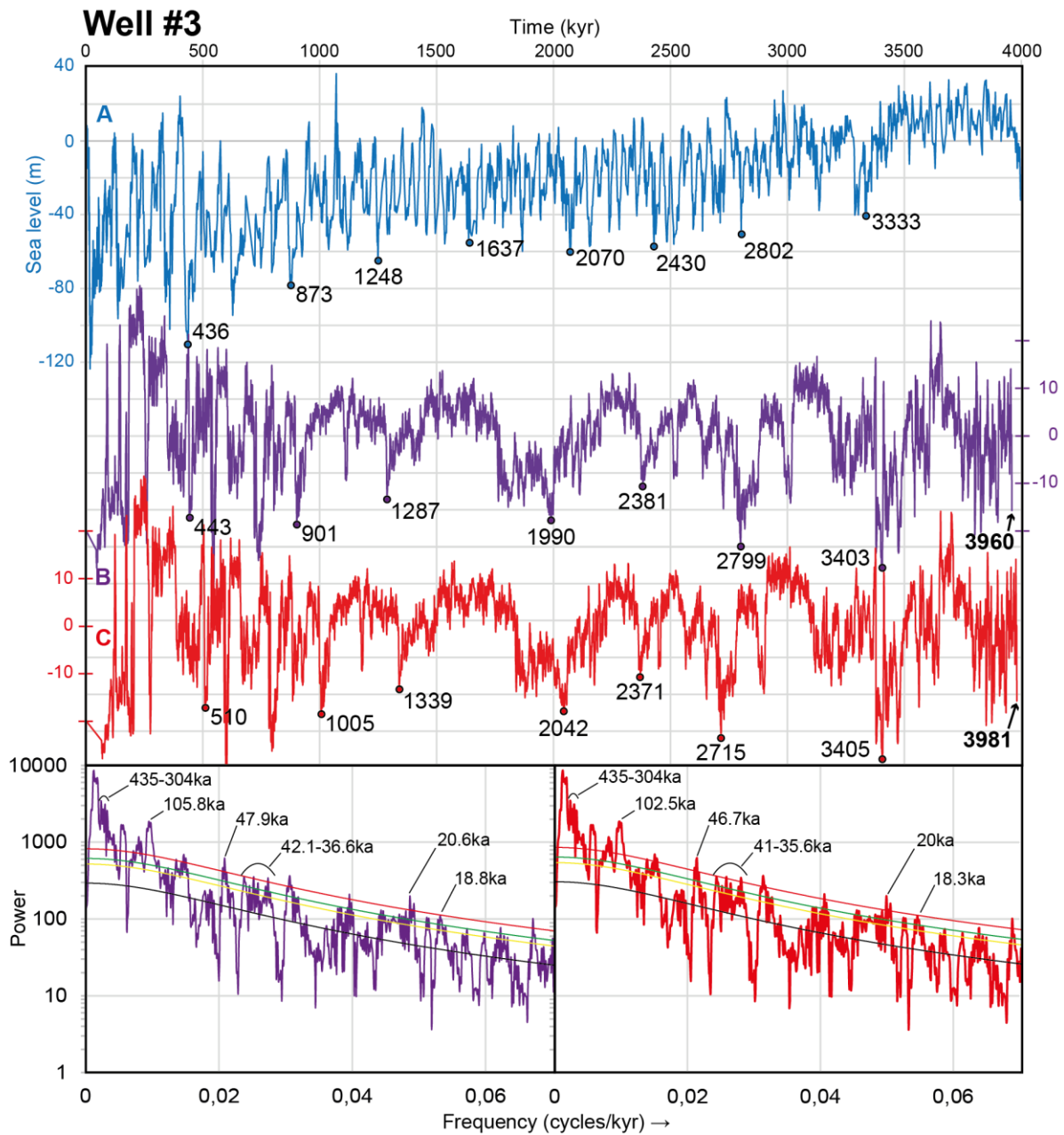


Figure S4.4: Cyclostratigraphic results of GR data of Well #3 (depths 132 to 1954 m KB, siliciclastic series). The upper panel shows; (A) global sea level variation from Miller et al. (2020); (B) the GR data of Well #3 in time after a tuning between the Earth's short eccentricity minima and the minima of the filter on the 46 m frequency; (C) the GR data of Well #3 in time after a tuning between the Earth's obliquity minima and the minima of the filter on the 21 m frequency. Ages noted along the curves corresponds to potential seismic sequence boundaries. The lower panels present the Multi-Taper-Method of curves B and C (see corresponding colours), with the main astronomical cyclicities. Red,

green, yellow and black lines represent the 99%, 95%, 90% and median Robust AR(1) confidence levels respectively.

4.8. Previous attempts and upcoming improvements

Various age models have been developed for wells #1, #2, and #3, all employing cyclostratigraphy based on gamma-ray (GR) data. Here after, we present distinct methodologies that lead to age models with highly comparable results.

4.8.1. Age model based on intervals

4.8.1.1. Method

The GR data have been subdivided into different intervals based on sequence stratigraphy. This subdivision allows reducing the effects of variations in sedimentation rate on the record of sedimentary cycles. Along Well #1, we decided to use the limits of the seismic sequences as well as the important variations of GR as limits of our intervals. The sharp changes of GR directly result from a variation of lithology (and therefore acoustic impedance) and are thus well visible in seismic reflection (since great variations of acoustic impedance results in increased seismic wave reflection). In the case of Well #2, we decided to use the same GR intervals as in Well #1. To do this, we extended the limits of these intervals via the 3D seismic block using horizons constructed by Paleoscan. Lastly, as Well #3 is located outside the block, we could not use a similar method. We decided, therefore, to use only the significant GR drops as interval boundaries. However, we relied on a visual correlation between wells to get the most similar cut-off possible across available wells.

The astronomical time calibration (or tuning) was done on the short (100 kyr) eccentricity cycle because it is well expressed throughout the Plio-Pleistocene series. We first established a floating timescale based on a pure 100 kyr periodicity. Then, the 100 kyr tuned GR was anchored at minima of the 405 kyr eccentricity cycles, based on the La2004 astronomical model (Laskar et al., 2004) assuming that some major shifts in GR match boundaries of prominent seismic sequences. Finally, we correlated the absolute-age tuned GR to the La2004 raw eccentricity, and checked the validation of our age model by considering the available biostratigraphic data at Well #3 (Cruz et al., 2019).

4.8.1.2. Results

Well #1

The MTM spectral analysis performed per intervals on GR data (*Figure S4.5*) shows two to three distinct peaks of frequency ratios close to the short eccentricity, obliquity and precession. The strongest peak for each interval corresponds to the short eccentricity cycle (97-128 kyr). In most of the intervals, the two other peaks match the obliquity (41 kyr) and precession (19-23 kyr). The short eccentricity wavelength ranges from 17 to 45 m, pointing to a significant change in sedimentation rate through Well #1. The COCO results further support the manual frequency ratio method (*Figure S4.6*).

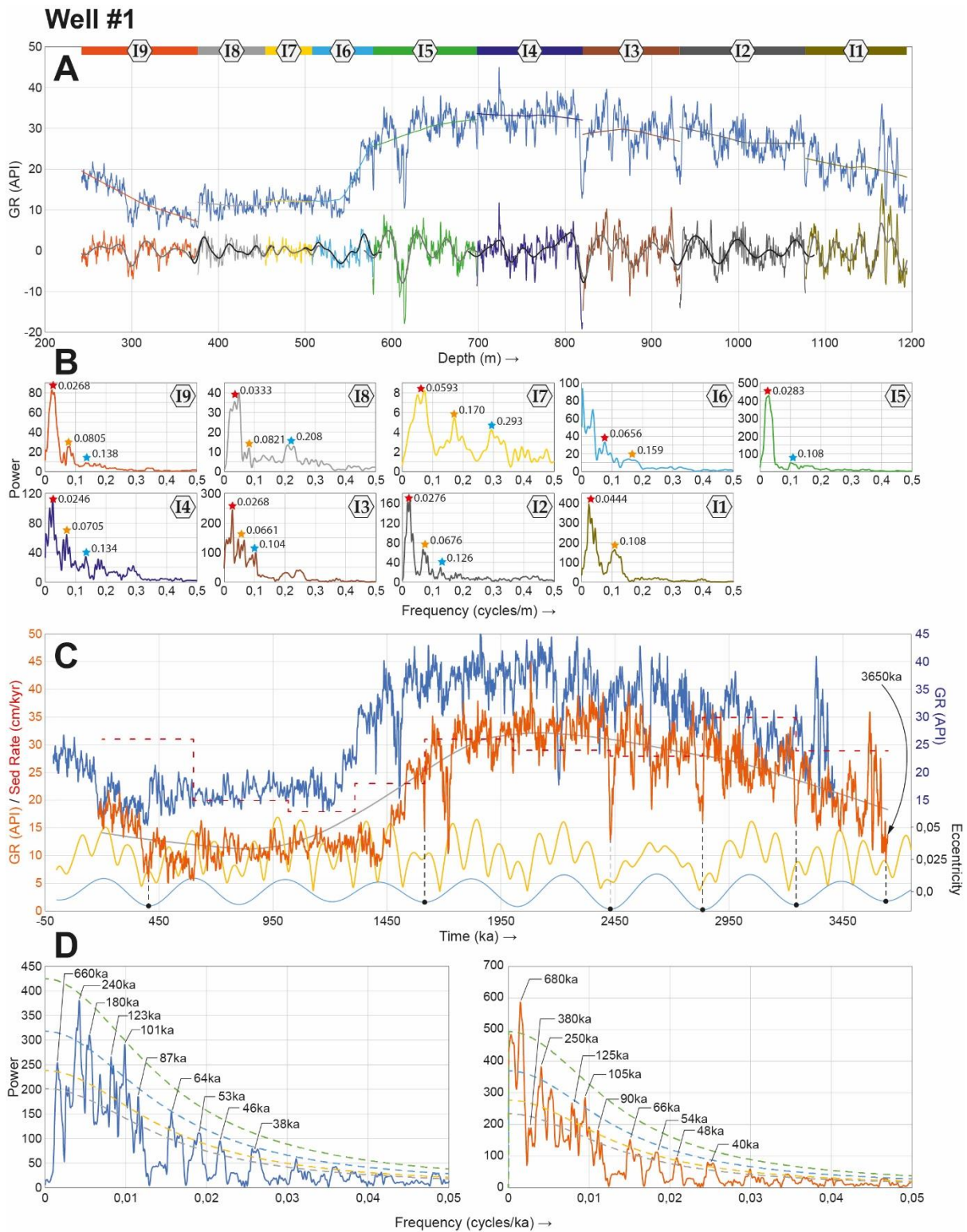


Figure S4.5: Cyclostratigraphic analysis of GR data of Well #1 (depths 242 to 1194 m, Plio-Pleistocene section). (A) Raw and detrended GR data along with the analysed stratigraphic intervals (labelled I1 through I19 from the oldest to the youngest). The filtered wavelength of the short eccentricity is also shown along with the detrended data. (B) 2π -MTM power spectra of the detrended stratigraphic intervals (mentioned by the color codes). Red, orange and blue stars on spectral peaks indicate possible short eccentricity, obliquity and precession related wavelengths. (C) The 100 kyr tuned GR data (blue: eccentricity).

tuned to a pure 100 kyr sine curve, orange: the 100 kyr tuned GR curve is anchored to 405 kyr eccentricity cycle minima) along with the raw La2004 eccentricity data (yellow curve) and the filtered 405 kyr cycle band (light blue curve). The red-dashed curve depicts sedimentation rate inferred from the 405 kyr anchored curve. (D) 2π -MTM power spectra of the tuned GR data to a pure 100 kyr sine (in blue) and those retuned to 405 kyr cycle minima (in orange), along with the robust red noise levels (median, 90%, 95% and 99% confidence levels).

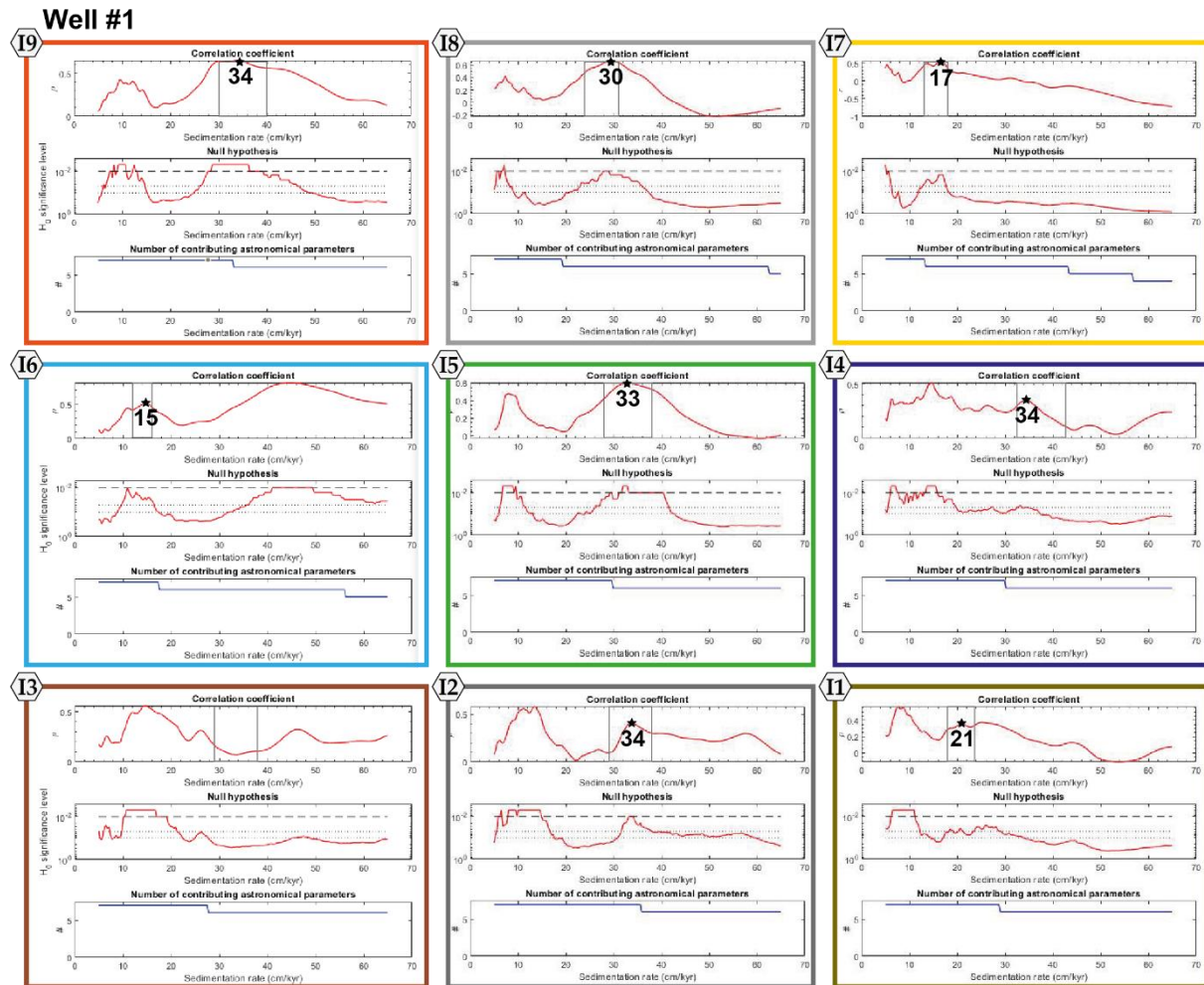


Figure S4.6: COCO results for each interval of the Well #1 compared with the sedimentation rates obtain through manual frequency ratio methodology. The calculation of sedimentation rate through manual frequency ratio method is represented by the black boxes in each interval. The black stars highlight the most probable sedimentation rate obtain with the comparison with both methodologies and the number is in cm/kyr.

The interval 7 reveals a similar pattern within the three wells. The amplitude of the peak corresponding to short eccentricity cycle (see the vertical axis entitled “power” in the Figures 4.8.1, 4.8.3 and, 4.8.5 for the interval 7; I7) decreases drastically by at least one order of magnitude making the other two cycles, related to obliquity (41 kyr) and precession (19-23 kyr), comparatively stronger (Figures 4.8.1, 4.8.3 and, 4.8.5). While the next two intervals (I8 and I9) contrast with a peak corresponding to short eccentricity parameter (97-128 kyr) with a

power 5 to 20 times greater than in I7 (*Figures 4.8.1, 4.8.3 and, 4.8.5*). Interval 4 in the wells (*Figures 4.8.1, and 4.8.5*), shows the same pattern with a decrease in the power of short eccentricity and an increase in precession and obliquity comparatively to adjacent intervals.

The 100 kyr tuning of the whole GR data (*Figure S4.5*) yields a duration of 3.4 Ma for the Plio-Pleistocene series in Well #1. The MTM spectral analysis of the tuned GR time series (*Figure S4.5*) reveals several peaks at 660, 240, 180, 123, 101, 87, 64, 53, 46 and 38 kyr. Then, we retuned the 100 kyr GR time series to the 405 kyr eccentricity cycle assuming that their minima correspond to the sharp drops in GR which correlate to boundaries of seismic sequences and major changes in the lithology.

Anchoring the 100 kyr floating time scale to the 405 kyr eccentricity minima allows an absolute age model for Well #1 (*Figure S4.5*). The MTM spectral analysis of this tuned dataset detects peaks of 125, 105, 90, and 40 kyr (*Figure S4.5*). The inferred sedimentation rate curve reveals lower values of 20, 18 and 23 cm/kyr for intervals I8, I7 and I6 respectively (from 0.6 to 1.5 Ma), and greater values of 31 cm/kyr and 35 cm/kyr for respectively I9 and I2 (*Figure S4.5*). In the *Figure S4.10*, we compare the sedimentation rates inferred from the 100 kyr tuned GR curve with the sedimentation rates estimated with the “eCOCO” approach. We observe an overall good correlation between the two method outputs, further supporting our cyclostratigraphic interpretation based on the manual frequency ratio method. Finally, we obtained an age for the first appearance of Amazon-related terrigenous sediments of 3.65 Ma in Well #1 (*Figure S4.5*).

Well #2

Within the Plio-Pleistocene series of Well #2, only its upper part is tectonically undeformed (*Figure 4.4*). Thus, we focused on cyclostratigraphy of its upper part (*Figure S4.7*). We extended the seismic intervals created within Well #1 using 3D seismic to separate the GR data of Well #2 with the same intervals (Intervals I6 through I9; *Figure S4.7*). The MTM spectral analysis of these intervals (*Figure S4.7*) shows two to three relevant GR peaks, with elevated power (*Figure S4.7*). The frequency ratio method allows attributing each of the three peaks, from the lowest to the highest frequency, to short eccentricity, obliquity and precession (*Figure S4.7*). The COCO results further support the manual frequency ratio method (*Figure S4.8*). The 100 kyr tuning of Well #2 (*Figure S4.7*) yields a duration of 1.67 Myr for the upper part of the Plio-Pleistocene series. Finally, the 100 kyr tuned GR data were anchored to the minima of 405 kyr eccentricity cycles (*Figure S4.7*). The MTM spectral analysis of the 100 kyr tuned GR time series is almost identical to the 405 kyr retuned GR time series. Therefore, only the MTM of

the 405 kyr retuned GR is presented (*Figure S4.7*). It reveals cycles of 440, 250, 116, 100, 55 and 38 kyr. The estimated sedimentation rate from tuning shows lower values of 20 cm/kyr, within interval I7 (from 0.8 to 1.2 Ma), and a higher value of 40 cm/kyr within Interval I9. Results of the “eCOCO” method reinforce the obtained sedimentation rates from the 100 kyr tuned GR data, with possibly one exception at the transition from Interval I7 to Interval I8 where the eCOCO fails in the detection of the optimal sedimentation rates (*Figure S4.11*). However, the COCO method applied per intervals (I7 and I8) highlight significant optimal sedimentation rate, especially within I8 (*Figure S4.8*).

Well #2

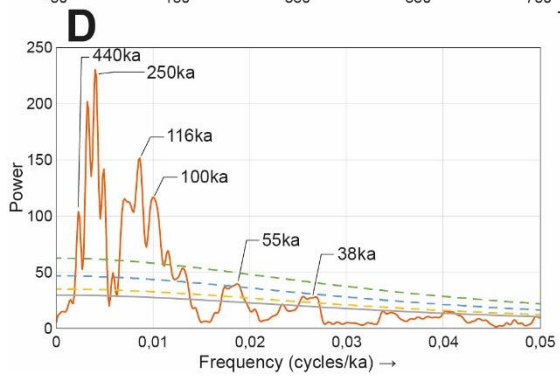
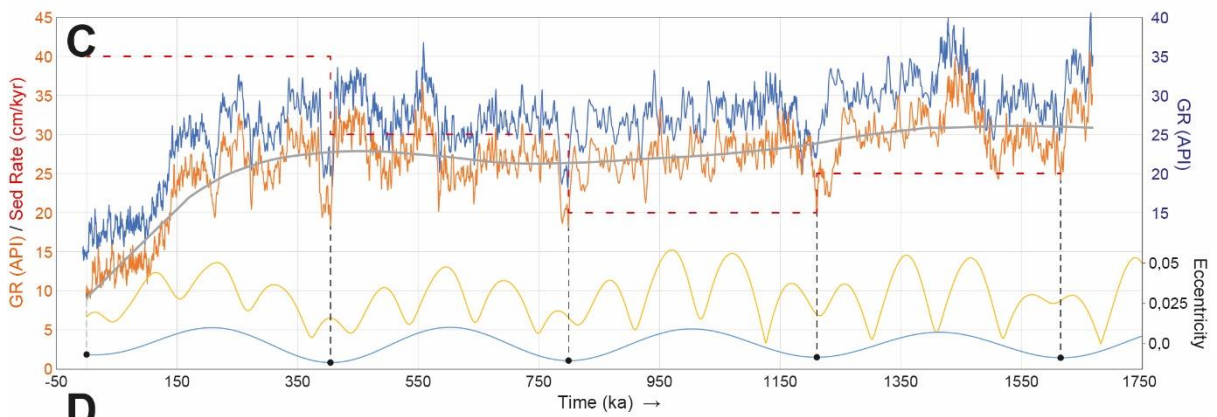
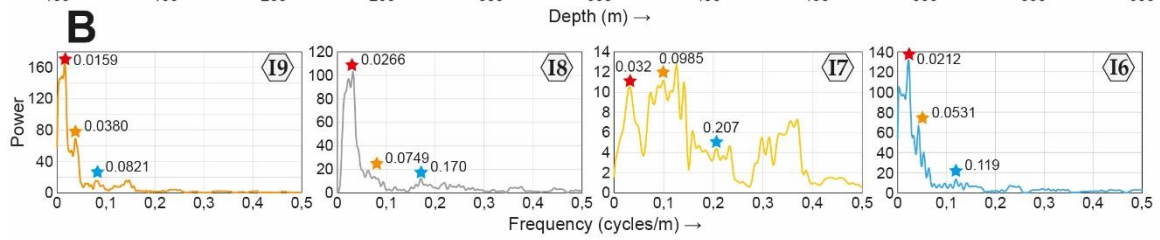
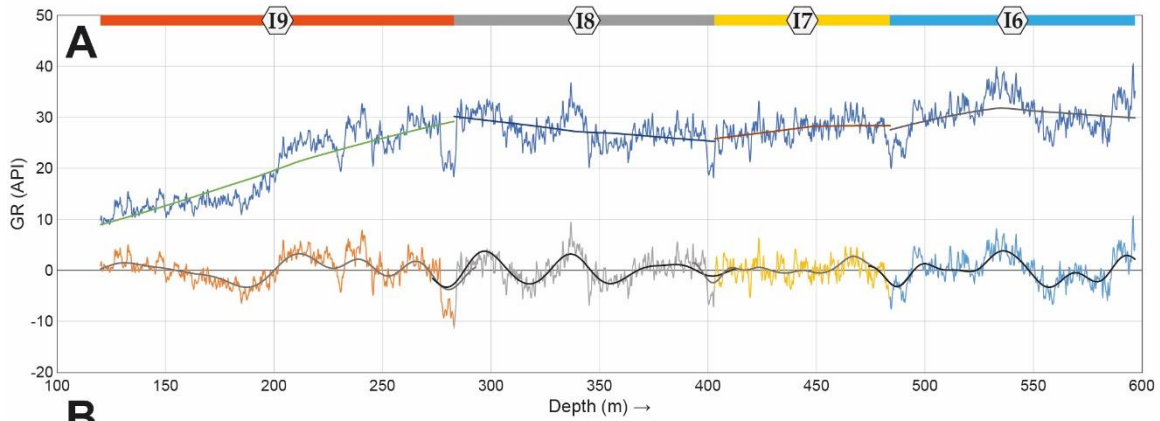


Figure S4.7: Cyclostratigraphic analysis of GR data of Well #2 (depths 120 to 596 m, upper Plio-Pleistocene section). (A) Raw and detrended GR data along with the analysed stratigraphic intervals (labelled I6 through I9 from the oldest to the youngest). The filtered wavelength of the short eccentricity is also shown along with the detrended data. (B) 2π -MTM power spectra of the detrended stratigraphic intervals (mentioned by the color codes). Red, orange and blue stars on spectral peaks indicate possible short eccentricity, obliquity and precession related wavelengths. (C) The 100 kyr tuned GR data (blue: tuned to a pure 100 kyr sine curve, orange: the 100 kyr tuned GR curve is anchored to 405 kyr eccentricity cycle minima) along with the raw La2004 eccentricity data (yellow curve) and the filtered 405 kyr cycle band (light blue curve). The red-dashed curve depicts sedimentation rate inferred from the 405 kyr anchored curve. (D) 2π -MTM power spectra of the anchored GR data to 405 kyr cycle minima (in orange), along with the robust red noise levels (median, 90%, 95% and 99% confidence levels).

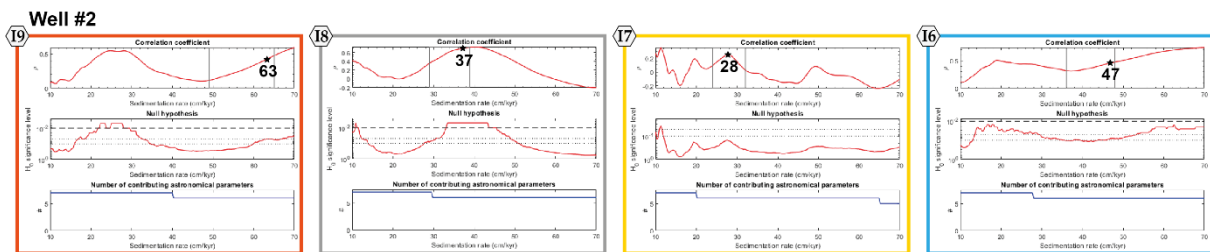


Figure S4.8: COCO results for each interval of the Well #2 compared with the sedimentation rates obtained through manual frequency ratio methodology. The calculation of sedimentation rate through manual frequency ratio method is represented by the black boxes in each interval. The black stars highlight the most probable sedimentation rate obtained with the comparison with both methodologies and the number is in cm/kyr.

Well #3

In Well #3, the MTM of each interval reveals a good correlation between the main GR peak with the lowest frequency and the short eccentricity parameter (97-128 kyr; red stars in Figure S4.9). The second and third peaks, with high power compared to mean value, correlates with the obliquity (41 kyr) and precession parameters (19-23 kyr; respectively orange and blue stars in Figure S4.9). The COCO results further support the manual frequency ratio method (Figure S4.10). The highlight of the short eccentricity cycles allows tuning GR data in depth with a pure 100 kyr periodicity signal to obtain a GR curve in time (blue curve, Figure S4.9).

The new GR curve in time indicates a time span of 4.23 Ma for the Plio-Pleistocene series along the Well #3 (blue curve, Figure S4.9). Finally, after the anchoring on the minima of the long eccentricity cycles, we obtain an age model for the GR data of the Well #3 (orange curve, Figure S4.9). This model generates an age of 4.3 Ma for the arrival of the first terrigenous sediments brought by the Amazon along Well #3 (orange curve, Figure S4.9). The MTM of

this curve attributes main cyclicities for 830, 350, 162, 114, 96 and 44 kyr (*Figure S4.9*). We also calculated sedimentation rates by comparing curves in time and depth; it highlights low sedimentation rates of 39 cm/kyr during I7 (0.8 to 1.2 Ma), and 35, 25 and 38 cm/kyr during I5, I4 and I3 respectively (from 1.6 to 2.8 Ma). Interval I1 (from 3.2 to 4.3 Ma) also reveal low sedimentation rates of 27 cm/kyr (*Figure S4.9*). Other intervals present high sedimentation rates between present-day to 0.8 Ma (I9 and I8) with value of 52 and 55 cm/kyr respectively as well as interval I6 (1.2 to 1.6 Ma) with a sedimentation rate of 54 cm/kyr and interval I2 (2.8 to 3.2 Ma) with the highest sedimentation rates recorded of 74 cm/kyr (*Figure S4.9*). Finally, the eCOCO inferred sedimentation rates track those estimated from the 100 kyr tuned GR data (*Figure S4.11*).

Well #3

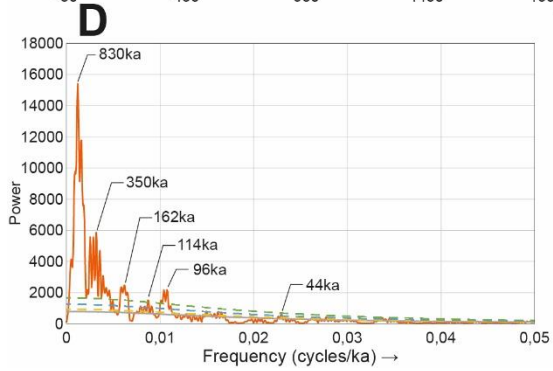
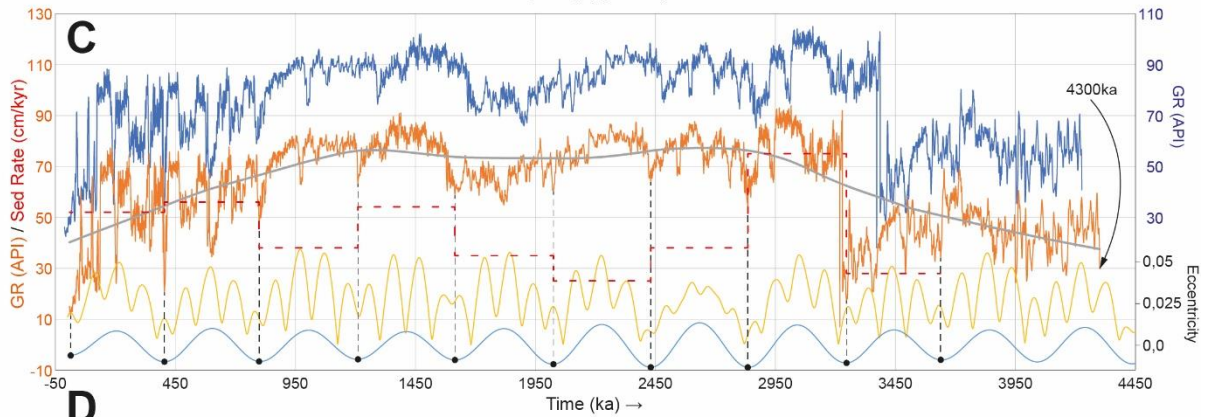
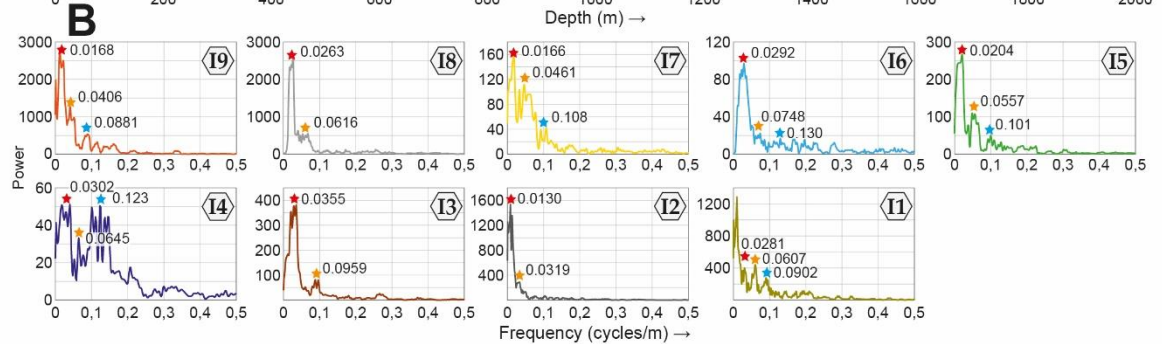
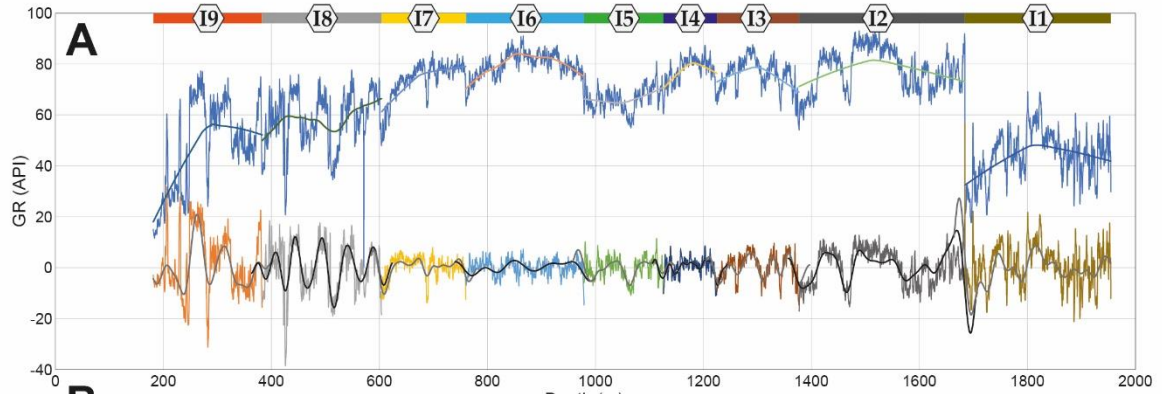


Figure S4.9: Cyclostratigraphic analysis of GR data of Well #3 (depths 181 to 1954 m, Plio-Pleistocene section). (A) Raw and detrended GR data along with the analysed stratigraphic intervals (labelled I1 through I9 from the oldest to the youngest). The filtered wavelength of the short eccentricity is also shown along with the detrended data. (B) 2π -MTM power spectra of the detrended stratigraphic intervals (mentioned by the color codes). Red, orange and blue stars on spectral peaks indicate possible short eccentricity, obliquity and precession related wavelengths. (C) The 100 kyr tuned GR data (blue: tuned to a pure 100 kyr sine curve, orange: the 100 kyr tuned GR curve is anchored to 405 kyr eccentricity cycle minima) along with the raw La2004 eccentricity data (yellow curve) and the filtered 405 kyr cycle band (light blue curve). The red-dashed curve depicts sedimentation rate inferred from the 405 kyr anchored curve. (D) 2π -MTM power spectra of the anchored GR data to 405 kyr cycle minima (in orange), along with the robust red noise levels (median, 90%, 95% and 99% confidence levels).

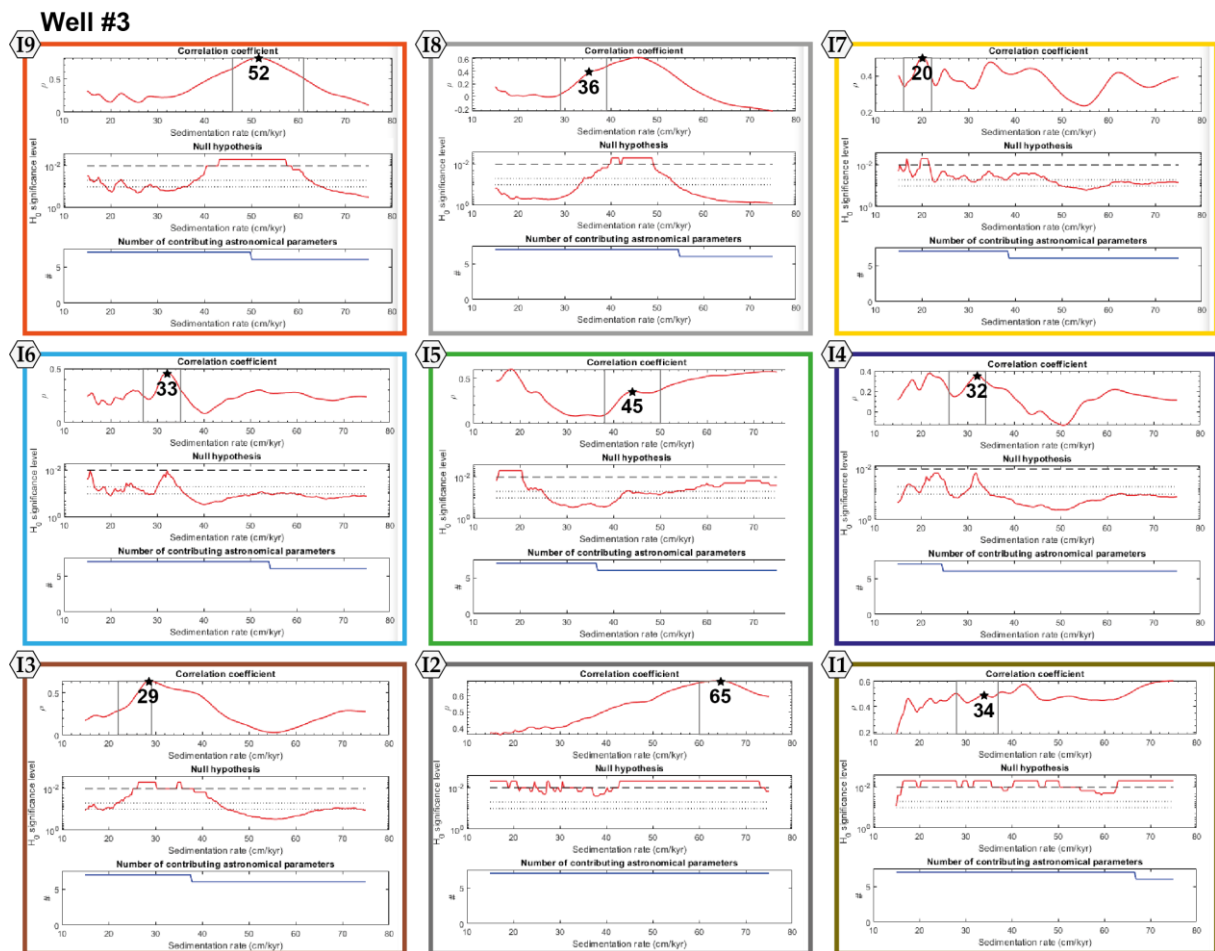


Figure S4.10: COCO results for each interval of the Well #3 compared with the sedimentation rates obtained through manual frequency ratio methodology. The calculation of sedimentation rate through manual frequency ratio method is represented by the black boxes in each interval. The black stars highlight the most probable sedimentation rate obtained with the comparison with both methodologies and the number is in cm/kyr.

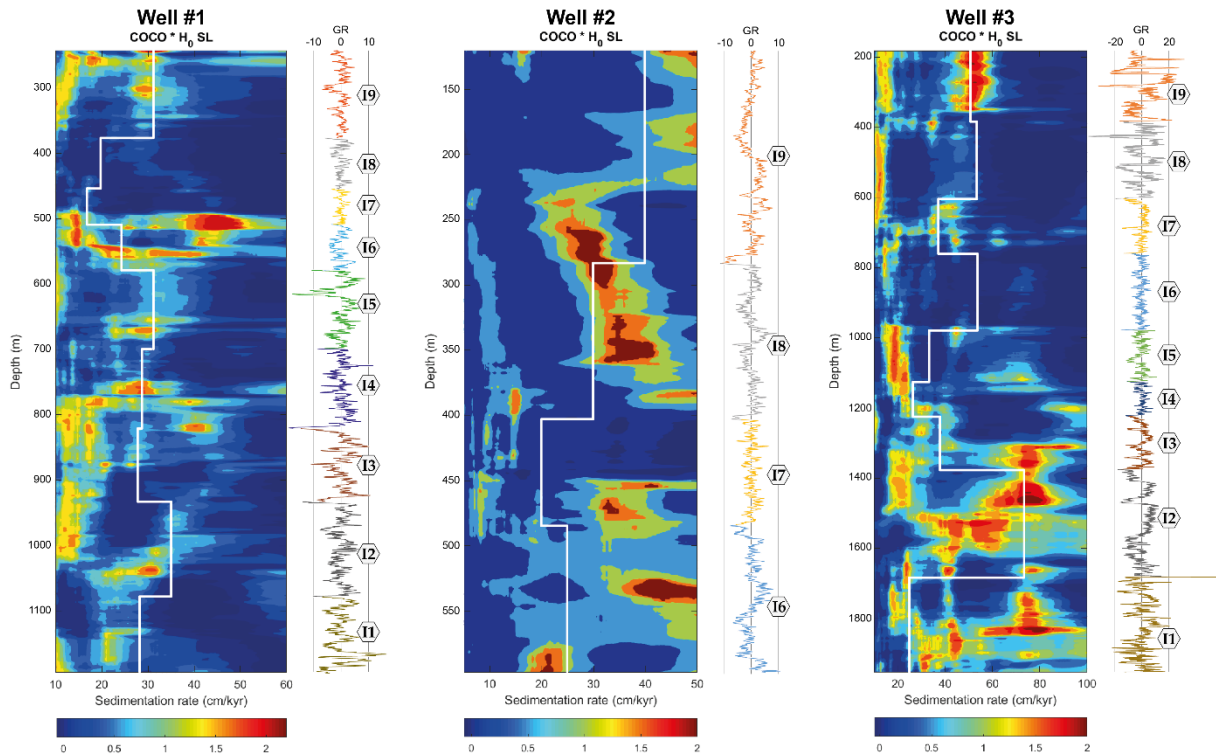


Figure S4.11: Results of the “eCOCO” method for the three wells along with sedimentation rates inferred from the 100 kyr tuned GR data (stair-like white curves). Pearson correlation coefficient, and Null hypothesis H_0 for non-orbital forcing estimated by the evolutive eCOCO approach. Sedimentation rate step is fixed at 0.2 cm/kyr. The used astronomical solution is from Laskar 2004 model (Laskar et al., 2004) with a middle age of the data at 2.0 Ma for wells #1 and #3, and 1.0 Ma for Well #2. The sliding window is fixed at 100, 150 and 200 m for wells #1, #2 and #3 respectively. A step of 1 m is fixed for the three wells.

4.8.2. HMM-Match

In the future, we would like to use the HMM-Match methodology, to obtain a better age model. We already tried on the Well #1 which cross the less deformed siliciclastic stratification. Here after, you will have a presentation of the methods and results associated with the HMM-Match.

4.8.2.1. Method

The HMM-Match is a probabilistic approach for aligning a single record with a designated target. In our study, the record refers to the gamma-ray (GR) dataset of Well #1, and the target is the sea level curve proposed by Miller et al. (2020), which is primarily based on the widely-used $\delta^{18}O$ compilation by Lisiecki and Raymo (2005). The HMM-Match method has found applications in a variety of disciplines including speech recognition (Levinson et al., 1986), music classification (Pardo et al., 2004), and notably in computational biology (Durbin et al., 1998). Recently, Lin et al. (2014) adapted this methodology to facilitate the alignment of

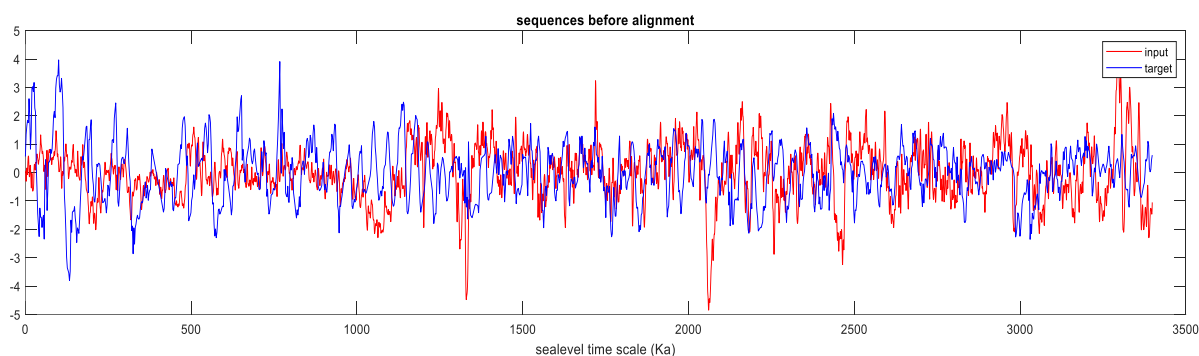
stratigraphic records. While this method has been successfully employed by other researchers primarily to correlate $\delta^{18}\text{O}$ records (Ahn et al., 2017), we propose its application to other geophysical datasets. The comprehensive methodological details of the HMM-Match are available in Lin et al. (2014).

To validate the aligned GR curve generated, we assessed the Confidence Limits and Median Solution, which disclose: the uncertainty in thousands of years (kyr) and; any stretching or squeezing applied to the initial GR data, respectively. Additionally, we performed MTM spectral analysis (Thomson, 1982) on the GR data before and after the HMM-Match procedure to compare cyclicities of both signals.

The HMM-Match method requires two age boundaries for operation, as the GR dataset does not start at the seafloor along the Well #1, we employed median sedimentation rates calculated by dividing the total age of the series by its thickness to infer the age at which the GR record begins. The second boundary corresponds to the beginning of the siliciclastic deposit which is dated between 3.7 and 4.1 Myr based on biostratigraphy. For our analysis, we chose an age of 3.7 Myr in Well #1. Indeed, due to its localization distant from the Well #3 and the Amazon River mouth, we can emit the hypothesis that the age of the first appearance of the siliciclastic series will be younger in Well #1 than in Well #3; where we have the only biostratigraphic age of 3.7-4.1 Myr.

4.8.2.2. Results

The Hidden Markov Model (HMM) match for Well #1 exhibits a strong correlation between the sea level curve by Miller et al. (2020), and the Gamma-Ray (GR) dataset (*Figure S4.12*). This match was established over the time interval of 0.3 to 3.7 Ma, but the software recalibrated the curve to starts at 0 Myr. The correlation could potentially be refined by choosing a younger starting point for the beginning of the GR acquisition. Indeed, the GR acquisition begins 74 m below the seafloor, corresponding to a time range of 250-277 kyr.



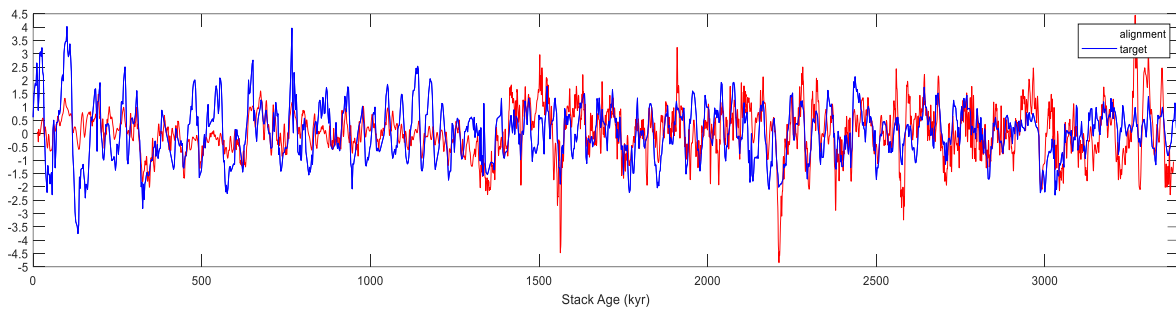


Figure S4.12: HMM-Match: Well #1 was correlated with the sea-level curve from Miller et al. (2020) spanning from 0.3 to 3.7 Myr. The starting age of the gamma-ray (GR) dataset from Well #1 was determined based on the mean sedimentation rate along the well. The upper age limit of the series was inferred from the projected biostratigraphic age data of Well #3. Both curves were normalized to zero. The first graph presents the sequences before alignment while the second graph present the results of the HMM-Match alignment.

The most significant result is the calculation of uncertainties, which reveals an exceptionally low mean uncertainty of 2-3 kyr (Figure S4.13). The highest level of uncertainty occurs around 1000 kyr and corresponds to a 30 kyr shift in the signal during alignment. This outcome underscores the strong correlation between the two curves and suggests that global sea-level changes exert a substantial influence on the sedimentary architecture of the Amazon Continental Margin.

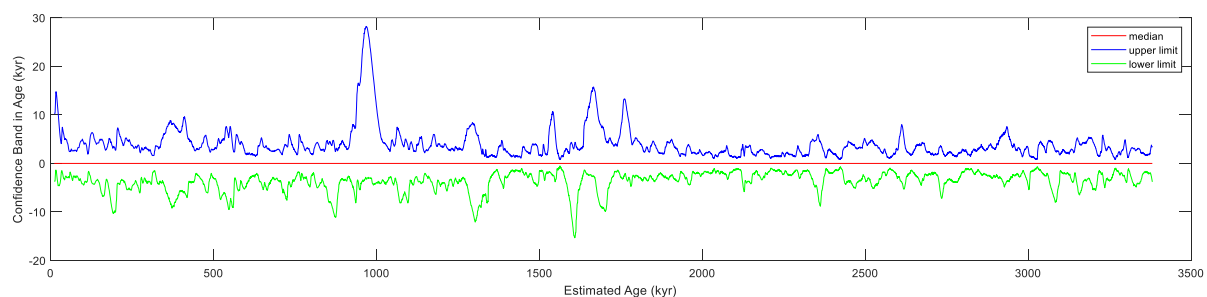


Figure S4.13: HMM-Match uncertainties. The 7 iterations of Run 3 attempted to minimize the adjustments between the Well #1 and sea level for the alignment (Match). The iterative procedure gives information about time assignments where multiple test alignments have high probability, which leads to greater uncertainty. In this case, the maximum uncertainty is +30 kyr at 1 Ma; otherwise, uncertainties are extremely low, on average around + 2 to 3 kyr.

Adjustments performed using the HMM-Match method are presented in Figure S4.14. The figure reveals predominant squeezing in the lower part of Well #1 and stretching in the upper part. This indicates that the sedimentation rate is higher at the base compared to the top of the series. This observation aligns with the initial infilling of the shelf edge during the early stages of formation deposition. As clinoforms reach the shelf edge, most sediments are subsequently

deposited along the slope and in the deep basin, thus limiting the sedimentation rate along the shelf.

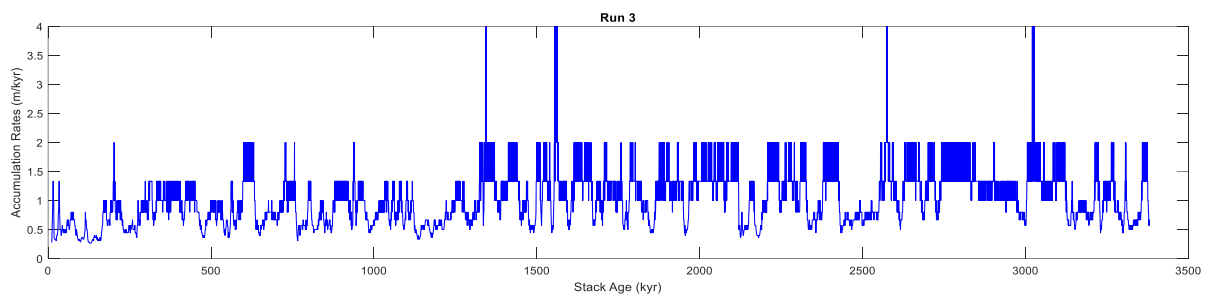


Figure S4.14: Adjustments of initial time scale assigned to Well #1 relative to the sea level time scale. A value of 1 indicates no adjustment; values greater than 1 indicate squeezing of Well #1 initial time scale; values less than 1 indicate stretching was required.

Finally, MTM analysis of the data before and after alignment, as well as MTM of the sea-level for the last 3.7 Myr, are presented in *Figure S4.15*. Prior to alignment, the GR dataset exhibits multiple frequencies, although it is already evident that astronomical frequencies at 106, 39.7, and 21.5 are present in the signal. However, following alignment, the power of the other frequencies substantially diminishes. This suggests that these other frequencies were also influenced by astronomical forcings but were not previously aligned due to significant variations in sedimentation rates. The power levels of obliquity and eccentricity are nearly equal, while the ~405 kyr frequency appears with low power. A strong 222 kyr frequency persists, but it is also present in the MTM analysis of the sea-level curve for the last 3.7 Myr.

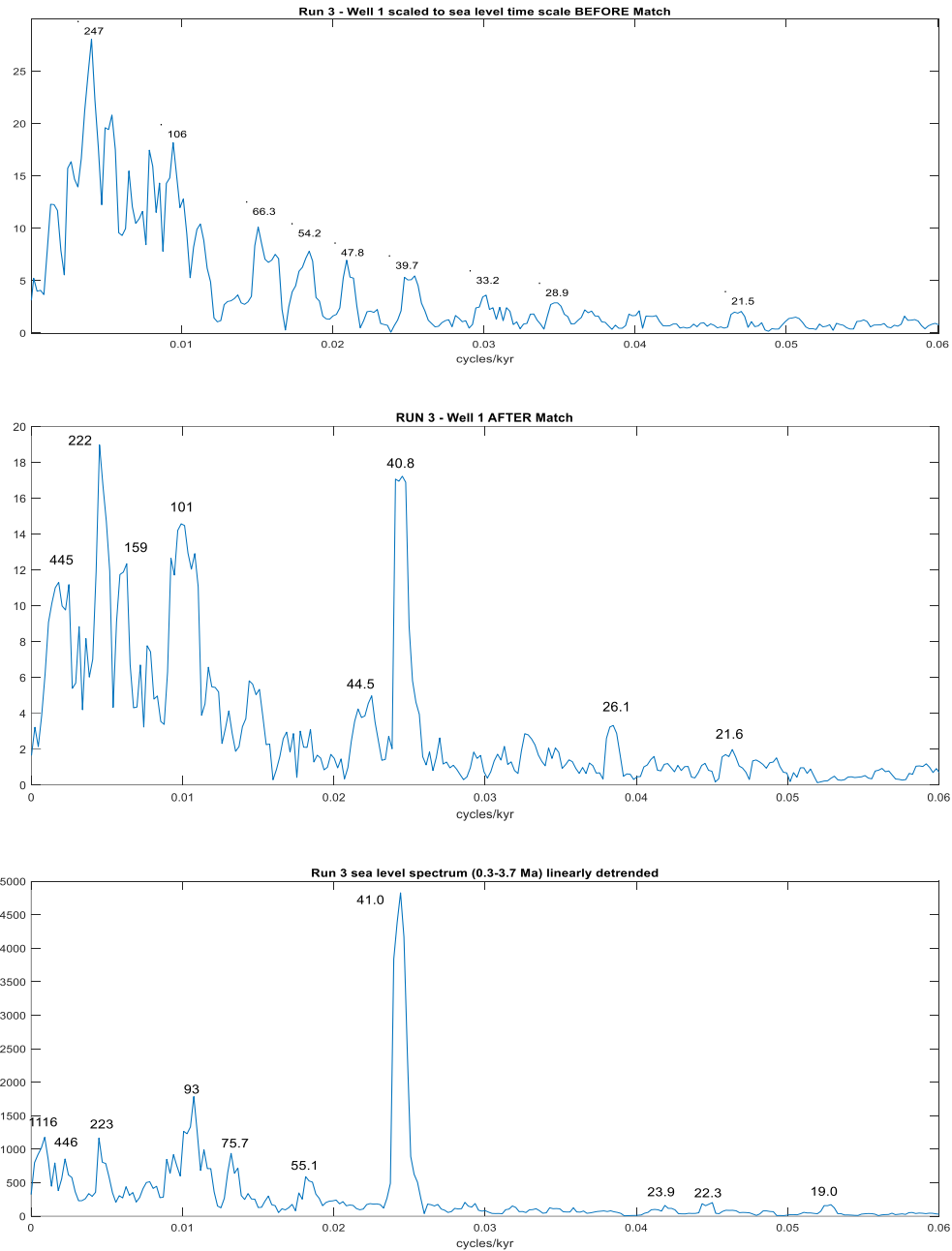
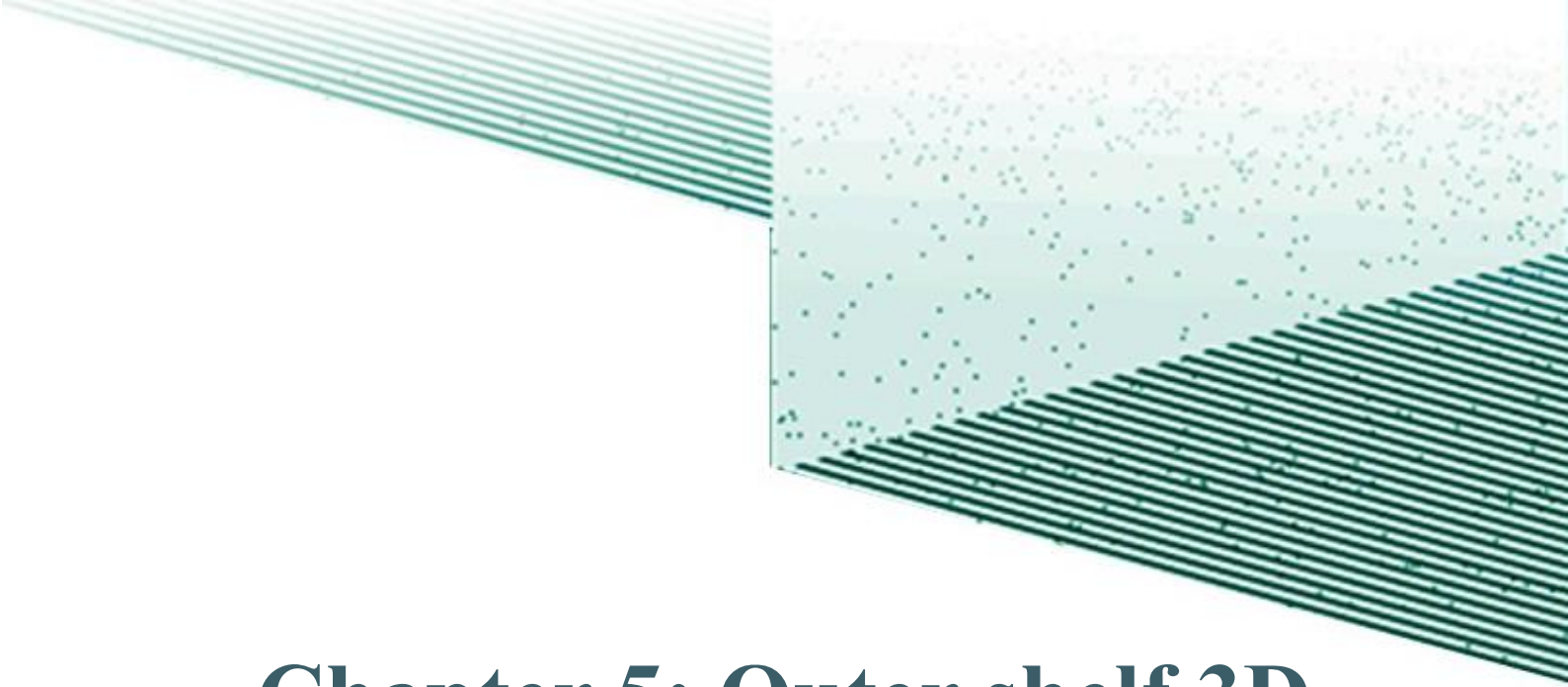


Figure S4.15: 2π MTM spectrum of different set of data. The first graph presents MTM of Well #1 assigned to time span of sea level target before HMM-Match. The second graph presents MTM of Well #1 after the HMM-Match. The third graph presents the MTM of Miller's Sea level curve (2020) between 0.3 to 3.7 Myr.

We believe that this method is highly effective, revealing a robust correlation and, consequently, a significant influence of eustatism on the margin's architecture. We plan to apply this methodology to Well #3 to generate another age model and assess its compatibility with existing models.



**Chapter 5: Outer shelf 3D
Geomorphological features
in the Plio-Pleistocene of the
Brazilian Equatorial
Margin: depositional system
driven by 405 kyr cyclicality.**

Outer shelf 3D Geomorphological features in the Plio-Pleistocene of the Brazilian Equatorial Margin: depositional system driven by 405 kyr cyclicality.

Final version of a scientific paper intended for submission to the journal *Geomorphology*.

Lucas Tortarolo^{a,b,d}, Christian Gorini^b, Marina Rabineau^a, Louis-Marin Bodiguel^a, David Menier^a, Quentin Gauthier^b, Antonio Tadeu Dos Reis^c, Slah Boulila^b, Damien Do Couto^b, Cleverson Guizan Silva^d

^a Laboratoire Geo-Océan, Institut Universitaire Européen de la Mer, UBO, UBS, IFREMER, CNRS, UMR6538, Rue Dumont d'Urville, 29280 Plouzané, France

^b Institut des Sciences de la Terre Paris (ISTEP), Sorbonne Université, CNRS, UMR 7193, 4 Pl. Jussieu, 75005 Paris, France

^c Departamento de Oceanografia Geologica, Universidade do Estado do Rio de Janeiro, Rua São Francisco Xavier, 524, Rio de Janeiro, RJ, Brazil

^d Departamento de Geologia e Geofísica, Universidade Federal Fluminense, Av. Gal. Milton Tavares de Souza, Campus da Praia Vermelha, Boa Viagem, Niterói, RJ, Brazil

corresponding author: lucas.tortarolo@univ-brest.fr

Abstract

The development of 3D seismic acquisition has introduced a new method for visualising past morphologies. This advancement is accompanied by the enhancement of interpretative software over the last decade, which enables the automatic picking of horizon stacks. The multitude of horizons generated allows for the observation of all geomorphological changes during sea-level variation cycles. This study employed this new methodology to explore a 3D seismic block located north of the Brazilian Equatorial Margin with the aim of deciphering the geomorphological evolution of the outer shelf since 3.7 million years (Myr). Indeed, 3.7 Myr corresponds to the first arrival of a substantial volume of sediments transported by the Amazon, in the study area, burying the ancient Amapá carbonate shelf. The high sedimentation rate, inducing significant accommodation due to flexural loading, ensures excellent preservation of the structures in the area, making the Brazilian Equatorial Margin a particularly suitable region for studying the evolution of past morphologies.

The study of the horizons reveals a succession of coastline morphologies, more than 120 km from the present-day shore, which evolves depending on sea level variation. Indeed,

during high sea-level, lagoonal environments are observed, with channel inlets connecting the lagoon to the ocean, sedimentary waves inside the lagoon, and tidal channels. During sea-level fall, the lagoon becomes disconnected from the ocean while sand ridges prograde. Lagoons therefore evolve to lakes. While sea-level keeps dropping, drainage channels erode the ridges deeply.

During the beginning of the transgression, after 2.5 Myr, erosion significantly affects the area, and cliffs are formed by wave action. The formation of these cliffs implies an absence of sediment supply from the Amazon at this time, leading to a change in current circulation during glacial periods around the area. The north-westward flow of the North Brazil Current could have been deflected to the east due to the migration of the Inter Tropical Convergence Zone to the south. However, when the current circulation returned to its present-day path, a vast amount of sediments buried the cliffs and allowed the preservation of this structure. These coastline morphologies are observed inside seismic sequence of 405,000 years and are induced by particularly significant sea-level falls associated with long eccentricity cycles.

Keywords: Brazilian Equatorial Margin, Amazon River Mouth Basin, Plio-Pleistocene, geomorphology, seismic and sequence stratigraphy, paleo-climate, sea level, coastline, Pirarucu Formation.

5.1. Introduction

Sea level has been rising over the past century due to climate change, and the rate has been increased in recent decades due to an increasing anthropogenic pressure. With the rapid growth of the human population, the impacts related to climate change, including sea level rise, will increase especially in coastal areas. To better understand how sea level variation impacts coastal morphologies, it is valuable to examine historical climate events and their effects on the planet. Notably, rapid sea level variation like Heinrich Events, which have caused significant changes in thermohaline circulation, shifts in the position of the Intertropical Convergence Zone (ITCZ), and alterations in global climate patterns (Lynch-Stieglitz et al., 2007). Other events, such as the super-interglacials (Droxler and Jorjy, 2021, 2013; Melles et al., 2012) correspond to unusually warm interglacials associated with exceptionally high sea level. Both of this super-interglacial, Marine Isotope Stages (MIS) 11c and 31, reveal maximum summer temperatures and annual precipitation values $\sim 4^{\circ}$ to 5°C and ~ 300 millimeters higher than those of MIS 1 and 5e (Melles et al., 2012).

The continental shelf serves as a remarkable laboratory for studying the influence of climate variations. Its shallow bathymetry makes it highly susceptible to eustatic variations

leading to changes in coastlines position and morphology. Additionally, its location at the interface of land and sea allows for recording global sea level changes and alterations in erosion rates within the river basins flowing along the margin.

The passive margin of Equatorial Brazil provides an exceptional example due to the combined effect of subsidence and a continuous influx of sediments transported by the Amazon River, the world's largest watershed (Dai and Trenberth, 2002; Milliman, 2001; Nittrouer et al., 1986). These massive sediment inputs have led to the deposition of a considerable volume of sediments on the continental shelf and within the deep Amazon Cone (Damuth and Kumar, 1975). The region exhibits a high subsidence rate and significant sedimentation rates along the shelf (Cruz, 2018; Figueiredo et al., 2009), enabling exceptional preservation of ancient morphologies, and allowing detailed studies using high-resolution 3D seismic data and well information presented in this paper.

While many studies focus on geomorphologies along the amazon deep sea fan, its channels, landslides scars or mud volcanoes (Damuth et al., 1988, 1983; Jegou et al., 2008; Lopez, 2001; M. A. Maslin et al., 1998), few geomorphologies have been identified and described along the shelf. Lastly, carbonates construction has been identified and have concentrate a lot of attention from the scientific community (Banha et al., 2022; dos Santos Filho et al., 2022; Francini-Filho et al., 2018; Giresse et al., 2022; Moura et al., 2016; Vale et al., 2022, 2018). However, studies focusing on the geomorphologies along the outer shelf of the Brazilian Equatorial Margin at a larger time scale remain unknown.

This study focuses on a 3D seismic block located northward of the Amazon canyon and covering mostly the outer shelf. Seismic horizons have been generated with a software specialised on 3D seismic interpretation: Paleoscan. The numerous horizons created allow a full interpretation of the geomorphological evolution of the silico-clastic sediments brought by the Amazon River during the last 3.7 Myr along the outer shelf (Cruz et al., 2019; Gorini et al., 2014; **Chapter 4**).

5.2. Geologic and stratigraphic framework of the Equatorial Brazilian Margin and the Amazon River Mouth Basin

The Brazilian Equatorial Margin is a dynamic region influenced by numerous physical factors. Winds, prominently easterlies and the seasonal shift of the Inter Tropical Convergence Zone (ITCZ), influence wind patterns and upper ocean parameters (Adam et al., 2016; Aguiar et al., 2022; Ruggiero, 2008; Schneider et al., 2014). The Intertropical Convergence Zone (ITCZ) moves between latitudes of 14°N to 2°S (Waliser and Gautier, 1993). So, during the boreal

winter and spring (i.e. DJF and MAM), winds blow predominantly from the northeast, while southeasterly winds are prevalent in the boreal summer and fall (i.e. JJA and SON) (Aguiar et al., 2022; Ruggiero, 2008). Tides, particularly the semidiurnal components, are dominant along the shelf, with M2 amplitudes reaching 1.75 m near 2° N (Fontes et al., 2008; Geyer et al., 1996). While, diurnal tidal constituents have smaller amplitudes of 0.06 to 0.08 m over the shelf (Nittrouer and DeMaster, 1996).

Surface and subsurface currents such as the North Brazil Current (NBC) and North Brazil Undercurrent (NBU) display seasonal variability. In the upper 300 m of the water column at 4°S, the NBC ranges from a maximum transport of 35 Sv (Sv= 1 million m³/s) in July and August to a minimum of 13 Sv in April and May (Johns et al., 1998). This current system can flow north westward or retroflect eastward, with retroflection more pronounced during boreal summer and fall (Garraffo et al., 2003; Johns et al., 1998).

The Amazon River's significant input discharges an average of 1.7×10^5 m³/s into the Equatorial Atlantic Ocean, with maximum flow reaching 2.2×10^5 m³/s in May and minimum flow around 1.05×10^5 m³/s in November (Milliman and Meade, 1983; Wright and Nittrouer, 1995). This plume affects salinity distribution and can be transported north westward by the North Brazilian Current (NBC) between 5°N and 10°N, especially from September to October (Lentz, 1995; Moller et al., 2010).

Climatic factors also play a role, with evidence from the Last Glacial Maximum (LGM) indicating increased precipitation in the Andes and changes in sediment transfer and deposition patterns across the South American continent and deep-sea fan (Baker and Fritz, 2015; Harris and Mix, 1999; Mason et al., 2019).

The present-day shore is characterized by a muddy coastline that spans nearly 1500 km from the Amazon River mouth to the Orinoco River (Anthony et al., 2010). This stretch gives rise to mangroves and wetland areas. These environments are distinctive features of a coast dominated by tides and fluvial inputs, receiving significant volume of sediment from the Amazon River, and being carried northward by the North Brazilian Current. The presence of deeper mud banks along the shelf significantly dissipates wave energy (Anthony et al., 2010).

The Offshore Amazon Basin, situated in the northwestern part of the Brazilian Equatorial Margin (*Figure 5.1*), covers an area of approximately 360,000 km² (Silva et al., 1999). Its general morphology consists of a depocenter in front of the Amazon River mouth, with sediment thickness reaching up to 9 km. The upper part of the basin comprises siliciclastic series associated with the massive volume of sediments imported from the Amazon River after the Transcontinental Amazon River Event (Cruz, 2018; Figueiredo et al., 2007). This event

marked a significant shift in the Amazon River's drainage pattern, expanding from only covering the coastal plain and adjacent craton to including a vast area that accounts for 60% of the South American continental surface. The timing of this sedimentation rate increase, corresponding to the onset of the Transcontinental Amazon River, is a subject of debate within the scientific community. Two main hypotheses have been proposed, depending on the data used. Studies based on continental data suggest a Plio-Pleistocene age for the onset of the Amazon River (Campbell, 2010; Campbell et al., 2006; Horbe et al., 2013; Latrubesse et al., 2010; Ribas et al., 2012; Rossetti et al., 2015, 2005), while studies utilising marine data indicate a late Miocene age for the same event (Damuth and Kumar, 1975; Dobson et al., 2001; Figueiredo et al., 2010, 2009; Gorini et al., 2014; Hoorn et al., 1995). However, the sediment influx does not occur simultaneously along the northwestern Brazilian Margin. Starting from the Amazon River mouth, the deltaic clinoforms extend along the shelf, stretching eastward and northward due to the influence of the North Brazilian Current (NBC), which affects the Amazon plume and allows a greater volume of sediments to migrate toward the northern part of the margin. In addition to the shelf region, the slope and basin are significantly affected by Amazonian sediments through the deep-sea fan and the canyon of the Amazon. Although the canyon does not align with the flow direction of the Amazon River, it is influenced by the NBC, resulting in a north-westward offset. In front of the canyon, the deep-sea fan spans approximately 380 km along the continental shelf and reaches depths ranging from 4600 to 4850 m.

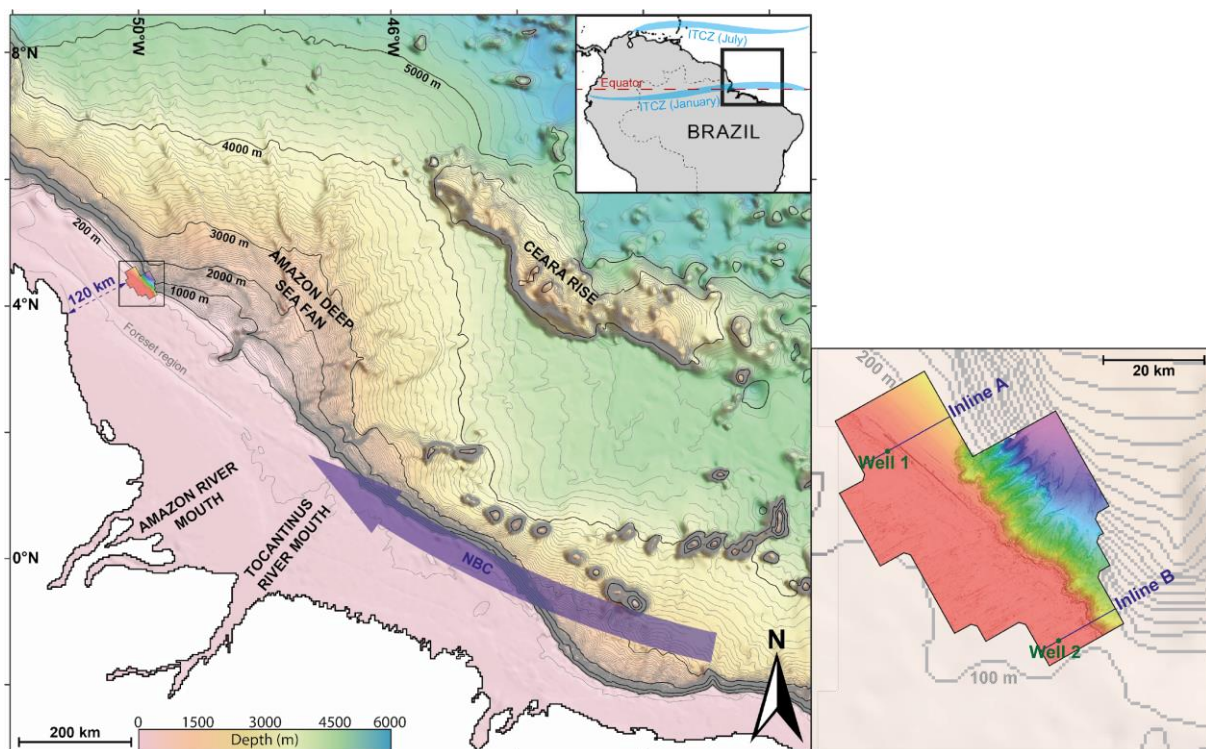


Figure 5.1: Bathymetric map of the NW Equatorial Brazilian Margin presenting the data used in this study. The 3D seismic block is shown with the seafloor horizon. The North Brazilian Current (NBC) is represented with a thick blue arrow. In the zoom box, two wells are noted in green and two inlines interpreted in figures 2 are in blue.

The seismic block (*Figure 5.1*), is located 200 km from the mouth of the Amazon River. In this region, carbonate growth of the Amapa carbonate series persisted for a longer period in the absence of sediments imported by the Amazon River (Cruz et al., 2019; Gorini et al., 2014; *Figure 5.2*). However, around 3.7 million years ago, the deltaic clinoforms of the Amazon River reached the study area (Cruz et al., 2019; Gorini et al., 2014; **Chapter 4**). The Plio-Pleistocene sedimentary series, primarily consisting of siliciclastic sediments from the Amazon, has been previously examined within the seismic block through a study that combined sequence stratigraphy and cyclostratigraphy (**Chapter 4**). *Figure 5.2* depicts two seismic lines crossing the 3D block and summarises the findings of this previous study (**Chapter 4**). Nine seismic sequences were identified and associated with 405 kyr cycles through cyclostratigraphy (Gorini et al., 2014; **Chapter 4**). By calibrating Gamma-Ray curves from three wells in the area, ages were determined for each seismic sequence. Furthermore, these sequences were classified into three mega-sequences based on their geometries (MS-I, MS-II, and MS-III). These mega-sequences were then linked to global climatic variations. MS-I corresponds to geometries with highly elongated bottomsets and low-dipping foresets. This period of time is corresponding with weak global sea-level amplitude variations between 3.65 Ma and 2.51 Ma (Miller et al., 2020). MS-II is characterised by foresets with steeper slopes and the presence of numerous erosive structures (landslides scars). This mega-sequence begins during the Intensification of Northern Hemisphere Glaciations (NHG; estimated at 2.51 Ma in the seismic block) and extends until 0.88 Ma. Finally, MS-III is marked by an increase in high angle foresets characterising forced regressions and a rapid shift of sediment deposit toward the slope. These variations have been attributed to the Mid-Pleistocene Transition (MPT; estimated at 0.88 Ma in the seismic block) and are coeval to an increase in global sea-level amplitude variations with a shift in the dominant climate cyclicity from predominantly obliquity-driven cycles (41 kyr) to eccentricity-driven cycles (95-125 kyr) (Berger and Loutre, 1994; Chalk et al., 2017; Clark et al., 2006; Piasias and Moore, 1981; Willeit et al., 2019).

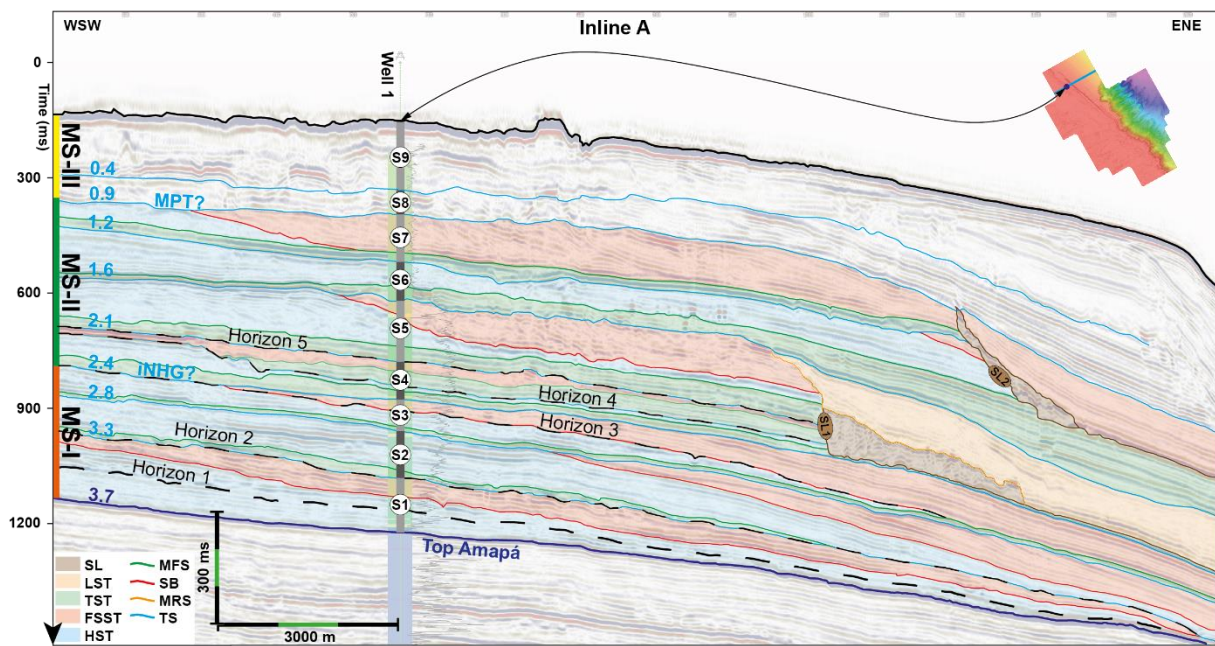


Figure 5.2: Sequence stratigraphy summary of the inline A (**Chapter 4**). Sequences S8 and S9 in the inline A are not detailed due to lack of data quality. Age of the seismic sequences (S1 to S9) boundaries (associated with the Transgressive Surface) are written on the left side of the inlines. Three Mega-Sequence (MS-I, MS-II and MS-III) encompass seismic sequences with geometrical similarities. Limits between each of this Mega-Sequence has been related to Earth climatic variation: NHG; intensification of Northern Hemisphere Glaciation at ~2.5 Ma and MPT; Mid-Pleistocene Transition at 1.2 to 0.7 Ma. The horizons presented in the next figures are localised along the Inline A with black dashed lines.

5.3. Data and methods

5.3.1. Seismic data

For sequence stratigraphy, we used a seismic 3D data block (BM-FZA-4/5 see Fig 1), which is approximately 60 km long and 40 km wide, covering an area of 1700 km². It is a PSTM (Pre-Stack Time Migration) survey composed of 2387 Inlines and 1733 Xlines separated by a 25-meter grid. The sample interval is 4 ms and the dominant frequency of the full-stack signal is 37 Hz, yielding a 10-20 m vertical resolution for velocity considered in between 1500 to 3000 m/s. The seismic block reaches 8900 ms Two Way Travel Time (TWTT).

The seismic block is located approximately 120 km from the closest coast. It covers the outer shelf and the upper slope of the northern Brazilian Equatorial Margin. Acquisition was done in water depth ranging from 80 to 1890 meters.

5.3.2. 3D seismic horizons creation

To gain a comprehensive understanding of the study area's evolution, specialised 3D seismic interpretation software, PALEOSCAN, was employed. A geo-model was constructed to obtain horizons rather than time slices. Prior to the geo-model's creation, fault sets were generated using PALEOSCAN's three-step automatic method. The initial step involved the generation of a variance seismic block, scanned to produce fault plane attributes. The second step entailed the filtering of extrema within the fault plane attribute block, referred to as fault thinning. The final step involved the extraction of faults from the fault thinning 3D block.

For the conception of the geo-model, a model grid is needed. The grid was established on the full seismic block using peak and trough picking at intervals of every 7 traces, and with a smoothing level of 7 pixels. The generated fault set was incorporated to prevent incorrect continuities during horizon propagation. The resulting model grid comprised an important number of patches (more than 60 000 000). PALEOSCAN's automatic interpretation was checked and refined to correct mis-propagations. However, the focus remained on the siliciclastic Plio-Pleistocene series of the block; older formations were not extensively refined beyond their main boundaries.

The automatic interpretation encountered difficulties around areas of landslides and slopes, where extensive deformation hindered the lateral continuity of reflectors. Additionally, in the upper part of the siliciclastic series, propagation inconsistencies occurred due to significant erosion along the shelf and poor data quality attributed to seismic processing that aimed to reach deep reservoir targets. Despite these challenges, manual checking and refining still employed automatic picking tools, as the dataset's size precluded fully manual picking. A horizon, consisting of a substantial number of points, enabled a resolution of ~25 meters. Select horizons were meticulously refined for use as examples of geomorphological features in the seismic block. Others, such as the boundaries of the siliciclastic series (Top of Amapá and Seafloor), were also refined to better constrain the model.

Ultimately, a geo-model was created using an interpolation size of 5 bins, a smooth size of 7 SMP, and a link probability of 2, constrained by faults. This geo-model generated 300 horizons between the Top of Amapá and the seafloor. These stacked horizons facilitated data navigation, supplementing Inline and Xline viewers and replacing the traditional time slice viewer. The approach revealed numerous structures, some of them are recurrent along the horizon stacks and the stack facilitated the observation of their cyclicity.

Attributes such as the Root Mean Square Amplitude (RMSA) and Contour Curvature were employed to improve our understanding of geomorphological evolution on the outer shelf. RMSA emphasised lateral lithological variations, thus aiding in the delineation of sandy structures like channels or canyon bottoms. Contour Curvature highlighted variations in horizon inclination. Additionally, signal deconvolution into various frequencies enhanced the definition of structural shapes. The processed images were presented in Red-Green-Blue visuals, enabling simultaneous observation of multiple frequencies. A flattening tool was also employed to better interpret structures by revealing their original shapes prior to the effects of subsidence.

For this study, five horizons within the seismic block have been carefully examined and are presented in *Figure 5.2*. These selected horizons serve as representative samples of the diverse geometries observed in the seismic block, encompassing all morphologies observed during MSs I and II.

5.4. Results

The construction of a horizon stack consisting of 300 seismic horizons enables an in-depth examination of potential 3D geomorphologies within the Plio-Pleistocene siliciclastic series. This horizon stack has been analysed using various attributes, such as RMS amplitude and contour curvature. Additionally, frequency filters targeting low, medium, and high frequencies—namely, 31, 39, and 50 Hz—were applied. Navigation through these 300 attribute-processed horizons reveals a temporal decrease in observable morphologies.

In the case of MS-I, a multitude of 3D structures are evident, with some horizons exhibiting shared geometries. These common geometries were correlated with similar environments, revealing a cyclical pattern in environmental variation. Conversely, MS-II features only a single dominant morphology and is further complicated by two substantial submarine landslides that remove significant portions of the outer shelf, thereby obstructing interpretation efforts.

MS-III, in contrast, does not present discernible 3D structures, except for carbonate reefs. These structures will be the focus of a separate scientific paper, as they do not directly pertain to coastal position. The absence of 3D structures in the upper intervals is attributed to decreasing data quality closer to the sea floor, a consequence of the seismic data being processed primarily for deep targets.

Subsequent chapters will present five selected horizons that encapsulate all the observed geomorphologies within MS-I and MS-II of the Plio-Pleistocene siliciclastic series, which range from 3.65 to 0.9 Ma (*Figure 5.2*). These horizons were extracted from the horizon stack

and underwent manual verification and refinement. The results are organised based on common geometries; hence, horizons 1 and 3 are discussed within the same chapter, as they both belong to the same seismic environment but exhibit minor variations.

5.4.1. 3D Geomorphologies along horizons 1 and 3

The most notable structures within the horizons 1 and 3 are channels oriented at N60°, perpendicular to the slope break and the present-day shoreline (*Figures 5.3 and 5.4*). Two types of channels have been identified. The first type (type 1) consists of straight channels with widths of approximately 800-1000 m within Horizon 1 (*Figure 5.3*) and around 250 m within Horizon 3 (*Figure 5.4*). These channels show minimal erosion, as indicated by an 18 ms Two Way Travel Time (TWTT; approximately 18m deep considering wave speed of 2km/s) between the base and the top of the channels. Their length varies from ten to thirty kilometers. In Horizon 1 (*Figure 5.3*), the southernmost channel exhibits smaller-scale structures within its bed (Internal features in Ch1). The channel section narrows towards the basin, and the structures dissipate before reaching the slope break (*Figures 5.3 and 5.4*).

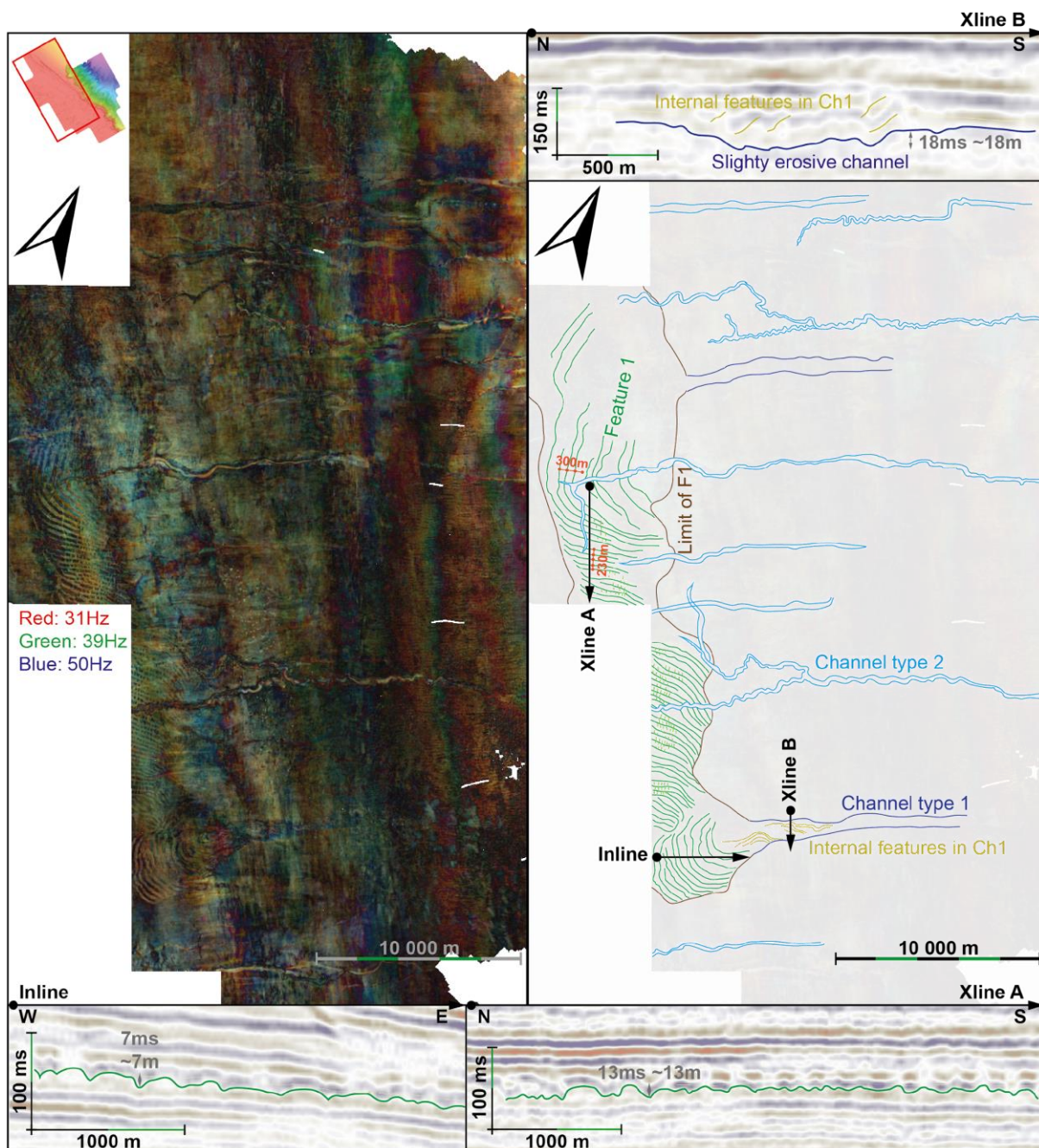


Figure 5.3: Seismic horizon 1 which is part of a Highstand System tract visualised from above with in the left panel the seismic data treated with a Red-Green-Blue frequency filter and on the right side, the interpretation of the main morphologies observed. Some seismic lines (Xline or Inline) are presented along the figures.

The termination point of the channels upstream is associated with other sedimentary structures. These structures (Features 1) form an arc around the channel terminations and exhibit troughs and crest topography specifically visible in the vertical 2D views (Figures 5.3 and 5.4). The amplitude of these undulations is approximately ten milliseconds TWTT (Xline A and Inline: Figure 5.3), and the distance between two crests varies between 200 and 300 m for Horizon 1 (Figure 5.3). The distance between crests also decreases further away from the

channels. These geometries extend over a restricted area (Limits of F1), parallel to the present-day coastline (N320°), with a width of eight kilometers in Horizon 1 (*Figure 5.3*). Within this zone, the orientation of crest lines varies significantly, but two patterns are observable. The crest lines tend to form semicircular structures around the upstream of the channels, and they tend to become tangential to the boundaries of the containing zone (Limits of F1) (*Figure 5.3*).

Similar trough and crest geometries are identified within Horizon 3 (*Figure 5.4*). However, they extend over a narrower zone (3 km), limited to a length of 9 km, still oriented around N320° (Limits of F1; *Figure 5.4*). The distance between two crests is approximately 120 meters within Horizon 3 (*Figure 5.4*). The height difference between top of crests and bottom of troughs is also reduced, around 2 ms TWTT (Xline and Inline: *Figure 5.4*). This value is close to the seismic resolution; however, the seismic amplitude also varies between the troughs and crests within the same reflector, allowing us to identify these structures.

Finally, a third type of structure is visible within the horizon 3 (*Figure 5.4*). These structures form upstream of the channels and are synchronous with them. They consist of reflectors inclined towards the mainland, forming clinoforms with a length of approximately a hundred meters and a height of around 50 ms TWTT (Features 2; *Figure 5.4*). These clinoforms develop into lobes at the outlet of the channels (towards the mainland). The reflectors inside these clinoforms have a greater amplitude than the surrounding area. These structures are shown only in Horizon 3 (*Figure 5.4*); however, they appear in other horizons of MS-I. These structures resemble the semicircular geometries observed upstream of the channels in Horizon 1 (*Figure 5.3*), but they are more deformed and exhibit a stronger seismic amplitude.

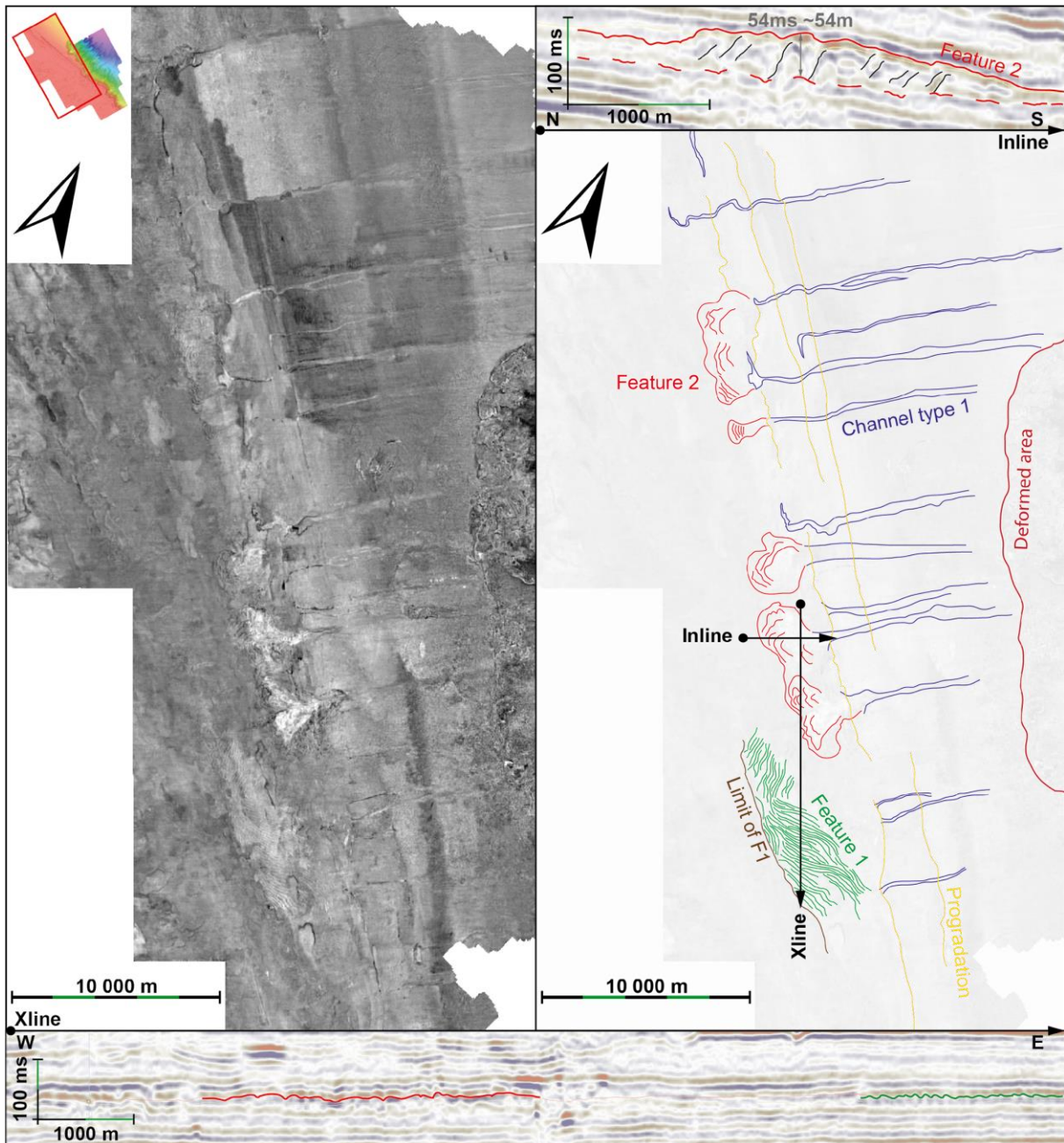


Figure 5.4: Seismic horizon 3 which is part of a Highstand System tract visualised from above with in the left panel the seismic data, in white positive amplitude and in black negative ones, on the right side, an interpretative scheme of the main morphologies is provided. Some seismic lines (Xline or Inline) are presented along the figures.

5.4.2. 3D Geomorphologies along horizon 2

The dominant geometry along Horizon 2, as observed in map view (Figure 5.5), consists of lineations oriented at N320°, which is parallel to the present-day coastline. The orientation of these structures changes as they extend toward the basin, shifting to N330° for the most distal lineations. Cross-sectional views (see Inline A, Figure 5.5) reveal that these lineations are, in

fact, strictly prograding clinoform boundaries. The width of these clinoforms ranges from 800 to 500 m, with the northern portion of the seismic block displaying wider clinoforms than the southern area. The height differential between the base (bottomsets) and the top (topsets) of a clinoform is approximately 25 ms in two-way travel time (TWTT).

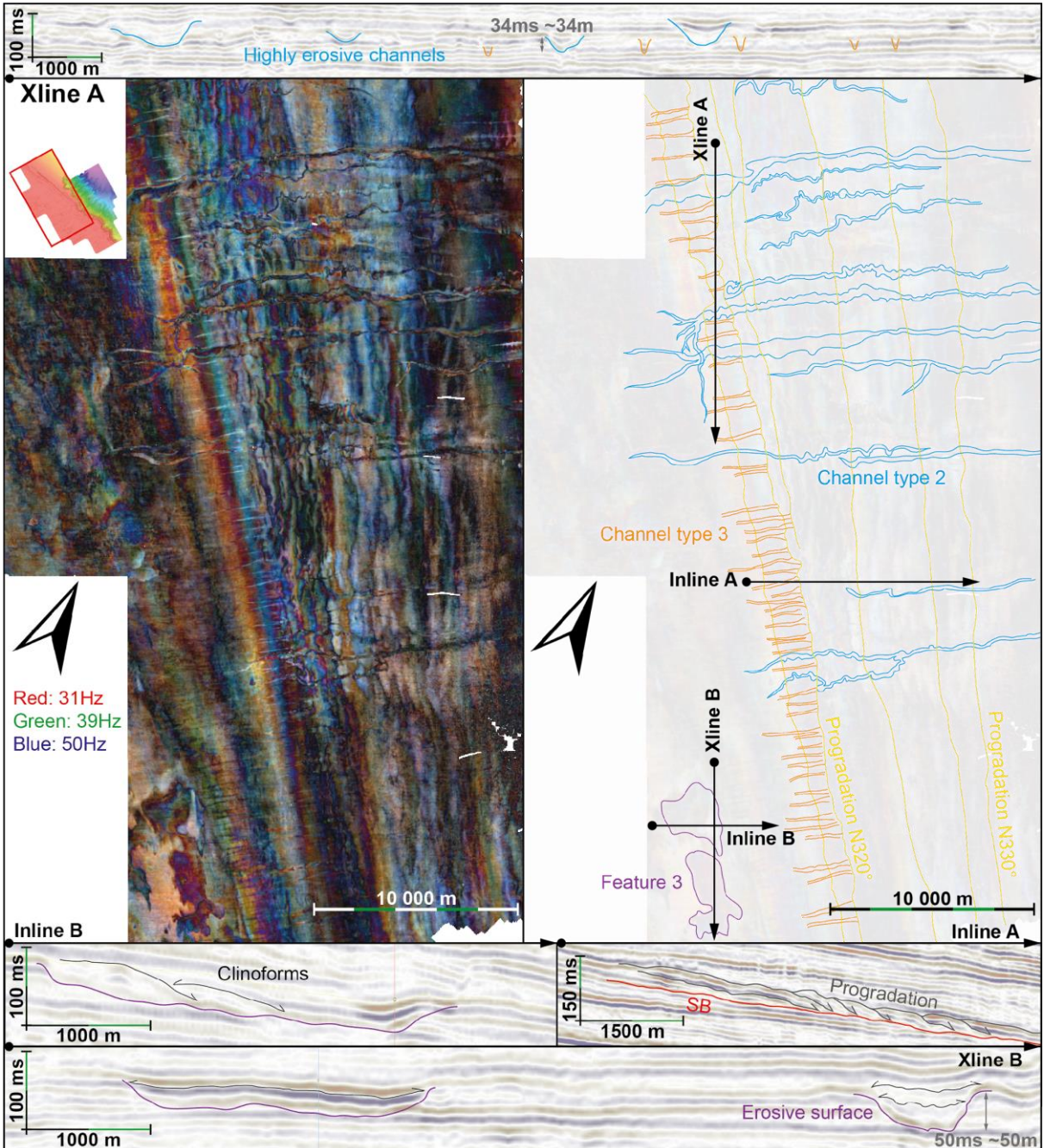


Figure 5.5: Seismic horizon 2 which is part of a Falling Stage System tract visualised from above with in the left panel the seismic data treated with a Red-Green-Blue frequency filter and on the right side, the interpretation of the main morphologies observed. Some seismic lines (Xline or Inline) are presented along the figures.

The second set of structures visible on Horizon 2 (*Figure 5.5*) comprises channels oriented at N60°, perpendicular to the present-day coastline. Two types of channels are observed: type 2 channels, which are highly meandering and erosive, and type 3 channels, which are rectilinear. Type 2 channels have an orientation of N60°, although their direction can drastically change near their upstream termination, sometimes exhibiting 90-degree turns. The length of type 2 channels is approximately 20 km, with a cross-sectional width of 200-300 m (*Figure 5.5*). The vertical difference between the base and the top of type 2 channels ranges from 25 to 50 ms TWTT. The surface area of type 2 channels decreases toward the basin and reaches a maximum where these channels intersect the first lineations oriented toward the continent. Notably, the frequency of channels with extensions of 10 to 30 km increases from 0-10 per horizon in Horizons 1 and 3 to 10-30 in Horizon 2 (*Figure 5.5*).

Type 3 channels display rectilinear geometries with lengths ranging from 2 to 4 km and widths around 100 m. The vertical difference between their base and top is around 5 ms TWTT (*Figure 5.5*). These channels are particularly abundant, spaced at intervals of approximately one kilometer. Their downstream terminations are abrupt and occur against the initial N320°-oriented progradations. Importantly, type 3 channels are observed only along the topsets of the first clinoform and are absent from subsequent clinoforms. This first clinoform is distinctive, being 2 to 3 km wide as opposed to subsequent clinoforms, which have an average width of less than one kilometer, and exhibiting a gentler slope (*Figure 5.5*).

The final set of structures observed in Horizon 2 are referred to as feature 2, which corresponds to depressions located in the most proximal (coastal) part of the seismic block, upstream of the progradations. These depressions are approximately 50 ms TWTT deep and filled with clinoforms that exhibit stronger seismic amplitudes than the surrounding reflectors. These structures are aligned along a N320° axis and have dimensions ranging from 2 to 4 km in width and 2 to 6 km in length (*Figure 5.5*).

5.4.3. 3D Geomorphologies along horizons 4 and 5

Horizons 4 and 5 disclose a principal structure denoted as Feature 4, which delineates the boundary between two seismic amplitude domains (*Figures 5.6 and 5.7*). In the proximal domain towards the southwest, the surface is flat and characterised by strong seismic amplitudes. In contrast, the distal domain towards the northeast comprises a highly eroded area associated with very low-amplitude reflectors (*Figure 5.6*). The eroded zone in the distal domain has lost approximately 57 ms TWTT of sedimentary deposits and is subsequently filled

by layers of continuous and subparallel reflectors with moderate amplitude. These reflectors exhibit onlap terminations towards the continent, consistent with a transgressive serie.

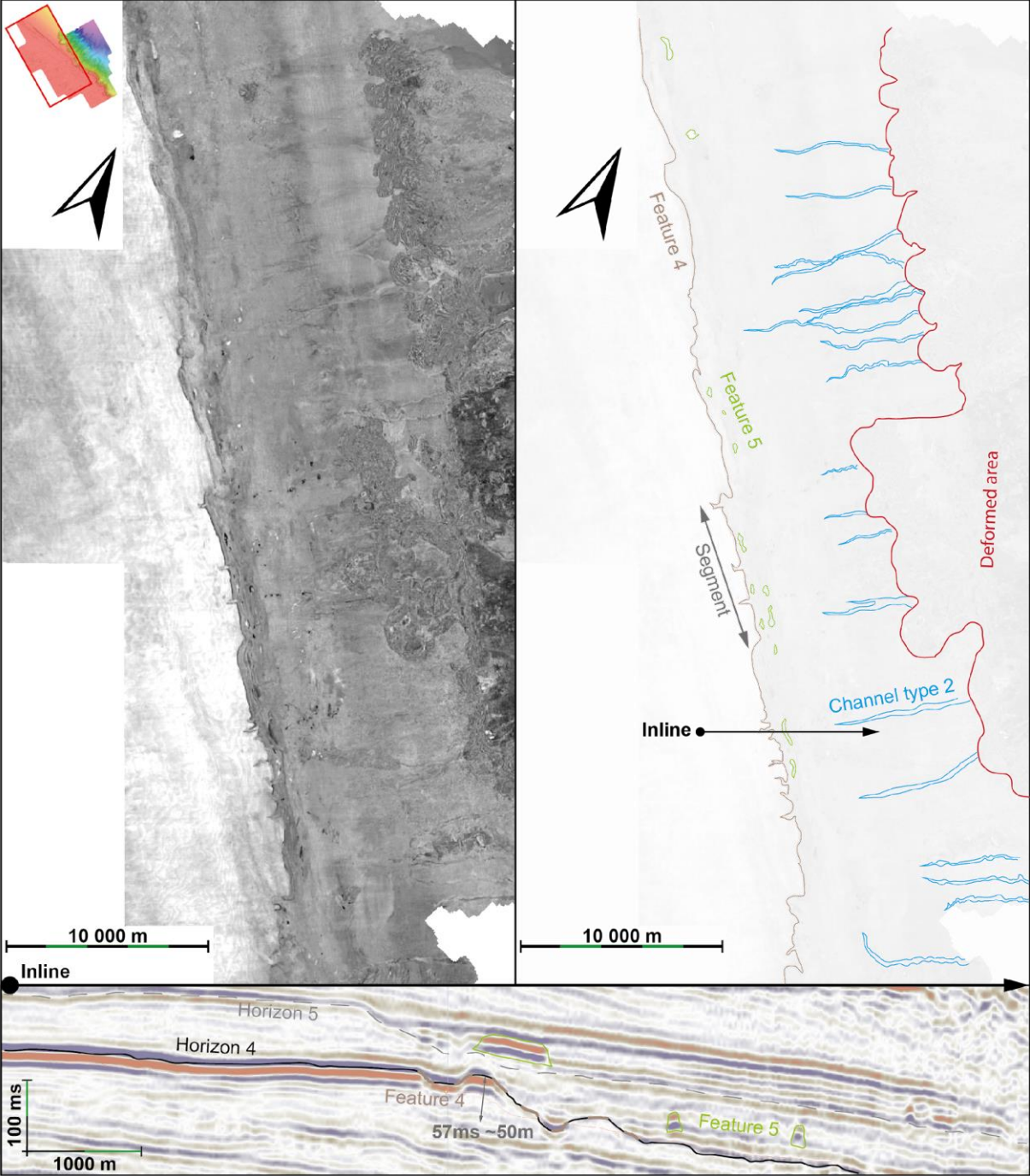


Figure 5.6: Seismic horizon 4 which is part of a Transgressive System tract visualised from above with in the left panel the seismic data, in white positive amplitude and in black negative ones, on the right side, an interpretative scheme of the main morphologies is provided. Some seismic lines (Xline or Inline) are presented along the figures.

Feature 4 is further marked by a significant slope change at the interface between the two amplitude domains, symbolising an erosive front. Viewed in map form, this feature

predominantly maintains a linear orientation of N320°, parallel to the present-day coastline. Despite its overall linearity, the structure is segmented with segment lengths ranging from 8 to 10 km and a limited offset of just a few hundred meters; the northern segment is consistently shifted eastward.

Horizon 5 shows a structure similar to Feature 4, but with less pronounced amplitude variations between the proximal and distal domains (*Figure 5.7*). The erosion affecting the distal area is also less severe, with a depth of 40 ms compared to the 57 ms in Horizon 4. Additionally, the boundary separating the proximal and distal domains is not perfectly linear, but rather displays semi-circular geometries with a diameter of 2000 m. The segmentation remains, although less noticeably, and the high-amplitude domain shows some eastward extensions with an orientation of N100°.

In the distal domain, at the base of the slope break, structures labelled as Feature 5 are less than 1000 m long and 100 m wide and display strong seismic amplitudes. These structures are components of a transgressive assemblage that fills the erosive embayment in Horizons 4 and 5. Feature 5 structures are asynchronous with Feature 4, but are visible in both horizons due to the intricate propagation of the seismic signals. Given that erosive features couldn't be solely mapped through individual reflectors, since erosion affects multiple older reflectors and there is no single reflector covering the entire eroded portion. Instead, multiple reflectors gradually onlap onto the erosive surface.

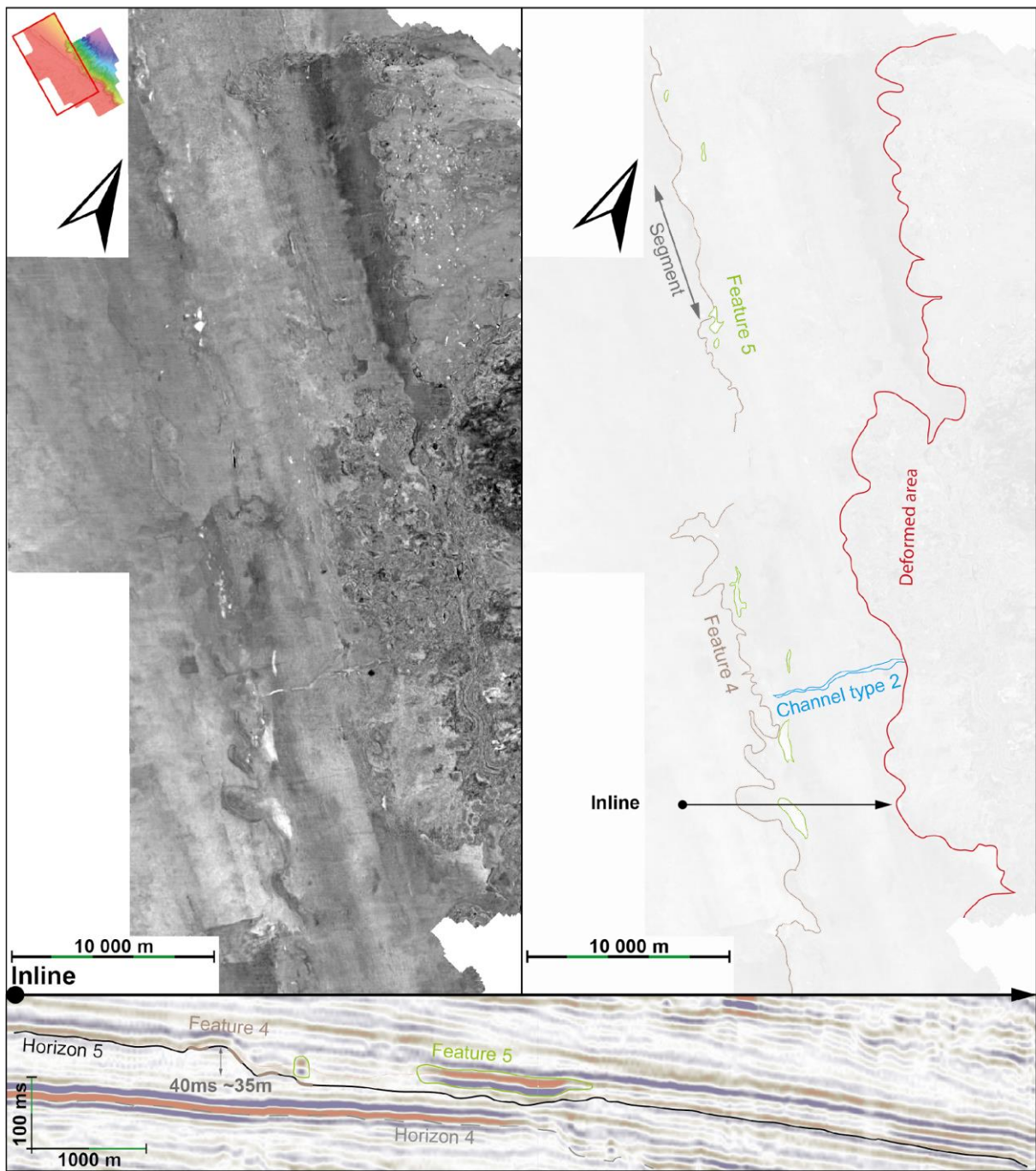


Figure 5.7: Seismic horizon 5 which is part of a Transgressive System tract visualised from above with in the left panel the seismic data, in white positive amplitude and in black negative ones, on the right side, an interpretative scheme of the main morphologies is provided. Some seismic lines (Xline or Inline) are presented along the figures.

5.5. Interpretation and Discussion

5.5.1. Barrier-Lagoon environment

Our observations of horizons 1 and 3, as depicted in *Figures 5.3 and 5.4*, reveal the presence of a sand ridge and/or barrier islands intersected by rectilinear channels (Channel type 1) establishing connections between the oceanic domain and a lagoonal area. These characteristics account for the relatively short lengths of channels, less than 30 km, and their significant widths, which can be attributed to substantial temporal shifts in channel positions. In Horizon 1 (*Figure 5.3*), sedimentary structures within the southernmost channel, resembling lateral accretion bars (Internal features in Ch1), suggest notable variations in channel direction. Erosive activity is notably restricted to the coastal barrier level, which aligns with the minimal erosion observed in Channel type 1. The channel inlet width in Horizon 1 (*Figure 5.3*) measures approximately one kilometer, aligning with typical inlet widths as outlined by Stutz and Pilkey (2011). The distance between the two channels in Horizon 1 (*Figure 5.3*) also approximates the average barrier island length in sub-tropical, wave-dominated settings (Stutz and Pilkey, 2011). Conversely, the dimensions of channels and the barrier island length in Horizon 3 (*Figure 5.4*) diverge from the typical barrier island morphologies described by Stutz and Pilkey (2011). This discrepancy is clarified through the investigation of additional features in Horizon 3 as explained in the next paragraph.

Horizon 3 (*Figure 5.4*) shows structures at the tip of channel terminations, facing the continent, distinguished by semi-circular forms with inclined reflectors (Feature 2). These features 2, are interpreted as washover fans, formed within the lagoon by wave action and disruption of prograding ridges and shoreline. An alternative hypothesis suggests the presence of a flood delta. However, the absence of deepening reflectors toward the ocean at the seaward channel ends is not in favour of an ebb delta, which is the complementary seaward part of the flood delta (De Swart and Zimmerman, 2009; FitzGerald, 1996). Consequently, washover fans serve as a better analogue. Thus, the channels in Horizon 3 are likely transient channels created during washover formation, and the coastline in this horizon represents a sand ridge rather than a barrier island (Pierce, 1970). This accounts for the channel dimensions not aligning with the inlet catalogue proposed by Stutz and Pilkey (2011).

Structures exhibiting trough and crest geometries within the lagoons are most likely subaqueous dunes resulting from currents induced by tidal or wave activities (Feature 1). These currents fill and empty the lagoon in a cyclical manner, explaining the observed alignment

between dune crest orientations and channel directions. Currents channelled through the inlets are likely to reconfigure the dunes into semi-circular formations around the channel mouths. Furthermore, the declining distance between successive dune crests farther from the channels correlates with a decrease in flow velocity due to available larger open space past the channel constrictions.

The lagoonal environment may be fully closed or partially open to the ocean, and subject to varying influences. Lagoons predominantly affected by tidal forces will manifest extensive flood and ebb deltas along with large tidal channels. Conversely, those under wave influence will predominantly feature washover fans. An analogue for the lagoonal environments observed in Horizons 1 and 3 is presented in Figure 8. This Analogue is from the North Carolina coastline (*Figure 5.8*). The east coast of the United States offers a variety of lagoonal and salt-marsh environments separated from the ocean by barrier islands or sand ridges (Lazarus and Armstrong, 2015; Sedgwick and Davis, 2003; Velasquez-Montoya et al., 2021). These environments could serve as analogues for the coastline along the Amazon Continental Margin during the times represented by Horizons 1 and 3, as well as other seismic horizons exhibiting similar geomorphic features.

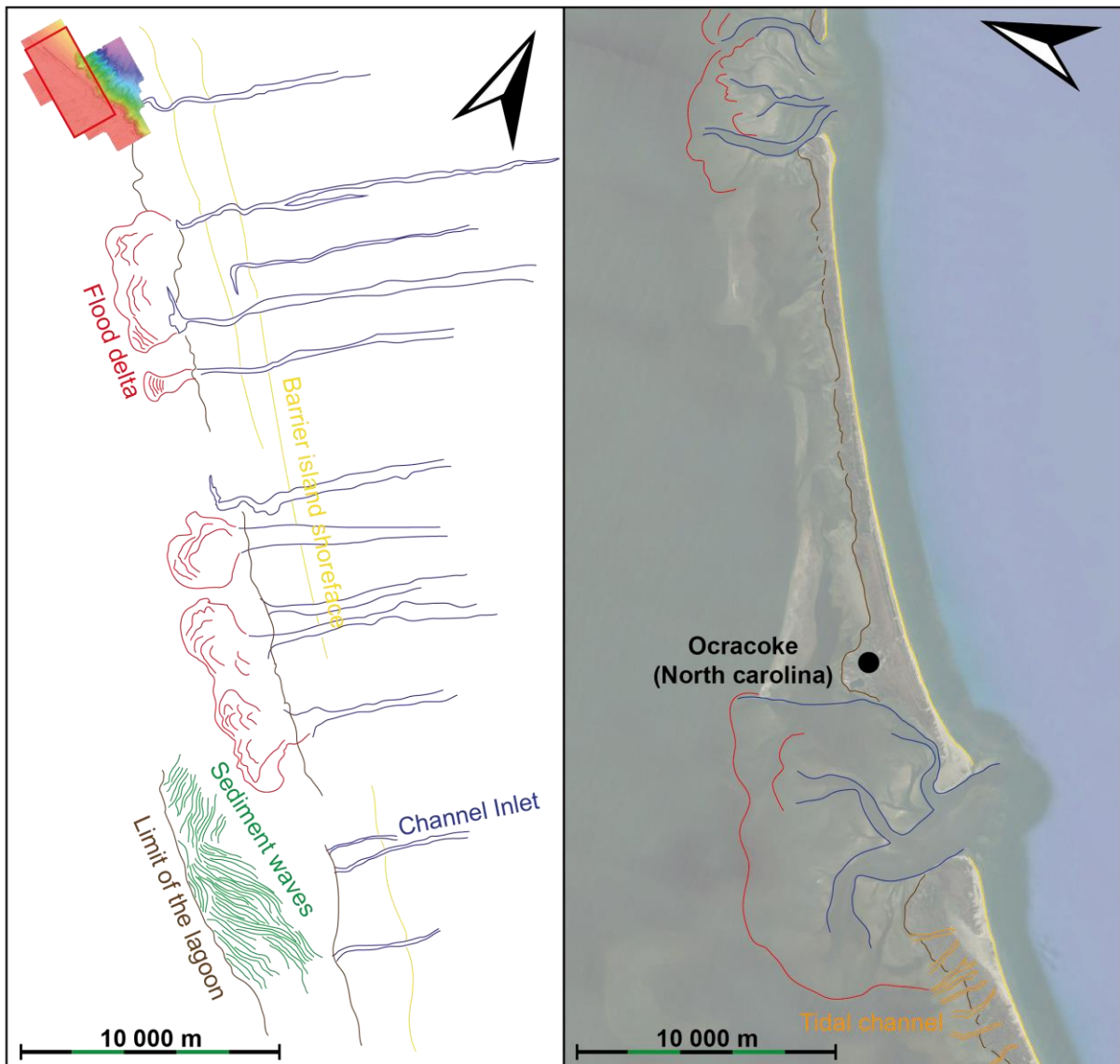


Figure 5.8: Satellite picture (google Earth courtesy) (on the right) of a potential analogue site in North Carolina, along the outer banks compared to the interpreted structures visualised in horizon 3 (on the left).

5.5.2. Strand Plain environment

Within Horizon 2 (Figure 5.5), we observe linear features running parallel to the current coastline, which we interpret as beach ridges resulting from a fall in sea level (noted Progradation in Figure 5.5). The spatial variation in the orientation of these ridges, along with their wider extension in the northern section, indicates that this area experiences a higher influx of sediments compared to its southern counterpart.

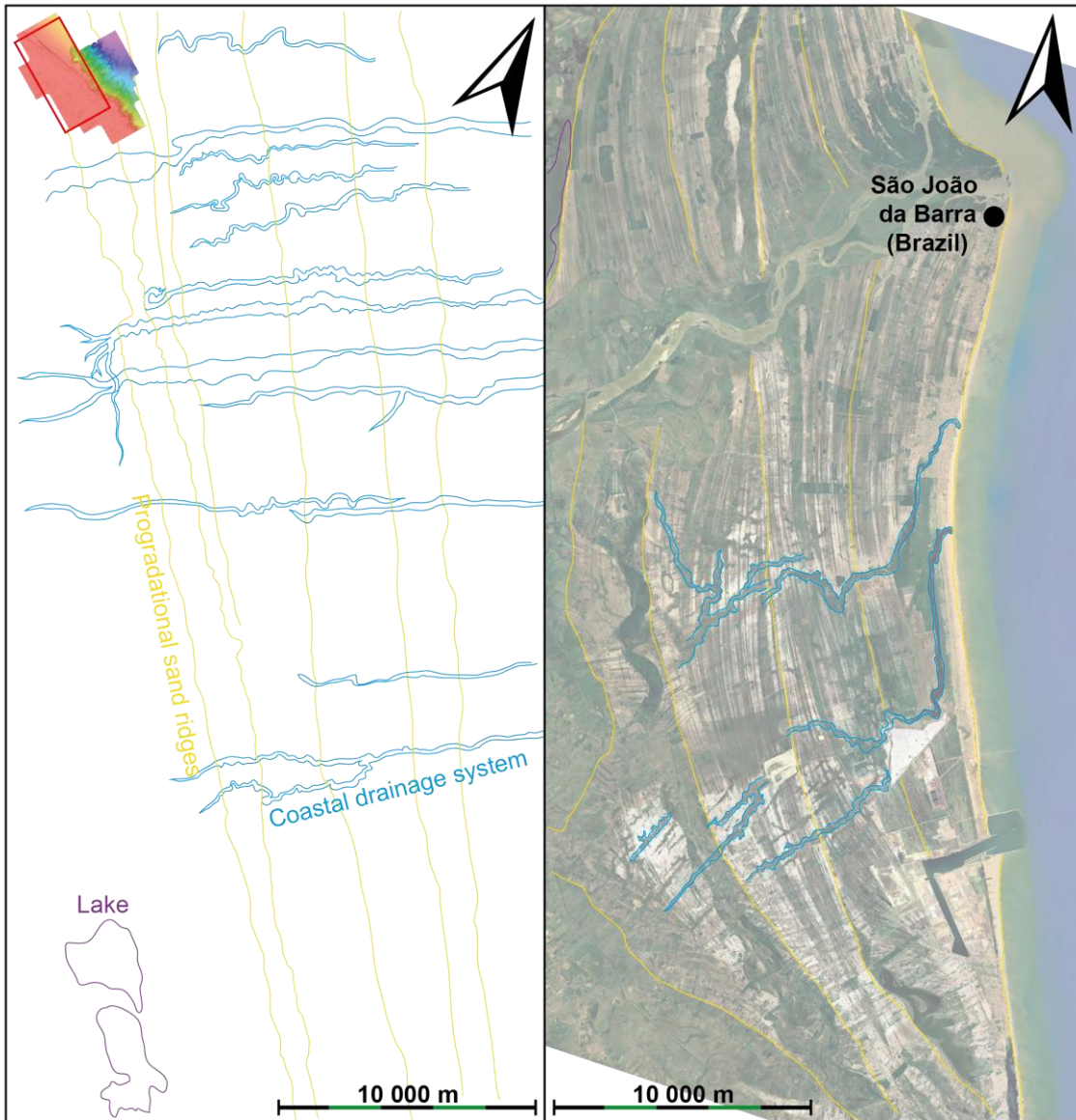
Channels intersecting the beach ridges perpendicularly exhibit significant erosion (Channel type 2, Figure 5.5), with their depths twice as great as those observed in the antecedent

lagoonal settings of horizons 1 and 3 (Channel type 1, *Figures 5.3 and 5.4*). This increased depth of incision supports the hypothesis of a sea-level fall, which naturally lowers the base level, leading to greater channel incision into the beach ridges. During these periods of declining sea-levels, these channels likely functioned as intermittent streams, draining only the coastal stranded plains formed by beach ridge progradation. Some channels, as illustrated in *Figure 5.5* (Channel type 2), undergo a 90-degree directional shift in their proximal segments, potentially representing drainage conduits situated either between or behind the beach ridges.

A specific category of channels (Channel type 3, *Figure 5.5*) is confined to the proximal region of the seismic block, a zone previously characterised by lagoons in horizons 1 and 3 (*Figures 5.3 and 5.4*). These channels are identified as tidal channels eroding the continental portion of the coastal barrier. The barrier, discernible in the seismic data of Horizon 2 (first progradation in the Inline A, *Figure 5.5*), stands as the most proximal progradational ridge, featuring a wider profile and gentler slope compared to subsequent ridges (Inline A, *Figure 5.5*). These morphological features validate the hypothesis of a shift in depositional environment, following the initiation of sea-level decline and ensuing beach ridge progradation, tidal influences on the lagoon cease, leading to the disappearance of these channels (Channel type 3). These channels exhibit a restricted erosive capacity, presumably unaffected by a lowering of the base level, and instead, they are potentially modulated by tidal-induced fluctuations in the lagoonal water levels.

The final features are depressions located in the proximal segment of the seismic block, aligning with former lagoon positions (Feature 3, *Figure 5.5*). These depressions are interpreted as lakes resulting from the desiccation of the lagoons that are progressively filled by sediments prograding from the continent.

Figure 5.9 presents an analogue situated at the mouth of the Rio Paraíba do Sul in the state of Rio de Janeiro (Carelli et al., 2018; da Rocha et al., 2013; Souza et al., 2022). da Rocha et al. (2013) indicate that the delta comprises a succession of regressive coastal barriers, which originated following the late Pleistocene interglacial maximum, approximately 80,000 years B.P. These barriers were likely shaped under falling sea-level conditions and possibly correspond with a substantial influx of ancient sediments from the Paraíba do Sul River, positioned to the south of its present mouth (da Rocha et al., 2013). A recent study reveals accelerated strand plain development over the last 450 years, attributable to enhanced sediment supply since the Little Ice Age (Souza et al., 2022).



Figure

5.9: Satellite picture (google Earth courtesy) (on the right) of a potential analogue site along the Rio de Janeiro state coastline in Brazil compared to the interpreted structures visible in Horizon 2 (on the left).

5.5.3. Abrasion coastline environment

The structures observed within Horizons 4 and 5, as illustrated in *Figures 5.6 and 5.7*, are interpreted as cliffs (Feature 4). In the proximal area, the high seismic amplitude zone is attributed to the alteration of sediments due to their exposure to subaerial conditions. In contrast, the distal area exhibits significant erosion, likely caused by wave action eroding several tens of meters of sedimentary deposits. Zones of elevated seismic amplitude in front of the cliffs are interpreted as beach rocks or carbonate buildups located at the base of the cliffs (Feature 5). This interpretation is supported by the observed seismic polarity inversions adjacent to these

structures. Carbonates are known to induce lateral variations in seismic amplitude, which, can lead to seismic polarity inversions.

Figure 5.10 provides an analogue for Horizons 4 and 5 based on the coastline of the Ceará state in northeastern Brazil. This coastline features a headland-beach-dune system characterised by sea cliffs formed under the continuous stress of unidirectional wind and wave activity (Claudino-Sales et al., 2018; Santos Jr et al., 2006; Vital et al., 2006). The morphodynamics of the Ceará coast are largely shaped by headlands, which disrupt the longshore sand transport upon contact, resulting in sediment accretion updrift of the headland and erosion downdrift (Claudino-Sales et al., 2018). The sea cliffs in this region exhibit significant relief, with heights ranging from 20 to 40 meters (Claudino-Sales et al., 2018; Santos Jr et al., 2006). Coastal erosion is notable along the Rio Grande do Norte coast and is mainly attributed to a decrease in fluvial sediment contribution and the formation of field dunes leading to sediment loss (Vital et al., 2006).

Additionally, coral reefs situated less than 5 km from the shore are documented along the coasts of Ceará and Bahia states (Carvalho and De Kikuchi, 2013; Galvão and Nolasco, 2013; Leão et al., 2016). These could correspond to the high-amplitude reflection patches with pronounced relief observed in the seismic block in front of the cliffs (Feature 5, *Figures 5.6 and 5.7*).

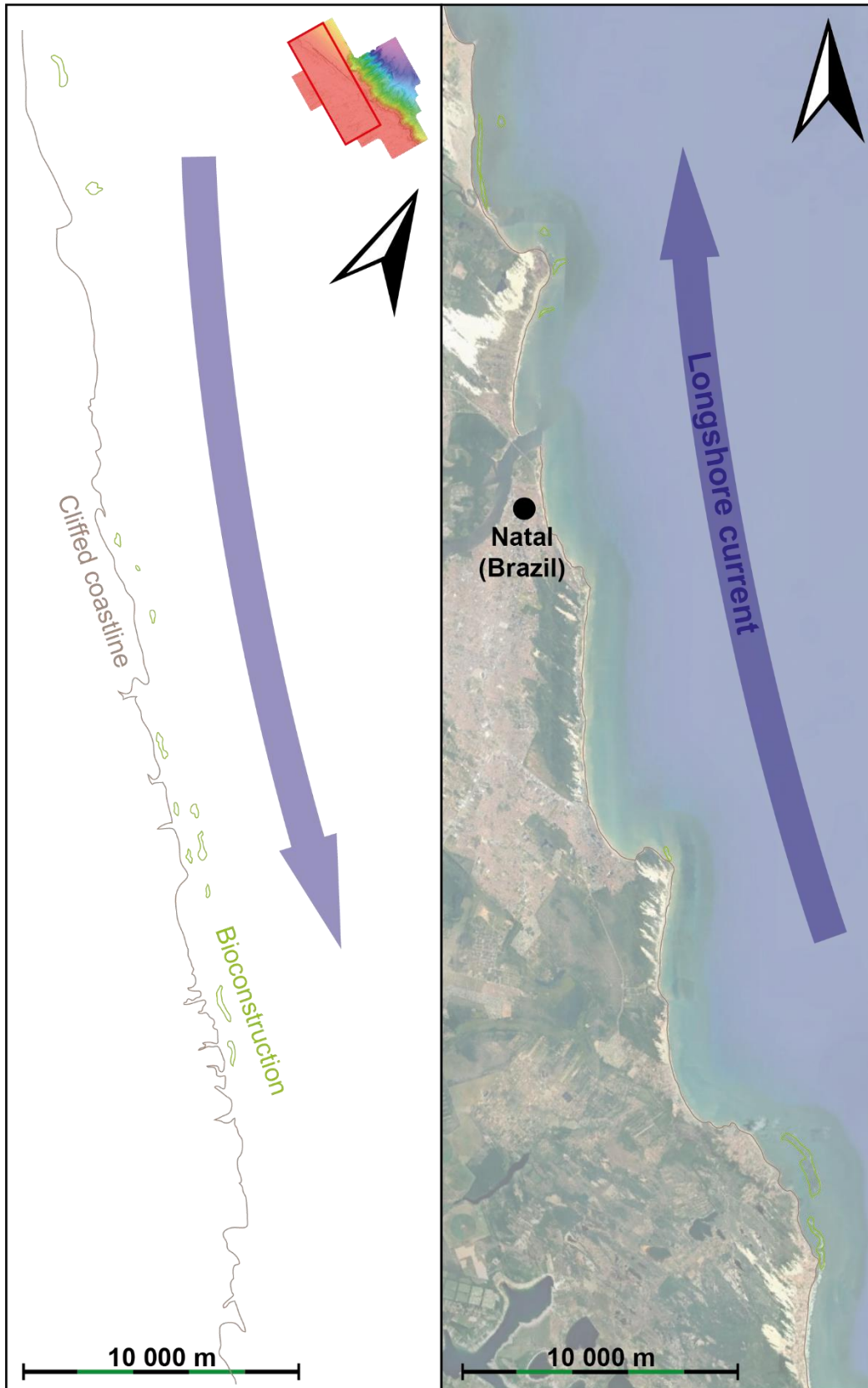


Figure 5.10: Satellite picture (google Earth courtesy) (on the right) of a potential analogue site along the Rio Grande Do Norte State coast in Brazil compared to interpreted structures of the Horizon 4 (on the left).

5.5.4. Shoreline record during exceptional lowstand

The examination of multiple horizons along the Brazilian Equatorial Margin has revealed coastal morphologies on the outer shelf (*Figure 5.11*). Such features have not been previously documented along the northern Brazilian Equatorial Margin for the Plio-Pleistocene period. However, similar formations of beach rocks dating from the Last Glacial Maximum have been observed along the French Guyana outer shelf by Giresse et al. (2022). Additionally, extensive reef systems attributed to the Last Glacial Maximum lowstand have also been documented along the Brazilian Equatorial margin (Banha et al., 2022; De Mahiques et al., 2019; Francini-Filho et al., 2018; Moura et al., 2016; Vale et al., 2018).

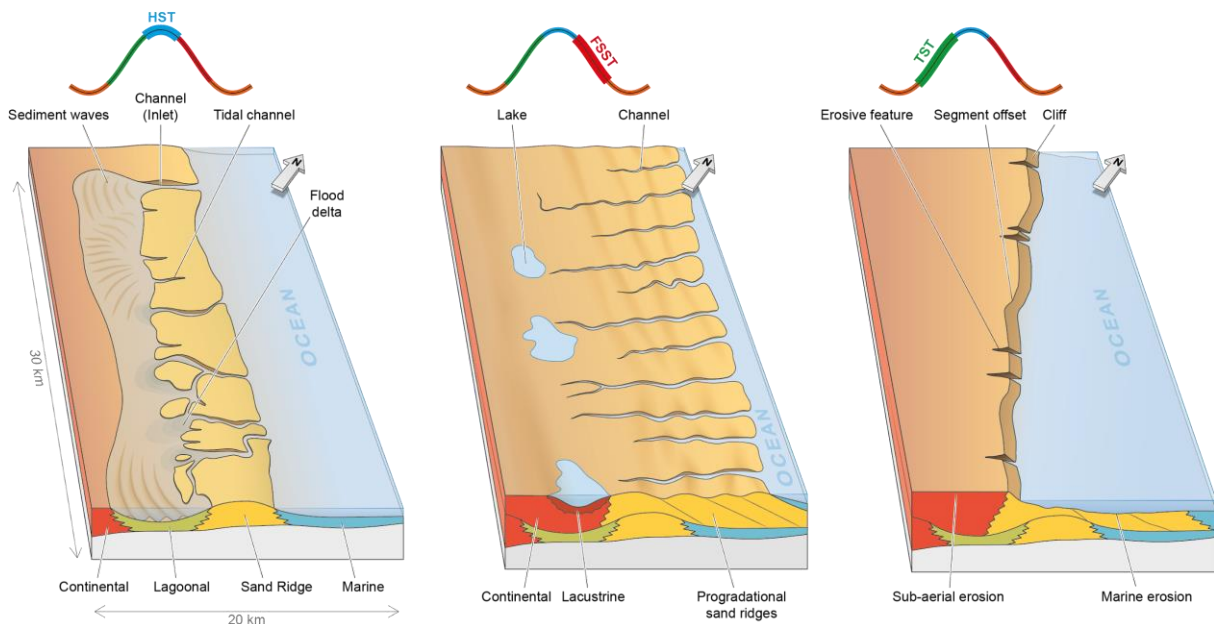


Figure 5.11: Simplified drawing of the different depositional environments related to each different system tract.

The geomorphologies observed exhibit cyclic variations, aligning with the seismic stratigraphic sequences interpreted in **Chapter 4**. These sequences are further correlated with the 405-kyr long eccentricity cycles (Gorini et al., 2014; **Chapter 4**), which are associated with significant sea-level falls during periods of low eccentricity (Miller et al., 2020). Consequently, the shoreline reaches the outer shelf exclusively during these extraordinary glacial lowstands in the Plio-Pleistocene. Additionally, increased sediment influx from the Amazon River during glacial intervals (Harris and Mix, 1999; Mason et al., 2019) enhances progradation rates, thereby enabling the coast to migrate toward the outer shelf.

The observed geomorphologies align closely with the classification of system tracts within the study area, as elaborated in **Chapter 4**. Progradational beach ridges that migrate basinward in downstepping patterns, as seen along Horizon 2, are associated with dramatic sea-

level falls (Taylor and Stone, 1996). In contrast, cliff geometries formed through retrogradational erosion by waves correspond to transgressive phases (Cattaneo and Steel, 2003; Curray, 1964). According to Curray's model (1964), the erosional domains identified along horizons 4 and 5 could represent ravinement surfaces, which evolve during periods of slow sea-level increase, allowing for more efficient erosion. On the other hand, rapid sea-level rises induce lower erosional potential due to rapid coastward migration (Cattaneo and Steel, 2003; Curray, 1964). The subsequent transgressive sediments that overlay these ravinement surfaces could be categorised as T-D: transgressive deposits situated above the wave ravinement surface in high-sediment supply settings (Cattaneo and Steel, 2003) also identified as the healing phase of Posamentier and Allen (1993). Considering their onlapping relationship with the underlying progradational phase, these deposits can be easily misinterpreted as lowstand deposits.

In general, lagoons (shallow coastal bodies of water) and barrier islands (long, narrow sandbars parallel to the shore) are usually associated with times when sea levels are either rising (transgressive) or remaining relatively stable (Friederichs et al., 2013; Green et al., 2013; Salzmann et al., 2013; Stutz and Pilkey, 2011). However, these morphologies are observed inside seismic units displaying sigmoid architecture associated with progradation and aggradation behaviour (**Chapter 4**). These characteristics suggest that considering seismic architecture, relative sea level is either stable or decreasing during the deposits of the lagoonal environment (Catuneanu, 2006). However, the formation of such lagoons may occur during short-lived episodes of sea-level rise associated with higher-frequency sea-level cycles which are not discernible in the seismic 2D architecture (Catuneanu, 2019).

The geomorphological patterns observed during cycles of sea-level fall align with findings concerning more recent sediments in southern Brazil (Hein et al., 2013). Specifically, Hein et al. (2013) described the evolution of depositional environments over the last 6 ka and noted the presence of a lagoonal environment around 3.3 ka. They attributed its formation to perturbations in the rate or direction of sea-level change, suggesting that a stable or slow rate of sea-level rise allows for the vertical accumulation of sediments on top of bars. This accumulation eventually leads to the emergence of subaerial barriers separated by multiple inlets and backed by a shallow lagoon. We also proposed a model for variations in depositional environments associated with sea level change along the Brazilian Equatorial margin in *figure 5.11*, based on our observations.

5.5.5. Change in the coastal current during Plio-Pleistocene Sea level falls

The observation of sea cliff morphology during low sea levels offers valuable insights into the paleocurrents that influenced the region. The segmentation and the general morphology and orientation of both paleo-cliffs at horizons 4 and 5 and sandspits at horizon 5 suggests a potential NW-SE current. Furthermore, the change in the orientation of progradation in horizon 2 implies a reduction in sediment supply towards the southern part of the study area possibly indicating the influence of a NW-SE current, transporting sediments from a river source distinct from the Amazon, or from a distinct distributary that would be situated to the north of the seismic block. These findings contrast with the present-day dominant current along the equatorial margin of Brazil, known as the North Brazil Current (NBC), which typically flows from SE to NW (Johns et al., 1998). This contrast highlights the significance of these paleocurrent observations and their impact on the formation of paleo-coasts in the region. Additionally, the absence of sedimentary deposits during the formation of paleo-cliffs suggests that sediment delivery from the Amazon does not extend to the study area, contributing to retrogressive erosion and the formation of the observed paleo-coasts via wave action (Cattaneo and Steel, 2003; Curray, 1964).

To understand this apparent shift in current direction, we analysed results from climate models that suggest a decrease in land temperature could weaken the Atlantic Meridional Overturning Circulation (AMOC) and drive the Intertropical Convergence Zone (ITCZ) southward (Lynch-Stieglitz et al., 2007). Such a shift would diminish the strength of the NBC while increasing the Brazilian Current (Nace et al., 2014), a phenomenon modelled for the Last Glacial Maximum (Chang et al., 2008). The seismic block observations suggest that this process could have happened multiple times throughout the Plio-Pleistocene, correlating with 405 kyr cycles. Specifically, morphologies indicative of a possible drastic alteration in current direction were observed at around ~3.3, ~2.4, ~2.1, and ~1.6 Ma (**Chapter 4**). Two hypotheses may explain this change, a global NBC inversion or a regional NBC alteration. The first one postulates a global inversion of the NBC's direction, and as already been modelled by Chang et al. (2008). However, given the NBC's pivotal role in mass and temperature exchanges between hemispheres, and its significant influence on the AMOC, the second hypothesis, less drastic is more plausible. Around latitudes 5 to 10 degrees North, the NBC bifurcates to form the Guyana Current, which continues along the South American coasts in a northwesterly direction, while a second branch generates the North Equatorial Countercurrent, flowing eastward towards the African coasts (Bourles et al., 1999; Dengler et al., 2004; Goes et al., 2005; Schott et al., 1995).

Should the ITCZ migrate southward, the NBC separation zone and eddies development area could reach the study site at 4° N, thereby altering coastal currents.

The observed variations in coastal currents play a crucial role in understanding the preservation of cliff structures documented in horizons 4 and 5. Typically, erosional features associated with sea-level rise are only discernible at the peak sea-level position, as prior features are eroded by wave action. However, in the seismic block, paleo-cliffs exhibit an exceptional preservation pattern. Initially, there is an absence of sediment deposition due to a change in current direction, which effectively disconnects the study area from the sediment influx originating from the Amazon. During this phase, the erosional features remain exposed. Subsequently, when the coastal current reverts to its contemporary SE-NW orientation, a significant volume of sediment from the Amazon is transported to the region. This sediment influx, in turn, leads to the preservation of these previously exposed features.

5.6. Conclusions

The study employs innovative horizon propagation techniques to analyse multiple horizons within a 3D seismic block located in the northern part of the Brazilian Equatorial Margin. The seismic block predominantly covers the outer shelf, and our research focuses on the progradation of siliciclastic sediments originating from the Amazon, which have been reaching the study area since 3.7 Ma. One notable finding is the presence of coastline morphologies extending more than 120 km from the coast during the upper Pliocene and lower Pleistocene periods. However, the progradation of the coastline to the outer shelf occurs only during particularly significant lowstands, which recur every 405 kyr in low eccentricity settings. High-frequency Sea level fluctuations, associated with obliquity, affect shoreline position along the inner shelf but do not lead to their advance to the outer shelf.

These morphological variations are closely linked to different System Tracts, which, in turn, correspond to sea level fluctuations. During the later stages of highstands, the outer shelf serves as a lagoonal environment, characterised by sediment waves within the lagoon, inlets and tidal channels. As sea levels rapidly decline, these lagoons become isolated from the ocean, eventually forming lakes at the former lagoon sites. Simultaneously, there is progradation of sand ridges towards the ocean. The subsequent drop in base level results in substantial erosion of these sand ridges. As sea levels begin to rise, wave action leads to the formation of cliffs along the outer shelf, and bioconstructions develop at the base of these cliffs.

The formation and preservation of these cliffs prompt a re-evaluation of coastal current dynamics. The various structures observed along the ancient coastline suggest the existence of

a longshore drift from north to south, along with longshore erosion, particularly towards the end of the sea level drop and mainly during the initial stages of the subsequent transgression. The extensive erosion indicated by cliff formation implies a lack of sediment input from the Amazon River into the area during the early phase of the transgression. However, the preservation of these cliffs, now buried beneath transgressive sediments, indicates the restoration of sediment transport during the transgression. This restoration of sediment delivery is concomitant with the renewed present-day south-to-north coastal current, known as the North Brazilian Current.

Declaration of interests

The authors declare that they have no known competing financial interests or personal relationships that could have appeared to influence the work reported in this paper.

Acknowledgments

This work was supported by the “Region Bretagne” as well as ISblue project: Interdisciplinary graduate School for the blue planet (ANR-17-EURE-0015) and co-funded by a grant from the French government under the program "Investissements d'Avenir" embedded in France 2030. This project was supported by the Region Bretagne and UMR6538 Geo-Ocean Joint Unit (CNRS, Univ Brest, Ifremer, Univ. Bretagne Sud). Lucas Tortarolo is a PhD student at “Université de Bretagne Occidentale (UBO, Univ Brest)” and Sorbonne University (SU) in France, and is in joint supervision with “Universidade Federal Fluminense (UFF)” in Brazil. This project is also a collaboration with the “Faculdade de Oceanografia” (UERJ) located in Brazil. Antonio Tadeu dos Reis also thanks “CNPq” and “FAPERJ” for the research grants (process #309779/2021-9 and process #200.427/2023, respectively). Cleverson Guizan Silva acknowledges “CNPq” for the research grant 311589/2022-7. Slah Boulila was supported by the French Agence Nationale de la Recherche (ANR-19-CE31-0002 AstroMeso), and the European Research Council (ERC) under the European Union’s Horizon 2020 Research and Innovation Program (Advanced Grant AstroGeo-885250).

This work employed Artificial Intelligence to correct and enhance the writing. The following prompt was utilised for this purpose: "Proofread my writing. Fix grammar and spelling mistakes. And make suggestions that will improve the clarity of my writing".

5.7. Supplementary contents

In this section, we present illustrative figures that depict typical coastal morphologies related to sea-level variation (*Figure S5.1*). We also include an exemplary representation of other morphological variations observed in the seismic records (*Figure S5.2*). We also provide a diagram that illustrates how the rate of sea-level rise influences sediment deposition during transgressive phases (*Figure S5.3*). Lastly, a diagram of the dynamics and evolution of headland-beach dune systems around the coastline of Brazil near Recife is presented in *Figure S5.4*.

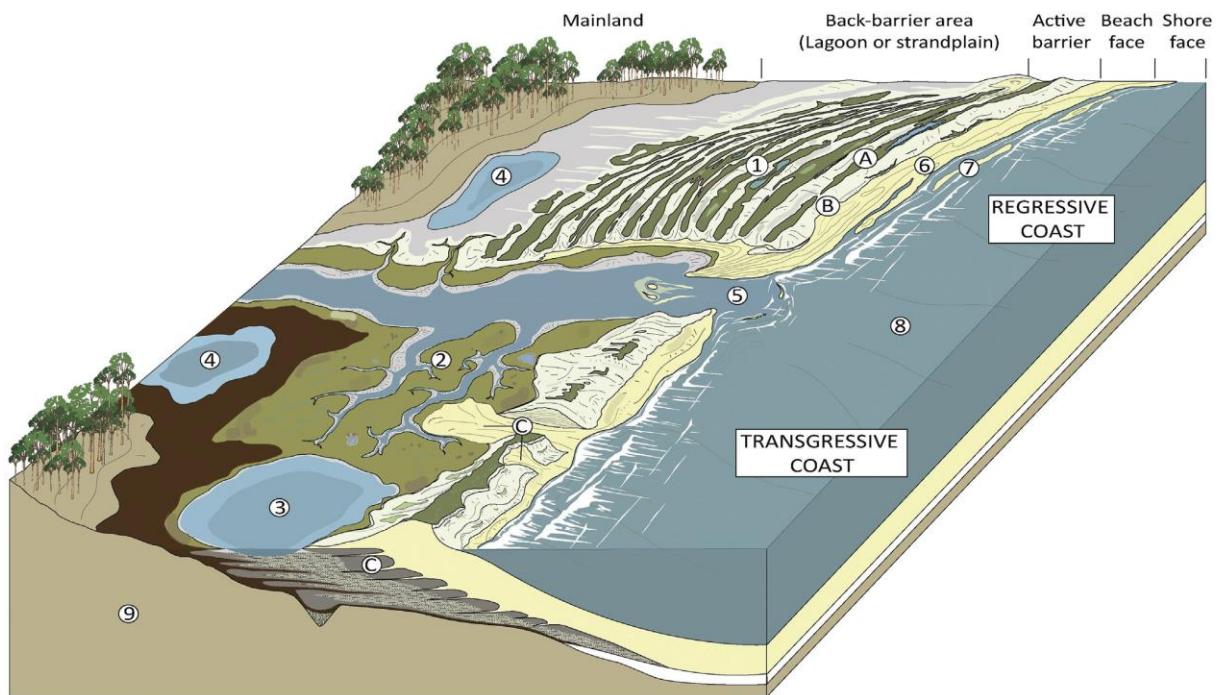


Figure S5.1: From Goslin and Clemmensen (2017): Schematic illustration of transgressive and regressive coastal barrier systems. Storm-wave induced markers are: A-Beach ridges, B-Storm scarps, C-Washover features. Coastal barrier sub-environments are: 1-Beach-ridge succession (strandplain); 2-Back-barrier lagoonal saltmarsh; 3-Brackish coastal mire; 4-Freshwater coastal lake, 5-Tidal inlet & flood/Ebb delta sedimentary features, 6-Beach berms, 7-Swash bars, 8-Shoreface, 9-Mainland/bedrock.

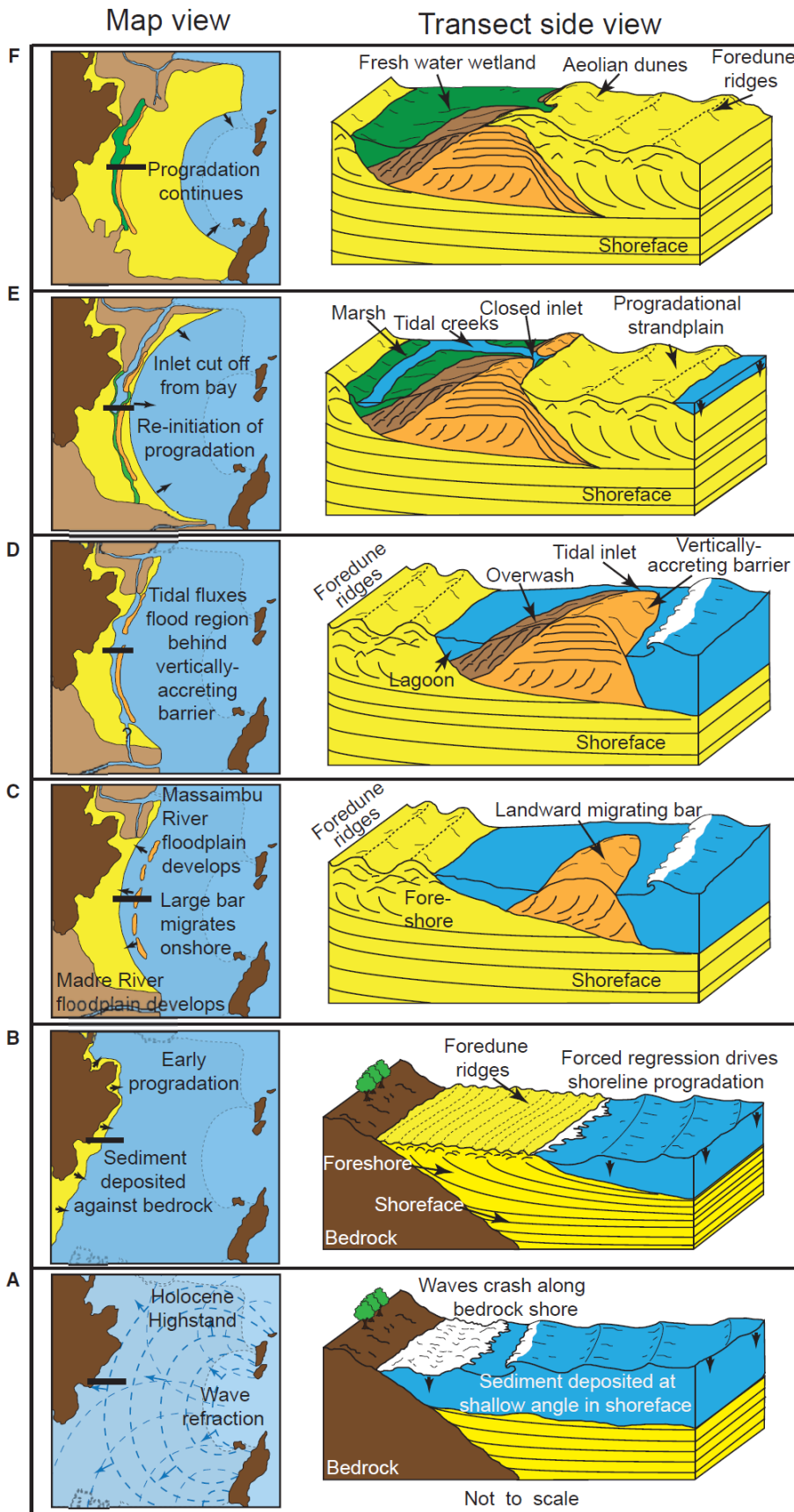


Figure S5.2: From Hein et al. (2013): Schematic six-stage evolutionary model of Pinheira (not to scale). Boxes on the left are all map views; righthand boxes are three-dimensional cross-sections of sections of the strandplain (locations shown as horizontal black bars in map views). Note the multiple changes in scale of transect side views throughout the progression as indicated by the black line in map views. (A) 6 to 5 ka: Sea-level highstand at Pinheira. Waves crash on the bedrock that forms the landward side of Pinheira while fine sediment, derived from the nearby Made and Massiambu River systems, is deposited in the nearshore zone. (B) 5 to 3.3 ka: Early progradation in the form of a normal regression. A large offshore sediment supply allows for the development of shallow offshore-dipping beds. As sea-level fall begins, the system transitions into steeper-dipping, offlapping beds typical of forced regression. (C) >3.3 ka: Onshore migration of a large quantity of sand as multiple intertidal bars due to perturbation in the rate or direction of sea-level change. (D) ca 3.3 ka: Slowly rising or stable sea-level allows for vertical accretion of sediments on top of bars, forming subaerial barriers, separated by multiple inlets, and backed by a shallow lagoon. The lagoon drains through a 250 m wide inlet in the barrier and probably is also connected to both the Madre and Massiambu drainage systems. Either a small rise in sea-level or a storm event results in overwash and the deposition of a washover unit in the backbarrier. (E) <3.3 ka: Sea-level fall reinitiates shoreline progradation. The seaward side of the barrier transitions into a progradational beach ridge/foredune ridge plain. The central inlet is filled with shoreface and/or foreshore sands and then closes as a result of falling sea-level and reduction in tidal prism. The lagoon begins closing and filling with both fine sand and marsh; drainage is primarily to the north. (F) ca 1 ka: Late stage progradation. The northernmost reaches of the lagoon continue to drain out through a small tributary to the Massiambu River. The remainder of the lagoon transitions into a lowland fresh water marsh. The palaeo-barrier has since been covered by an aeolian dune that nucleated upon the high-profile barrier feature.

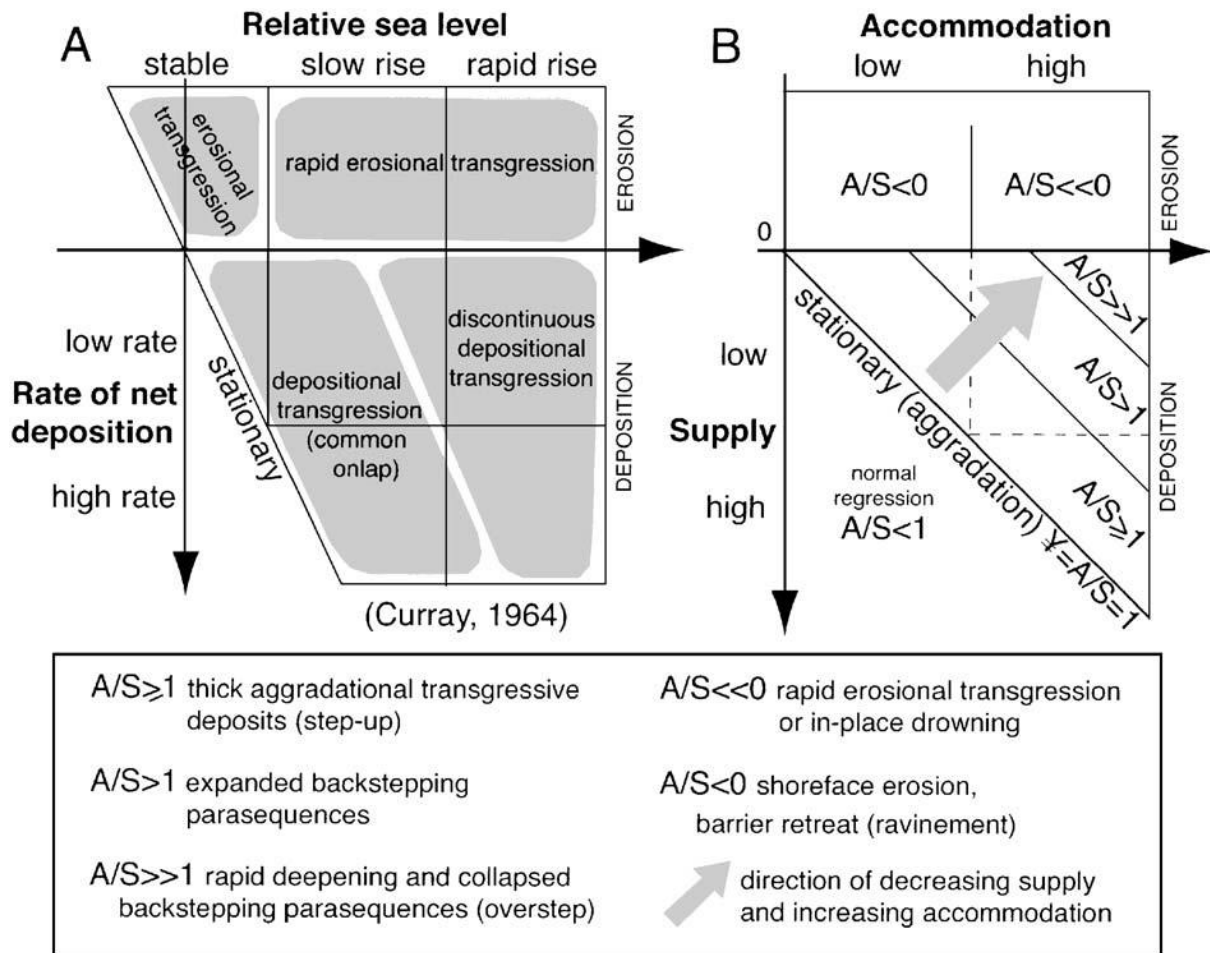


Figure S5.3: From Cattaneo and Steel (2002): (A) Transgressive part of the transgression– regression diagram of Curray (1964). (B) Revised version of the diagram. Depositional regime w (as defined by Thorne and Swift, 1991) is expressed as the accommodation– supply ratio (A/S). See text for discussion.

Evolution of Headland-Beach-Dune System

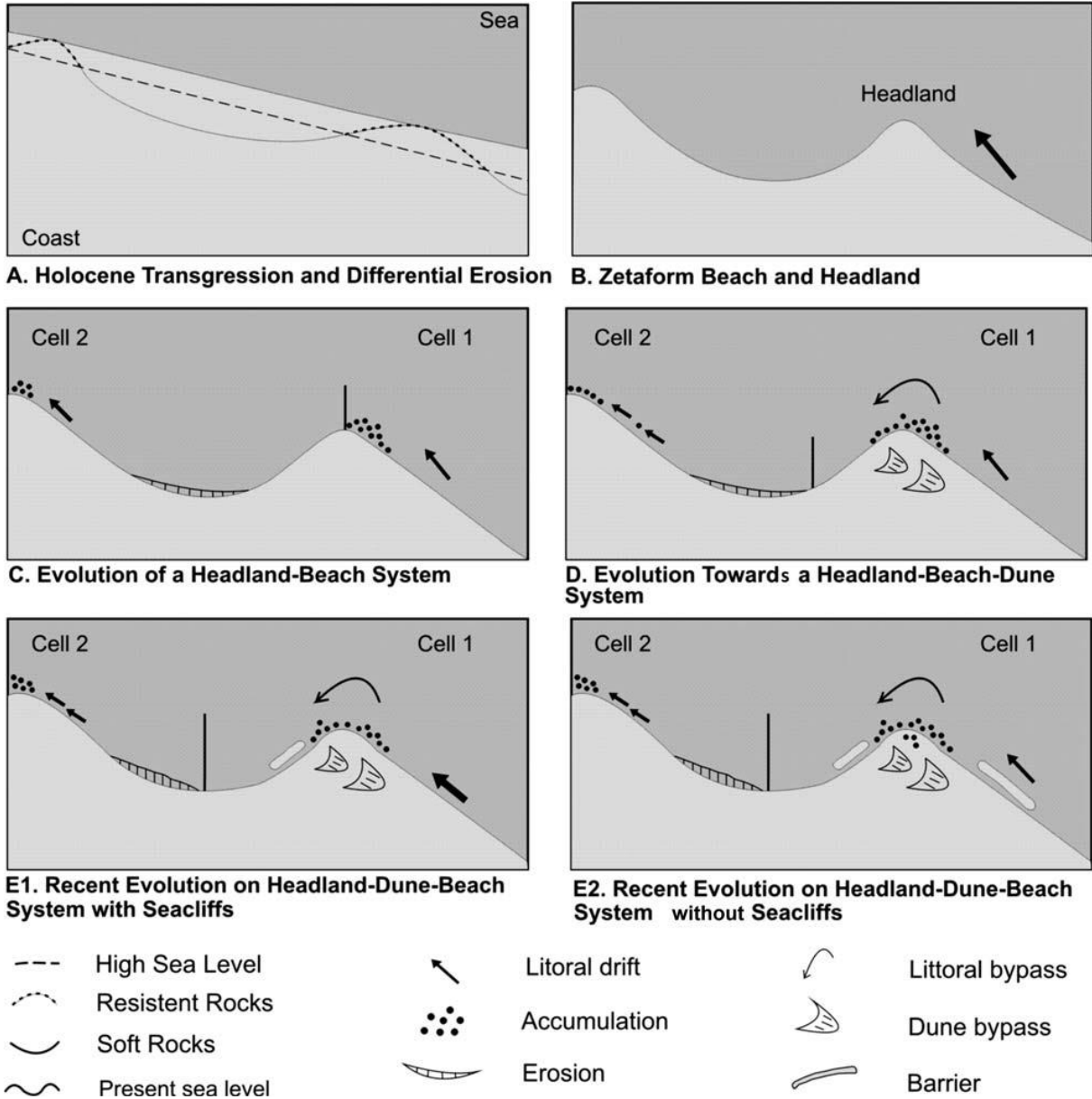
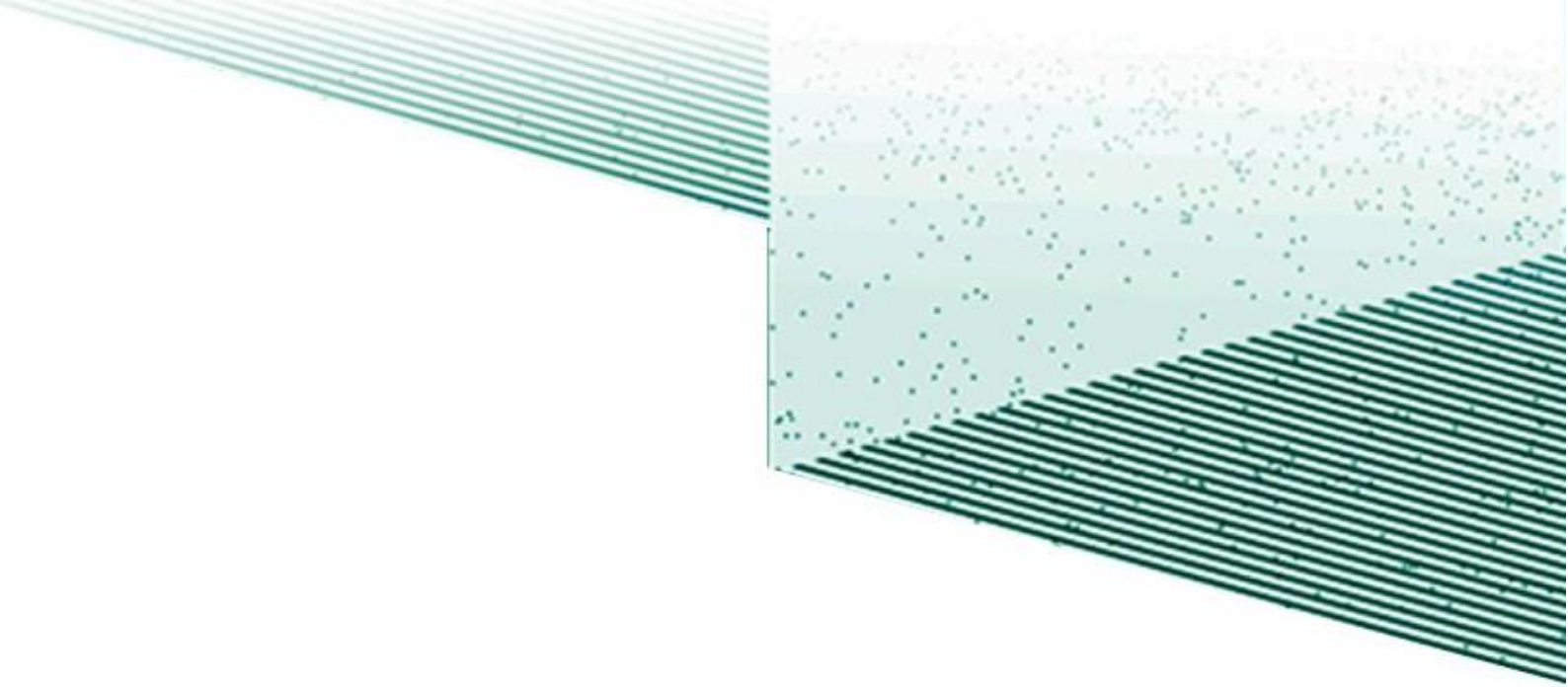


Figure S5.4: From Claudino-Sales et al. (2018): Illustration of the dynamics and evolution of headland-beach dune systems.



**Chapter 6: Cyclic growth of
the Amazon Reef System
during the last 2.5 Ma.**

Cyclic growth of the Amazon Reef System during the last 2.5 Ma.

Final version of a scientific paper intended for submission to Nature, Science or Geology.

Lucas Tortarolo^{a,b,c}, André W. Droxler^d, Marina Rabineau^a, Chrisian Gorini^b, Antonio Tadeu Dos Reis^e, Damien Do Couto^b, Slah Boulila^b, Cleverson Guizan Silva^d

^a Laboratoire Geo-Océan, Institut Universitaire Européen de la Mer, UBO, UBS, IFREMER, CNRS, UMR6538, Rue Dumont d'Urville, 29280 Plouzané, France

^b Institut des Sciences de la Terre Paris (ISTEP), Sorbonne Université, CNRS, UMR 7193, 4 Pl. Jussieu, 75005 Paris, France

^c Departamento de Geologia e Geofísica, Universidade Federal Fluminense, Av. Gal. Milton Tavares de Souza, Campus da Praia Vermelha, Boa Viagem, Niterói, RJ, Brazil

^d Department of Earth, Environmental and Planetary Sciences, Rice University, 6100 Main St., Houston, TX 77005, USA

^e Departamento de Oceanografia Geológica, Universidade do Estado do Rio de Janeiro, Rua São Francisco Xavier, 524, Rio de Janeiro, RJ, Brazil

corresponding author: lucas.tortarolo@univ-brest.fr

Abstract

Since the 1970s, the potential existence of a carbonate biogenic reef along the Amazon Continental Margin (ACM) has been a subject of scientific speculation. However, conclusive evidence of reefal organisms, including black corals, sponges, and red algae, was only observed in 2016, leading to the term "Great Amazon Reef System" (GARS). This discovery sparked a lively debate among scientists and policy makers regarding the reef size, in terms of its thickness and extent, and its overall characteristics, particularly in the context of establishing, along the ACM shelf edge, a marine protected area, excluding future oil and gas exploration. Our study is based upon a 3D high-resolution seismic block analysis from the north-western ACM and reveals both present and ancient sea floor features, thus tracing back in time the GARS's geological development. In the study area, we observe a modern sea floor relief measuring 26 km in length, 1 km in width, and 50 m in height. Sub-sea floor seismic data indicates that similar carbonate structures have existed since the early Quaternary, or the last ~ 2.5 million years ago, with a distinguishable 405,000-year cyclic growth pattern. The oldest phases are expressed by low-relief small patch reefs, less than 1 km² in surface area, whereas

younger phases exhibited barrier-reef-like edifices, similar in size to the present-day ridge, observed on the seafloor. Our findings suggest that cyclic intensification of Northern Hemisphere Glaciation, since approximately 2.6 Ma, has influenced sea level variations, thereby facilitating reef development along the ACM. During long low-eccentricity 405,000-year cycles, more extreme sea level lowstands channelled, through canyons, the Amazon sedimentary plumes into the adjacent deep basins, reducing, therefore, the turbidity along the shelf edge and, consequently, enhancing the reef growth, especially during the initial deglacial sea level rises. Starting from the Mid-Brunhes Transition, these conditions have occurred at a higher frequency of approximately 100,000 years. During the middle deglaciation phases, the reefs, incapable of adapting to rapid sea level rises, became overgrown by slow-growing black corals, sponges, and red algae.

Keywords: Quaternary, seismic and sequence stratigraphy, sea level, carbonate, Great Amazon Reef System (GARS), super-interglacial stages, Marine Isotopic Stage 11, 3D seismic geomorphology.

6.1. The Amazon Reef System

The Amazon is the largest river on Earth by water discharge and has a sediment flux at its mouth in the order of $1.2 \cdot 10^9$ metric tons per year (Meade et al., 1985). This massive volume of sediments is presently, either deposited along the inner shelf or deflected north-westward by the North Brazilian Current (NBC). Silico-clastic sediments, therefore, greatly increase the turbidity of the water and tend to bury the potential carbonates fraction. Unexpectedly in spite of those conditions, an extensive neritic carbonate reef system occurs along the shelf edge of the Amazon Continental Margin (ACM). The occurrence of a reef system was already suggested in the 70's with the work of Kempf (1970) and Milliman et al. (1975), and reef-associated species of fish and sponges were observed by Colette and Rützler (1977) and Moura et al. (1999). More recently, a dedicated survey of the Amazon shelf edge itself revealed the composition of the Amazon reef system and its geographical extent (Moura et al., 2016). Several subsequent studies have demonstrated the presence of diverse reef-associated living organisms along the entire shelf edge margin in a depth range from 70 to 220 m water-depth (Banha et al., 2022; De Mahiques et al., 2019; Francini-Filho et al., 2018; Vale et al., 2018). Based on these findings, it has been concluded that this reef system is, therefore, still active today despite its important water-depth (Banha et al., 2022; De Mahiques et al., 2019; Francini-Filho et al., 2018; Moura et al., 2016; Vale et al., 2018). Black corals, sponges, and red algae

are currently the main bio constructor of the reef system (De Mahiques et al., 2019; Francini-Filho et al., 2018; Moura et al., 2016; Vale et al., 2022, 2018).

Once the existence of the Amazon Reef System was demonstrated over the last decade, hydrocarbon exploration and production were significantly reduced along the ACM, triggering controversies regarding the geographical extent and age of the reef system. With regard to geographical extent, Moura et al. (2016) firstly proposed for the Amazon Reef System an overall surface area of more than 9,500 km² (*Figure 6.1*). Subsequently, Francini-Filho et al. (2018) increased by a factor five the surface area occupied by the living reef, estimating that the Amazon Reef System covers about 56 000 km² (*Figure 6.1*). On the contrary, dos Santos Filho et al. (2022), based on bathymetric, surface sediments and 2D seismic reflection data, reduced the size of the reef system to 13,478 km² (*Figure 6.1*). With regard to the age, Milliman and Barretto (1975) suggested that the reef system along the Amazon shelf edge established itself during the Last Glacial Maximum (LGM) and grew since. Vale et al. (2022) proposed more precise ages for the bioconstruction observed in the northern part of the ACM, along the shelf edge, confirming the establishment and subsequent growth of the reef during the last glacial sea level lowstand as defined by Yokoyama et al. (2018). Moreover, Vale et al. (2022) also show that active organisms colonise the observed high-relief structures and, therefore, these structures have developed for a certain time up to present-day.

This study focuses on the evolution of the carbonate sedimentation along the ACM, back in time, based upon a 3D high-resolution seismic block that allows not only the exploration of the present-day seafloor morphology, but, most importantly, the buried geomorphology beneath the seafloor. The study attempts to answer specific questions such as: is the present-day reef, observed along the Amazon shelf edge, unique to the last glacial and subsequent deglaciation or did similar reefs grow also during previous glacial sea level lowstands? Which mechanisms allow the development of carbonate structures and why are they limited to the outer shelf?

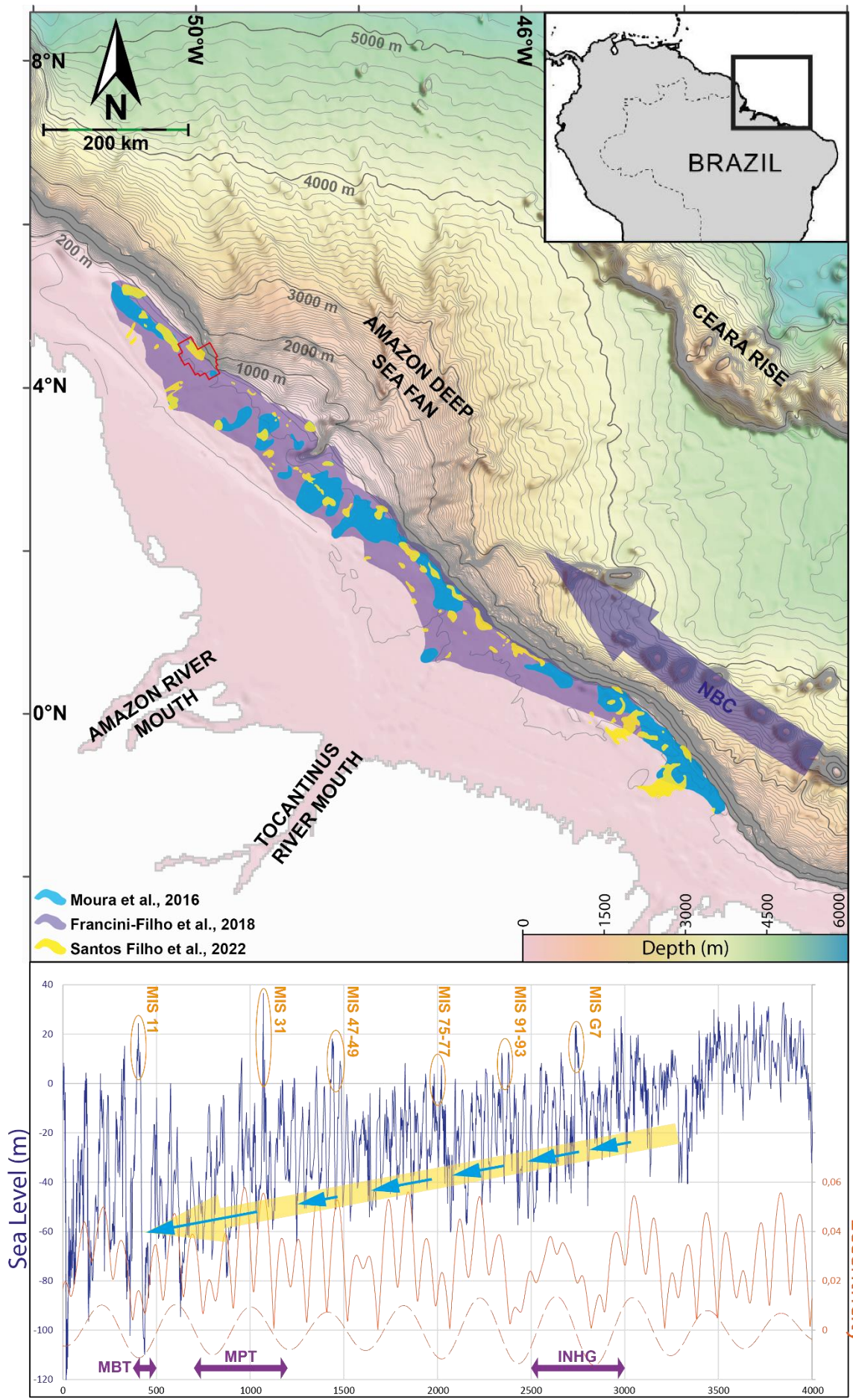


Figure 6.1: Bathymetric map of the Amazon Continental Margin, a thick blue arrow shows the North Brazilian Current (NBC). The extension of the Great Amazon Reef System calculated by Moura et al. (2016), Francini-Filho et al. (2018) and dos Santos Filho et al. (2022) is represented by superposed coloured areas in light blue, dark blue and yellow respectively. The 3D seismic block studied is delimited by red geometry. The graph below the map shows sea level variation from Miller et al. (2020; dark blue curve) during the last 4 Myr and its relationship with Earth Eccentricity (orange curve) parameters of 100 kyr and 405 kyr (red dashed curve is an extraction of the 405 kyr cyclicity only). Super-interglacials are indicated by orange ovals (Droxler and Jorry, 2021; Melles et al., 2012). Main climatic events time extends are presented by purple arrows. Lastly main trend in global climate and the subsequent main regressions are shown by a thick yellow arrow and light blue arrows respectively.

6.2. Seismic sequence and ACM evolution

This study focuses on the Quaternary sedimentary sequences accumulated on top of the Neogene Amapá Platform, a carbonate shelf buried by silico-clastic sediments when the Amazon River connected, in the late Miocene, to the Andean Mountains. Based on 2D sequence stratigraphy, Gorini et al. (2014) identified a series of seismic sequences along the ACM and proposed, with additional borehole sedimentary data sets, including biostratigraphic constraints, that each individual sequence was related to a 405 kyr cycle. A recent study, based on 3D seismic analysis correlated with cyclostratigraphy and placed into a more precise sequence stratigraphy framework, validated the hypothesis of a dominant 405 kyr cyclicity (**Chapter 4**). Moreover, main climatic events also greatly affected the sedimentary architecture along the ACM. Indeed, distinct changes in the geometries of the sediment accumulation along the ACM, initially observed by Gorini et al. (2014) and in **Chapter 4** in a 3D seismic interpretation, identified two main mega-sequences inside the Plio-Pleistocene series, attributed to two main climatic events. The mega-sequence boundary, identified at 2.4 Ma by Gorini et al. (2014; SB G) and in **Chapter 4** (top of MS-I), corresponds to an increase in sediments supply and marked erosion development along the shelf edge, linked to the Intensification of Northern Hemisphere Glaciation (INHG) between 3.0 to 2.5 Ma (Bartoli et al., 2005; Kleiven et al., 2002; Maslin et al., 1998; Wohlfarth et al., 2008). Cruz et al. (2019) also observed an increase in sedimentation rates at 2.5 Ma. The INHG triggered sea level to significantly fall, resulting in a basinward displacement of the coastline which greatly affected the sub-aerial erosion rates along the shelf edge. A second climatic event occurred at 0.9 Ma, associated with the transition from an Earth climate dominated by 40 kyr cycles to one influenced by 100 kyr cycles, and reveals a change in the seismic unit thickness on the outer shelf (**Chapter 4**). This shift is called

the Mid-Pleistocene Transition and is dated between 1.2 to 0.7 Ma (Berger and Loutre, 1994; Chalk et al., 2017; Clark et al., 2006; Pias and Moore, 1981; Willeit et al., 2019).

6.3. Development of the present-day Amazon Reef System

The topography of the present-day seafloor along the ACM shelf edge displays a pronounced high-relief N330°-oriented ridge (*Figure 6.2*), characterised by strong seismic reflection amplitudes, and resembles the characteristics of a carbonate barrier-reef (Burgess et al., 2013; do Nascimento Silva et al., 2018; Hinestrosa et al., 2014; Khanna et al., 2017). Lithologies encountered within the first meters drilled in Well #1 reveal the presence of calcarenites. Although the well does not intersect the barrier itself, it cuts through oblique structures that occupy a 20 km-wide area behind it which can be interpreted as the inner reef. Seismic reflectors associated with these oblique structures display high-amplitude reflections comparable to those of the barrier itself (*Figure 6.2*) and are oriented N315°. The barrier is further accompanied by an adjacent erosive trough on its seaward side. The height differential from the base of this trough to the flat-topped crest of the barrier is approximately 59 meters, based on a velocity of 1.5 km/s along the water column (*Figure 6.2*). The barrier spans 26 km in length and 1 km in width, narrows toward the north, while in the south, it broadens and evolves into a complex topographical area punctuated by multiple pinnacles like isolated reefs (*Figure 6.2*).

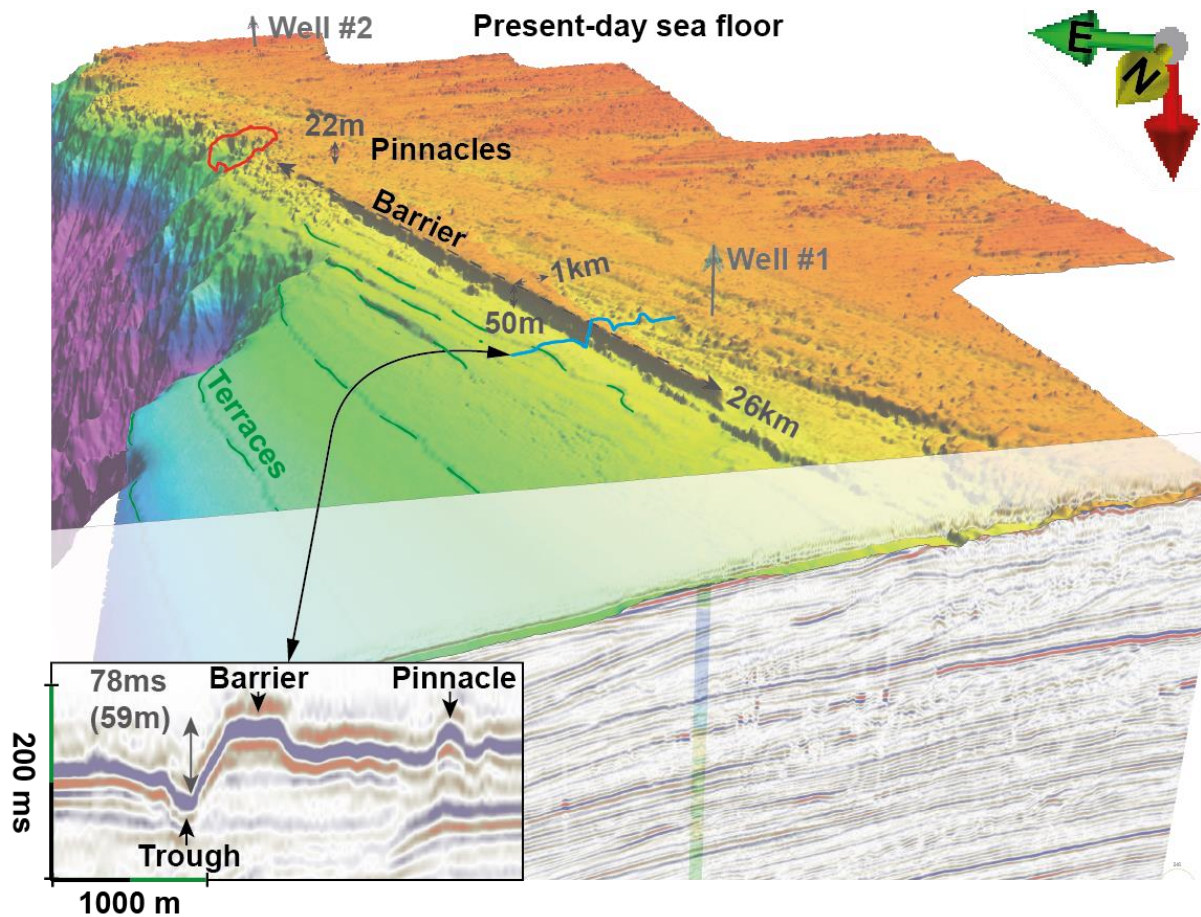


Figure 6.2: Present-day 3D sea floor horizon extracted from seismic data. Colour gradients represent Z value in ms with shallow area in red and deepest part in purple. The red circled area represents one of the dive sites depicted in Lavagnino et al. (2020) and Vale et al. (2022). Seismic line showing cross-section geometries is visible in the left bottom corner. Two wells cross the seismic block, one in the northern area (Well #1) and, one in the southern tip (Well #2). The orientation of the pictures is highlighted by three arrows on the top right corner, yellow one points North, green one points East while the red one is vertical.

These observations are corroborated by a 2017 oceanographic cruise that included three dives along the ACM (Lavagnino et al., 2020; Vale et al., 2022). Data from this expedition unveil a concentration of high-relief structures, particularly in the southern section of the seismic block (Lavagnino et al., 2020; Vale et al., 2022). Samples from this region primarily consist of boundstone with ages ranging from 16,395 to 12,160 yr BP, indicative of the onset of sea level rise following the Last Glacial Maximum (Yokoyama et al., 2018). The presence of ooids and Sabellaria tubes lends support to the idea of carbonate development in shallow environments (Aviz et al., 2021; Davies et al., 1978; Duguid et al., 2010; Harris et al., 2019; Tucker and Wright, 1990). Vale et al. (2022) proposed a maximum paleodepth of 18 meters for the boundstone samples, consistent with characteristic barrier depths. Thus, the carbonate

barrier and the front trough are inferred to have formed in response to high energy shallow-water wave action during periods of rising sea levels (Kendall and Schlager, 1981).

The northern outer shelf/slope domain within the seismic block exhibits a gentle gradient punctuated by terraces with top depths at 143, 165, 193, 240, and 314 meters (*Figure 6.2; Figure S6.1*). The transition to the slope domain occurs at a depth of ~390 meters. These deeper terraces are unlikely to result from coastal erosion during the Last Glacial Maximum; even after accounting for subsidence rates of 300 m/Myr (Cruz et al., 2019), terraces exceeding a depth of 190 meters are too deep to be attributable to such erosive processes. Rather, these terraces may be linked to storm-induced wave action affecting the upper 100 meters of the water column, a phenomenon noted on other shelves (Casalbore et al., 2017; Martinez-Martos et al., 2016; Pillans, 1990; Wagle et al., 1994), alternatively they may be due to the action of currents as also seen at the limit between water-masses creating distinct erosive terraces (Hernández-Molina et al., 2014, 2009; Muñoz et al., 2013; Viana, 2002; Viana et al., 2002).

Despite the vitality of the present-day coral assemblages (De Mahiques et al., 2019; Francini-Filho et al., 2018; Moura et al., 2016; Vale et al., 2022, 2018), their growth rates are insufficient to form the most substantial structures observed. It is suggested that these coral assemblages have adapted to the changing environmental conditions ushered in by rising sea levels, as evidenced by parallel developments in both Hawaii and the Gulf of Papua (Harper et al., 2022; Sanborn et al., 2017; Webster et al., 2009, 2007).

6.4 Previous development of Barrier Reef System

3D seismic analysis reveals that the present-day reef is not a unique feature. Indeed, deeper (and older) reef structures have been identified in the 3D seismic block, which can also be more than 50 meters high and cover several hundreds of square kilometers (*Figure 6.3*). Horizon 4 is such an example (*Figure 6.4*) with similar structures as those observed on present-day sea-floor (i.e., barriers, terraces, pinnacles) as seen on both seismic horizon and seismic profiles (see zoomed line in *Figure 6.4*).

However, all carbonate build-ups are disconnected from one another and, therefore, do not appear to represent continuous deposition (*Figure 6.3*). The build-ups appear systematically at the base of each seismic sequence and are mainly observed within the transgressive system tracts as identified in **Chapter 4**. Carbonate volume calculations during each transgressive interval yield volumes of 0.0405 km³ at 2.4 Ma, 0.264 km³ at 2.1 Ma, 0.806 km³ at 1.6 Ma, 5.09 km³ at 1.2 Ma, and 5.73 km³ at 0.4 Ma revealing a continuous increase in carbonate volume since 2.4 Ma. It also reveal an important change in carbonate volume at 1.6 Ma, with an increase

of carbonate volume, more than five times compared to the older carbonates development. So, we suggest a similar composition and origin for the older barrier-reef system than that of the present day system that have been sampled (De Mahiques et al., 2019; Francini-Filho et al., 2018; Moura et al., 2016; Vale et al., 2022, 2018).

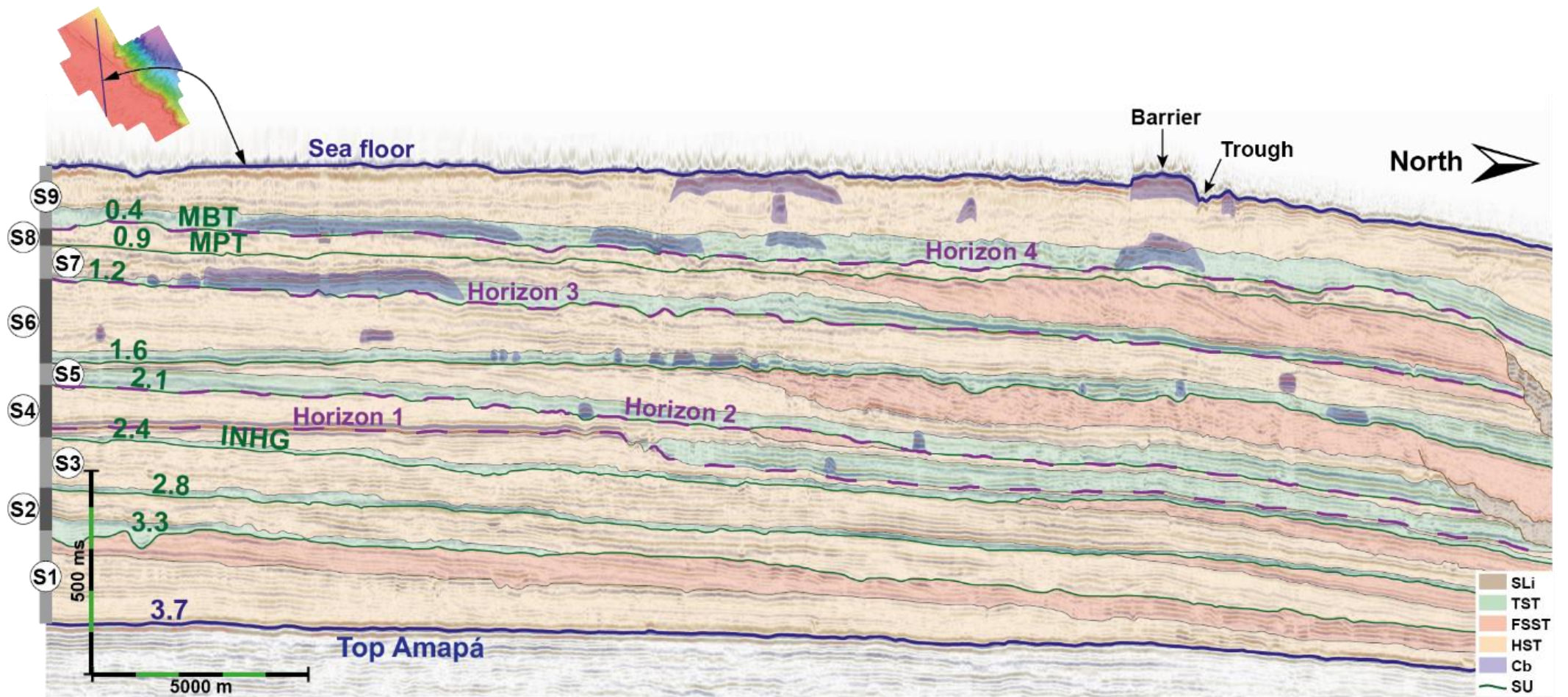


Figure 6.3: Sequence stratigraphy from the **Chapter 4** adapted on an arbitrary line crossing most of the bioconstruction observed (dark blue area). Position of the line is shown on the map view of the seismic block on the top left of the figure. Nine seismic sequences have been observed (S1 to S9). Boundaries of the seismic sequences (SU) correspond to the transgressive surface. Age of the seismic sequences (S1 to S9) are written on the left side of the line in dark green. Earth climatic variation: INHG; intensification of Northern Hemisphere Glaciation at ~2.6 Ma and MPT; Mid-Pleistocene Transition at 1.2 to 0.7 Ma could correspond to main changes in the sediments architecture and are associated with specific boundaries between seismic sequences S3 to S4 and S7 to S8 respectively. Purple dashed lines correspond to the horizons presented in the figure 2. SLi = Submarine Landslide; TST = Transgressive System Tract; FSST = Falling Stage System Tract; HST = Highstand System Tract; Cb = Carbonates.

6.5. Initiation of carbonates development

Before 2.4 Myr, the seismic data does not display barrier-type build-ups (Figure 6.4). After 2.4 Myr, transgressions following maximum regressions at 2.4 Ma, 2.1 Ma, and 1.6 Ma, show small patches of high-amplitude reflectors exhibiting build-up behaviour. Horizons 1 and 2 mark the earliest bioconstructions following the burial of the Amapá carbonated platform (Figures 6.3 and 6.4). These bioconstructions occur at the bases of paleo-cliffs (**Chapter 5**) and exhibit limited horizontal extensions, generally below one kilometer. However, they can reach thicknesses up to 50 meters (Figure 6.4).

Focusing on this specific seismic facies denoted by high-amplitude reflectors with build-up behaviour (shown in dark blue colour and labelled as Cb for carbonates in Figure 6.3), their first appearance is within the seismic sequence S4, dated between 2.4 and 2.1 Ma (**Chapter 4**). We propose that the Intensification of Northern Hemisphere Glaciation (INHG) between 3.0 and 2.5 Ma, along with the resultant climate and sea level fluctuations, fostered carbonate development along the ACM (Bartoli et al., 2005; Kleiven et al., 2002; Lisiecki and Raymo, 2007; M. A. Maslin et al., 1998). Notably, limited sea level changes during the Pliocene inhibited sediment transport toward and past the outer shelf, as suggested by Milliman et al. (1975). While, after the INHG, during the Pleistocene, increase in sea level fluctuations (up to more than hundred meters) allow sediments to bypass the shelf and be funnelled by the Amazon Canyon towards the deep-sea fan (Milliman et al., 1975). Therefore, important sea level fall reduces rates of siliciclastic sedimentation along the shelf edge, creating favourable conditions for shallow coral reef organisms. These conditions are further favoured by the sandy hard substratum associated with the topsets of regressive prisms (De Mahiques et al., 2019; Vale et al., 2022).

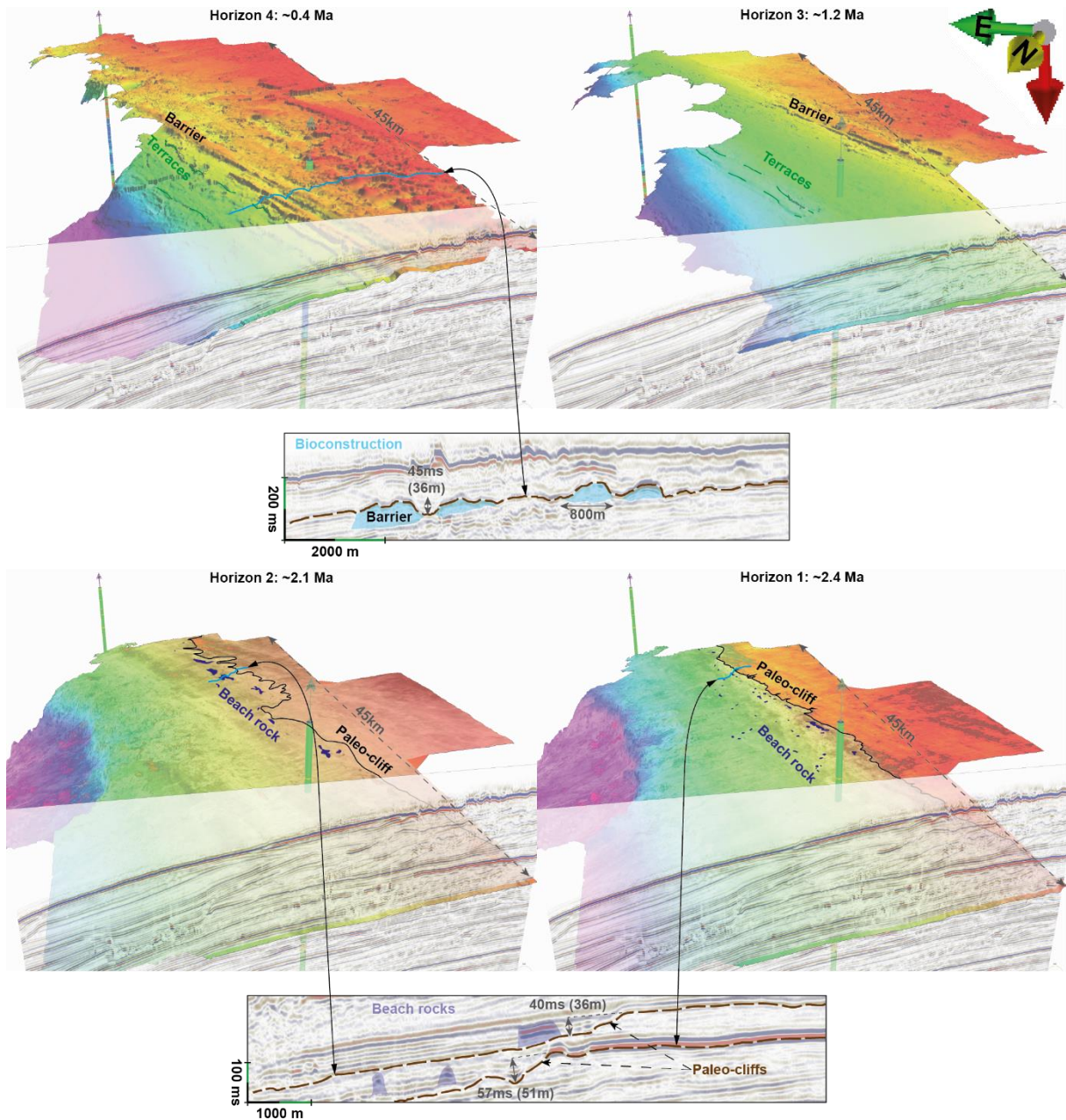


Figure 6.4: 3D horizons extracted from seismic data presenting important carbonate development. Colour gradients represent Z value in ms with shallow area in red and deepest part in purple. The red circled area represents one of the dive sites depicted in Lavagnino et al. (2020) and Vale et al. (2022). Seismic line showing cross-section geometries is visible in the left bottom corner. Two wells cross the seismic block, one in the northern area (Well #1) and, one in the southern tip (Well #2). The orientation of the pictures is highlighted by three arrows on the top right corner, yellow one points North, green one points East while the red one is vertical.

6.6. Carbonates flourishing

Horizon 3 marks the first bioconstruction in the Plio-Pleistocene series that fits the "barrier" typology (Figure 6.4) (Burgess et al., 2013; do Nascimento Silva et al., 2018; Hineostrota et al.,

2014; Khanna et al., 2017). The barrier in this horizon is situated farther from the shelf edge compared to those in Horizon 4 and present-day seafloor. The outer shelf features terraces. The barrier is relatively short, with a length of approximately 15 km, and the inner shelf exhibits few high-amplitude reflectors corresponding to inner shelf carbonate development (*Figure 6.3*). Comparison between the sea-level curve and the regional age model suggests Horizon 3 may align with a super-glacial event preceding the MIS-31 super-interglacial stage (Droxler and Jorry, 2021; Melles et al., 2012). High-amplitude reflectors in the outer shelf (*Figure 6.3*) may be indicative of rhodolith bed development at greater depths, as confirmed by current observations at depths exceeding 40 m (Moura et al., 2016). Between 1.2 Ma and 0.4 Ma, seismic data do not indicate carbonate structures.

Horizon 4 exhibits a more developed inner shelf compared to horizon 3, as well as multiple, elongated barriers (*Figure 6.4*). The barrier position in horizon 4 also shifted toward the ocean compared to horizon 3. In horizon 4, the proximal section of the block, situated behind the barriers, contains abundant bioconstructions aligned along N60° axes, which is perpendicular to the barrier orientation of N330°. The northern section of the block features a denser concentration of constructions compared to its southern counterpart (*Figure 6.4*). Lithological descriptions from Well #1 confirm the presence of several meters of calcarenite rocks.

The barrier's upsizing and its seaward migration (from Horizon 3 to Horizon 4) could be attributed to higher sea-level variation at 0.4 Ma (Horizon 4) due to the Mid-Brunhes Transition, which impacts global sea-level amplitude, reaching a height of 120 m over the past 405 kyr (Lisiecki and Raymo, 2005; Miller et al., 2020).

6.7. Pleistocene cyclic growth

The cyclical development of carbonates along the ACM is proved by their consistent presence since 2.4 Ma in each transgressive system within the seismic sequence, as well as by the age dating of these horizons through sequence stratigraphy and a model grounded in cyclostratigraphy (Gorini et al., 2014; **Chapter 4**). Between 2.4 and 0.4 Ma, carbonates have manifested in 405 kyr cycles related to the long eccentricity parameter, facilitating substantial sea-level drops followed by significant interglacial periods. These pronounced interglacial episodes correspond to the super-interglacials of MIS 11, MIS 31, MIS-47, MIS-75-MIS-77 and MIS-91-MIS-93 (Droxler and Jorry, 2021; Melles et al., 2012). Carbonates typically formed during the early transgressive phases of these super-interglacials. Since the Mid-Brunhes Transition, the northern outer shelf of the ACM has seen recurrent development of

carbonate structures (*Figure 6.3*). Among the main glacial events since this transition—MISs-2, -6, -8, -10, and -12, however, sea level fall during MIS-8 was relatively moderate, only reaching -70 m compared to the average -100 m observed for other MIS stages (Lisiecki and Raymo, 2005; Miller et al., 2020). Therefore, these significant glacial stages could align with distinct carbonate structures observed across four horizons in the latest seismic sequence (*Figure 6.3*). Although each transgressive event interrupted reef bioconstruction, leading to isolated reefal structures.

6.8. Hydrodynamical changes triggering carbonates development

The absence of backstepping reef-barriers on the inner shelf, typically induced by sea-level rise, coupled with the diminishment of build-up features toward the continent, suggests an alteration of favourable environmental conditions for carbonates growth along the ACM during periods of elevated sea levels. This alteration is thought to be correlated with shifts in the depositional centre of Amazon sediments. Milliman et al. (1975) assert that during sea-level highstands, the Amazon River's sediment inputs are deflected north-westward by the North Brazil Current (NBC), contributing to the formation of shelfal deltaic clinoforms that comprise the contemporary Amazon shelf delta. In this phase, both the Amazon Canyon and Deep-Sea Fan are essentially inactive, designating the shelf as the primary depot centre for sediments (Damuth et al., 1988; Lopez, 2001; Milliman et al., 1975). Conversely, during periods of sea-level lowering and lowstands, the Amazon Canyon is prime area for sediment transfer towards the slope, thereby inducing deep-sea fan growth (Damuth et al., 1988; Lopez, 2001; Milliman et al., 1975). Under these conditions, the bulk of sediment is channelled to the slope and deep basin, so that more propitious circumstances for the growth of reef organisms occur along the outer shelf. Furthermore, alterations in current patterns may divert the sediment plume, enabling enhanced carbonate accretion along the northernmost extremity of the Amazon shelf (North of the Amazon Canyon). This hypothesis is supported by the documented southward migration of the ITCZ during glacial periods (Broccoli et al., 2006; Chiang et al., 2003; Wang et al., 2004). Investigations centred on Ceara Rise sediments, suggested a similar argument to account for the observed increase in sedimentation rates along the rise. Specifically, shifts in wind patterns could amplify the retroflexion of the NBC, thereby transporting the majority of Amazon sediments in an eastward direction (instead of the present-day northward direction) (Harris and Mix, 1999; Rühlemann et al., 2001).

At a finer scale, the southern portion of the block is situated near the Amazon Canyon, potentially facilitating the introduction of greater volumes of siliciclastic sediments. In contrast,

the northern section experiences reduced influence from Amazon-derived sediments. This differential sedimentary input may encourage more vigorous carbonate development in the northern area, culminating in the formation of barrier reef features.

6.9. Conclusions and perspectives

The analysis of a 3D seismic block covering the outer shelf of the ACM northward of the Amazon Canyon, a primary carbonate barrier system is observed through time. This most recent structure is formed during the Last Glacial Maximum under shallow water conditions. The emergence of a barrier feature at this time suggests significantly reduced siliciclastic input, related to the funnelling of Amazonian sediments through the canyon toward the deep-sea fan during sea level lowstands. This barrier is now a drowned coral reef, similar to those observed along the coasts of Hawaii and Papua New Guinea. The study of 3D seismic horizons revealed numerous carbonate structures. Carbonate development started following the intensification of Northern Hemisphere Glaciation approximately 2.5 million years ago. Initially, these carbonates constituted small patches of high-amplitude and high-relief reflectors situated in front of erosive structures but with small lateral extent. These carbonate formations are predominantly part of the transgressive series and tend to develop during the initial stages of sea level rise following particularly low sea levels. Carbonate growth exhibits a cyclical pattern and correlates with the 405 kyr eccentricity cycles. This cyclicity has been also observed among super glacial stages and we believed that carbonates develop at the early stage of main deglaciation, before interglacial periods at MIS-91-MIS-93, MIS-75-MIS-77, MIS-47, and MIS-31. During these periods of low eccentricity amplitude, significant global sea level lowstands occur. The coastline consequently migrates to the shelf edge, and siliciclastic sediments are captured by the Amazon Canyon, thereby creating favourable conditions for coral reef development. The first “real” and continuous carbonate reef-barrier structure started around 1.1 million years ago, and was favoured by an unusually low sea level during the Mid-Pleistocene Transition. Subsequent to the Mid-Brunhes Transition, the frequency of significant sea level lows increased, and carbonate barriers appear to develop approximately every 100,000 years starting during lowstands and growing during early deglaciation of interglacial: MIS-11, -9, -7 and -5.

Declaration of interests

The authors declare that they have no known competing financial interests or personal relationships that could have appeared to influence the work reported in this paper.

Acknowledgments

This work was supported by the “Region Bretagne” as well as ISblue project: Interdisciplinary graduate School for the blue planet (ANR-17-EURE-0015) and co-funded by a grant from the French government under the program "Investissements d'Avenir" embedded in France 2030. This project was supported by the Region Bretagne and UMR6538 Geo-Ocean joint Unit (CNRS, Univ Brest, Ifremer, Univ. Bretagne Sud). Lucas Tortarolo is a PhD student at “Université de Bretagne Occidentale (UBO, Univ Brest)” and Sorbonne University (SU) in France, and is in joint supervision with “Universidade Federal Fluminense (UFF)” in Brazil. This project is also a collaboration with the “Faculdade de Oceanografia” (UERJ) located in Brazil. Antonio Tadeu dos Reis also thanks “CNPq” and “FAPERJ” for the research grants (process #309779/2021-9 and process #200.427/2023, respectively). Cleverson Guizan Silva acknowledges “CNPq” for the research grant 311589/2022-7. Slah Boulila was supported by the French Agence Nationale de la Recherche (ANR-19-CE31-0002 AstroMeso), and the European Research Council (ERC) under the European Union’s Horizon 2020 Research and Innovation Program (Advanced Grant AstroGeo-885250).

This work employed Artificial Intelligence to correct and enhance the writing. The following prompt was utilized for this purpose: "Proofread my writing. Fix grammar and spelling mistakes. And make suggestions that will improve the clarity of my writing".

6.10. Supplementary contents

6.10.1. Introduction to the Super-interglacial stages

As it is well established, sea level has greatly fluctuated through the Cenozoic, in particular since the initial growth of major ice sheets in Antarctica at the beginning of the Oligocene. With their major extension at the Middle Miocene climatic transition, overall global sea level systematically fell and the amplitudes of its fluctuations increased (Miller et al., 2020). Following the Pliocene climatic optimum (Miller et al., 2020), the global sea level fall became even more significant and the amplitudes of its fluctuations increased systematically through time since the onset and intensification of major Northern Hemisphere Glaciations (NHG: 2.5-3.0 Ma, Bartoli et al., 2005; Kleiven et al., 2002; Lisiecki and Raymo, 2007; M. A. Maslin et al., 1998; *Figure 6.1*). Simultaneously as this global downward trend in sea level during the Pleistocene, astronomical cycles induced variations in sea level on the Milankovitch scale. During the early Pleistocene prior to the Mid-Pleistocene Transition (MPT: 1.25-0.7 Ma; *Figure 6.1*), 41 kyr obliquity glacial cycles induced low amplitude and high frequency sea level cycles (Clark et al., 2006; Lisiecki and Raymo, 2005). Whereas, after the MPT, glacial cycles of 100 kyr eccentricity induced sea level fluctuations of high amplitude and low frequency (Miller et al., 2020). Post MPT, the intensity of each glacial cycle, increased systematically with maximum ice volume at glacial peaks: Marine Isotope Stage MIS -12, -6, and -2, the latter referred to as Last Glacial Maximum (LGM) when sea level reach at least – 130 m (Lambeck and Chappell, 2001; Yokoyama et al., 2018, 2000). The first 130 m plus sea level rise amplitude occurred in the mid-Bruhnes at the MIS-12 glacial to MIS-11 interglacial deglaciation, MIS-11 being recognized as the last unusually long and intense interglacial, centered at about 405,000 years (Droxler et al., 2003).

In a 2.8 million years-long climate record retrieved from the high latitude arctic Lake El'gygytgyn, Melles et al. (2012) demonstrated that MIS-11 (0.4 Ma) was the last of several Quaternary super-interglacials, characterised by unusually warm conditions and identified as MIS-31 (1.1 Ma), MIS-49-MIS-55 (1.5-1.6 Ma) and MIS-77 (2.0 Ma) (*Figure 6.1*). As for the super-interglacial MIS-11 linked to unusually low Earth orbit eccentricity (Droxler et al., 2003 and references herein), Roychowdhury (2018) highlighted the link between the Quaternary super-interglacials and low amplitude eccentricity associated with the 405 kyr cyclicity. Bassinot et al. (1994) and Droxler et al. (1990) observed dissolution intervals in long Quaternary periplatform and pelagic carbonate records, which are interpreted as being related

to some of the above-mentioned Quaternary super-interglacials. More recently, in some atolls, Droxler and Jorry (2021) suggested that Quaternary intervals of maximum neritic carbonate accumulation, separated by a series of exposure horizons, were linked to these super-interglacials (Droxler and Jorry, 2021) and to periods of unusually high sea level (Miller et al., 2020).

6.10.2. Data and methods

We used a seismic 3D data block, which is approximately 60 km long and 40 km wide, covering an area of 1700 km² (*Figure 6.1*). It is a PSTM (Pre-Stack Time Migration) survey composed of 2387 Inlines and 1733 Xlines separated by a 25-meter grid. The sample interval is 4 ms and the dominant frequency of the full-stack signal is 37 Hz, yielding a 10-20 m vertical resolution for velocity considered in between 1500 to 3000 m/s.

Two wells cross the seismic block and offer lithological descriptions and Gamma-Ray (GR) data. The resolution of GR data ranges from 15 to 20 cm, and their values are expressed in API (American Petroleum Institute) units.

To merge the time and depth domain, we used a velocity of 1.5 km/s along the water column. While, checkshots were used as well as an additional statistical wavelet creation carried on Paleoscan Software (<https://www.eliis-geo.com>) to create a time/depth model. However, deterministic wavelets known to be more accurate could not be performed due to the lack of geophysical data along the Plio-Pleistocene series. The time-depth relationship is therefore not accurate and even if some major transitions are well defined thanks to High Amplitude Reflectors correlated to the main shift in the GR, the uncertainty should be considered to be about 20 meters.

In order to obtain horizons instead of time slices, a geo-model was built, using Paleoscan software, with an automatic tracking of reflections, conversion to horizons and stratigraphic organisation. However, we also did manual interpretations of the main horizons to check, refine and update the geo-model. In our case study, along the Plio-Pleistocene series, 300 horizons were generated. Horizons are the key to identify geomorphological features.

Different attributes were used to better highlight the bioconstruction. The Z values (Present-day horizon as well as horizons 3-4; *Figure 6.2*) and Contour Curvature attributes were specifically used to highlight the building behaviour of carbonates. While, Root Mean Square (RMS) amplitudes were used to spot the lithological change between carbonates and muddy sedimentary cover (Horizons 1-2 are composite images of RMS amplitude and Z value; *Figure 6.2*).

Geobodies were used to delineate the bioconstructions along the Plio-Pleistocene series. Creation of geobodies has been done using the seismic amplitude selector mode proposed by Paleoscan software. In horizons where the only structures of high-amplitude reflection were the bioconstructions we automatically select all high amplitude areas. However, in some horizons, other features present high amplitude reflection. In this scenario, we manually select the high amplitude patches corresponding to bioconstruction. Volume computation for each geobodies allowed us to obtain the volume of each bioconstruction.

6.10.3. Supplementary figures

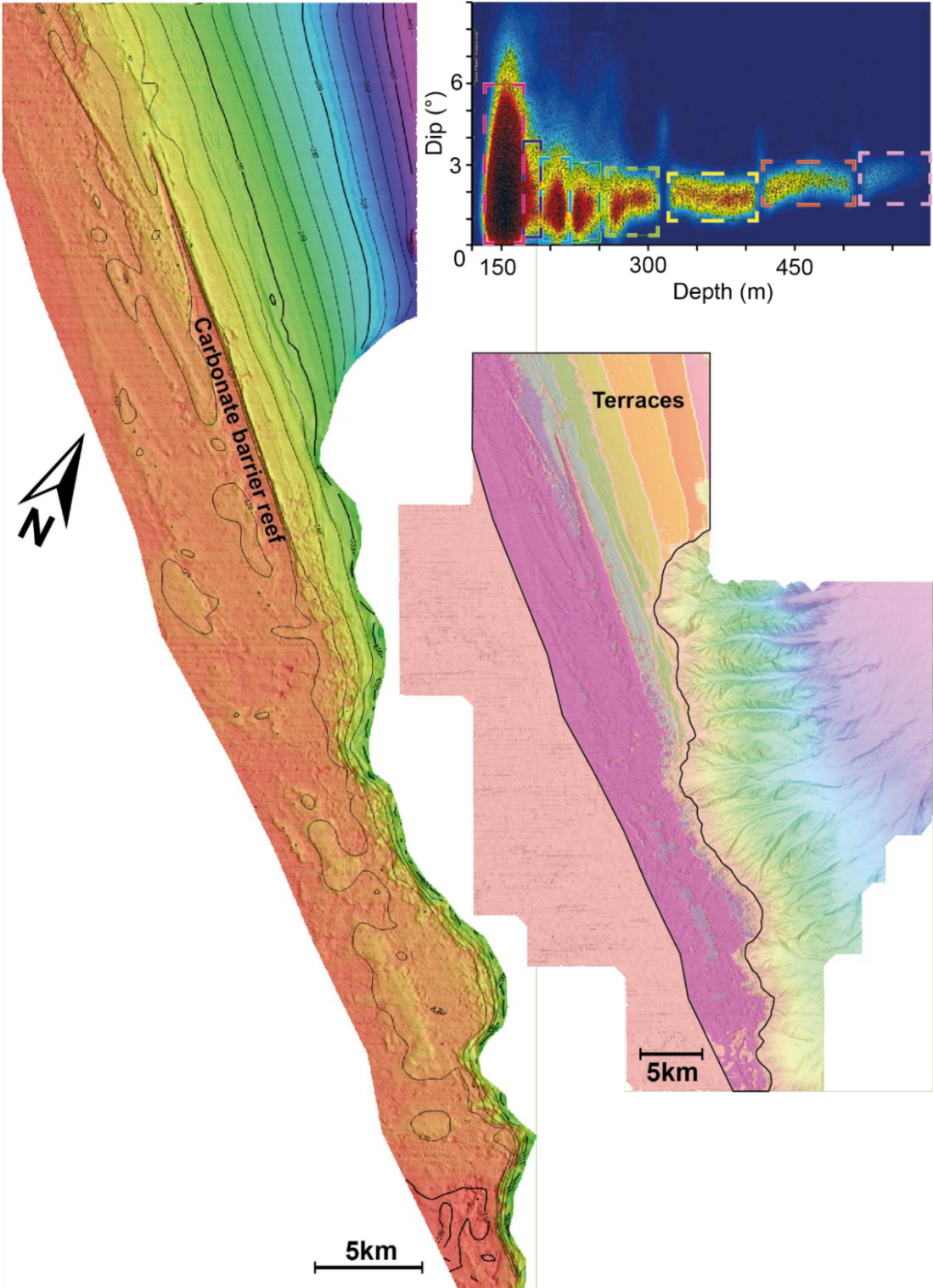
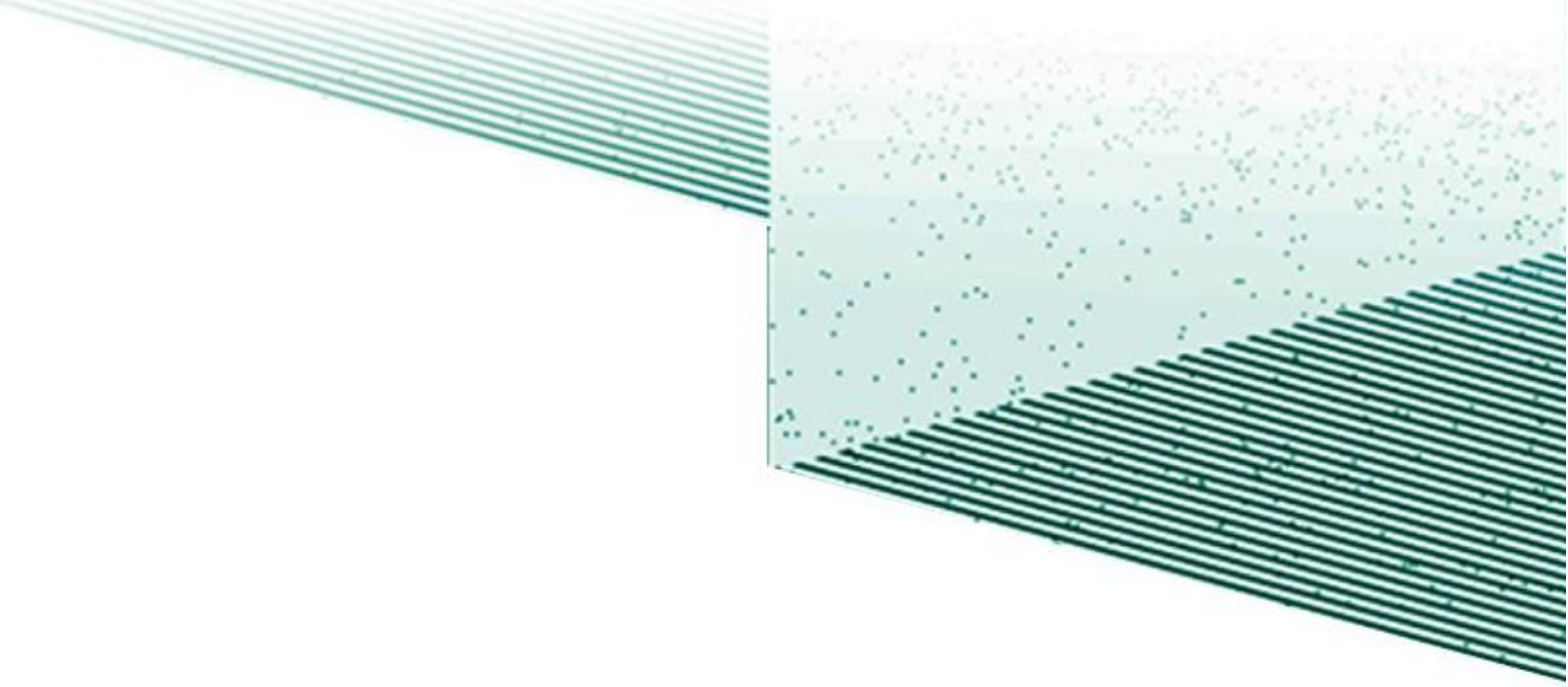


Figure S6.1: Map of the present-day outer shelf seafloor presenting the Carbonate barrier reef feature and the terraces. The outer shelf map is an extraction from the full seismic block (bottom right). Colour gradients represent depth value in m with shallow area in red (<120m) and deepest part in purple (>400m). The terraces have been extracted through filtering of points along a dip/depth graph (top right).



Chapter 7: General discussion and perspectives

7.1. Transition from Amapá carbonate to the siliciclastic sediment derived of the Amazon

The seismic block, located over 200 kilometers from the mouth of the Amazon River, has remained preserved from the considerable influx of siliciclastic sediments brought by the Amazon, following the transcontinental Amazon event. Although the precise timing of this transcontinental event is still under discussion, there is irrefutable evidence of an increase in siliciclastic sediment influx to the Amazon Continental Margin dating back at least 10 million years (Cruz et al., 2019; Figueiredo et al., 2009; Hoorn et al., 2010). During the time interval required for the deltaic siliciclastic clinoforms to migrate toward the study area, carbonate formations continue to thrive, as demonstrated by (Gorini et al., 2014). Biostratigraphic data show that the Amapá carbonates persist in the northern section of the offshore Amazon Basin at least until 5.58-4.1 Myr (Sn4; Cruz et al., 2019). The construction of a 3D seismic horizon atop the Amapá platform enhances our understanding of the transition from carbonate to siliciclastic sedimentation in the region (*Figure 7.1*).

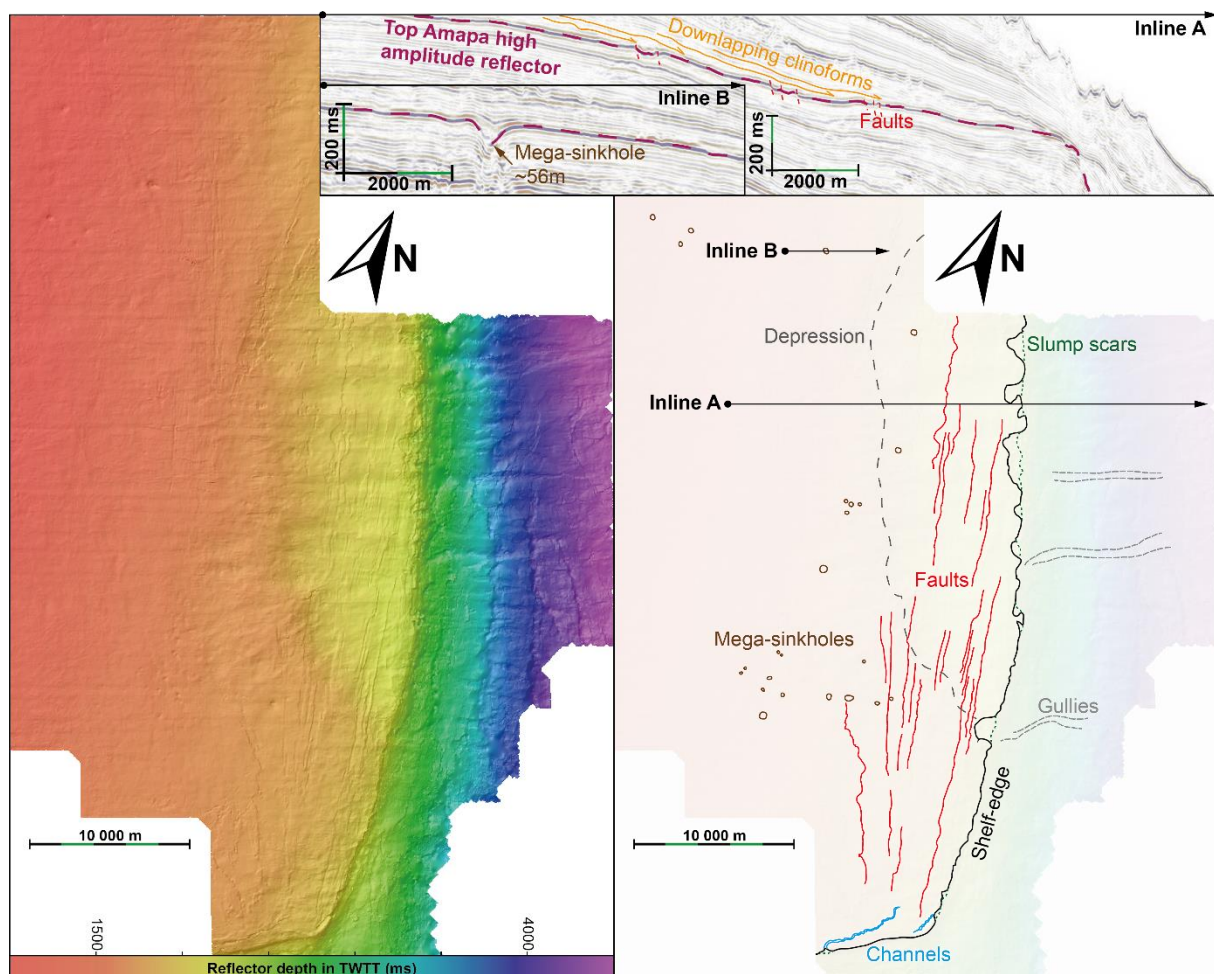


Figure 7.1: Z value along the Top Amapá horizon depicting a typical flat topped carbonate shelf. The outer shelf is highly deformed and affected by faults. The slope is very steep and shows gullies. The shelf is greatly affected by mega-sinkholes revealing emersion of the shelf at the end of the Amapá serie.

Firstly, the cessation of carbonate sedimentation does not appear to be directly correlated with the influx of siliciclastic sediments. Indeed, the presence of mega-sinkholes at the top of the carbonate formation suggests a phase of emersion, which may be attributable to a global sea-level decline around 4 Ma (Gi20; Lisiecki and Raymo, 2005; Miller et al., 2020) or even earlier, during the Sidufjall magnetostratigraphic period (4.8 Myr; Miller et al., 2020) (*Figure 7.1*). Miller et al. (2020) describe a sea level approximately 20 meters above present-day levels between 4.6 to 4.1 Ma. Subsequently, a significant sea-level drop occurs (Gi20), followed by peaks of highstand between 3.9 and 3.3 Ma that were even higher, reaching around 30 meters during Gi13. The sea-level fall at 4 Myr is calculated to be approximately -32 meters below present-day levels by Miller et al. (2020). During this period, the shelf edge was comprised of a carbonate mound with significant relief (Gorini et al., 2014), making it more susceptible to drowning compared to the deeper inner shelf. The depths of the sinkholes, calculated to be around 50 meters (based on a wave speed of 1.7 km/s), well correlate with the Gi20 event, which showed a sea-level drop of approximately 50 meters: from the 20-meter highstand above present-day levels before 4 Myr to 32 meters below present-day levels during the Gi20 lowstand at 4 Myr (*Figure 7.1*). Carozzi (1981) previously demonstrated that the Amapá carbonate platform was subject to periods of extensive subaerial exposure when conditions transitioned from high-stand to low-stand sea levels. Microfacies analysis reveals that during these periods of subaerial exposure, large-scale underground circulation of freshwater occurred, resulting in extensive secondary porosity through dissolution (Carozzi, 1981).

Furthermore, during the subsequent transgression, siliciclastic series did not establish a significant presence, as indicated by the lack of substantial transgressive sedimentary sequences. Only a thin sandy layer of 10m thick is observed at the top of Amapá and may be associated with a transgressive lag. In contrast, reflectors on top exhibit progradational behaviour with downlap terminations (*Figure 7.1*). Consequently, the initial siliciclastic series form the bottomsets of a progradational highstand systems tract, extending along the margin in a northeasterly direction. The only biostratigraphic age available in proximity to the seismic block is part of this highstand package and has been dated to between 3.7 and 4.1 Myr by Cruz et al. (2019). Furthermore, Cruz (2018) proposed correlating this age, which is associated with the Sn5 horizon in their study, with a high sea level at 3.7 Myr. This is consistent with our age

model and supports our hypothesis of a long-standing highstand occurring from 4.0 to 3.3 Myr. The first evidence of a significant sea-level fall in the siliciclastic record is observed at the termination of seismic sequence S1 and is dated at 3.3 Myr according to the age model based on cyclostratigraphy.

A significant number of faults are visible along the top of Amapá (*Figure 7.1*). These faults are of the normal type, parallel to the shelf edge, and exhibit an offset of 30 ms TWTT, which corresponds to approximately 25 m (assuming a wave speed of 1.7 km/s). These faults are essential for accommodating the tilt and deformation of the shelf due to sediment loading along the margin. At the southern tip of the seismic block, a prominent canyon approximately 425 m deep cuts the shelf edge and affects the shelf itself. The substantial impact of this structure and its extension toward the shelf resemble the present-day canyon of the Amazon, suggesting that this could be a paleo-canyon of the Amazon. The first series of sediments infilling the canyon exhibit low-amplitude, aggrading reflectors with onlap terminations on its flanks, indicative of a lowstand infill of the canyon or the onset of transgression, characterized by retrogradational stacking of onlapping reflectors (*Figure 7.2*). Subsequently, a set of medium-amplitude reflectors covers both the shelf and the lowstand series within the canyon. This set of medium-amplitude reflectors displays downlap terminations and could be associated with a prograding highstand, characterized by muddy bottomsets covering both the shelf and the upper part of the canyon.

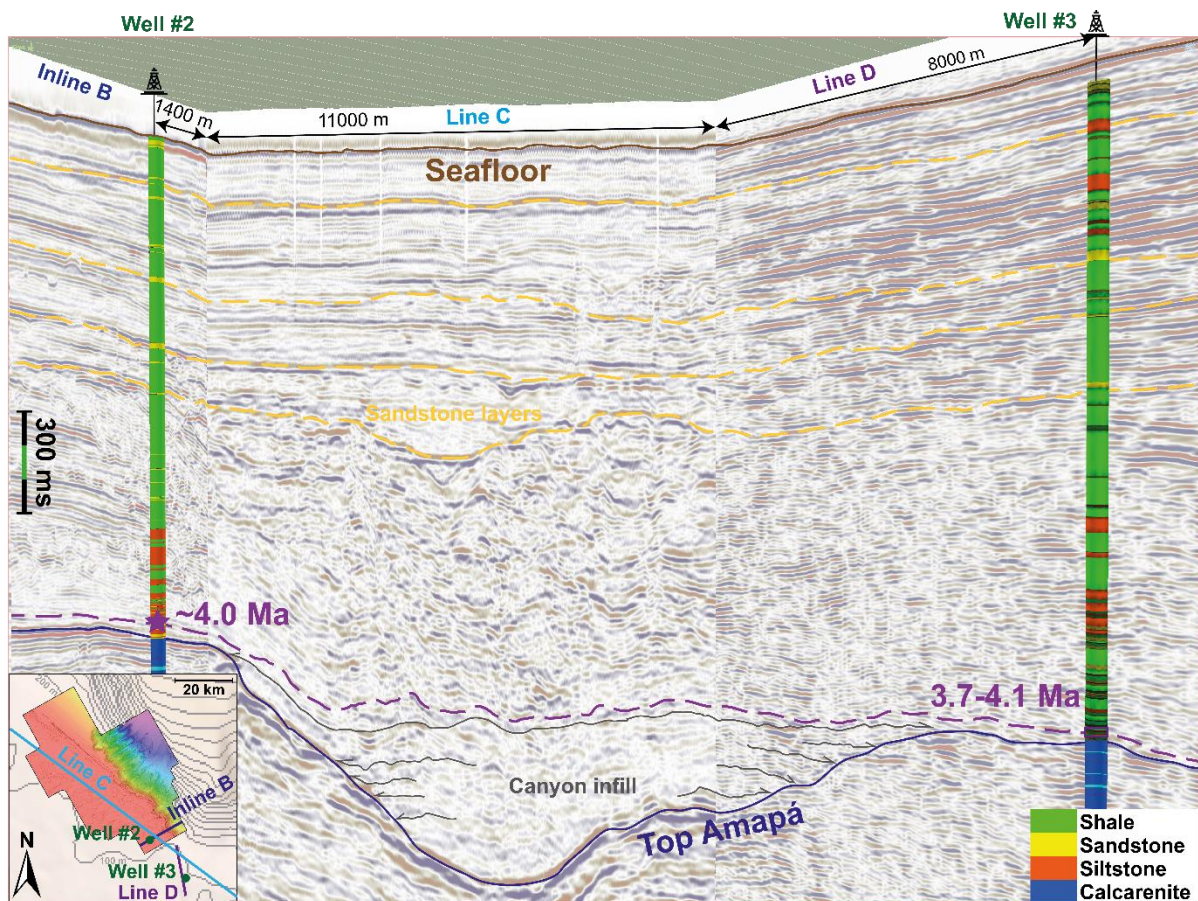


Figure 7.2: 3D seismic viewer revealing the correlation used to propagate the biostratigraphic age from Well #3 to the seismic block through two 2D seismic lines named C and D. The small box in the bottom left shows the position of the different lines and wells compared to the seismic block position. The top of Amapá is eroded by a major canyon. The bottom part of the canyon is fulfilled by reflectors with onlapping terminations noted canyon infill in the figure. While the upper part shows easy to propagate and correlate sandy layers which are highlighted in yellow. The position of the samples used for biostratigraphy correspond to the first set of reflectors which covers the canyon and the adjacent shelf (purple dashed line).

7.2. Plio-Pleistocene climate impact on sediment architecture of the Amazon Continental Margin

Between 4 Myr and 3.3 Myr, global sea levels were exceptionally high, exceeding current levels by more than 10 meters (Miller et al., 2020). During this period, only the bottomsets of highstand clinoforms were observed to extend to the outer shelf. Indications of north-eastward prograding wedges suggest that sediments from the paleo-Amazon River were likely transported to the inner shelf by alongshore currents. This phenomenon parallels contemporary conditions, in which sediments transported by the North Brazil Current give rise to prograding subaqueous clinoforms (Nittrouer et al., 1986; Nittrouer and DeMaster, 1996). These

observations indicate that by the early Pliocene, the entire Amazon shelf was already experiencing conditions akin to those of the present-day. These conditions were characterized by a significant reduction in carbonate production attributed to environmental stressors such as increased turbidity and nutrient availability, leading to eutrophication (Cruz et al., 2019).

However, a significant change occurred around 3.3 Myr, when sea levels dropped to approximately 40 meters below current levels (Miller et al., 2020). At that point, the outer shelf began to exhibit outbuilding clinoforms, which are part of the Falling Stage System Tracts (FSST), along with a downward shift of toplaps. Isochore mapping of seismic sequence S1 revealed a distinct north-eastward progradation of sediments. However, it's worth noting that this deposition was largely confined to the inner shelf and did not extend to the shelf edge (*Figure 7.3*). The depositional environment underwent a transition from lagoonal settings during the late highstand stage to strand plains during the falling stage as discussed in **Chapter 5**. Subsequent transgressive series displayed retrograding and aggrading reflectors with onlap terminations overlaying older FSST deposits. The following two seismic sequences, S2 and S3, exhibited similar variations in reflector geometries and depositional environments. Nevertheless, isochore maps of these sequences highlight a general basinward migration of sediments, evidenced by the sequence's thickest part moving from the inner shelf in S1 to the shelf edge in S3 (*Figure 7.3*).

Sediment thickness

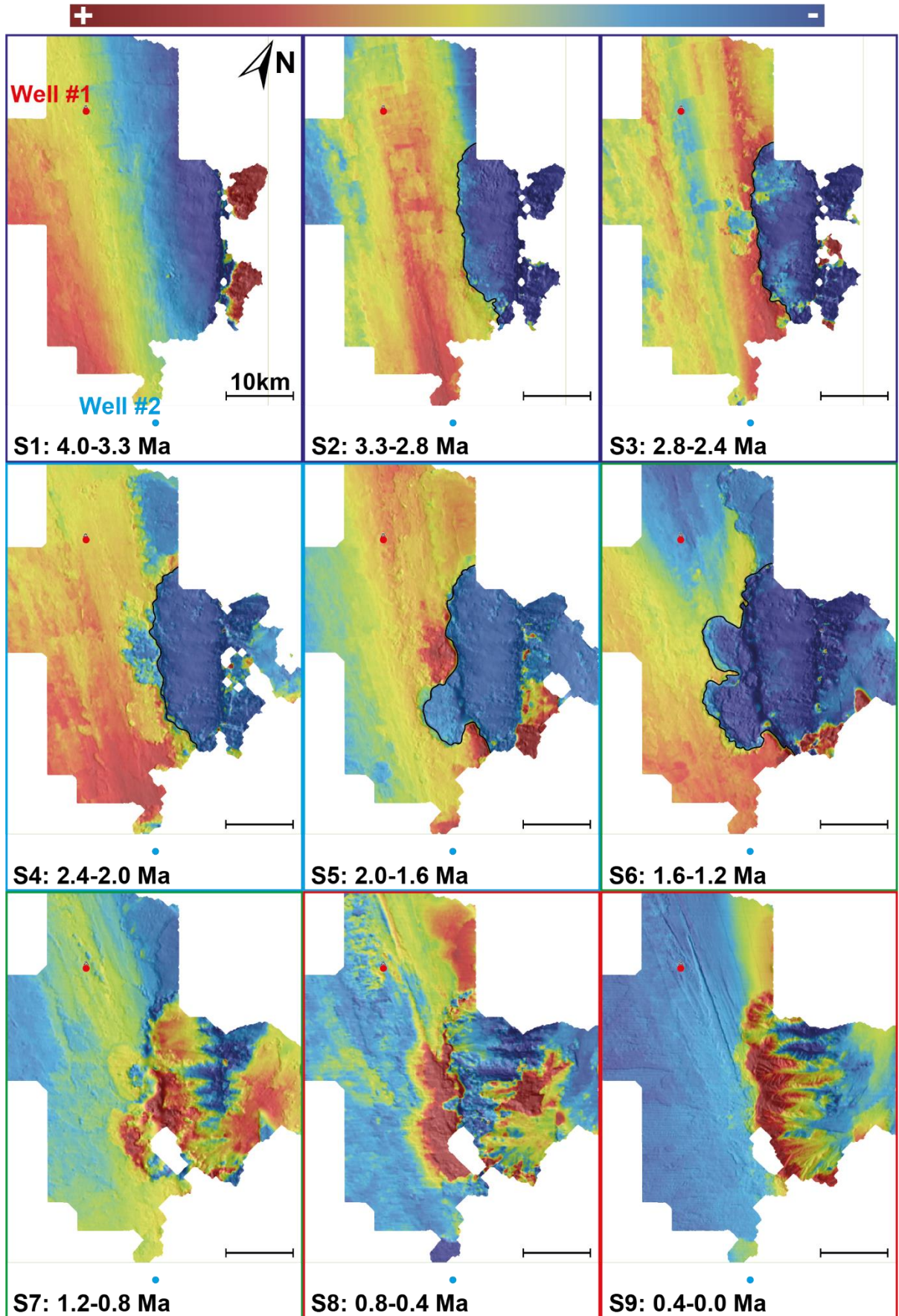


Figure 7.3: Isochore maps for the nine seismic sequences observed within the siliciclastic sedimentary series. Due to the substantial variability in sequence thickness, it was impractical to employ a consistent colour grading across all sequences; as a result, quantitative values are not presented in these maps. Black lines on the maps serve to delineate features indicative of submarine landslide scars.

After seismic sequence 3, notable changes in geometries and geomorphologies become apparent, marking the transition from Mega-Sequence I to Mega-Sequence II. This transition is characterized by thicker transgressive series, increased erosion, and steeper foreset geometries within clinoforms during FSST. According to the age model, detailed in **Chapter 4**, this transition occurs at approximately 2.4 Myr. This shift is associated with the intensification of Northern Hemisphere Glaciation, as indicated by a significant increase in $\delta^{18}\text{O}$ values at Marine Isotope Stage (MIS) 100, which corresponds to approximately 2.54 Ma. This isotopic shift aligns with the initial prominent occurrence of ice-rafted debris in the northern North Atlantic (Miller et al., 2020; Shackleton et al., 1984). However, it's important to note that between MIS G10 (approximately 2.8 Ma) and MIS100, there is a gradual increase in glacial-interglacial $\delta^{18}\text{O}$ amplitudes, suggesting a continuous rather than abrupt transition. According to Miller et al. (2020), this period was characterized by incrementally larger glaciations with relatively consistent deglaciations. Increased sedimentation rates likely played a significant role in the changes in seismic geometries. These changes could be attributed to enhanced erosion resulting from the intensified Northern Hemisphere Glaciation, as well as from Andean glaciation and variations in precipitation over the Amazon drainage basin during colder glacial periods (Harris and Mix, 1999; Mason et al., 2019). Additionally, a transition in pollen data at 2.6 Ma reflects an increase in sedimentation rates and the onset of open vegetation in the high Andes from 2.6 Ma to 0.8 Ma (transition between zones C and D as described by Hoorn et al. (2017).

The isochore map reveals a reversal in the sedimentary depot-center's position, which had migrated basin ward from S1 to S3 but now shifts continent ward in S4 (*Figure 7.3*). This reversal can be attributed to two primary factors: firstly, a notable increase in subsidence rates along the margin (Cruz et al., 2019), providing more space for sediment accumulation; and secondly, a significant rise in global sea levels around 2.4 million years ago (Ma), causing the coastline to shift continent ward. During the early transgressive stages of Mega-Sequence II, a new geomorphological feature becomes apparent: the development of paleo-cliff morphologies along the shelf edge, indicating sediment starvation during this period (as discussed in **Chapter 5**). This observation, along with erosive features and thicker transgressive intervals, suggests an increase in eustatic variation amplitude throughout Mega-Sequence II.

During Mega-Sequence III (0.9 Ma to present-day), both the morphology and location of Falling Stage Systems Tracts (FSSTs) undergo substantial changes along this passive margin. These shifts are attributed to alterations in the dominant orbital parameters affecting climate. Specifically, following the Mid-Pleistocene Transition (MPT), the Earth's climate exhibits a 97-128 kyr cyclicality, accompanied by pronounced variations in sea level (Berger and Loutre, 1994; Chalk et al., 2017; Clark et al., 2006; Pisias and Moore, 1981; Willeit et al., 2019). Notably, the largest sea-level changes reaching up to 130 meters below present levels, during the Cenozoic were associated with quasi-100-ka terminations in the last 800,000 years (Miller et al., 2020). In comparison, the major precessional (19 and 23 kyr) and tilt (41 kyr) scale sea-level lowering of the past 800,000 years ranged from 10 to 60 meters and were directly influenced by Milankovitch pacing (Miller et al., 2020). Consequently, shorter-duration seismic unit emerge, aligning with these shorter eccentricity cycles, in contrast to the previously observed 405 kyr seismic sequences (as discussed in **Chapter 4**). The decline in sea level associated with glacial stages yields significant shifts in coastline position, resulting in regressive prisms forming along the slope—referred to as forced regressions (**Chapter 4**) (*Figure 7.4*). With substantial sea-level declines, available space for sediment deposition on the outer shelf diminishes, leading to sediment migration toward the slope. In seismic sequence S8, forced regressions mainly result in progradation, with minimal aggradation. In contrast, seismic sequence S9 exhibits aggradation surpassing progradation. This pattern correlates with the Mid-Brunhes Event, characterized over the last 405 kyr by warmer interglacial periods (Jouzel et al., 2007), elevated atmospheric CO₂ levels (Lüthi et al., 2008), and an overall rise in mean sea level (Barth et al., 2018; Mitsui and Boers, 2022). The association between forced regressions and shorter eccentricity cycles following the Mid-Pleistocene Transition (MPT) has also been observed in other deltaic systems (Lafosse et al., 2018; Rabineau et al., 2006). Simultaneously, an increase in erosive features is noted. During periods of low sea level, the shoreline extends to the outer shelf, making most of the shelf susceptible to aerial erosion. In transgressive phases, patch reefs proliferate around the outer shelf atop the shelf-edge deltas formed during forced regressions. Lastly, an increase in carbonate production is noted during the transition from S8 to S9, which is attributed to the Marine Isotope Stage (MIS) 11 event at approximately 0.4 Ma (Droxler and Jorry, 2021).

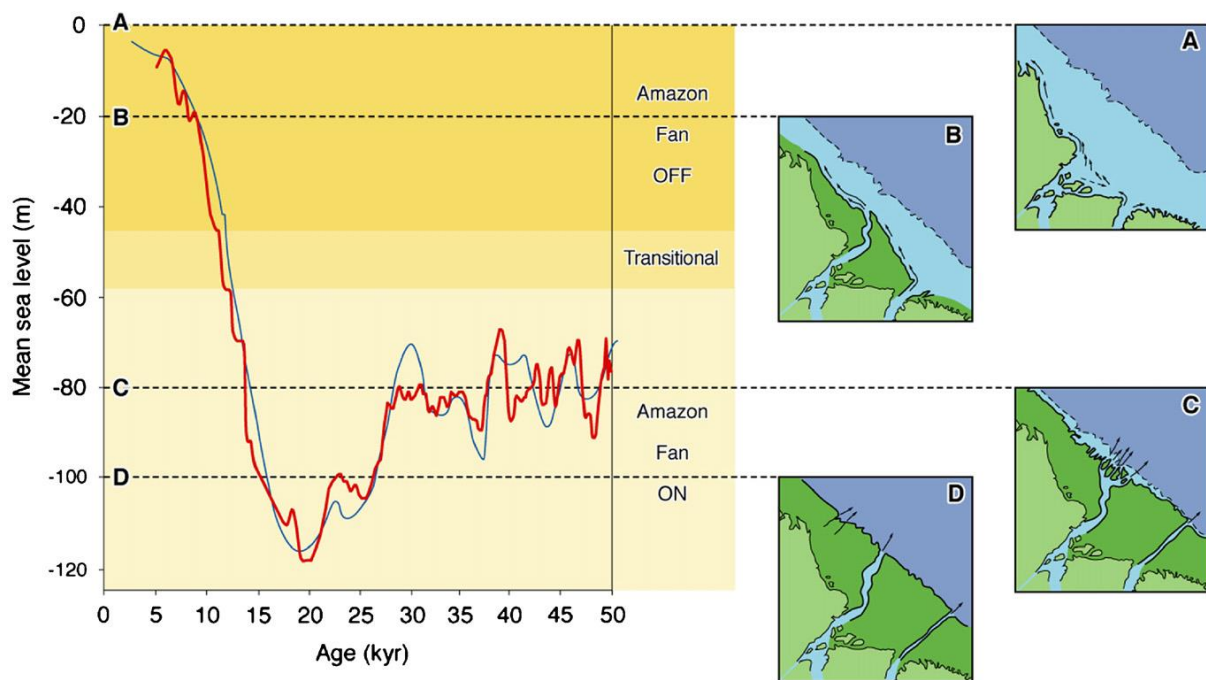


Figure 7.4: From Maslin et al. (2006): Comparison of the composite relative global sea level curves with the Milliman et al. (1975) theoretical model of changing morphology of the continental shelf and Amazon delta with lowering sea level. Red sea level curve is a composite of coral and Red Sea data and for comparison the blue curve is a composite coral and benthic oxygen isotope record. This study suggests that small changes in marine transgression or regression when sea level is below 50m can change the sediment supply to the Fan. This results in either channel floor aggradation or channel floor erosion and thus an avulsion event.

7.3. Submarine landslides and canyons evolution along the ACM

Within the 50 km of shelf edge covered by the seismic block, noticeable heterogeneity is apparent in both the intensity of erosion and the infill processes in the canyons (Figure 7.5). Specifically, there is significant infill by Amazonian sediments towards the south and an increased rate of erosion towards the north (Figure 7.5). The siliciclastic infills within the canyons are categorized into two distinct seismic units. One unit comprises a stack of medium-amplitude reflectors with a predominantly prograding pattern and steep foresets, capped by one or two high-amplitude reflectors (Figure 7.5 and figure 4.4 in **Chapter 4**). These seismic characteristics are indicative of falling stage system tracts or forced regressions. Another seismic unit, characterized by low-amplitude, highly continuous reflectors with onlap terminations and pronounced aggrading behavior, is observed at the bottom of the canyons. This unit is linked with lowstand system tracts or early transgressions. Notably, no deposits in the canyons were observed to be associated with highstand system tracts, suggesting that the canyons are not active during periods of high sea level.

Nine instances of forced regressions were observed, primarily developing within the canyon heads over the past 0.9 Myr (**Chapter 4**). These have been correlated with the late Pleistocene's 100 kyr glacial-interglacial cycles. Comparable geometries and cyclicities have been documented in various global margins, including the Mediterranean Sea and the Gulf of Mexico (Anderson and Fillon, 2004; Lobo and Ridente, 2014; Rabineau et al., 2006, 2005; Ridente et al., 2009). These forced regressions are better preserved in the southern portion of the seismic block, a preservation attributed to increased subsidence and sedimentation rates, facilitated by the block's proximity to the Amazon deep-sea fan.

Significant subsidence affects the study area; however, its influence varies considerably. As geomorphological evidence indicates the presence of a coastline within the seismic block, it can be approximated that sedimentation consistently counterbalances subsidence. The siliciclastic series under study starts atop a carbonate mound that developed in shallow waters. Consequently, the series' thickness is a good approximation of subsidence over the past 4.0 Myr. Considerable variability in the thickness of the siliciclastic series, and thus in subsidence rates, is observed across the seismic block. For instance, along Well #2, situated in the block's southern part, the series measures 1510 m in thickness. In contrast, the series along Well #1 in the northern section is only 1026 m thick. This thickness was not compared with that observed along Well #3, which is 1822 m thick, due to differing paleogeomorphological conditions at the terminus of the Amapá formation, where a paleo-embayment already existed (*Figure 7.2*).

Contrary to findings that bottom currents significantly influence canyon positions, as demonstrated in multiple geographical settings such as southern Brazil (Viana et al., 2002, 1999), the Sea of China (He et al., 2013; Zhu et al., 2010), offshore Gabon (Rasmussen, 1994; Seranne and Abeigne, 1999), and Australia (Leach and Wallace, 2001), observations in the study area indicate no along-shelf migration of canyons. Such migrations in various margins have been attributed to bottom currents, specifically intermediate-water currents flowing between 300 and 2000 m (Stow et al., 2002). Although the North Brazil Current (NBC) extends to a depth of 800 m (Talley, 2011), its expected impact on canyon positions along the Brazilian equatorial margin is not evident. Specifically, the cross-line shown in *Figure 7.5* lacks evidence for either canyon migration or lateral accretion packages, phenomena described by the model proposed by He et al. (2013) (*Figure 7.6*).

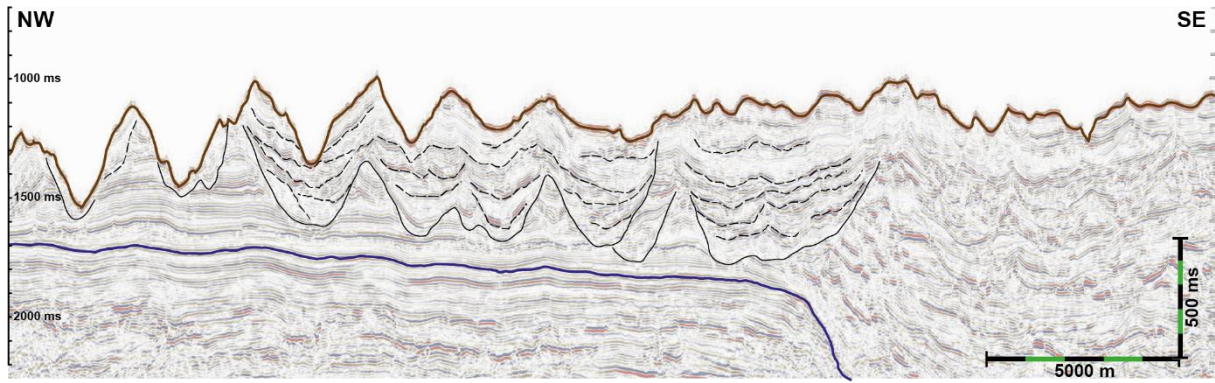


Figure 7.5: Arbitrary line crossing the canyons along the slope in the seismic block. Erosion is less active in the southeastern part, whereas the northwestern part experiences high levels of erosion. Similarly, substantial infill occurs in the southeastern canyons, while almost no infill is evident in the northwestern ones. Contrary to expectations related to the influence of the North Brazil Current (NBC), the canyons do not exhibit a north-westward deflection. Thick black line represents the basal erosive limit of canyons. Dashed black lines show stacked unit limits inside canyons.

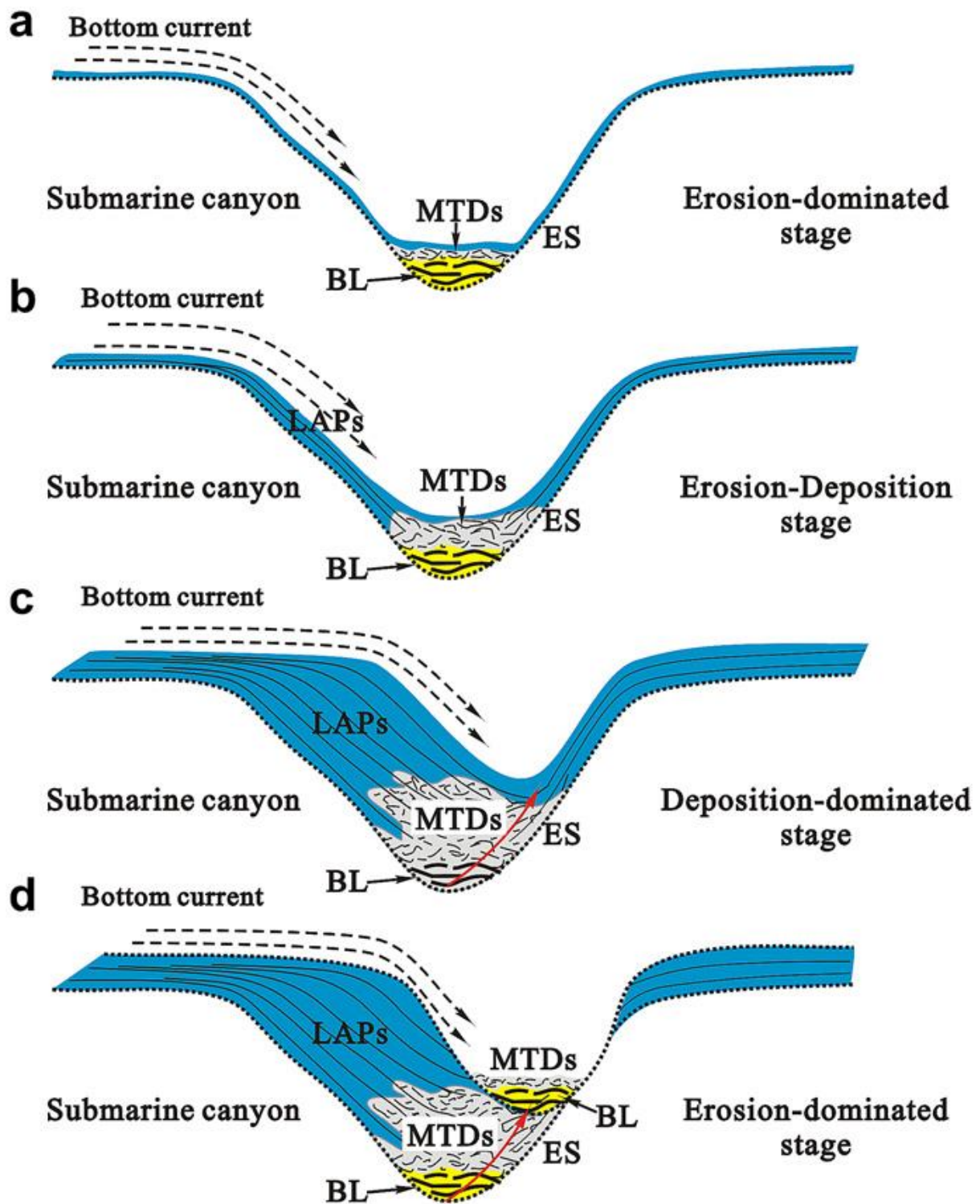


Figure 7.6: From He et al. (2013): Evolutionary model of the submarine canyons within a single canyon form. Three stages have been divided: erosion-dominated stage, erosion-deposition stage and deposition-dominated stage. ES: erosion surface; BL: basal lag; MTDs: mass transport deposition; LAPs, lateral accretion packages.

7.4. North Brazil Current variation, hints from the seismic record of the ACM shelf edge

Multiple lines of evidence within the seismic block suggest a shift in current direction along the Amazon Continental Margin (ACM). The initial signs of this shift become evident through the altered orientation of prograding beach ridges during a rapid sea-level fall at approximately 3.3 Ma, indicating a reduction in sediment supply to the southern part of the study area (as discussed in **Chapter 5**). Furthermore, erosional periods characterized by sea cliff morphologies at 2.4, 2.1, and 1.6 Ma along the entire shelf edge suggest an absence of sediment input during early transgressions. The formation of sea cliff morphology is the result of a sudden cessation of sediment supply during early transgression. This is followed by significant deposition of siliciclastic sediments during the middle to late phases of transgression, which contributes to the preservation of these paleo-cliffs. The segmentation of these cliffs, along with the morphologies of sand spits, may be attributed to updrift accretion and downdrift erosion, both of these processes serve as indicators of paleo-current direction (Claudino-Sales et al., 2018) (**Chapter 5**).

Notably, the presence of carbonate development observed within the seismic block suggest alterations in water column parameters. In contemporary conditions influenced by the Amazon plume carbonate formation faces challenges. High water turbidity reduces light penetration, while the substantial input of siliciclastic sediments overwhelms carbonate particles (as discussed in **Chapter 6**). Paleo-records indicate that carbonate build-up occurs only during the early stages of transgression, and the absence of backstepping barriers coupled with the discontinuity in carbonate formation, confirms that optimal conditions for their growth are intermittent. Furthermore, during the middle to late transgression phases, carbonate formation ceases and is subsequently overlaid by siliciclastic sediments (as detailed in **Chapters 5 and 6**). These observations corroborate the idea that conditions suitable for carbonate formation occur sporadically at 2.4, 2.1, 1.6, 1.2, 0.4 Ma and during early transgressive stage only.

Finally, two additional observations strongly support the hypothesis of a change in currents intensity or/and direction along the ACM: firstly, the canyons do not exhibit any north-westward migration, and secondly, the geometry of the Amazon deep-sea fan displays a symmetrical semi-circular shape. These observations contradict any preferential sediment deflection toward the northwest by the North Brazil Current (NBC).

These observations deviate from the typical behaviour of the North Brazil Current (NBC), which dominates along the equatorial margin of Brazil, flowing from southeast to northwest as documented by Johns et al. (1998). The NBC transports warm, saline water from the tropical South Atlantic to the northern hemisphere and extends to intermediate water depths of approximately 800 m as reported by Talley (2011).

We propose two hypotheses to account for the geomorphological features observed along the seismic block: either a reversal of the North Brazil Current (NBC) or a displacement of the northward bifurcation of the NBC. Both hypotheses are grounded in the concept of a southward shift of the Intertropical Convergence Zone (ITCZ) during glacial periods.

Numerous climate simulations associate North Atlantic Cold Events with decreased Atlantic meridional overturning circulation (AMOC) as demonstrated by studies such as Broccoli et al. (2006); Vellinga and Wood (2002); Zhang et al. (2011); Zhang and Delworth (2005). This reduction is often linked to a southward shift of the ITCZ and its associated wind and precipitation belts, as indicated by research like that of Chiang et al. (2003) and Vellinga and Wu (2004). Such a shift could potentially weaken the NBC while strengthening the Brazilian Current (Nace et al., 2014), a process modelled for the Last Glacial Maximum (Chang et al., 2008).

However, it's worth noting that due to the NBC's crucial role in mass and temperature exchanges between hemispheres and its significant influence on the AMOC, a complete reversal of this current is considered unlikely, despite its proposal by Chang et al. (2008).

The second hypothesis is based on a southward displacement of the NBC bifurcation. In the present-day scenario, the NBC bifurcates around latitudes 6–7°N, giving rise to the Guyana Current flowing north-westward and the North Equatorial Counter Current flowing eastward as documented by Bourles et al. (1999); Dengler et al. (2004); Goes et al. (2005) and Schott et al. (1995). This bifurcation leads to the development of numerous eddies, which have a substantial impact on both current direction and intensity Dengler et al. (2004); Fratantoni and Richardson (2006); and Richardson et al. (1994). A southward migration of the Intertropical Convergence Zone (ITCZ) could potentially shift this bifurcation zone and the area where these eddies develop to the vicinity of the study site at 4°N. This, in turn, could result in significant alterations to coastal currents in the region.

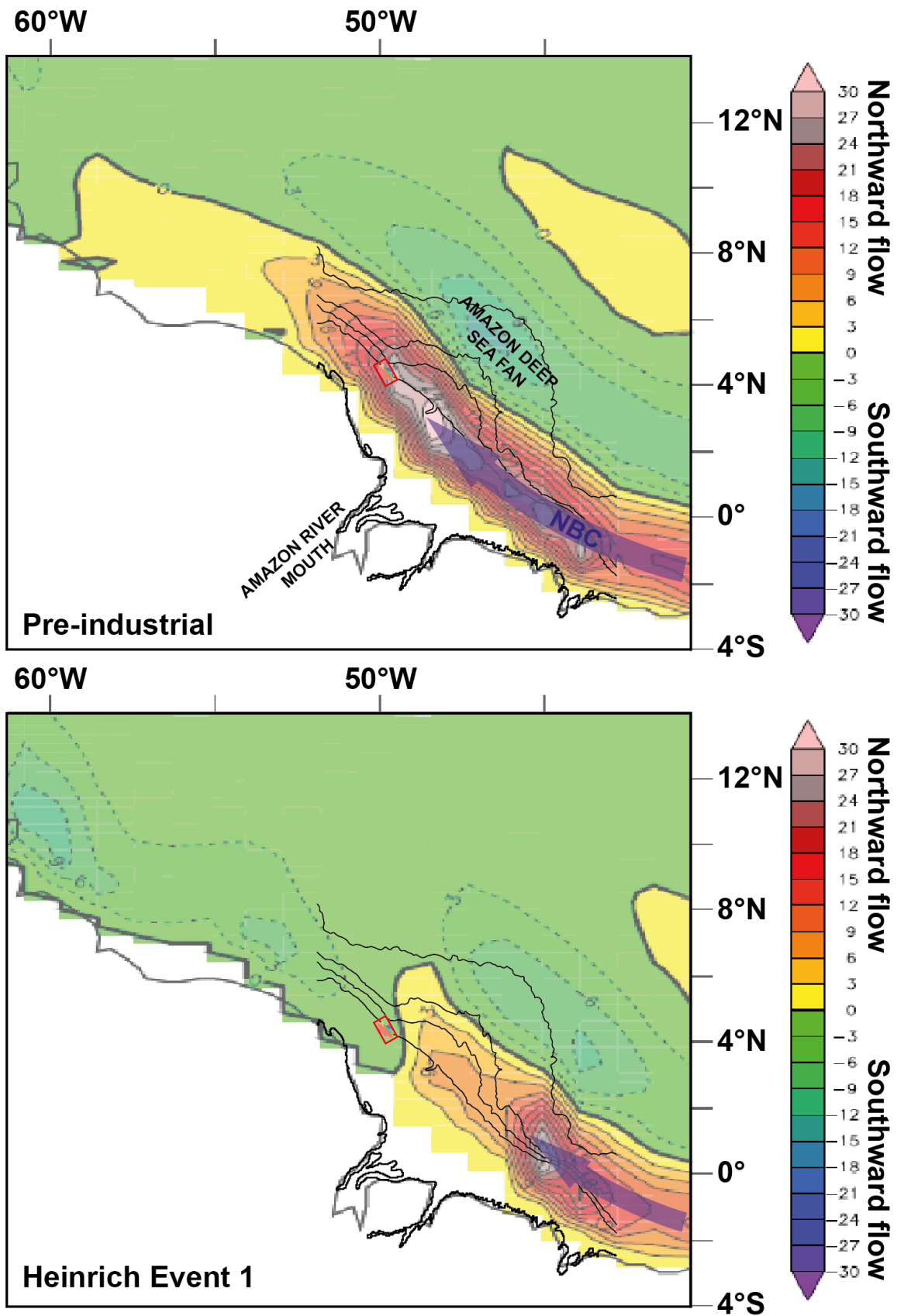


Figure 7.7: Models of the meridional velocities at 100 m depth along the north-eastern part of South America for two climatic states: preindustrial and the Heinrich Event 1 using a global coupled model with 1 degree resolution (CCSM3). Positive value indicates a northward flow, while negative indicates

a southward flow. The values are expressed in cm/s. Study area is represented by a red square. The thick black line indicates the present-day coastline. The thin black lines represent from the coast to the basin, 200, 2000, 3000 and 4000 m isobath respectively. NBC means North Brazil Current. It is clear that in the present-day configuration, the NBC deflect most of the sediment from the Amazon northward along the coastline of Brazil and the Guianas. While during Heinrich Event 1, the NBC is greatly reduced and is deflected around 3°N, while a southward flow affects the northern Brazilian coastline.

We used a global climate model (CCSM3) to investigate the potential impact of Atlantic Cold Events on the North Brazil Current (NBC) (*Figure 7.7*). The model's simulations suggest that during Heinrich Event 1, the northward flow of the NBC could experience a significant reduction both in its northward extent and velocity. Notably, the bifurcation of the NBC, which currently occurs around 6-7°N, may shift to approximately 3°N, as illustrated in the model's results (*Figure 7.7*). This southward shift could lead to prevailing eastward flows along the Brazilian Equatorial Margin during glacial periods, directing Amazon-derived sediments straight into the deep basin. It's important to note that due to certain constraints in our model, we were unable to simulate older events. Nevertheless, we posit that the carbonate build-up observed on the seafloor today could have flourished in response to the displacement of the ITCZ and the associated alterations in the NBC. Given that we have observed several other instances of carbonate build-up and geomorphological evidence that align with these triggering mechanisms, it is plausible to infer that changes in NBC intensity constitute a recurring phenomenon. These changes are likely to coincide with significant lowstands and glacial periods, exhibiting 405 kyr cyclicity throughout the Pleistocene and increasing to a 100 kyr frequency following the Mid-Brunhes Transition (as discussed in **Chapter 6**).

Furthermore, we observe significant variations in the flow of the North Brazil Current (NBC) at a seasonal timescale, which are closely linked to the migration of the Intertropical Convergence Zone (ITCZ). The NBC exhibits noteworthy seasonal variability, with transport rates ranging from a maximum of 36 Sv during the austral winter to a minimum of 13 Sv during the austral fall (Johns et al., 1998). This seasonal fluctuation aligns with the north-south movement of the Intertropical Convergence Zone (ITCZ) and associated wind stress curl changes. Nikiema et al. (2007) conducted an investigation to understand the consequences of a southward migration shift in the Intertropical Convergence Zone (ITCZ), leading to dominant northeast trade winds along the latitude of the Amazon River Mouth. Their salinity and surface velocity model maps (*Figure 7.8*) suggest that under such conditions, water masses and consequently, sediments could be deflected southward or constrained around the river mouth. It's important to note that while Nikiema et al.'s (2007) models primarily focus on annual variability in the ITCZ position, they do not account for other factors that could impact the

margin over longer timescales, such as significant changes in shelf surface between interglacial and glacial stages. Nevertheless, these models offer valuable insights into the effects on the Amazon Continental Margin when dominant northeasterly winds emerge due to a southward shift in the ITCZ.

In contrast to the southeast trade winds, which predominantly direct the plume northward, the northeast trade winds tend to confine it near the river mouth by counteracting the river's discharge (Nikiema et al., 2007). While the introduction of direct north winds could theoretically drive the plume south-eastward, such a phenomenon has not been observed and is improbable, due to the Coriolis force, which sustains eastward dominant wind stress. Nikiema et al. (2007) consider multiple processes that affect the margin, including tides, winds, currents, and river inputs, and they conclude that current dynamics are the primary drivers of hydrodynamics in the area. This leads us to suggest that observed changes in coastal morphologies within the seismic block are likely attributable to shifts in current dynamics.

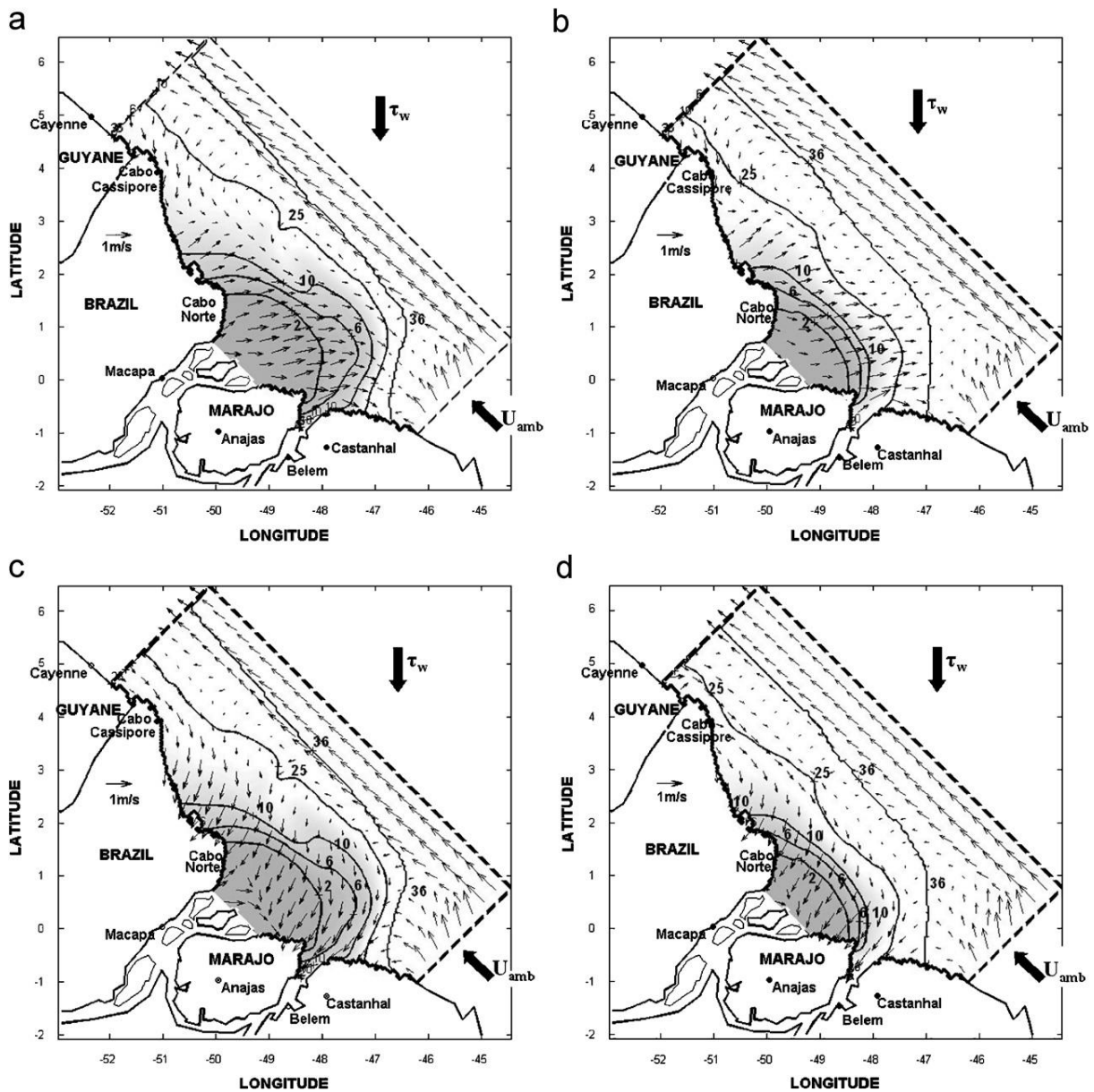


Figure 7.8: From Nikiema et al. (2007): Surface salinity contour and surface velocity (m/s) after 200 h for north wind forcing. The tidal is introduced and the Amazon River discharges is (a, c) 230 000m³/s and (b, d) 90 000m³/s, and 11 000 m³/s for Para/Tocantins River: (a) and (b) during ebb; (c) and (d) during flood.

We propose that during the early transgression phase following significant glacial periods and associated lowstands, a southward migration of the ITCZ leads to a shift in the bifurcation position of the NBC, moving it to at least 3°N latitude. This repositioning allows for a dominant eastward flow in the first 800 meters of the water column around 3°N. Consequently, Amazonian sediments are directed through the canyon and into the deep basin. Under these conditions, the northern part of the ACM remains free of Amazonian sediment deposition, while a southwest-to-northeast coastal current facilitates retrogradational erosion along the shoreline. These changing conditions create a favourable environment for carbonate

organism to inhabit, leading to buildup of reefs. However, as transgression progresses, both the intensity and extent of the NBC increase, directing Amazonian sediments back towards the northern part of the ACM and burying the cliffs and carbonate buildups. The seismic horizons that provide evidence of such NBC variations are dated at 3.3, 2.4, 2.1, 1.6, 1.2, and 0.4 Ma (**Chapter 4**). These ages correspond to periods of particularly low Earth eccentricity at 405 kyr intervals and are associated with significant lowstands (Laskar et al., 2011; Miller et al., 2020).

We propose that orbital parameters play a crucial role in triggering major glacial events during the late Pliocene and Pleistocene, exerting a substantial influence on Earth's climate. Following the Mid-Brunhes Transition, the glacial conditions necessary for carbonate buildup and consequently, NBC variations, occur with greater frequency, approximately every 100 kyr (**Chapter 6**).

7.5. Long eccentricity parameter, major influence in global climate

Our study reveals that the sedimentary records of the Amazon Continental Margin (ACM) are significantly influenced by long-term eccentricity cycles. Although the 405 kyr signal appears weak in comparison to the 97-128 and 41 kyr signals in the gamma-ray (GR) data, the seismic architecture and geomorphological features underscore the impact of 405 kyr cyclicity in our study area. A subdued long eccentricity signal in the GR data is consistent with existing literature; long eccentricity is discernible in delta 18O and delta 13C records, but has been relatively weak for the past 1.6 Myr (Lisiecki and Raymo, 2005; Wang et al., 2010).

However, the impact of the 405 kyr cycle remains relatively underexplored, as 100 kyr and obliquity cycles have generally been acknowledged as the dominant periodicities during the Pliocene and Pleistocene epochs (Lisiecki and Raymo, 2005). It is widely accepted that obliquity controlled glacial-interglacial stages prior to the Mid-Pleistocene Transition (MPT), and short-term eccentricity cycles did so afterwards, long-term climate shifts and certain major glacial-interglacial events seem to align with the 405 kyr cycle. Evidence from sediment cores taken from Arctic Lake El'gygytyn in Northeastern Russia suggests that some interglacial periods were notably warmer than others based on sedimentological facies, with summer temperatures ranging 3-5°C above current levels (Melles et al., 2012). According to the 2.8-million-year-long climate record from Lake El'gygytyn, Melles et al. (2012) identified several Quaternary super-interglacials, such as MIS-11 (0.4 Ma), as unusually warm periods that also included MIS-31 (1.1 Ma), MIS-49-55 (1.5-1.6 Ma), MIS-77 (2.0 Ma), and MIS-87-91-93 (2.4 Ma). Additional corroborative evidence from periplatform and pelagic carbonate records suggests that dissolution intervals are associated with these Quaternary super-interglacials

(Bassinot et al., 1994; Droxler et al., 1990). Recent studies in some atolls have further linked periods of maximal neritic carbonate accumulation to these super-interglacials and to intervals of unusually high sea levels (Droxler and Jorry, 2021; Miller et al., 2020). Such "Super Interglacials" cannot be accounted for solely by greenhouse gas concentrations and astronomical forcing (Roychowdhury, 2018), suggesting the involvement of amplifying feedback mechanisms. As for the super-interglacial MIS-11 linked to unusually low Earth orbit eccentricity (Droxler et al., 2003, and references herein), Roychowdhury (2018) highlighted the link between the Quaternary super-interglacials and low amplitude eccentricity associated with the 405 kyr cyclicity (*Figure 7.9*). Roychowdhury (2018) observed that during periods of extremely low eccentricity, obliquity becomes the sole dominant astronomical factor influencing high-latitude climate and ice volume, as precessional frequencies are absent. As a result, climate responses in the Northern and Southern Hemispheres become synchronous, and Antarctic ice-sheet variations align with Northern Hemisphere insolation.

Throughout most of the Plio-Pleistocene epoch, Earth's orbital eccentricity remains above a certain threshold, resulting in significant out-of-phase precessional variations in Earth's climate. It was only when eccentricity fell below this threshold, rendering Earth's orbit around the Sun nearly circular, that Antarctic ice-sheet dynamics began to align with those of the Northern Hemisphere, both influenced by Northern Hemisphere insolation (Roychowdhury, 2018). During these low-eccentricity periods, local insolation in both hemispheres varied in unison, responding solely to obliquity changes. As eccentricity started to increase, making Earth's orbit increasingly elliptical, out-of-phase precessional variations in local insolation re-emerged (Roychowdhury, 2018). Consequently, Antarctic ice-sheets began to respond to local Southern Hemisphere insolation, which then started to vary asynchronously with Northern Hemisphere local insolation. This asynchrony led to the Southern Hemisphere "missing a beat" in the 23-kyr precessional glacial-interglacial cycles (Roychowdhury, 2018). Depending on the prevailing obliquity during these low-eccentricity periods, Antarctica could experience either an extended glacial or interglacial phase immediately following a low-eccentricity orbit. For instance, at approximately 1.13 Ma, when eccentricity was below 0.01 and obliquity was high, Antarctica underwent a prolonged warming phase from about 1.14 to 1.1 Ma (Roychowdhury, 2018). This resulted in a preconditioning effect conducive to an unusually warm super-interglacial. Conversely, at around 1.3 Ma, when eccentricity was also below 0.01 but obliquity was low, Antarctica experienced a prolonged cooling, which did not set the stage for subsequent super-interglacial conditions (Roychowdhury, 2018). Importantly, while low-eccentricity orbits

preceded almost all identified super-interglacials, the reverse was not necessarily true: not all low-eccentricity orbits were followed by super-interglacial.

In our analysis, we posit that in addition to well-recognized super-interglacial, periods of extreme glaciation, or super-glacial, also exist and often precede these prominent super-interglacial events. Notably, we have identified significant lowstands potentially corresponding to multiple climatic events, including M2 at 3.3 Myr, G10 at 2.8 Myr, MIS-96-98-100 around 2.51 Myr, MIS-78 at 2.07 Myr, MIS-58 at 1.63 Myr, MIS-38 at 1.45 Myr, MIS-22 at 0.88 Myr, and MIS-12 at 0.43 Myr. In low-eccentricity conditions, the climate systems of the Northern and Southern Hemispheres became synchronized, thereby amplifying the effects of obliquity, regardless of whether the climate was in a glacial or interglacial state. This synchronization culminated in extreme climatic conditions that exerted more significant impacts than the more commonly studied glacial-interglacial cycles that were primarily associated with obliquity before the Mid-Pleistocene Transition (MPT) and with short-period eccentricity afterward. Understanding Earth's climate response to these long-period eccentricity variations is crucial, especially given the current climate scenario closely resembles these low-eccentricity settings. Although previous studies have already suggested focusing on MIS-11 to better anticipate future climate conditions (Droxler and Jorry, 2013), we argue that equal attention should be devoted to examining super-glacial periods to gain a comprehensive understanding of Earth's climate variability under these conditions.

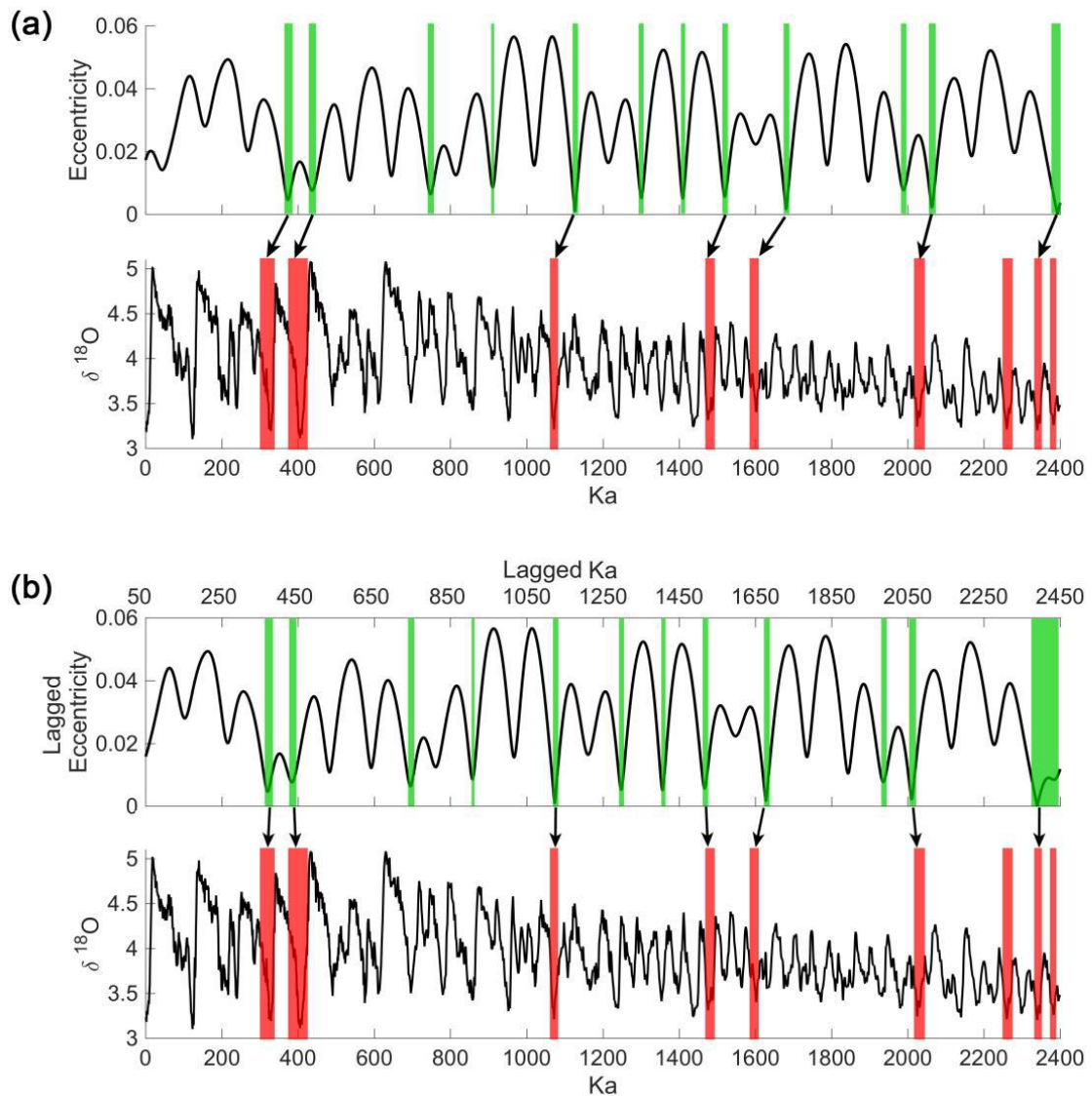


Figure 7.9: From Roychowdhury, (2018): Schematic diagram showing that most “super-interglacials” are preceded by periods of extreme low eccentricity. (a) Variations in the eccentricity component of orbital forcing over the last 2.4 million years together with $\delta^{18}O$ values from the “LR04” benthic stack (Lisiecki and Raymo, 2005). (b) Variations in the eccentricity component shifted by 50 kyr together with $\delta^{18}O$ values showing how the low eccentricity periods match up with the “super-interglacials”. Periods of extremely low eccentricity are shaded in green, and the “super-interglacials” identified from the Lake El’gytgyr record are shaded in red.

7.6. Perspectives

Ongoing and future scientific papers planned:

Multiple avenues for future work emerge from this study. In addition to the three scientific papers already drafted, we aim to publish a paper focusing on the North Brazil Current

(NBC) and its evolution during glacial periods. This paper will compile all existing evidence and incorporate a regional oceanographic model that accounts for variations in the Intertropical Convergence Zone (ITCZ) and changes in the shelf surface during glacial periods. Another planned scientific paper is entitled "Deposition and Erosion in the Deep Equatorial Canyons: Autocyclic or Allocyclic Control?" This paper will examine the canyons along the seismic block's shelf edge, which appear to be connected to submarine landslide scars that alter the morphology of the shelf edge and influence canyon evolution. These canyons are also partially infilled by nine forced regressive prisms (that we mapped during the PhD), potentially associated with 100 kyr eccentricity cycles. Subsidence and sediment input also significantly affect the canyons; those closer to the deep-sea fan and the Amazon River mouth exhibit less erosive and more aggradational behaviours.

A complete astronomically calibrated age model for the post rift succession of the Brazilian Equatorial Margin:

Additionally, we intend to create an age model based on cyclostratigraphy for the Amapá carbonate formation. Boulila et al. (2020) have already constructed an age model for the Limoeiro formation, the first post-rift formation along the margin. During this PhD project, we have also built an age model for the third and most recent post-rift formation. Creating an age model for the Amapá formation, the second post-rift unit, would complete an astronomically calibrated age model of the post-rift formations from 100 Ma to the present day along the Brazilian Equatorial margin.

Seeking for early deglacial carbonates along the Amazon Continental margin:

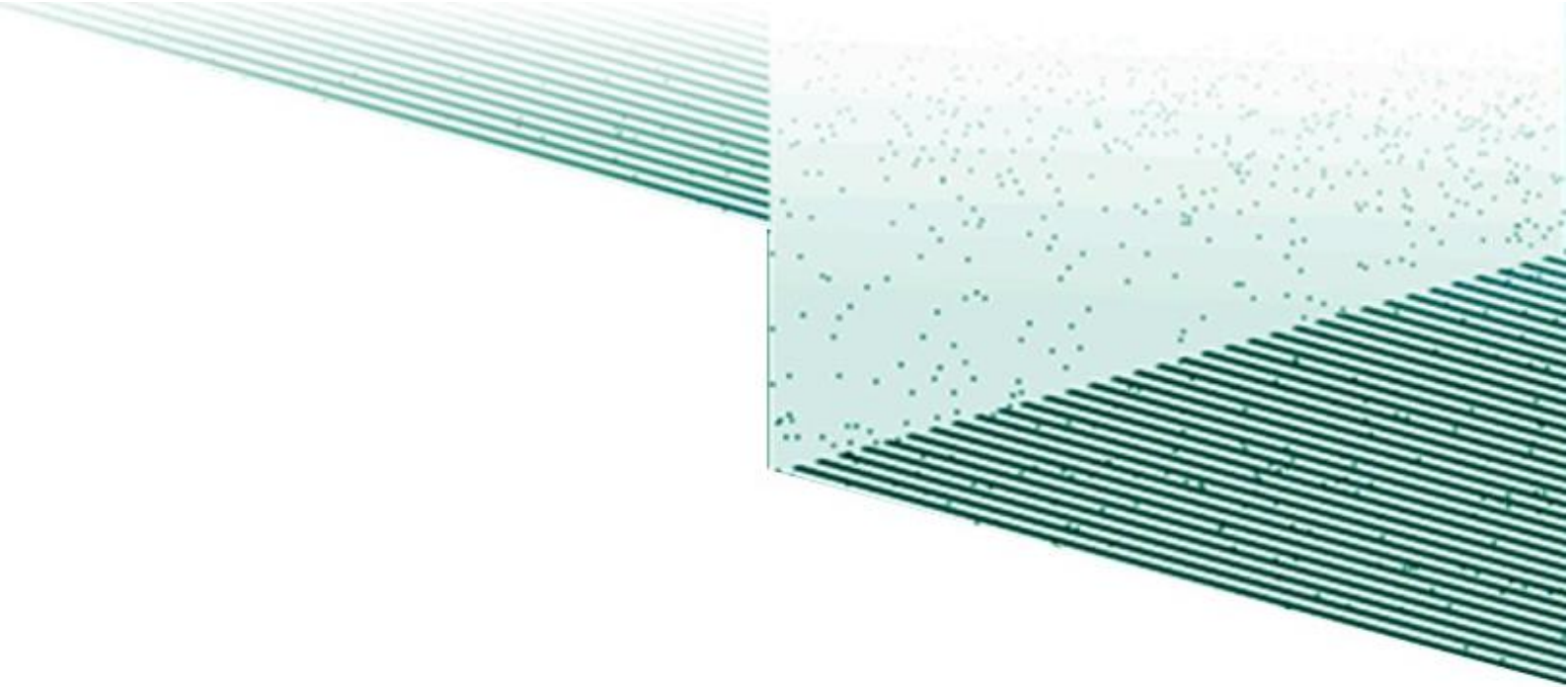
The discovery of extensive carbonate build-ups on the contemporary seafloor, traceable to the Last Glacial Maximum, indicates that carbonate activity was more important than previously suggested by the sole observations of red algae, sponges, and black corals. We advocate for the expansion of efforts to comprehensively map these carbonate formations. We aim to use proximal 3D seismic data to uncover additional build-ups. Such formations have already been located to the north of our study area within another 3D seismic block. Investigating for comparable structures to the south of the Amazon canyon would be particularly helpful, as it may clarify whether the Amazon River's plume deflects eastward or southward. A southward flow of the plume would inhibit carbonate formation in the southern regions of the Amazon Continental Margin during glacial epochs. Additionally, obtaining cores from these build-up features would yield invaluable data regarding their conditions of

establishment and their chronological development. In that regard, we still hope that the IODP 387 mission planned in proximity to our study area will occur and enable me to embark on the expedition for this dedicated carbonate thematic full understanding.

Integrating Shelf, Slope, and Deep-Basin Processes:

The recent oceanographic cruise Amagas-Amaryllis provides a new avenue for advancing our understanding of the Brazilian Equatorial Margin. While our research primarily concentrates on the outer shelf and shelf edge, it has the potential to be integrated with deeper processes recorded during the Amagas mission, such as landslides, turbidites or mass transport deposits. The extensive 3D seismic data sets acquired by oil and gas companies, which spans from the deep basin to the shelf, should be used to investigate on a broader scale the dynamics of siliciclastic deposition and migration in response to sea-level fluctuations, as well as gravity-driven tectonics and landslides.

And then, finally, it would be necessary to dedicate a specific effort, probably collective, to gather, compare, and relate a full calenda of events from erosion in the Andes and the Amazon Craton, to timing of transport within the Amazon and its tributaries, to deposition on the coast, shelf, and deeps sea settings. This would probably take a number of years...but is an exciting perspective!



References

- Adam, O., Bischoff, T., Schneider, T., 2016. Seasonal and Interannual Variations of the Energy Flux Equator and ITCZ. Part I: Zonally Averaged ITCZ Position. *J. Clim.* 29, 3219–3230. <https://doi.org/10.1175/JCLI-D-15-0512.1>
- Aguiar, A.L., Marta-Almeida, M., Cruz, L.O., Pereira, J., Cirano, M., 2022. Forcing mechanisms of the circulation on the Brazilian Equatorial Shelf. *Cont. Shelf Res.* 247, 104811. <https://doi.org/10.1016/j.csr.2022.104811>
- Ahn, S., Khider, D., Lisiecki, L.E., Lawrence, C.E., 2017. A probabilistic Pliocene–Pleistocene stack of benthic $\delta^{18}\text{O}$ using a profile hidden Markov model. *Dyn. Stat. Clim. Syst.* 2. <https://doi.org/10.1093/climsys/dzx002>
- Ainsworth, R.B., 1994. Marginal marine sedimentology and high resolution sequence analysis; Bearpaw-Horseshoe Canyon transition, Drumheller, Alberta. *Bull. Can. Pet. Geol.* 42, 26–54.
- Ainsworth, R.B., 1992. Sedimentology and sequence stratigraphy of the Upper Cretaceous. (In Bearpaw–Horseshoe Canyon transition, Drumheller, Alberta: AAPG Annual Convention Field Trip Guidebook).
- Ainsworth, R.B., 1991. Sedimentology and high resolution sequence stratigraphy of the Bearpaw-Horseshoe Canyon transition (Upper Cretaceous), Drumheller, Alberta. Canada.
- Albert, J.S., Val, P., Hoorn, C., 2018. The changing course of the Amazon River in the Neogene: center stage for Neotropical diversification. *Neotropical Ichthyol.* 16, e180033. <https://doi.org/10.1590/1982-0224-20180033>
- Anderson, J.B., Fillon, R.H. (Eds.), 2004. Late Quaternary Stratigraphic Evolution of the Northern Gulf of Mexico Margin. SEPM (Society for Sedimentary Geology). <https://doi.org/10.2110/pec.04.79>
- Anthony, E.J., Gardel, A., Gratiot, N., Proisy, C., Allison, M.A., Dolique, F., Fromard, F., 2010. The Amazon-influenced muddy coast of South America: A review of mud-bank–shoreline interactions. *Earth-Sci. Rev.* 103, 99–121. <https://doi.org/10.1016/j.earscirev.2010.09.008>
- Aviz, D., Santos, C.R.M.D., Rosa Filho, J.S., 2021. Sabellariid (Polychaeta: Annelida) reefs as nursery ground for the hermit crab *Clibanarius symmetricus* (Randall, 1840) on the Amazonian coast of Brazil. *Mar. Biol. Res.* 17, 21–30. <https://doi.org/10.1080/17451000.2021.1887494>
- Bailey, I., Hole, G.M., Foster, G.L., Wilson, P.A., Storey, C.D., Trueman, C.N., Raymo, M.E., 2013. An alternative suggestion for the Pliocene onset of major northern

- hemisphere glaciation based on the geochemical provenance of North Atlantic Ocean ice-rafted debris. *Quat. Sci. Rev.* 75, 181–194.
<https://doi.org/10.1016/j.quascirev.2013.06.004>
- Baker, P.A., Fritz, S.C., 2015. Nature and causes of Quaternary climate variation of tropical South America. *Quat. Sci. Rev.* 124, 31–47.
<https://doi.org/10.1016/j.quascirev.2015.06.011>
- Bakker, P., 2002. Image structure analysis for seismic interpretation. s.n.], [S.I.
- Banha, T.N.S., Luiz, O.J., Asp, N.E., Pinheiro, H.T., Magris, R.A., Cordeiro, R.T.S., Mahiques, M.M., Mies, M., Giglio, V.J., Omachi, C.Y., Siegle, E., Nogueira, L.C., Thompson, C.C., Thompson, F.L., Nora, V., Horta, P.A., Rezende, C.E., Sumida, P.Y.G., Ferreira, C.E.L., Floeter, S.R., Francini-Filho, R.B., 2022. The Great Amazon Reef System: A fact. *Front. Mar. Sci.* 9, 1088956.
<https://doi.org/10.3389/fmars.2022.1088956>
- Barth, A.M., Clark, P.U., Bill, N.S., He, F., Pisias, N.G., 2018. Climate evolution across the Mid-Brunhes Transition. *Clim. Past* 14, 2071–2087. <https://doi.org/10.5194/cp-14-2071-2018>
- Bartoli, G., Sarnthein, M., Weinelt, M., Erlenkeuser, H., Garbe-Schönberg, D., Lea, D.W., 2005. Final closure of Panama and the onset of northern hemisphere glaciation. *Earth Planet. Sci. Lett.* 237, 33–44. <https://doi.org/10.1016/j.epsl.2005.06.020>
- Basile, C., Mascle, J., Guiraud, R., 2005. Phanerozoic geological evolution of the Equatorial Atlantic domain. *J. Afr. Earth Sci.* 43, 275–282.
<https://doi.org/10.1016/j.jafrearsci.2005.07.011>
- Bassinot, F.C., Beaufort, L., Vincent, E., Labeyrie, L.D., Rostek, F., Müller, P.J., Quidelleur, X., Lancelot, Y., 1994. Coarse fraction fluctuations in pelagic carbonate sediments from the tropical Indian Ocean: A 1500-kyr record of carbonate dissolution. *Paleoceanography* 9, 579–600. <https://doi.org/10.1029/94PA00860>
- Bayona, G., Cortes, M., Jaramillo, C., Ojeda, G., Aristizabal, J.J., Reyes-Harker, A., 2008. An integrated analysis of an orogen-sedimentary basin pair: Latest Cretaceous-Cenozoic evolution of the linked Eastern Cordillera orogen and the Llanos foreland basin of Colombia. *Geol. Soc. Am. Bull.* 120, 1171–1197. <https://doi.org/10.1130/B26187.1>
- Beardsley, R.C., Candela, J., Limeburner, R., Geyer, W.R., Lentz, S.J., Castro, B.M., Cacchione, D., Carneiro, N., 1995. The M2 tide on the Amazon Shelf. *J. Geophys. Res.* 100, 2283. <https://doi.org/10.1029/94JC01688>

- Behling, H., W. Arz, H., Pätzold, J., Wefer, G., 2000. Late Quaternary vegetational and climate dynamics in northeastern Brazil, inferences from marine core GeoB 3104-1. *Quat. Sci. Rev.* 19, 981–994. [https://doi.org/10.1016/S0277-3791\(99\)00046-3](https://doi.org/10.1016/S0277-3791(99)00046-3)
- Berends, C.J., Köhler, P., Lourens, L.J., Van De Wal, R.S.W., 2021. On the Cause of the Mid-Pleistocene Transition. *Rev. Geophys.* 59, e2020RG000727. <https://doi.org/10.1029/2020RG000727>
- Berger, A., 1984. Accuracy and frequency stability of the Earth's orbital elements during the Quaternary., in: *Milankovitch and Climate: Understanding the Response to Astronomical Forcing.*
- Berger, A., Loutre, M.F., 1994. Precession, Eccentricity, Obliquity, Insolation and Paleoclimates, in: Duplessy, J.-C., Spyridakis, M.-T. (Eds.), *Long-Term Climatic Variations*. Springer Berlin Heidelberg, Berlin, Heidelberg, pp. 107–151. https://doi.org/10.1007/978-3-642-79066-9_5
- Berger, A., Loutre, M.F., Dehant, V., 1989. Astronomical frequencies for pre-Quaternary palaeoclimate studies. *Terra Nova* 1, 474–479. <https://doi.org/10.1111/j.1365-3121.1989.tb00413.x>
- Bermudez, M.A., Van Der Beek, P., Bernet, M., 2011. Asynchronous Miocene-Pliocene exhumation of the central Venezuelan Andes. *Geology* 39, 139–142. <https://doi.org/10.1130/G31582.1>
- Bertemes, F., Northe, A., Schmotz, K., 2007. Les douves circulaires de Goseck, une contribution à la compréhension des premiers édifices culturels monumentaux d'Europe centrale. 137–168.
- Billups, K., Lindley, C., Fislér, J., Martin, P., 2006. Mid Pleistocene climate instability in the subtropical northwestern Atlantic. *Glob. Planet. Change* 54, 251–262. <https://doi.org/10.1016/j.gloplacha.2006.06.025>
- Bott, M.H.P., 1992. Passive margins and their subsidence. *J. Geol. Soc.* 149, 805–812. <https://doi.org/10.1144/gsjgs.149.5.0805>
- Boulila, S., Brange, C., Cruz, A.M., Laskar, J., Gorini, C., Reis, T.D., Silva, C.G., 2020. Astronomical pacing of Late Cretaceous third- and second-order sea-level sequences in the Foz do Amazonas Basin. *Mar. Pet. Geol.* 117, 104382. <https://doi.org/10.1016/j.marpetgeo.2020.104382>
- Boulila, S., Laskar, J., Haq, B.U., Galbrun, B., Hara, N., 2018. Long-term cyclicities in Phanerozoic sea-level sedimentary record and their potential drivers. *Glob. Planet. Change* 165, 128–136. <https://doi.org/10.1016/j.gloplacha.2018.03.004>

- Bourles, B., Molinari, R.L., Johns, E., Wilson, W.D., Leaman, K.D., 1999. Upper layer currents in the western tropical North Atlantic (1989-1991). *J. Geophys. Res. Oceans* 104, 1361–1375. <https://doi.org/10.1029/1998JC900025>
- Brandão, J.A.S.L., Feijó, F.J., 1994. Amazon river mouth Basin; Bacia da foz do Amazonas. *Bol. Geocienc. Petrobras* 8.
- Brescia, M., D'Argenio, B., Ferreri, V., Longo, G., Pelosi, N., Rampone, S., Tagliaferri, R., 1996. Neural net aided detection of astronomical periodicities in geologic records. *Earth Planet. Sci. Lett.* 139, 33–45. [https://doi.org/10.1016/0012-821X\(96\)84608-5](https://doi.org/10.1016/0012-821X(96)84608-5)
- Brierley, C.M., Fedorov, A.V., 2016. Comparing the impacts of Miocene–Pliocene changes in inter-ocean gateways on climate: Central American Seaway, Bering Strait, and Indonesia. *Earth Planet. Sci. Lett.* 444, 116–130. <https://doi.org/10.1016/j.epsl.2016.03.010>
- Broccoli, A.J., Dahl, K.A., Stouffer, R.J., 2006. Response of the ITCZ to Northern Hemisphere cooling: ITCZ RESPONSE TO N. HEMISPHERE COOLING. *Geophys. Res. Lett.* 33, n/a-n/a. <https://doi.org/10.1029/2005GL024546>
- Burgess, P.M., Winefield, P., Minzoni, M., Elders, C., 2013. Methods for identification of isolated carbonate buildups from seismic reflection data. *AAPG Bull.* 97, 1071–1098. <https://doi.org/10.1306/12051212011>
- Campbell, K.E., 2010. Late Miocene onset of the Amazon River and the Amazon deep-sea fan: Evidence from the Foz do Amazonas Basin: COMMENT. *Geology* 38, 212–212. <https://doi.org/10.1130/G30633C.1>
- Campbell, K.E., Frailey, C.D., Romero-Pittman, L., 2006. The Pan-Amazonian Ucayali Peneplain, late Neogene sedimentation in Amazonia, and the birth of the modern Amazon River system. *Palaeogeogr. Palaeoclimatol. Palaeoecol.* 239, 166–219. <https://doi.org/10.1016/j.palaeo.2006.01.020>
- Carelli, T.G., Plantz, J.B., Borghi, L., 2018. Facies and paleoenvironments in Paraíba do Sul Deltaic Complex area, North of Rio de Janeiro state, Brazil. *J. South Am. Earth Sci.* 86, 431–446. <https://doi.org/10.1016/j.jsames.2018.07.005>
- Carozzi, A.V., 1981. Porosity models and oil exploration of Amapa Carbonates, Paleogene, Foz Do Amazonas Basin, offshore NW Brazil. *J. Pet. Geol.* 4, 3–34. <https://doi.org/10.1111/j.1747-5457.1981.tb00521.x>
- Cartwright, J., Huuse, M., 2005. 3D seismic technology: the geological “Hubble.” *Basin Res.* 17, 1–20. <https://doi.org/10.1111/j.1365-2117.2005.00252.x>

- Carvalho, R.C., De Kikuchi, R.K.P., 2013. ReefBahia, an integrated GIS approach for coral reef conservation in Bahia, Brazil. *J. Coast. Conserv.* 17, 239–252.
<https://doi.org/10.1007/s11852-013-0243-6>
- Casalbore, D., Falese, F., Martorelli, E., Romagnoli, C., Chiocci, F.L., 2017. Submarine depositional terraces in the Tyrrhenian Sea as a proxy for paleo-sea level reconstruction: Problems and perspective. *Quat. Int.* 439, 169–180.
<https://doi.org/10.1016/j.quaint.2016.02.027>
- Cattaneo, A., Steel, R.J., 2003. Transgressive deposits: a review of their variability. *Earth-Sci. Rev.* 62, 187–228. [https://doi.org/10.1016/S0012-8252\(02\)00134-4](https://doi.org/10.1016/S0012-8252(02)00134-4)
- Catuneanu, O., 2019. Scale in sequence stratigraphy. *Mar. Pet. Geol.* 106, 128–159.
<https://doi.org/10.1016/j.marpetgeo.2019.04.026>
- Catuneanu, O., 2006. *Principles of Sequence Stratigraphy*, Elsevier. ed.
- Catuneanu, O., Abreu, V., Bhattacharya, J.P., Blum, M.D., Dalrymple, R.W., Eriksson, P.G., Fielding, C.R., Fisher, W.L., Galloway, W.E., Gibling, M.R., Giles, K.A., Holbrook, J.M., Jordan, R., Kendall, C.G.St.C., Macurda, B., Martinsen, O.J., Miall, A.D., Neal, J.E., Nummedal, D., Pomar, L., Posamentier, H.W., Pratt, B.R., Sarg, J.F., Shanley, K.W., Steel, R.J., Strasser, A., Tucker, M.E., Winker, C., 2009. Towards the standardization of sequence stratigraphy. *Earth-Sci. Rev.* 92, 1–33.
<https://doi.org/10.1016/j.earscirev.2008.10.003>
- Catuneanu, O., Galloway, W.E., Kendall, C.G.S. t. C., Miall, A.D., Posamentier, H.W., Strasser, A., Tucker, M.E., 2011. Sequence Stratigraphy: Methodology and Nomenclature. *Newsl. Stratigr.* 44, 173–245. <https://doi.org/10.1127/0078-0421/2011/0011>
- Chalk, T.B., Hain, M.P., Foster, G.L., Rohling, E.J., Sexton, P.F., Badger, M.P.S., Cherry, S.G., Hasenfratz, A.P., Haug, G.H., Jaccard, S.L., Martínez-García, A., Pälike, H., Pancost, R.D., Wilson, P.A., 2017. Causes of ice age intensification across the Mid-Pleistocene Transition. *Proc. Natl. Acad. Sci.* 114, 13114–13119.
<https://doi.org/10.1073/pnas.1702143114>
- Chang, P., Zhang, R., Hazeleger, W., Wen, C., Wan, X., Ji, L., Haarsma, R.J., Breugem, W.-P., Seidel, H., 2008. Oceanic link between abrupt changes in the North Atlantic Ocean and the African monsoon. *Nat. Geosci.* 1, 444–448. <https://doi.org/10.1038/ngeo218>
- Charbonnier, G., Boulila, S., Spangenberg, J.E., Vermeulen, J., Galbrun, B., 2023. Astrochronology of the Aptian stage and evidence for the chaotic orbital motion of

- Mercury. *Earth Planet. Sci. Lett.* 610, 118104.
<https://doi.org/10.1016/j.epsl.2023.118104>
- Charrier, R., Pinto, L., Rodriguez, M.P., 2007. Tectonostratigraphic evolution of the Andean Orogen in Chile.
- Chiang, J.C.H., Biasutti, M., Battisti, D.S., 2003. Sensitivity of the Atlantic Intertropical Convergence Zone to Last Glacial Maximum boundary conditions: LGM ATLANTIC ITCZ. *Paleoceanography* 18, n/a-n/a. <https://doi.org/10.1029/2003PA000916>
- Chima, K.I., Gorini, C., Rabineau, M., Granjeon, D., Do Couto, D., Leroux, E., Hoggmascall, N., 2020. Pliocene and Pleistocene stratigraphic evolution of the western Niger Delta intraslope basins: A record of glacio-eustatic sea-level and basin tectonic forcings. *Glob. Planet. Change* 195, 103355. <https://doi.org/10.1016/j.gloplacha.2020.103355>
- Clark, P.U., Archer, D., Pollard, D., Blum, J.D., Rial, J.A., Brovkin, V., Mix, A.C., Pisias, N.G., Roy, M., 2006. The middle Pleistocene transition: characteristics, mechanisms, and implications for long-term changes in atmospheric pCO₂. *Quat. Sci. Rev.* 25, 3150–3184. <https://doi.org/10.1016/j.quascirev.2006.07.008>
- Claudino-Sales, V., Wang, P., Carvalho, A.M., 2018. Interactions between Various Headlands, Beaches, and Dunes along the Coast of Ceará State, Northeast Brazil. *J. Coast. Res.* 342, 413–428. <https://doi.org/10.2112/JCOASTRES-D-16-00173.1>
- Cleveland, W.S., 1979. Robust locally weighted regression and smoothing scatterplots. *J. Am. Stat. Assoc.* 74, 829–836.
- Cobbold, P.R., Rossello, E.A., Roperch, P., Arriagada, C., Gómez, L.A., Lima, C., 2007. Distribution, timing, and causes of Andean deformation across South America. *Geol. Soc. Lond. Spec. Publ.* 272, 321–343. <https://doi.org/10.1144/GSL.SP.2007.272.01.17>
- Colette, B.B., Rützler, K., 1977. Reef fishes over sponge bottoms off the mouth of the amazon river. Presented at the Third International Coral Reef Symposium, Miami, Florida: University of Miami.
- Cordsen, A., Galbraith, M., Peirce, J., 2000. Planning Land 3-D Seismic Surveys,. *Soc. Explor. Geophys.*
- Costa, J.B.S., Léa Bemerguy, R., Hasui, Y., Da Silva Borges, M., 2001. Tectonics and paleogeography along the Amazon river. *J. South Am. Earth Sci.* 14, 335–347. [https://doi.org/10.1016/S0895-9811\(01\)00025-6](https://doi.org/10.1016/S0895-9811(01)00025-6)
- Crivellari, S., Chiessi, C.M., Kuhnert, H., Häggi, C., da Costa Portilho-Ramos, R., Zeng, J.-Y., Zhang, Y., Schefuß, E., Mollenhauer, G., Hefter, J., Alexandre, F., Sampaio, G.,

- Mulitza, S., 2018. Increased Amazon freshwater discharge during late Heinrich Stadial 1. *Quat. Sci. Rev.* 181, 144–155. <https://doi.org/10.1016/j.quascirev.2017.12.005>
- Cruz, P.A.M., Reis, A.T., Suc, J.P., Silva, C.G., Praeg, D., Granjeon, D., Rabineau, M., Popescu, S.M., Gorini, C., 2019. Neogene evolution and demise of the Amapá carbonate platform, Amazon continental margin, Brazil. *Mar. Pet. Geol.* 105, 185–203. <https://doi.org/10.1016/j.marpetgeo.2019.04.009>
- Cruz, P.A.M., 2018. Integrated geological and geophysical studies applied to understanding the evolution of the Offshore Amazon Basin (Thèse de doctorat en géologie). Sorbonne Université, Paris.
- Curray, J.R., 1964. Transgression and regression. *Mar. Geol. Shepard commemorative volume*, Macmilan, 175–203.
- Curry, W.B., Shackleton, N.J., Richter, C., Party, S.S., 1995. Ocean Drilling Program Leg 154 Preliminary Report. *Proc. ODP Initial Rep.* Citeseer.
- da Rocha, T.B., Fernandez, G.B., De Oliveira Peixoto, M.N., 2013. Applications of ground-penetrating radar to investigate the Quaternary evolution of the south part of the Paraíba do Sul river delta (Rio de Janeiro, Brazil). *J. Coast. Res.* 65, 570–575. <https://doi.org/10.2112/SI65-097.1>
- Dagg, M., Benner, R., Lohrenz, S., Lawrence, D., 2004. Transformation of dissolved and particulate materials on continental shelves influenced by large rivers: plume processes. *Cont. Shelf Res.* 24, 833–858. <https://doi.org/10.1016/j.csr.2004.02.003>
- Dai, A., Trenberth, K.E., 2002. Estimates of Freshwater Discharge from Continents: Latitudinal and Seasonal Variations. *J. Hydrometeorol.* 3, 660–687. [https://doi.org/10.1175/1525-7541\(2002\)003<0660:EOFDFC>2.0.CO;2](https://doi.org/10.1175/1525-7541(2002)003<0660:EOFDFC>2.0.CO;2)
- Damuth, J.E., Flood, R.D., Kowsmann, R.O., Belderson, R.H., Gorini, M.A., 1988. Anatomy and Growth Pattern of Amazon Deep-Sea Fan as Revealed by Long-Range Side-Scan Sonar (GLORIA) and High-Resolution Seismic Studies. *AAPG Bull.* 72. <https://doi.org/10.1306/703C9109-1707-11D7-8645000102C1865D>
- Damuth, J.E., Kowsmann, R.O., Flood, R.D., Belderson, R.H., Gorini, M.A., 1983. Age relationships of distributary channels on Amazon deep-sea fan: Implications for fan growth pattern. *Geology* 11, 470. [https://doi.org/10.1130/0091-7613\(1983\)11<470:ARODCO>2.0.CO;2](https://doi.org/10.1130/0091-7613(1983)11<470:ARODCO>2.0.CO;2)
- Damuth, J.E., Kumar, N., 1975. Amazon Cone: Morphology, Sediments, Age, and Growth Pattern. *Geol. Soc. Am. Bull.* 86, 863. [https://doi.org/10.1130/0016-7606\(1975\)86<863:ACMSAA>2.0.CO;2](https://doi.org/10.1130/0016-7606(1975)86<863:ACMSAA>2.0.CO;2)

- Darros de Matos, R.M., 2000. Tectonic evolution of the equatorial South Atlantic, in: Mohriak, W., Taiwani, M. (Eds.), *Geophysical Monograph Series*. American Geophysical Union, Washington, D. C., pp. 331–354.
<https://doi.org/10.1029/GM115p0331>
- Davies, P.J., Bubela, B., Ferguson, J., 1978. The formation of ooids. *Sedimentology* 25, 703–730. <https://doi.org/10.1111/j.1365-3091.1978.tb00326.x>
- De Mahiques, M.M., Siegle, E., Francini-Filho, R.B., Thompson, F.L., De Rezende, C.E., Gomes, J.D., Asp, N.E., 2019. Insights on the evolution of the living Great Amazon Reef System, equatorial West Atlantic. *Sci. Rep.* 9, 13699.
<https://doi.org/10.1038/s41598-019-50245-6>
- De Matos, R.M.D., Mohriak, W.U., Talwani, M., 2000. Tectonic evolution of the equatorial South Atlantic, in: *Geophysical Monograph Series*. American Geophysical Union, Washington, D. C., pp. 331–354. <https://doi.org/10.1029/GM115p0331>
- De Schepper, S., Gibbard, P.L., Salzmann, U., Ehlers, J., 2014. A global synthesis of the marine and terrestrial evidence for glaciation during the Pliocene Epoch. *Earth-Sci. Rev.* 135, 83–102. <https://doi.org/10.1016/j.earscirev.2014.04.003>
- De Schepper, S., Groeneveld, J., Naafs, B.D.A., Van Renterghem, C., Hennissen, J., Head, M.J., Louwye, S., Fabian, K., 2013. Northern Hemisphere Glaciation during the Globally Warm Early Late Pliocene. *PLoS ONE* 8, e81508.
<https://doi.org/10.1371/journal.pone.0081508>
- De Swart, H.E., Zimmerman, J.T.F., 2009. Morphodynamics of Tidal Inlet Systems. *Annu. Rev. Fluid Mech.* 41, 203–229. <https://doi.org/10.1146/annurev.fluid.010908.165159>
- Dengler, M., Schott, F.A., Eden, C., Brandt, P., Fischer, J., Zantopp, R.J., 2004. Break-up of the Atlantic deep western boundary current into eddies at 8° S. *Nature* 432, 1018–1020. <https://doi.org/10.1038/nature03134>
- do Nascimento Silva, L.L., Gomes, M.P., Vital, H., 2018. The Açu Reef morphology, distribution, and inter reef sedimentation on the outer shelf of the NE Brazil equatorial margin. *Cont. Shelf Res.* 160, 10–22. <https://doi.org/10.1016/j.csr.2018.03.011>
- Dobson, D.M., Dickens, G.R., Rea, D.K., 2001. Terrigenous sediment on Ceara Rise: a Cenozoic record of South American orogeny and erosion. *Palaeogeogr. Palaeoclimatol. Palaeoecol.* 165, 215–229. [https://doi.org/10.1016/S0031-0182\(00\)00161-9](https://doi.org/10.1016/S0031-0182(00)00161-9)
- dos Santos Filho, J.R., Anjos, J.V.M., Silva, C.G., Barros Filho, A.K.D., Dias, G.T.M., Figueiredo, A.G., Cecilio, A.B., 2022. Resizing the extension of the mesophotic

- “reefs” in the Brazilian Equatorial Margin using bioclastic facies and seabed morphology. (preprint). In Review. <https://doi.org/10.21203/rs.3.rs-1927169/v1>
- Dowsett, H.J., Caballero Gill, R.P., 2010. Pliocene Climate. *Stratigraphy* 7.
- Driscoll, N. W., Karner, G.D., 1994. Flexural deformation due to Amazon Fan loading: A feedback mechanism affecting sediment delivery to margins. *Geology* 22, 1015–1018.
- Droxler, A.W., Alley, R.B., Howard, W.R., Poore, R.Z., Burckle, L.H., 2003. Unique and exceptionally long interglacial marine isotope stage 11: Window into Earth warm future climate, in: Droxler, A.W., Poore, R.Z., Burckle, L.H. (Eds.), *Geophysical Monograph Series*. American Geophysical Union, Washington, D. C., pp. 1–14. <https://doi.org/10.1029/137GM01>
- Droxler, A.W., Haddad, G.A., Mucciarone, D.A., Cullen, J.L., 1990. Pliocene-Pleistocene aragonite cyclic variations in holes 714a and 716b (the Maldives) compared with hole 633a (the Bahamas): Records of climate-induced CaCO₃ preservation at intermediate water depths. *Texas*. <https://doi.org/10.2973/odp.proc.sr.115.1990>
- Droxler, A.W., Jorry, S.J., 2021. The Origin of Modern Atolls: Challenging Darwin’s Deeply Ingrained Theory. *Annu. Rev. Mar. Sci.* 39.
- Droxler, A.W., Jorry, S.J., 2013. Deglacial Origin of Barrier Reefs Along Low-Latitude Mixed Siliciclastic and Carbonate Continental Shelf Edges. *Annu. Rev. Mar. Sci.* 5, 165–190. <https://doi.org/10.1146/annurev-marine-121211-172234>
- Duguid, S.M., Kyser, T.K., James, N.P., Rankey, E.C., 2010. Microbes and ooids. *J. Sediment. Res.* 80, 236–251.
- Durbin, R., Eddy, S.R., Krogh, A., Mitchison, G., 1998. *Biological Sequence Analysis: Probabilistic Models of Proteins and Nucleic Acids*, 1st ed. Cambridge University Press. <https://doi.org/10.1017/CBO9780511790492>
- Ehlers, T.A., Poulsen, C.J., 2009. Influence of Andean uplift on climate and paleoaltimetry estimates. *Earth Planet. Sci. Lett.* 281, 238–248. <https://doi.org/10.1016/j.epsl.2009.02.026>
- Eisma, D., van der Marel, H.W., 1971. Marine muds along the Guyana coast and their origin from the Amazon basin. *Contrib. Mineral. Petrol.* 31, 321–334. <https://doi.org/10.1007/BF00371152>
- Eldrett, J.S., Harding, I.C., Wilson, P.A., Butler, E., Roberts, A.P., 2007. Continental ice in Greenland during the Eocene and Oligocene. *Nature* 446, 176–179. <https://doi.org/10.1038/nature05591>

- Esput, N., Funicello, F., Martinod, J., Guillaume, B., Regard, V., Faccenna, C., Brusset, S., 2008. Flat subduction dynamics and deformation of the South American plate: Insights from analog modeling: FLAT SLAB AND UPPER PLATE DEFORMATION. *Tectonics* 27, n/a-n/a. <https://doi.org/10.1029/2007TC002175>
- Figueiredo, J. de J.P., Zalàn, P.V., Soares, E.F., 2007. Bacia da foz do Amazonas. *Bol. Geociências Petrobrás* 299–309.
- Figueiredo, J., Hoorn, C., van der Ven, P., Soares, E., 2010. Late Miocene onset of the Amazon River and the Amazon deep-sea fan: Evidence from the Foz do Amazonas Basin: Reply. *Geology* 38, e213–e213. <https://doi.org/10.1130/G31057Y.1>
- Figueiredo, J., Hoorn, C., van der Ven, P., Soares, E., 2009. Late Miocene onset of the Amazon River and the Amazon deep-sea fan: Evidence from the Foz do Amazonas Basin. *Geology* 37, 619–622. <https://doi.org/10.1130/G25567A.1>
- Fischer, A.G., D’Argenio, B., Silva, I.P., Weissert, H., Ferreri, V., 2004. Cyclostratigraphic approach to Earth’s history: an introduction.
- FitzGerald, D.M., 1996. Geomorphic Variability and Morphologic and Sedimentologic Controls on Tidal Inlets. *J. Coast. Res.* 1.
- Flagg, C.N., Gordon, R.L., McDowell, S., 1986. Hydrographic and current observations on the continental slope and shelf of the western equatorial Atlantic. *J. Phys. Oceanogr.* 16, 1412–1429.
- Flood, R.D., Piper, D.J.W., Shipboard Scientific Party, 1995. PODPIR (Proceedings of the Ocean Drilling Program, Initial Reports No. 155).
- Fontes, R.F.C., Castro, B.M., Beardsley, R.C., 2008. Numerical study of circulation on the inner Amazon Shelf. *Ocean Dyn.* 58, 187–198. <https://doi.org/10.1007/s10236-008-0139-4>
- Francini-Filho, R.B., Asp, N.E., Siegle, E., Hocevar, J., Lowyck, K., D’Avila, N., Vasconcelos, A.A., Baitelo, R., Rezende, C.E., Omachi, C.Y., Thompson, C.C., Thompson, F.L., 2018. Perspectives on the Great Amazon Reef: Extension, Biodiversity, and Threats. *Front. Mar. Sci.* 5, 142. <https://doi.org/10.3389/fmars.2018.00142>
- Fratantoni, D.M., Richardson, P.L., 2006. The Evolution and Demise of North Brazil Current Rings*. *J. Phys. Oceanogr.* 36, 1241–1264. <https://doi.org/10.1175/JPO2907.1>
- Friederichs, Y.L., Reis, A.T.D., Silva, C.G., Toulemonde, B., Maia, R.M.D.C., Guerra, J.V., 2013. Arquitetura sísmica do sistema fluvio-estuarino da Baía de Sepetiba preservado

- na estratigrafia rasa da plataforma adjacente, Rio de Janeiro, Brasil. *Braz. J. Geol.* 43, 124–138. <https://doi.org/10.5327/Z2317-48892013000100011>
- Galvão, T.A., Nolasco, M.C., 2013. Urbanization and coral reefs in Guarajuba Beach, north coast of Bahia, Brazil. *Ocean Coast. Manag.* 77, 50–58. <https://doi.org/10.1016/j.ocecoaman.2012.03.013>
- Garraffo, Z.D., Johns, W.E., P.Chassignet, E., Goni, G.J., 2003. North Brazil Current rings and transport of southern waters in a high resolution numerical simulation of the North Atlantic, in: *Elsevier Oceanography Series*. Elsevier, pp. 375–409. [https://doi.org/10.1016/S0422-9894\(03\)80155-1](https://doi.org/10.1016/S0422-9894(03)80155-1)
- Garziglia, S., Migeon, S., Ducassou, E., Loncke, L., Mascle, J., 2008. Mass-transport deposits on the Rosetta province (NW Nile deep-sea turbidite system, Egyptian margin): Characteristics, distribution, and potential causal processes. *Mar. Geol.* 250, 180–198. <https://doi.org/10.1016/j.margeo.2008.01.016>
- Garzione, C.N., Hoke, G.D., Libarkin, J.C., Withers, S., MacFadden, B., Eiler, J., Gosh, P., Mulch, A., 2008. Rise of the Andes. *Science* 320, 1304–1307.
- Gensac, E., Martinez, J.-M., Vantrepotte, V., Anthony, E.J., 2016. Seasonal and inter-annual dynamics of suspended sediment at the mouth of the Amazon river: The role of continental and oceanic forcing, and implications for coastal geomorphology and mud bank formation. *Cont. Shelf Res.* 118, 49–62. <https://doi.org/10.1016/j.csr.2016.02.009>
- Geyer, W.R., Beardsley, R.C., Lentz, S.J., Candela, J., Limeburner, R., Johns, W.E., Castro, B.M., Soares, I.D., 1996. Physical oceanography of the Amazon shelf. *Cont. Shelf Res.* 16, 575–616. [https://doi.org/10.1016/0278-4343\(95\)00051-8](https://doi.org/10.1016/0278-4343(95)00051-8)
- Geyer, W.R., Kineke, G.C., 1995. Observations of currents and water properties in the Amazon Frontal Zone. *J. Geophys. Res.* 100, 2321. <https://doi.org/10.1029/94JC02657>
- Giachini Tosetto, E., Bertrand, A., Neumann-Leitão, S., Nogueira Júnior, M., 2022. The Amazon River plume, a barrier to animal dispersal in the Western Tropical Atlantic. *Sci. Rep.* 12, 537. <https://doi.org/10.1038/s41598-021-04165-z>
- Giresse, P., Loncke, L., Heuret, A., Longueville, F., Casanova, A., Sadaoui, M., 2022. Beachrocks of the last low sea level, substrate of the barrier reef system along the outer Guiana shelf (preprint). In Review. <https://doi.org/10.21203/rs.3.rs-2028202/v2>
- Goes, M., Molinari, R., Da Silveira, I., Wainer, I., 2005. Retroreflections of the North Brazil Current during February 2002. *Deep Sea Res. Part Oceanogr. Res. Pap.* 52, 647–667. <https://doi.org/10.1016/j.dsr.2004.10.010>

- Gorini, C., Haq, B.U., dos Reis, A.T., Silva, C.G., Cruz, A., Soares, E., Grangeon, D., 2014. Late Neogene sequence stratigraphic evolution of the *Foz do Amazonas* Basin, Brazil. *Terra Nova* 26, 179–185. <https://doi.org/10.1111/ter.12083>
- Gradstein, F.M., Ogg, J.G., Schmitz, M., Ogg, G. (Eds.), 2012. The geologic time scale 2012, 1st ed. ed. Elsevier, Amsterdam ; Boston.
- Green, A.N., Cooper, J.A.G., Leuci, R., Thackeray, Z., 2013. Formation and preservation of an overstepped segmented lagoon complex on a high-energy continental shelf. *Sedimentology* 60, 1755–1768. <https://doi.org/10.1111/sed.12054>
- Gupta, R., Cheret, T., Pauget, F., Lacaze, S., 2008. Automated Geomodelling a Nigeria Case Study, in: 70th EAGE Conference and Exhibition Incorporating SPE EUROPEC 2008. Presented at the 70th EAGE Conference and Exhibition - Workshops and Fieldtrips, European Association of Geoscientists & Engineers, Rome, Italy,. <https://doi.org/10.3997/2214-4609.20147601>
- Haberle, S.G., 1999. Late Quaternary Vegetation and Climate Change in the Amazon Basin Based on a 50,000 Year Pollen Record from the Amazon Fan, ODP Site 932.
- Haq, B.U., Hardenbol, J., Vail, P.R., 1987. Chronology of Fluctuating Sea Levels Since the Triassic. *Science* 235, 1156–1167. <https://doi.org/10.1126/science.235.4793.1156>
- Harper, B.B., Droxler, A.W., Webster, J.M., Montagna, P., Yokoyama, Y., Humblet, M., Jorry, S.J., Beaufort, L., Tachikawa, K., Bard, E., Pons-Branchu, E., 2022. Shelf-edge deglacial reef establishment and subsequent partial demise: Response to distinct pulses of sea-level rise associated with environmental changes. *Coral Reefs Sea-Level Change Quat. Rec. Model.* 141–171. <https://doi.org/10.54780/IASSP49/05>
- Harris, P., Diaz, M.R., Eberli, G.P., 2019. The Formation and Distribution of Modern Ooids on Great Bahama Bank. *Annu. Rev. Mar. Sci.* 11, 491–516. <https://doi.org/10.1146/annurev-marine-010318-095251>
- Harris, S.E., Mix, A.C., 1999. Pleistocene Precipitation Balance in the Amazon Basin Recorded in Deep Sea Sediments. *Quat. Res.* 51, 14–26. <https://doi.org/10.1006/qres.1998.2008>
- Haug, G.H., Tiedemann, R., 1998. Effect of the formation of the Isthmus of Panama on Atlantic Ocean thermohaline circulation. *Nature* 393, 673–676. <https://doi.org/10.1038/31447>
- Hay, W.W., 1996. Tectonics and climate. *Geol. Rundsch.* 85, 409–437. <https://doi.org/10.1007/BF02369000>

- Hays, J.D., Imbrie, J., Shackleton, N.J., 1976. Variations in the Earth's Orbit: Pacemaker of the Ice Ages: For 500,000 years, major climatic changes have followed variations in obliquity and precession. *Science* 194, 1121–1132. https://doi.org/DOI: 10.1007/978-1-349-04699-7_16
- Haywood, A.M., Dowsett, H.J., Dolan, A.M., 2016. Integrating geological archives and climate models for the mid-Pliocene warm period. *Nat. Commun.* 7, 10646. <https://doi.org/10.1038/ncomms10646>
- Haywood, A.M., Dowsett, H.J., Valdes, P.J., Lunt, D.J., Francis, J.E., Sellwood, B.W., 2009. Introduction. Pliocene climate, processes and problems. *Philos. Trans. R. Soc. Math. Phys. Eng. Sci.* 367, 3–17. <https://doi.org/10.1098/rsta.2008.0205>
- He, Y., Xie, X., Kneller, B.C., Wang, Z., Li, X., 2013. Architecture and controlling factors of canyon fills on the shelf margin in the Qiongdongnan Basin, northern South China Sea. *Mar. Pet. Geol.* 41, 264–276. <https://doi.org/10.1016/j.marpetgeo.2012.03.002>
- Head, M.J., Gibbard, P.L., 2015. Early–Middle Pleistocene transitions: Linking terrestrial and marine realms. *Quat. Int.* 389, 7–46. <https://doi.org/10.1016/j.quaint.2015.09.042>
- Head, M.J., Gibbard, P.L., 2005. Early-Middle Pleistocene transitions: an overview and recommendation for the defining boundary. *Geol. Soc. Lond. Spec. Publ.* 247, 1–18. <https://doi.org/10.1144/GSL.SP.2005.247.01.01>
- Head, M.J., Pillans, B., Farquhar, S.A., 2008. The Early–Middle Pleistocene Transition: characterization and proposed guide for the defining boundary. *Episodes* 31, 255–259.
- Hein, C.J., FitzGerald, D.M., Cleary, W.J., Albernaz, M.B., De Menezes, J.T., Klein, A.H.D.F., 2013. Evidence for a transgressive barrier within a regressive strandplain system: Implications for complex coastal response to environmental change. *Sedimentology* 60, 469–502. <https://doi.org/10.1111/j.1365-3091.2012.01348.x>
- Helland-Hansen, W., Gjelberg, J.G., 1994. Conceptual basis and variability in sequence stratigraphy: a different perspective. *Sediment. Geol.* 92, 31–52.
- Herbert, T.D., Lawrence, K.T., Tzanova, A., Peterson, L.C., Caballero-Gill, R., Kelly, C.S., 2016. Late Miocene global cooling and the rise of modern ecosystems. *Nat. Geosci.* 9, 843–847. <https://doi.org/10.1038/ngeo2813>
- Hernández-Molina, F.J., Llave, E., Preu, B., Ercilla, G., Fontan, A., Bruno, M., Serra, N., Gomiz, J.J., Brackenridge, R.E., Sierro, F.J., Stow, D.A.V., García, M., Juan, C., Sandoval, N., Arnaiz, A., 2014. Contourite processes associated with the Mediterranean Outflow Water after its exit from the Strait of Gibraltar: Global and conceptual implications. *Geology* 42, 227–230. <https://doi.org/10.1130/G35083.1>

- Hernández-Molina, F.J., Paterlini, M., Violante, R., Marshall, P., De Isasi, M., Somoza, L., Rebesco, M., 2009. Contourite depositional system on the Argentine Slope: An exceptional record of the influence of Antarctic water masses. *Geology* 37, 507–510. <https://doi.org/10.1130/G25578A.1>
- Hilgen, F.J., Hinnov, L.A., Abdul Aziz, H., Abels, H.A., Batenburg, S., Bosmans, J.H.C., De Boer, B., Hüsing, S.K., Kuiper, K.F., Lourens, L.J., Rivera, T., Tuenter, E., Van De Wal, R.S.W., Wotzlaw, J.-F., Zeeden, C., 2015. Stratigraphic continuity and fragmentary sedimentation: the success of cyclostratigraphy as part of integrated stratigraphy. *Geol. Soc. Lond. Spec. Publ.* 404, 157–197. <https://doi.org/10.1144/SP404.12>
- Hinestrosa, G., Webster, J.M., Beaman, R.J., Anderson, L.M., 2014. Seismic stratigraphy and development of the shelf-edge reefs of the Great Barrier Reef, Australia. *Mar. Geol.* 353, 1–20. <https://doi.org/10.1016/j.margeo.2014.03.016>
- Hinnov, L.A., 2013. Cyclostratigraphy and its revolutionizing applications in the earth and planetary sciences. *Geol. Soc. Am. Bull.* 125, 1703–1734. <https://doi.org/10.1130/B30934.1>
- Hinnov, L.A., 2000. New Perspectives on Orbitally Forced Stratigraphy. *Annu. Rev. Earth Planet. Sci.* 28, 419–475. <https://doi.org/10.1146/annurev.earth.28.1.419>
- Hodell, D.A., Channell, J.E.T., Curtis, J.H., Romero, O.E., Röhl, U., 2008. Onset of “Hudson Strait” Heinrich events in the eastern North Atlantic at the end of the middle Pleistocene transition (~640 ka)?: PLEISTOCENE HEINRICH EVENTS. *Paleoceanography* 23, n/a-n/a. <https://doi.org/10.1029/2008PA001591>
- Hoorn, C., 1997. Palynology of the Pleistocene glacial/interglacial cycles of the Amazon Fan (Holes 940A, 944A, and 946A)., in: Flood, R.D., Piper, D.J.W., Klaus, A., Peterson, L.C. (Eds.), *Proceedings of the Ocean Drilling Program, 155 Scientific Results, Proceedings of the Ocean Drilling Program. Ocean Drilling Program*, pp. 397–410. <https://doi.org/10.2973/odp.proc.sr.155.1997>
- Hoorn, C., 1994. Fluvial palaeoenvironments in the intracratonic Amazonas Basin (Early Miocene-early Middle Miocene, Colombia). *Palaeogeogr. Palaeoclimatol. Palaeoecol.* 109, 1–54. [https://doi.org/10.1016/0031-0182\(94\)90117-1](https://doi.org/10.1016/0031-0182(94)90117-1)
- Hoorn, C., 1993. Marine incursions and the influence of Andean tectonics on the Miocene depositional history of northwestern Amazonia: results of a palynostratigraphic study. *Palaeogeogr. Palaeoclimatol. Palaeoecol.* 105, 267–309. [https://doi.org/10.1016/0031-0182\(93\)90087-Y](https://doi.org/10.1016/0031-0182(93)90087-Y)

- Hoorn, C., Bogotá-A, G.R., Romero-Baez, M., Lammertsma, E.I., Flantua, S.G.A., Dantas, E.L., Dino, R., do Carmo, D.A., Chemale, F., 2017. The Amazon at sea: Onset and stages of the Amazon River from a marine record, with special reference to Neogene plant turnover in the drainage basin. *Glob. Planet. Change* 153, 51–65. <https://doi.org/10.1016/j.gloplacha.2017.02.005>
- Hoorn, C., Guerrero, J., Sarmiento, G.A., Lorente, M.A., 1995. Andean tectonics as a cause for changing drainage patterns in Miocene northern South America. *Geology* 23, 237. [https://doi.org/10.1130/0091-7613\(1995\)023<0237:ATAACF>2.3.CO;2](https://doi.org/10.1130/0091-7613(1995)023<0237:ATAACF>2.3.CO;2)
- Hoorn, C., Paxton, C.G.M., Crampton, W.G.R., Burgess, P., Marshall, L.G., Lundberg, J.G., Räsänen, M.E., Linna, A.M., 1996. Miocene Deposits in the Amazonian Foreland Basin. *Science* 273, 122–122. <https://doi.org/10.1126/science.273.5271.122>
- Hoorn, C., Wesselingh, F.P., Ter Steege, H., Bermudez, M.A., Mora, A., Sevink, J., Sanmartín, I., Sanchez-Meseguer, A., Anderson, C.L., Figueiredo, J.P., Jaramillo, C., Riff, D., Negri, F.R., Hooghiemstra, H., Lundberg, J., Stadler, T., Särkinen, T., Antonelli, A., 2010. Amazonia Through Time: Andean Uplift, Climate Change, Landscape Evolution, and Biodiversity. *Science* 330, 927–931. <https://doi.org/10.1126/science.1194585>
- Horbe, A.M.C., Motta, M.B., de Almeida, C.M., Dantas, E.L., Vieira, L.C., 2013. Provenance of Pliocene and recent sedimentary deposits in western Amazônia, Brazil: Consequences for the paleodrainage of the Solimões-Amazonas River. *Sediment. Geol.* 296, 9–20. <https://doi.org/10.1016/j.sedgeo.2013.07.007>
- Horton, B.K., 2018. Sedimentary record of Andean mountain building. *Earth-Sci. Rev.* 178, 279–309. <https://doi.org/10.1016/j.earscirev.2017.11.025>
- House, M.R., 1995. Orbital forcing timescales: an introduction. *Geol. Soc. Lond. Spec. Publ.* 85, 1–18. <https://doi.org/10.1144/GSL.SP.1995.085.01.01>
- Hu, C., Montgomery, E., Schmitt, R., Mullerkarger, F., 2004. The dispersal of the Amazon and Orinoco River water in the tropical Atlantic and Caribbean Sea: Observation from space and S-PALACE floats. *Deep Sea Res. Part II Top. Stud. Oceanogr.* 51, 1151–1171. [https://doi.org/10.1016/S0967-0645\(04\)00105-5](https://doi.org/10.1016/S0967-0645(04)00105-5)
- Hungerbühler, D., Steinmann, M., Winkler, W., Seward, D., Egüez, A., Peterson, D.E., Helg, U., Hammer, C., 2002. Neogene stratigraphy and Andean geodynamics of southern Ecuador. *Earth-Sci. Rev.* 57, 75–124. [https://doi.org/10.1016/S0012-8252\(01\)00071-X](https://doi.org/10.1016/S0012-8252(01)00071-X)

- Hunt, D., Tucker, M.E., 1992. Stranded parasequences and the forced regressive wedge systems tract: deposition during base-level fall. *Sediment. Geol.* 81, 1–9.
[https://doi.org/10.1016/0037-0738\(92\)90052-S](https://doi.org/10.1016/0037-0738(92)90052-S)
- Hunt, D.W., 1992. Application Of Sequence Stratigraphic Concepts To The Cretaceous Urganian Carbonate Platform, Southeast France. Durham University.
- Imbrie, J., 1985. A theoretical framework for the Pleistocene ice ages: William Smith Lecture. *J. Geol. Soc.* 142, 417–432.
- Immonen, N., 2013. Surface microtextures of ice-rafted quartz grains revealing glacial ice in the Cenozoic Arctic. *Palaeogeogr. Palaeoclimatol. Palaeoecol.* 374, 293–302.
<https://doi.org/10.1016/j.palaeo.2013.02.003>
- Jacobs, M.B., Ewing, M., 1969. Suspended particulate matter: concentration in the major oceans. *Science* 163, 380–383.
- Jakob, K.A., Wilson, P.A., Pross, J., Ezard, T.H.G., Fiebig, J., Repschläger, J., Friedrich, O., 2020. A new sea-level record for the Neogene/Quaternary boundary reveals transition to a more stable East Antarctic Ice Sheet. *Proc. Natl. Acad. Sci.* 117, 30980–30987.
<https://doi.org/10.1073/pnas.2004209117>
- James, D.E., Sacks, I.S., 1999. Cenozoic formation of the Central Andes: A geophysical perspective.
- Jansen, E., Sjøholm, J., 1991. Reconstruction of glaciation over the past 6 Myr from ice-borne deposits in the Norwegian Sea. *Nature* 349, 600–603.
<https://doi.org/10.1038/349600a0>
- Jaramillo, C., Hoorn, C., Perrigo, A., Antonelli, A., 2018. Evolution of the Isthmus of Panama: biological, paleoceanographic and paleoclimatological implications. *Montains Clim. Biodivers.* 4, 323–338.
- Jegou, I., Savoye, B., Pirmez, C., Droz, L., 2008. Channel-mouth lobe complex of the recent Amazon Fan: The missing piece. *Mar. Geol.* 252, 62–77.
<https://doi.org/10.1016/j.margeo.2008.03.004>
- Johns, W.E., Lee, T.N., Beardsley, R.C., Candela, J., Limeburner, R., Castro, B., 1998. Annual Cycle and Variability of the North Brazil Current. *J. Phys. Oceanogr.* 28, 103–128. [https://doi.org/10.1175/1520-0485\(1998\)028<0103:ACAVOT>2.0.CO;2](https://doi.org/10.1175/1520-0485(1998)028<0103:ACAVOT>2.0.CO;2)
- Johns, W.E., Lee, T.N., Schott, F.A., Zantopp, R.J., Evans, R.H., 1990. The North Brazil Current retroflexion: Seasonal structure and eddy variability. *J. Geophys. Res.* 95, 22103. <https://doi.org/10.1029/JC095iC12p22103>

- Johns, W.E., Zantopp, R.J., Goni, Gustavo.J., 2003. Cross-gyre transport by North Brazil Current rings, in: Elsevier Oceanography Series. Elsevier, pp. 411–441.
[https://doi.org/10.1016/S0422-9894\(03\)80156-3](https://doi.org/10.1016/S0422-9894(03)80156-3)
- Jouzel, J., Masson-Delmotte, V., Cattani, O., Dreyfus, G., Falourd, S., Hoffmann, G., Minster, B., Nouet, J., Barnola, J.M., Chappellaz, J., Fischer, H., Gallet, J.C., Johnsen, S., Leuenberger, M., Loulergue, L., Luethi, D., Oerter, H., Parrenin, F., Raisbeck, G., Raynaud, D., Schilt, A., Schwander, J., Selmo, E., Souchez, R., Spahni, R., Stauffer, B., Steffensen, J.P., Stenni, B., Stocker, T.F., Tison, J.L., Werner, M., Wolff, E.W., 2007. Orbital and Millennial Antarctic Climate Variability over the Past 800,000 Years. *Science* 317, 793–796. <https://doi.org/10.1126/science.1141038>
- Kemp, A.E.S., Grigorov, I., Pearce, R.B., Naveira Garabato, A.C., 2010. Migration of the Antarctic Polar Front through the mid-Pleistocene transition: evidence and climatic implications. *Quat. Sci. Rev.* 29, 1993–2009.
<https://doi.org/10.1016/j.quascirev.2010.04.027>
- Kempf, M., 1970. Notes on the benthic bionomy of the N-NE Brazilian shelf. *Mar Biol.*
- Kendall, C.G.St.C., Schlager, W., 1981. Carbonates and relative changes in sea level. *Mar. Geol.* 44, 181–212. [https://doi.org/10.1016/0025-3227\(81\)90118-3](https://doi.org/10.1016/0025-3227(81)90118-3)
- Khanna, P., Droxler, A.W., Nittrouer, J.A., Tunnell Jr, J.W., Shirley, T.C., 2017. Coralgall reef morphology records punctuated sea-level rise during the last deglaciation. *Nat. Commun.* 8, 1046. <https://doi.org/10.1038/s41467-017-00966-x>
- Kleiven, H.F., Jansen, E., Fronval, T., Smith, T.M., 2002. Intensification of Northern Hemisphere glaciations in the circum Atlantic region (3.5–2.4 Ma)–ice-rafted detritus evidence.
- Knies, J., Gaina, C., 2008. Middle Miocene ice sheet expansion in the Arctic: Views from the Barents Sea: ICE SHEET EXPANSION IN THE ARCTIC. *Geochem. Geophys. Geosystems* 9, n/a-n/a. <https://doi.org/10.1029/2007GC001824>
- Kuehl, S.A., DeMaster, D.J., Nittrouer, C.A., 1986. Nature of sediment accumulation on the Amazon continental shelf. *Cont. Shelf Res.* 6, 209–225. [https://doi.org/10.1016/0278-4343\(86\)90061-0](https://doi.org/10.1016/0278-4343(86)90061-0)
- Kump, L.R., Brantley, S.L., Arthur, M.A., 2000. Chemical Weathering, Atmospheric CO₂, and Climate. *Annu. Rev. Earth Planet. Sci.* 28, 611–667.
<https://doi.org/10.1146/annurev.earth.28.1.611>
- Lafosse, M., Gorini, C., Le Roy, P., Alonso, B., d’Acremont, E., Ercilla, G., Rabineau, M., Vázquez, J.T., Rabaute, A., Ammar, A., 2018. Late Pleistocene-Holocene history of a

- tectonically active segment of the continental margin (Nekor basin, Western Mediterranean, Morocco). *Mar. Pet. Geol.* 97, 370–389.
<https://doi.org/10.1016/j.marpetgeo.2018.07.022>
- Lambeck, K., Chappell, J., 2001. Sea Level Change Through the Last Glacial Cycle. *Science* 292, 679–686. <https://doi.org/10.1126/science.1059549>
- Laskar, J., 1999. The limits of Earth orbital calculations for geological time-scale use. *Philos. Trans. R. Soc. Lond. Ser. Math. Phys. Eng. Sci.* 357, 1735–1759.
<https://doi.org/10.1098/rsta.1999.0399>
- Laskar, J., Fienga, A., Gastineau, M., Manche, H., 2011. La2010: a new orbital solution for the long-term motion of the Earth. *Astron. Astrophys.* 532, A89.
<https://doi.org/10.1051/0004-6361/201116836>
- Laskar, J., Joutel, F., Boudin, F., 1993. Orbital, precessional, and insolation quantities for the Earth from -20 Myr to + 10 Myr. *Astron. Astrophys.* 270, 522–533.
- Laskar, J., Robutel, P., Joutel, F., Gastineau, M., Correia, A.C.M., Levrard, B., 2004. A long-term numerical solution for the insolation quantities of the Earth. *Astron. Astrophys.* 428, 261–285. <https://doi.org/10.1051/0004-6361:20041335>
- Latrubesse, E.M., Cozzuol, M., da Silva-Caminha, S.A.F., Rigsby, C.A., Absy, M.L., Jaramillo, C., 2010. The Late Miocene paleogeography of the Amazon Basin and the evolution of the Amazon River system. *Earth-Sci. Rev.* 99, 99–124.
<https://doi.org/10.1016/j.earscirev.2010.02.005>
- Lavagnino, A.C., Bastos, A.C., Amado Filho, G.M., De Moraes, F.C., Araujo, L.S., De Moura, R.L., 2020. Geomorphometric Seabed Classification and Potential Megahabitat Distribution in the Amazon Continental Margin. *Front. Mar. Sci.* 7, 190.
<https://doi.org/10.3389/fmars.2020.00190>
- Lazarus, E.D., Armstrong, S., 2015. Self-organized pattern formation in coastal barrier washover deposits. *Geology* 43, 363–366. <https://doi.org/10.1130/G36329.1>
- Le Bouteiller, P., Lafuerza, S., Charléty, J., Reis, A.T., Granjeon, D., Delprat-Jannaud, F., Gorini, C., 2019. A new conceptual methodology for interpretation of mass transport processes from seismic data. *Mar. Pet. Geol.* 103, 438–455.
<https://doi.org/10.1016/j.marpetgeo.2018.12.027>
- Leach, A.S., Wallace, M.W., 2001. Cenozoic submarine canyon systems in cool water carbonates from the Otway Basin, Victoria, Australia. Presented at the PESA East Australasian Basins Symposium, Melbourne, Victoria, Australia, pp. 465–473.

- Leão, Z.M.A.N., Kikuchi, R.K.P., Ferreira, B.P., Neves, E.G., Sovierzoski, H.H., Oliveira, M.D.M., Maida, M., Correia, M.D., Johnsson, R., 2016. Brazilian coral reefs in a period of global change: A synthesis. *Braz. J. Oceanogr.* 64, 97–116.
<https://doi.org/10.1590/S1679-875920160916064sp2>
- Lentz, S.J., 1995. Seasonal variations in the horizontal structure of the Amazon Plume inferred from historical hydrographic data. *J. Geophys. Res.* 100, 2391.
<https://doi.org/10.1029/94JC01847>
- Lentz, S.J., Fewings, M.R., 2012. The Wind- and Wave-Driven Inner-Shelf Circulation. *Annu. Rev. Mar. Sci.* 4, 317–343. <https://doi.org/10.1146/annurev-marine-120709-142745>
- Li, M., Hinnov, L., Kump, L., 2019. Acycle: Time-series analysis software for paleoclimate research and education. *Comput. Geosci.* 127, 12–22.
<https://doi.org/10.1016/j.cageo.2019.02.011>
- Lin, L., Khider, D., Lisiecki, L.E., Lawrence, C.E., 2014. Probabilistic sequence alignment of stratigraphic records. *Paleoceanography* 29, 976–989.
<https://doi.org/10.1002/2014PA002713>
- Lisiecki, L.E., Raymo, M.E., 2007. Plio–Pleistocene climate evolution: trends and transitions in glacial cycle dynamics. *Quat. Sci. Rev.* 26, 56–69.
<https://doi.org/10.1016/j.quascirev.2006.09.005>
- Lisiecki, L.E., Raymo, M.E., 2005. A Pliocene–Pleistocene stack of 57 globally distributed benthic $\delta^{18}\text{O}$ records. *Paleoceanography* 20. <https://doi.org/10.1029/2004PA001071>
- Lobo, F.J., Ridente, D., 2014. Stratigraphic architecture and spatio-temporal variability of high-frequency (Milankovitch) depositional cycles on modern continental margins: An overview. *Mar. Geol.* 352, 215–247. <https://doi.org/10.1016/j.margeo.2013.10.009>
- Lomask, J., Guitton, A., 2007. Volumetric flattening: an interpretation tool. *Lead. Edge* 26, 888–897. <https://doi.org/10.1190/1.2756869>
- Lopez, M., 2001. Architecture and depositional pattern of the Quaternary deep-sea fan of the Amazon. *Mar. Pet. Geol.* 18, 479–486. [https://doi.org/10.1016/S0264-8172\(00\)00071-4](https://doi.org/10.1016/S0264-8172(00)00071-4)
- Lumley, D.E., 2001. Time-lapse seismic reservoir monitoring. *GEOPHYSICS* 66, 50–53.
<https://doi.org/10.1190/1.1444921>
- Lüthi, D., Le Floch, M., Bereiter, B., Blunier, T., Barnola, J.-M., Siegenthaler, U., Raynaud, D., Jouzel, J., Fischer, H., Kawamura, K., Stocker, T.F., 2008. High-resolution carbon

- dioxide concentration record 650,000–800,000 years before present. *Nature* 453, 379–382. <https://doi.org/10.1038/nature06949>
- Lutome, M.S., Lin, C., Chunmei, D., Zhang, X., Bishanga, J.M., 2022. 3D geocellular modeling for reservoir characterization of lacustrine turbidite reservoirs: Submember 3 of the third member of the Eocene Shahejie Formation, Dongying depression, Eastern China. *Pet. Res.* 7, 47–61. <https://doi.org/10.1016/j.ptlrs.2021.08.005>
- Lynch-Stieglitz, J., Adkins, J.F., Curry, W.B., Dokken, T., Hall, I.R., Herguera, J.C., Hirschi, J.J.-M., Ivanova, E.V., Kissel, C., Marchal, O., Marchitto, T.M., McCave, I.N., McManus, J.F., Mulitza, S., Ninnemann, U., Peeters, F., Yu, E.-F., Zahn, R., 2007. Atlantic Meridional Overturning Circulation During the Last Glacial Maximum. *Science* 316, 66–69. <https://doi.org/10.1126/science.1137127>
- Malhi, Y., Roberts, J.T., Betts, R.A., Killeen, T.J., Li, W., Nobre, C.A., 2008. Climate Change, Deforestation, and the Fate of the Amazon. *Science* 319, 169–172. <https://doi.org/10.1126/science.1146961>
- Marincovich, L., Gladenkov, A.Yu., 1999. Evidence for an early opening of the Bering Strait. *Nature* 397, 149–151. <https://doi.org/10.1038/16446>
- Marshall, L.G., Lundberg, J.G., 1996. Miocene Deposits in the Amazonian Foreland Basin. *Science* 273, 123–124. <https://doi.org/10.1126/science.273.5271.123.b>
- Martinez, M., Dera, G., 2015. Orbital pacing of carbon fluxes by a ~9-My eccentricity cycle during the Mesozoic. *Proc. Natl. Acad. Sci.* 112, 12604–12609. <https://doi.org/10.1073/pnas.1419946112>
- Martinez-Martos, M., Galindo-Zaldivar, J., Lobo, F.J., Pedrera, A., Ruano, P., Lopez-Chicano, M., Ortega-Sánchez, M., 2016. Buried marine-cut terraces and submerged marine-built terraces: The Carchuna-Calahonda coastal area (southeast Iberian Peninsula). *Geomorphology* 264, 29–40. <https://doi.org/10.1016/j.geomorph.2016.04.010>
- Maslin, M., Knutz, P.C., Ramsay, T., 2006. Millennial-scale sea-level control on avulsion events on the Amazon Fan. *Quat. Sci. Rev.* 25, 3338–3345. <https://doi.org/10.1016/j.quascirev.2006.10.012>
- Maslin, M., Mikkelsen, N., Vilela, C., Haq, B., 1998a. Sea-level –and gas-hydrate–controlled catastrophic sediment failures of the Amazon Fan. *Geology* 26, 1107. [https://doi.org/10.1130/0091-7613\(1998\)026<1107:SLAGHC>2.3.CO;2](https://doi.org/10.1130/0091-7613(1998)026<1107:SLAGHC>2.3.CO;2)

- Maslin, M.A., Li, X.S., Loutre, M.-F., Berger, A., 1998b. The contribution of orbital forcing to the progressive intensification of Northern Hemisphere glaciation. *Quat. Sci. Rev.* 17, 411–426. [https://doi.org/10.1016/S0277-3791\(97\)00047-4](https://doi.org/10.1016/S0277-3791(97)00047-4)
- Maslin, M.A., Haug, G.H., Sarnthein, M., Tiedemann, R., 1996. The progressive intensification of northern hemisphere glaciation as seen from the North Pacific.
- Maslin, M.A., Haug, G.H., Sarnthein, M., Tiedemann, R., Erlenkeuser, H., Stax, R., 1995. Northwest Pacific site 882: The initiation of Northern Hemisphere Glaciation. *Proc. Ocean Drill. Program, Proceedings of the Ocean Drilling Program* 145. <https://doi.org/10.2973/odp.proc.sr.145.1995>
- Mason, C.C., Romans, B.W., Stockli, D.F., Mapes, R.W., Fildani, A., 2019. Detrital zircons reveal sea-level and hydroclimate controls on Amazon River to deep-sea fan sediment transfer. *Geology* 47, 563–567. <https://doi.org/10.1130/G45852.1>
- McClymont, E.L., Sosdian, S.M., Rosell-Melé, A., Rosenthal, Y., 2013. Pleistocene sea-surface temperature evolution: Early cooling, delayed glacial intensification, and implications for the mid-Pleistocene climate transition. *Earth-Sci. Rev.* 123, 173–193. <https://doi.org/10.1016/j.earscirev.2013.04.006>
- Meade, R.H., Dunne, T., Richey, J.E., Santos, U.D.M., Salati, E., 1985. Storage and Remobilization of Suspended Sediment in the Lower Amazon River of Brazil. *Science* 228.
- Melles, M., Brigham-Grette, J., Minyuk, P.S., Nowaczyk, N.R., Wennrich, V., DeConto, R.M., Anderson, P.M., Andreev, A.A., Coletti, A., Cook, T.L., Haltia-Hovi, E., Kukkonen, M., Lozhkin, A.V., Rosén, P., Tarasov, P., Vogel, H., Wagner, B., 2012. 2.8 Million Years of Arctic Climate Change from Lake El'gygytyn, NE Russia. *Science* 337, 315–320. <https://doi.org/10.1126/science.1222135>
- Merkel, R.H., 1979. Geologic Analysis, in: *Well Log Formation Evaluation*.
- Meyers, S.R., Sageman, B.B., 2007. Quantification of deep-time orbital forcing by average spectral misfit. *Am. J. Sci.* 307, 773–792. <https://doi.org/10.2475/05.2007.01>
- Miller, K.G., Browning, J.V., Schmelz, W.J., Kopp, R.E., Montain, G.S., Wright, J.D., 2020. Cenozoic sea-level and cryospheric evolution from deep-sea geochemical and continental margin records. *Sci. Adv.* 6.
- Milliman, J.D., 2001. River inputs. *Encycl. Ocean Sci.* <https://doi.org/doi:10.1006/rwos.2001.0074>.

- Milliman, J.D., Barretto, H.T., 1975. Relict magnesian calcite oolite and subsidence of the Amazon shelf. *Sedimentology* 22, 137–145. <https://doi.org/10.1111/j.1365-3091.1975.tb00288.x>
- Milliman, J.D., Meade, R.H., 1983. World-Wide Delivery of River Sediment to the Oceans. *J. Geol.* 91, 1–21. <https://doi.org/10.1086/628741>
- Milliman, J.D., Summerhayes, C.P., Barretto, H.T., 1975. Quaternary Sedimentation on the Amazon Continental Margin: A Model. *Geol. Soc. Am. Bull.* 86, 610. [https://doi.org/10.1130/0016-7606\(1975\)86<610:QSOTAC>2.0.CO;2](https://doi.org/10.1130/0016-7606(1975)86<610:QSOTAC>2.0.CO;2)
- Mitchum, R.M., Vail, P.R., Thompson, S., 1977. Seismic Stratigraphy and Global Changes of Sea Level, Part 2 The Depositional Sequence as a Basic Unit for Stratigraphic Analysis¹, in: *Seismic Stratigraphy — Applications to Hydrocarbon Exploration*. American Association of Petroleum Geologists. <https://doi.org/10.1306/M26490C4>
- Mitsui, T., Boers, N., 2022. Machine learning approach reveals strong link between obliquity amplitude increase and the Mid-Brunhes transition. *Quat. Sci. Rev.* 277, 107344. <https://doi.org/10.1016/j.quascirev.2021.107344>
- Molleri, G.S.F., Novo, E.M.L. de M., Kampel, M., 2010. Space-time variability of the Amazon River plume based on satellite ocean color. *Cont. Shelf Res.* 30, 342–352. <https://doi.org/10.1016/j.csr.2009.11.015>
- Montgomery, D.R., Balco, G., Willett, S.D., 2001. Climate, tectonics, and the morphology of the Andes. *Geology* 29, 579. [https://doi.org/10.1130/0091-7613\(2001\)029<0579:CTATMO>2.0.CO;2](https://doi.org/10.1130/0091-7613(2001)029<0579:CTATMO>2.0.CO;2)
- Mora, A., Baby, P., Roddaz, M., Parra, M., Brusset, S., Hermoza, W., Espurt, N., 2010. Tectonic History of the Andes and Sub-Andean Zones: Implications for the Development of the Amazon Drainage Basin, in: Hoorn, C., Wesselingh, F.P. (Eds.), *Amazonia: Landscape and Species Evolution*. Wiley, pp. 38–60. <https://doi.org/10.1002/9781444306408.ch4>
- Moran, K., Backman, J., Brinkhuis, H., Clemens, S.C., Cronin, T., Dickens, G.R., Eynaud, F., Gattacceca, J., Jakobsson, M., Jordan, R.W., Kaminski, M., King, J., Koc, N., Krylov, A., Martinez, N., Matthiessen, J., McInroy, D., Moore, T.C., Onodera, J., O'Regan, M., Pälike, H., Rea, B., Rio, D., Sakamoto, T., Smith, D.C., Stein, R., St John, K., Suto, I., Suzuki, N., Takahashi, K., Watanabe, M., Yamamoto, M., Farrell, J., Frank, M., Kubik, P., Jokat, W., Kristoffersen, Y., 2006. The Cenozoic palaeoenvironment of the Arctic Ocean. *Nature* 441, 601–605. <https://doi.org/10.1038/nature04800>

- Moura, R.L., Amado-Filho, G.M., Moraes, F.C., Brasileiro, P.S., Salomon, P.S., Mahiques, M.M., Bastos, A.C., Almeida, M.G., Silva, J.M., Araujo, B.F., Brito, F.P., Rangel, T.P., Oliveira, B.C.V., Bahia, R.G., Paranhos, R.P., Dias, R.J.S., Siegle, E., Figueiredo, A.G., Pereira, R.C., Leal, C.V., Hajdu, E., Asp, N.E., Gregoracci, G.B., Neumann-Leitão, S., Yager, P.L., Francini-Filho, R.B., Fróes, A., Campeão, M., Silva, B.S., Moreira, A.P.B., Oliveira, L., Soares, A.C., Araujo, L., Oliveira, N.L., Teixeira, J.B., Valle, R.A.B., Thompson, C.C., Rezende, C.E., Thompson, F.L., 2016. An extensive reef system at the Amazon River mouth. *Sci. Adv.* 2, e1501252. <https://doi.org/10.1126/sciadv.1501252>
- Moura, R.L., Martins Rodrigues, M.C., Francini-Filho, R.B., Sazima, I., 1999. Unexpected richness of reef corals near the southern Amazon River mouth. *Coral Reefs* 18, 170–170. <https://doi.org/10.1007/s003380050175>
- Mpodozis, C., Ramos, V., 1990. The andes of Chile and Argentina., *Geology of the Andes and Its Relation to Hydrocarbon and Mineral Resources: Circum-Pacific Council for Energy and Mineral Resources, Earth Science Series.*
- Muller-Karger, F.E., McClain, C.R., Richardson, P.L., 1988. The dispersal of the Amazon's water. *Nature* 333, 56–59. <https://doi.org/10.1038/333056a0>
- Muñoz, A., Acosta, J., Cristobo, J., Druet, M., Uchupi, E., 2013. Geomorphology and shallow structure of a segment of the Atlantic Patagonian margin. *Earth-Sci. Rev.* 121, 73–95. <https://doi.org/10.1016/j.earscirev.2013.03.002>
- Murray, C.D., Dermott, S.F., 1999. *Solar system dynamics.* Cambridge University Press, Cambridge ; New York.
- Mutti, E., Bernoulli, D., Lucchi, F.R., Tinterri, R., 2009. Turbidites and turbidity currents from Alpine 'flysch' to the exploration of continental margins. *Sedimentology* 56, 267–318. <https://doi.org/10.1111/j.1365-3091.2008.01019.x>
- Nace, T.E., Baker, P.A., Dwyer, G.S., Silva, C.G., Rigsby, C.A., Burns, S.J., Giosan, L., Otto-Bliesner, B., Liu, Z., Zhu, J., 2014. The role of North Brazil Current transport in the paleoclimate of the Brazilian Nordeste margin and paleoceanography of the western tropical Atlantic during the late Quaternary. *Palaeogeogr. Palaeoclimatol. Palaeoecol.* 415, 3–13. <https://doi.org/10.1016/j.palaeo.2014.05.030>
- Newall, R.S., Atkinson, R.J.C., 1956. Stonehenge: A review. *Antiquity* 30, 137–141. <https://doi.org/doi:10.1017/S0003598X00026648>
- Nikiema, O., Devenon, J.-L., Baklouti, M., 2007. Numerical modeling of the Amazon River plume. *Cont. Shelf Res.* 27, 873–899. <https://doi.org/10.1016/j.csr.2006.12.004>

- Nikolov, T., Petrov, N., 2014. MAIN FACTORS INFLUENCING CLIMATE CHANGE: A REVIEW.
- Nittrouer, C.A., DeMaster, D.J., 1996. The Amazon shelf setting: tropical, energetic, and influenced by a large river. *Cont. Shelf Res.* 16, 553–573.
[https://doi.org/10.1016/0278-4343\(95\)00069-0](https://doi.org/10.1016/0278-4343(95)00069-0)
- Nittrouer, C.A., Kuehl, S.A., Demaster, D.J., Kowsmann, R.O., 1986. The deltaic nature of Amazon shelf sedimentation. *Geol. Soc. Am. Bull.* 97, 444.
[https://doi.org/10.1130/0016-7606\(1986\)97<444:TDNOAS>2.0.CO;2](https://doi.org/10.1130/0016-7606(1986)97<444:TDNOAS>2.0.CO;2)
- Nittrouer, C.A., Wright, L.D., 1994. Transport of particles across continental shelves. *Rev. Geophys.* 32, 85. <https://doi.org/10.1029/93RG02603>
- Noble, D.C., McKEE, E.H., Mourier, T., Mégard, F., 1990. Cenozoic stratigraphy, magmatic activity, compressive deformation, and uplift in northern Peru. *Geol. Soc. Am. Bull.* 102, 1105–1113. [https://doi.org/10.1130/0016-7606\(1990\)102<1105:CSMACD>2.3.CO;2](https://doi.org/10.1130/0016-7606(1990)102<1105:CSMACD>2.3.CO;2)
- Nogueira, A.C.R., Silveira, R., Guimarães, J.T.F., 2013. Neogene–Quaternary sedimentary and paleovegetation history of the eastern Solimões Basin, central Amazon region. *J. South Am. Earth Sci.* 46, 89–99. <https://doi.org/10.1016/j.jsames.2013.05.004>
- O’Dea, A., Lessios, H.A., Coates, A.G., Eytan, R.I., Restrepo-Moreno, S.A., Cione, A.L., Collins, L.S., De Queiroz, A., Farris, D.W., Norris, R.D., Stallard, R.F., Woodburne, M.O., Aguilera, O., Aubry, M.-P., Berggren, W.A., Budd, A.F., Cozzuol, M.A., Coppard, S.E., Duque-Caro, H., Finnegan, S., Gasparini, G.M., Grossman, E.L., Johnson, K.G., Keigwin, L.D., Knowlton, N., Leigh, E.G., Leonard-Pingel, J.S., Marko, P.B., Pyenson, N.D., Rachello-Dolmen, P.G., Soibelzon, E., Soibelzon, L., Todd, J.A., Vermeij, G.J., Jackson, J.B.C., 2016. Formation of the Isthmus of Panama. *Sci. Adv.* 2, e1600883. <https://doi.org/10.1126/sciadv.1600883>
- Paillard, D., Labeyrie, L., Yiou, P., 1996. Macintosh Program performs time-series analysis. *Eos Trans. Am. Geophys. Union* 77, 379–379. <https://doi.org/10.1029/96EO00259>
- Parra, S.M., Valle-Levinson, A., Mariño-Tapia, I., Enriquez, C., Candela, J., Sheinbaum, J., 2016. Seasonal variability of saltwater intrusion at a point-source submarine groundwater discharge: Seasonal intrusion at submarine spring. *Limnol. Oceanogr.* 61, 1245–1258. <https://doi.org/10.1002/lno.10286>
- Paumard, V., Bourget, J., Durot, B., Lacaze, S., Wilson, T., 2018. Full-volume interpretation methods: Applications for quantitative seismic stratigraphy and geomorphology of the

- Lower Barrow Group, Northwest Australia. ASEG Ext. Abstr. 2018, 1–6.
<https://doi.org/10.1071/ASEG2018abP009>
- Payton, C.E., 1977. Seismic stratigraphy—applications to hydrocarbon exploration, American Association of Petroleum Geologists.
- Perovano, R., Reis, A.T.D., Silva, C.G., Vendeville, B.C., Gorini, C., Oliveira, V.D., Araújo, É.F.D.S., 2009. O processo de colapso gravitacional da seção marinha da bacia da foz do Amazonas - margem equatorial brasileira. *Rev. Bras. Geofísica* 27, 459–484.
<https://doi.org/10.1590/S0102-261X2009000300012>
- Pierce, J.W., 1970. Tidal Inlets and Washover Fans. *J. Geol.* 78, 230–234.
<https://doi.org/10.1086/627504>
- Pillans, B., 1990. Pleistocene marine terraces in New Zealand: A review. *N. Z. J. Geol. Geophys.* 33, 219–231. <https://doi.org/10.1080/00288306.1990.10425680>
- Pisias, N.G., Moore, T.C., 1981. The evolution of Pleistocene climate: A time series approach. *Earth Planet. Sci. Lett.* 52, 450–458. [https://doi.org/10.1016/0012-821X\(81\)90197-7](https://doi.org/10.1016/0012-821X(81)90197-7)
- Popov, Y.A., Pevzner, S.L., Pimenov, V.P., Romushkevich, R.A., 1999. New geothermal data from the Kola superdeep well SG-3. *Tectonophysics* 306, 345–366.
[https://doi.org/10.1016/S0040-1951\(99\)00065-7](https://doi.org/10.1016/S0040-1951(99)00065-7)
- Posamentier, H.W., Allen, G.P., 1993. Variability of the sequence stratigraphic model: effects of local basin factors. *Sediment. Geol., Basin Analysis and Dynamics of Sedimentary Basin Evolution* 86, 91–109. [https://doi.org/10.1016/0037-0738\(93\)90135-R](https://doi.org/10.1016/0037-0738(93)90135-R)
- Posamentier, H.W., Vail, P.R., 1988. Eustatic controls on clastic deposition II—sequence and systems tract models., in: Wilgus, C.K., Hastings, B.S., Posamentier, H.W., Van Wagoner, J., Ross, C.A., Kendall, C.G.St.C. (Eds.), *Sea-Level Changes: An Integrated Approach*. <https://doi.org/10.2110/pec.88.42>
- Posamentier, H.W., Allen, G.P., 1999. *Siliciclastic sequence stratigraphy—concepts and applications.*, SEPM Society for Sedimentary Geology.
- Preto, N., Hinnov, L.A., De Zanche, V., Mietto, P., Hardie, L.A., 2004. The Milankovitch interpretation of the Latemar platform cycles (Dolomites, Italy): Implications for geochronology, biostratigraphy, and Middle Triassic carbonate accumulation.
<https://doi.org/10.2110/pec.04.81>
- Quinn, T.R., Tremaine, S., Duncan, M., 1991. A three million year integration of the earth's orbit. *Astron. J.* 101, 2287. <https://doi.org/10.1086/115850>

- Rabineau, M., Berné, S., Aslanian, D., Olivet, J.-L., Joseph, P., Guillocheau, F., Bourillet, J.-F., Ledrezen, E., Granjeon, D., 2005. Sedimentary sequences in the Gulf of Lion: A record of 100,000 years climatic cycles. *Mar. Pet. Geol.* 22, 775–804.
<https://doi.org/10.1016/j.marpetgeo.2005.03.010>
- Rabineau, M., Berné, S., Olivet, J.-L., Aslanian, D., Guillocheau, F., Joseph, P., 2006. Paleo sea levels reconsidered from direct observation of paleoshoreline position during Glacial Maxima (for the last 500,000 yr). *Earth Planet. Sci. Lett.* 252, 119–137.
<https://doi.org/10.1016/j.epsl.2006.09.033>
- Rabineau, M., Leroux, E., Aslanian, D., Bache, F., Gorini, C., Moulin, M., Molliex, S., Droz, L., Dos Reis, A.T., Rubino, J.L., Guillocheau, F., Olivet, J.L., 2014. Quantifying subsidence and isostatic readjustment using sedimentary paleomarkers, example from the Gulf of Lion. *Earth Planet. Sci. Lett.* 388, 353–366.
<https://doi.org/10.1016/j.epsl.2013.11.059>
- Räsänen, M.E., Linna, A.M., Santos, J.C.R., Negri, F.R., 1995. Late Miocene Tidal Deposits in the Amazonian Foreland Basin. *Science* 269, 386–390.
<https://doi.org/10.1126/science.269.5222.386>
- Rasmussen, E.S., 1994. The relationship between submarine canyon fill and sea-level change: an example from Middle Miocene offshore Gabon, West Africa. *Sediment. Geol.* 90, 61–75.
- Raymo, M.E., 1994. The initiation of Northern Hemisphere glaciation. *Annu. Rev. Earth Planet. Sci.* 22, 353–383.
- Raymo, M.E., Oppo, D.W., Curry, W., 1997. The Mid-Pleistocene climate transition: A deep sea carbon isotopic perspective. *Paleoceanography* 12, 546–559.
<https://doi.org/10.1029/97PA01019>
- Raymo, M.E., Ruddiman, W.F., 1992. Tectonic forcing of late Cenozoic climate. *Nature* 359, 117–122.
- Reis, A.T., Araújo, E., Silva, C.G., Cruz, A.M., Gorini, C., Droz, L., Migeon, S., Perovano, R., King, I., Bache, F., 2016. Effects of a regional décollement level for gravity tectonics on late Neogene to recent large-scale slope instabilities in the Foz do Amazonas Basin, Brazil. *Mar. Pet. Geol.* 75, 29–52.
<https://doi.org/10.1016/j.marpetgeo.2016.04.011>
- Reis, A.T., Perovano, R., Silva, C.G., Vendeville, B.C., Araújo, E., Gorini, C., Oliveira, V., 2010. Two-scale gravitational collapse in the Amazon Fan: a coupled system of

- gravity tectonics and mass-transport processes. *J. Geol. Soc.* 167, 593–604.
<https://doi.org/10.1144/0016-76492009-035>
- Ribas, C.C., Aleixo, A., Nogueira, A.C.R., Miyaki, C.Y., Cracraft, J., 2012. A palaeobiogeographic model for biotic diversification within Amazonia over the past three million years. *Proc. R. Soc. B Biol. Sci.* 279, 681–689.
<https://doi.org/10.1098/rspb.2011.1120>
- Richardson, P.L., Hufford, G.E., Limeburner, R., Brown, W.S., 1994. North Brazil Current retroflection eddies. *J. Geophys. Res.* 99, 5081. <https://doi.org/10.1029/93JC03486>
- Richardson, P.L., Walsh, D., 1986. Mapping climatological seasonal variations of surface currents in the tropical Atlantic using ship drifts. *J. Geophys. Res.* 91, 10537.
<https://doi.org/10.1029/JC091iC09p10537>
- Richey, J.E., Meade, R.H., Salati, E., Devol, A.H., Nordin Jr, C.F., Santos, U.D., 1986. Water discharge and suspended sediment concentrations in the Amazon River: 1982–1984. *Water Resour. Res.* 22, 756–764.
- Ridente, D., Trincardi, F., Piva, A., Asioli, A., 2009. The combined effect of sea level and supply during Milankovitch cyclicity: Evidence from shallow-marine $\delta^{18}\text{O}$ records and sequence architecture (Adriatic margin). *Geology* 37, 1003–1006.
<https://doi.org/10.1130/G25730A.1>
- Roddaz, M., Baby, P., Brusset, S., Hermoza, W., Maria Darrozes, J., 2005a. Forebulge dynamics and environmental control in Western Amazonia: The case study of the Arch of Iquitos (Peru). *Tectonophysics* 399, 87–108.
<https://doi.org/10.1016/j.tecto.2004.12.017>
- Roddaz, M., Brusset, S., Baby, P., Hérail, G., 2006. Miocene tidal-influenced sedimentation to continental Pliocene sedimentation in the forebulge–backbulge depozones of the Beni–Mamore foreland Basin (northern Bolivia). *J. South Am. Earth Sci.* 20, 351–368. <https://doi.org/10.1016/j.jsames.2005.11.004>
- Roddaz, M., Viers, J., Brusset, S., Baby, P., Hérail, G., 2005b. Sediment provenances and drainage evolution of the Neogene Amazonian foreland basin. *Earth Planet. Sci. Lett.* 239, 57–78. <https://doi.org/10.1016/j.epsl.2005.08.007>
- Rodger, M., Watts, A.B., Greenroyd, C.J., Peirce, C., Hobbs, R.W., 2006. Evidence for unusually thin oceanic crust and strong mantle beneath the Amazon Fan. *Geology* 34, 1081. <https://doi.org/10.1130/G22966A.1>
- Rossetti, D.F., Cohen, M.C.L., Tatum, S.H., Sawakuchi, A.O., Cremon, É.H., Mittani, J.C.R., Bertani, T.C., Munita, C.J.A.S., Tudela, D.R.G., Yee, M., Moya, G., 2015. Mid-Late

- Pleistocene OSL chronology in western Amazonia and implications for the transcontinental Amazon pathway. *Sediment. Geol.* 330, 1–15.
<https://doi.org/10.1016/j.sedgeo.2015.10.001>
- Rossetti, D.F., Mann de Toledo, P., Góes, A.M., 2005. New geological framework for Western Amazonia (Brazil) and implications for biogeography and evolution. *Quat. Res.* 63, 78–89. <https://doi.org/10.1016/j.yqres.2004.10.001>
- Rousse, S., Gilder, S., Farber, D., McNulty, B., R. Torres, V., 2002. Paleomagnetic evidence for rapid vertical-axis rotation in the Peruvian Cordillera ca. 8 Ma. *Geology* 30, 75.
[https://doi.org/10.1130/0091-7613\(2002\)030<0075:PEFRVA>2.0.CO;2](https://doi.org/10.1130/0091-7613(2002)030<0075:PEFRVA>2.0.CO;2)
- Roychowdhury, R., 2018. Eccentricity Modulation of Precessional Variation in the Earth's Climate Response to Astronomical Forcing: A Solution to the 41-kyr Mystery. University of Massachusetts Amherst. <https://doi.org/10.7275/10678045.0>
- Ruddiman, W.F., Raymo, M.E., 1988. Northern Hemisphere climate régimes during the past 3 Ma: possible tectonic connections. *Philos. Trans. R. Soc. Lond. B Biol. Sci.* 318, 411–430. <https://doi.org/10.1098/rstb.1988.0017>
- Ruffell, A.H., Worden, R. H., 1999. Palaeoclimate Controls on Spectral Gamma-Ray Radiation from Sandstones, in: Worden, Richard H., Morad, S. (Eds.), *Clay Mineral Cements in Sandstones*. Blackwell Publishing Ltd., Oxford, UK, pp. 93–108.
<https://doi.org/10.1002/9781444304336.ch4>
- Ruggiero, G., 2008. Estudo numérico do efeito da Pluma do Rio Amazonas na dinâmica da porção oeste do Oceano Atlântico Equatorial. Universidade Federal do Rio Grande, Rio Grande, Brasil.
- Rühlemann, C., Diekmann, B., Mulitza, S., Frank, M., 2001. Late Quaternary changes of western equatorial Atlantic surface circulation and Amazon lowland climate recorded in Ceará Rise deep-sea sediments. *Paleoceanography* 16, 293–305.
<https://doi.org/10.1029/1999PA000474>
- Salzmann, L., Green, A., Cooper, J.A.G., 2013. Submerged barrier shoreline sequences on a high energy, steep and narrow shelf. *Mar. Geol.* 346, 366–374.
<https://doi.org/10.1016/j.margeo.2013.10.003>
- Sanborn, K.L., Webster, J.M., Yokoyama, Y., Dutton, A., Braga, J.C., Clague, D.A., Paduan, J.B., Wagner, D., Rooney, J.J., Hansen, J.R., 2017. New evidence of Hawaiian coral reef drowning in response to meltwater pulse-1A. *Quat. Sci. Rev.* 175, 60–72.
<https://doi.org/10.1016/j.quascirev.2017.08.022>

- Santos Jr, O.F., Amaral, R.F., Scudelari, A.C., 2006. Failure Mechanisms of a Coastal Cliff in Rio Grande do Norte State, NE Brazil. *J. Coast. Res.* 629–632.
- Schackleton, N.J., Hall, M.A., Pate, D., 1995. Pliocene stable isotope stratigraphy of Site 846. *Proc Ocean Drill Program Sci Results* 138, 337–355.
<https://doi.org/10.2973/odp.proc.sr.138.1995>
- Schaller, H., Vasconcelos, D.D., Castro, J.C., 1971. Estratigrafia preliminar da bacia sedimentar da foz do rio Amazonas., in: *Congresso Brasileiro de Geologia*. pp. 189–202.
- Schneider, T., Bischoff, T., Haug, G.H., 2014. Migrations and dynamics of the intertropical convergence zone. *Nature* 513, 45–53. <https://doi.org/10.1038/nature13636>
- Schott, F.A., Stramma, L., Fischer, J., 1995. The warm water inflow into the western tropical Atlantic boundary regime, spring 1994. *J. Geophys. Res.* 100, 24745.
<https://doi.org/10.1029/95JC02803>
- Sedgwick, P.E., Davis, R.A., 2003. Stratigraphy of washover deposits in Florida: implications for recognition in the stratigraphic record. *Mar. Geol.* 200, 31–48.
[https://doi.org/10.1016/S0025-3227\(03\)00163-4](https://doi.org/10.1016/S0025-3227(03)00163-4)
- Sempere, T., Hérail, G., Oller, J., Bonhomme, M.G., 1990. Late Oligocene-early Miocene major tectonic crisis and related basins in Bolivia. *Geology* 18, 946.
[https://doi.org/10.1130/0091-7613\(1990\)018<0946:LOEMMT>2.3.CO;2](https://doi.org/10.1130/0091-7613(1990)018<0946:LOEMMT>2.3.CO;2)
- Sepulchre, P., Arsouze, T., Donnadieu, Y., Dutay, J.-C., Jaramillo, C., Le Bras, J., Martin, E., Montes, C., Waite, A.J., 2014. Consequences of shoaling of the Central American Seaway determined from modeling Nd isotopes. *Paleoceanography* 29, 176–189.
<https://doi.org/10.1002/2013PA002501>
- Seranne, M., Abeigne, C.-R.N., 1999. Oligocene to Holocene sediment drifts and bottom currents on the slope of Gabon continental margin (west Africa) Consequences for sedimentation and southeast Atlantic upwelling. *Sediment. Geol.*
- Shackleton, N.J., Backman, J., Zimmerman, H., Kent, D.V., Hall, M.A., Roberts, D.G., Schnitker, D., Baldauf, J.G., Desprairies, A., Homrighausen, R., Huddleston, P., Keene, J.B., Kaltenback, A.J., Krumsiek, K.A.O., Morton, A.C., Murray, J.W., Westberg-Smith, J., 1984. Oxygen isotope calibration of the onset of ice-rafting and history of glaciation in the North Atlantic region. *Nature* 307, 620–623.
<https://doi.org/10.1038/307620a0>
- Shanmugam, G., 2016. Submarine fans: A critical retrospective (1950–2015). *J. Palaeogeogr.* 5, 110–184. <https://doi.org/10.1016/j.jop.2015.08.011>

- Shephard, G.E., Müller, R.D., Liu, L., Gurnis, M., 2010. Miocene drainage reversal of the Amazon River driven by plate–mantle interaction. *Nat. Geosci.* 3, 870–875.
<https://doi.org/10.1038/ngeo1017>
- Sheriff, R.E., Geldart, L.P., 1995. *Exploration seismology.*, Cambridge university press.
- Silva, C.C., Dos Reis, A.T., Perovano, R.J., Gorini, M.A., Dos Santos, M.V.M., Jeck, I.K., Tavares, A.A.A., Gorini, C., 2016. Multiple Megaslides and Their Significance for the Miocene Stratigraphic Evolution of the Offshore Amazon Basin, in: Lamarche, G., Mountjoy, J., Bull, S., Hubble, T., Krastel, S., Lane, E., Micallef, A., Moscardelli, L., Mueller, C., Pecher, I., Woelz, S. (Eds.), *Submarine Mass Movements and Their Consequences, Advances in Natural and Technological Hazards Research.* Springer International Publishing, Cham, pp. 49–60.
https://doi.org/10.1007/978-3-319-20979-1_5
- Silva, S.R.P., Maciel, R.R., Severino, M.C.G., 1999. Cenozoic tectonics of Amazon Mouth Basin. *Geo-Mar. Lett.* 18, 256–262. <https://doi.org/10.1007/s003670050077>
- Silva, S.R.P., Maciel, R.R., Severino, M.C.G., 1998. Cenozoic tectonics of Amazon Mouth Basin. *Geo-Mar. Lett.* 18, 256–262. <https://doi.org/10.1007/s003670050077>
- Smith, W.H.F., Sandwell, D.T., 1997. Global Sea Floor Topography from Satellite Altimetry and Ship Depth Soundings. *Science* 277, 1956–1962.
<https://doi.org/10.1126/science.277.5334.1956>
- Soares, E.A.A., D’Apolito, C., Jaramillo, C., Harrington, G., Caputo, M.V., Barbosa, R.O., Bonora Dos Santos, E., Dino, R., Gonçalves, A.D., 2017. Sedimentology and Palynostratigraphy of a Pliocene-Pleistocene (Piacenzian to Gelasian) deposit in the lower Negro River: Implications for the establishment of large rivers in Central Amazonia. *J. South Am. Earth Sci.* 79, 215–229.
<https://doi.org/10.1016/j.jsames.2017.08.008>
- Soares Júnior, A.V., Costa, J.B.S., Hasui, Y., 2008. Evolução da margem atlântica equatorial do Brasil: Três fases distensivas. *Geosciencias* 27, 427–437.
- Soares Júnior, A.V., Hasui, Y., Costa, J.B.S., Machado, F.B., 2011. Evolução do rifteamento e paleogeografia da margem atlântica equatorial do Brasil: Triássico ao Holoceno. *Geosciencias* 30, 669–692.
- Souza, A.D.O., Lämmle, L., Filho, A.P., Donadio, C., 2022. Recent geomorphological changes in the Paraíba do Sul delta, South America East Coast. *Prog. Phys. Geogr. Earth Environ.* 46, 566–588. <https://doi.org/10.1177/03091333221077614>

- Souza, J.M.G., Cubas, N., Rabe, C., Letouzey, J., Divies, R., Praeg, D.B., Granjeon, D., Cruz, A.M., Silva, C.G., Dos Reis, A.T., Gorini, C., 2020. Controls on overpressure evolution during the gravitational collapse of the Amazon deep-sea fan. *Mar. Pet. Geol.* 121, 104576. <https://doi.org/10.1016/j.marpetgeo.2020.104576>
- Steinmann, M., Hungerbühler, D., Seward, D., Winkler, W., 1999. Neogene tectonic evolution and exhumation of the southern Ecuadorian Andes: a combined stratigraphy and fission-track approach. *Tectonophysics* 307, 255–276. [https://doi.org/10.1016/S0040-1951\(99\)00100-6](https://doi.org/10.1016/S0040-1951(99)00100-6)
- Stow, D.A., Faugères, J.C., Howe, J.A., Pudsey, C.J., Viana, A.R., 2002. Bottom currents, contourites and deep-sea sediment drifts: current state-of-the-art. *Geol. Soc. Lond. Mem.* 22, 7–20. <https://doi.org/10.1144/GSL.MEM.2002.022.01.02>
- Stramma, L., Fisher, J., Brandt, P., Schott, F., 2003. Circulation, variability and near-equatorial meridional flow in the central tropical Atlantic. *Oceanography* 68, 1–22.
- Stramma, L., Schott, F., 1999. The mean flow field of the tropical Atlantic Ocean. *Deep Sea Res. Part II Top. Stud. Oceanogr.* 46, 279–303. [https://doi.org/10.1016/S0967-0645\(98\)00109-X](https://doi.org/10.1016/S0967-0645(98)00109-X)
- Strasser, A.H., Hilgen, F.J., Heckel, P.H., 2006. Cyclostratigraphy concepts, definitions, and applications. *Newsl. Stratigr.* 42, 75–114. <https://doi.org/10.1127/0078-0421/2006/0042-0075>
- Stutz, M.L., Pilkey, O.H., 2011. Open-Ocean Barrier Islands: Global Influence of Climatic, Oceanographic, and Depositional Settings. *J. Coast. Res.* 272, 207–222. <https://doi.org/10.2112/09-1190.1>
- Talley, L.D., 2011. *Descriptive physical oceanography: an introduction*, Academic press. ed.
- Taylor, M., Stone, G.W., 1996. Beach-Ridges: A Review. *J. Coast. Res.* 612–621.
- Telford, W.N.M., Geldart, L.P., Sheriff, R.E., 1990. *Applied geophysics*. Camb. Univ. Press Camb. UK.
- Thomson, D.J., 1982. Spectrum estimation and harmonic analysis. *Proc. IEEE* 70, 1055–1096. <https://doi.org/10.1109/PROC.1982.12433>
- Tucker, M.E., Wright, V.P., 1990. *Carbonate sedimentology*. Blackwell Sci. Publ. 1–27.
- Uenzelmann-Neben, G., Gruetzner, J., 2018. Chronology of Greenland Scotland Ridge overflow: What do we really know? *Mar. Geol.* 406, 109–118. <https://doi.org/10.1016/j.margeo.2018.09.008>

- Urlaub, M., Talling, P.J., Masson, D.G., 2013. Timing and frequency of large submarine landslides: implications for understanding triggers and future geohazard. *Quat. Sci. Rev.* 72, 63–82. <https://doi.org/10.1016/j.quascirev.2013.04.020>
- Vail, P.R., Mitchum Jr, R.M., Thompson, S., 1977. Seismic stratigraphy and global changes of sea level: Part 3. Relative changes of sea level from Coastal Onlap: section 2. Application of seismic reflection Configuration to Stratigraphic Interpretation.
- Vale, N.F., Amado-Filho, G.M., Braga, J.C., Brasileiro, P.S., Karez, C.S., Moraes, F.C., Bahia, R.G., Bastos, A.C., Moura, R.L., 2018. Structure and composition of rhodoliths from the Amazon River mouth, Brazil. *J. South Am. Earth Sci.* 84, 149–159. <https://doi.org/10.1016/j.jsames.2018.03.014>
- Vale, N.F., Braga, J.C., De Moura, R.L., Salgado, L.T., De Moraes, F.C., Karez, C.S., De Carvalho, R.T., Salomon, P.S., Menandro, P.S., Amado-Filho, G.M., Bastos, A.C., 2022. Distribution, morphology and composition of mesophotic ‘reefs’ on the Amazon Continental Margin. *Mar. Geol.* 447, 106779. <https://doi.org/10.1016/j.margeo.2022.106779>
- Van Wagoner, J.C., Posamentier, H.W., Mitchum Jr, R.M., Vail, P.R., Sarg, J.F., Loutit, T.S., Hardenbol, J., 1988. An overview of the fundamentals of sequence stratigraphy and key definitions., in: Wilgus, C.K., Hastings, B.S., Posamentier, H.W., Van Wagoner, J., Ross, C.A., Kendall, C.G.St.C. (Eds.), *Sea-Level Changes: An Integrated Approach*. SEPM (Society for Sedimentary Geology). <https://doi.org/10.2110/pec.88.42>
- Vanneste, M., Forsberg, C.F., Glimsdal, S., Harbitz, C.B., Issler, D., Kvalstad, T.J., Løvholt, F., Nadim, F., 2013. Submarine Landslides and Their Consequences: What Do We Know, What Can We Do?, in: Margottini, C., Canuti, P., Sassa, K. (Eds.), *Landslide Science and Practice*. Springer Berlin Heidelberg, Berlin, Heidelberg, pp. 5–17. https://doi.org/10.1007/978-3-642-31427-8_1
- Varadi, F., Runnegar, B., Ghil, M., 2003. Successive Refinements in Long-Term Integrations of Planetary Orbits. *Astrophys. J.* 592, 620–630. <https://doi.org/10.1086/375560>
- Velasquez-Montoya, L., Sciaudone, E.J., Smyre, E., Overton, M.F., 2021. Vulnerability Indicators for Coastal Roadways Based on Barrier Island Morphology and Shoreline Change **Predictions**. *Nat. Hazards Rev.* 22, 04021003. [https://doi.org/10.1061/\(ASCE\)NH.1527-6996.0000441](https://doi.org/10.1061/(ASCE)NH.1527-6996.0000441)
- Vellinga, M., Wood, R.A., 2002. Global Climatic Impacts of a Collapse of the Atlantic Thermohaline Circulation. *Clim. Change* 54, 251–267.

- Vellinga, M., Wu, P., 2004. Low-Latitude Freshwater Influence on Centennial Variability of the Atlantic Thermohaline Circulation. *J. Clim.* 17, 4498–4511.
<https://doi.org/10.1175/3219.1>
- Viana, A.R., 2002. Seismic expression of shallow- to deep-water contourites along the south-eastern Brazilian margin. *Mar. Geophys. Res.* 22, 509–521.
- Viana, A.R., Almeida Jr., W., Machado, L.C., 1999. Different Styles Of Canyon Infill Related To Gravity And Bottom Current Processes : Examples From The Upper Slope Of The Se Brazilian Margin, in: 6th International Congress of the Brazilian Geophysical Society. Presented at the 6th International Congress of the Brazilian Geophysical Society, European Association of Geoscientists & Engineers, Rio de Janeiro, Brazil.,
<https://doi.org/10.3997/2214-4609-pdb.215.sbgf014>
- Viana, A.R., Hercos, C.M., De Almeida Jr, W., Magalhães, J.L., De Andrade, S.B., 2002. Evidence of bottom current influence on the Neogene to Quaternary sedimentation along the northern Campos Slope, SW Atlantic Margin. *Geol. Soc. Lond. Mem.* 22, 249–259.
- Vital, H., Amaro, V.E., Silveira, I.D., 2006. Coastal Erosion on the Rio Grande do Norte State (Northeastern Brazil): Causes and Factors Versus Effects and Associated Processes. *J. Coast. Res.* 1306–1309.
- Vonhof, H.B., Wesselingh, F.P., Kaandorp, R.J.G., Davies, G.R., Van Hinte, J.E., Guerrero, J., Räsänen, M., Romero-Pittman, L., Ranzi, A., 2003. Paleogeography of Miocene Western Amazonia: Isotopic composition of molluscan shells constrains the influence of marine incursions. *Geol. Soc. Am. Bull.* 115, 983–993.
<https://doi.org/10.1130/B25058.1>
- Wagle, B.G., Vora, K.H., Karisiddaiah, S.M., Veerayya, M., Almeida, F., 1994. Holocene submarine terraces on the western continental shelf of India; Implications for sea-level changes. *Mar. Geol.* 117, 207–225. [https://doi.org/10.1016/0025-3227\(94\)90016-7](https://doi.org/10.1016/0025-3227(94)90016-7)
- Waliser, D.E., Gautier, C., 1993. A satellite-derived climatology of the ITCZ. *J. Clim.* 6, 2162–2174.
- Wang, P., Tian, J., Lourens, L.J., 2010. Obscuring of long eccentricity cyclicity in Pleistocene oceanic carbon isotope records. *Earth Planet. Sci. Lett.* 290, 319–330.
<https://doi.org/10.1016/j.epsl.2009.12.028>
- Wang, X., Auler, A.S., Edwards, R.L., Cheng, H., Cristalli, P.S., Smart, P.L., Richards, D.A., Shen, C.-C., 2004. Wet periods in northeastern Brazil over the past 210 kyr linked to distant climate anomalies. *Nature* 432, 740–743. <https://doi.org/10.1038/nature03067>

- Webster, J.M., Braga, J.C., Clague, D.A., Gallup, C., Hein, J.R., Potts, D.C., Renema, W., Riding, R., Riker-Coleman, K., Silver, E., Wallace, L.M., 2009. Coral reef evolution on rapidly subsiding margins. *Glob. Planet. Change* 66, 129–148. <https://doi.org/10.1016/j.gloplacha.2008.07.010>
- Webster, J.M., Wallace, L.M., Clague, D.A., Braga, J.C., 2007. Numerical modeling of the growth and drowning of Hawaiian coral reefs during the last two glacial cycles (0-250 kyr). *Geochem. Geophys. Geosystems* 8. <https://doi.org/10.1029/2006GC001415>
- Weedon, G.P., Coe, A.L., Gallois, R.W., 2004. Cyclostratigraphy, orbital tuning and inferred productivity for the type Kimmeridge Clay (Late Jurassic), Southern England. *J. Geol. Soc.* 161, 655–666. <https://doi.org/10.1144/0016-764903-073>
- Weedon, G.P., Jenkyns, H.C., 1999. Cyclostratigraphy and the Early Jurassic timescale: data from the Belemnite Marls, Dorset, southern England. *Eological Soc. Am. Bull.* 111, 1823–1840.
- Westerhold, T., Röhl, U., Frederichs, T., Bohaty, S.M., Zachos, J.C., 2015. Astronomical calibration of the geological timescale: closing the middle Eocene gap. *Clim. Past* 11, 1181–1195. <https://doi.org/10.5194/cp-11-1181-2015>
- Willeit, M., Ganopolski, A., Calov, R., Brovkin, V., 2019. Mid-Pleistocene transition in glacial cycles explained by declining CO₂ and regolith removal. *Sci. Adv.* 5, eaav7337.
- Williams, G.E., 1993. History of the Earth's obliquity. *Earth-Sci. Rev.* 34, 1–45.
- Wise, J.M., Noble, D.C., Zanetti, K.A., Spell, T.L., 2008. Quechua II contraction in the Ayacucho intermontane basin: Evidence for rapid and episodic Neogene deformation in the Andes of central Perú. *J. South Am. Earth Sci.* 26, 383–396. <https://doi.org/10.1016/j.jsames.2008.08.012>
- Wohlfarth, B., Björck, S., Funder, S., Houmark-Nielsen, M., Ingólfsson, O., Lunkka, J.P., Vorren, T., 2008. Quaternary of Norden. *Episodes J. Int. Geosci.* 31, 73–81.
- Wolff, B., Carozzi, A.V., 1984. *Microfacies, depositional environments, and diagenesis of the Amapá carbonates (Paleocene–middle Miocene)*, University of Illinois at Urbana-Champaign. ed. Foz do Amazonas Basin, offshore NE Brazil.
- Wright, L.D., Nittrouer, C.A., 1995. Dispersal of River Sediments in Coastal Seas: Six Contrasting Cases. *Estuaries* 18, 494. <https://doi.org/10.2307/1352367>
- Wu, H., Zhang, S., Jiang, G., Hinnov, L., Yang, T., Li, H., Wan, X., Wang, C., 2013. Astrochronology of the Early Turonian–Early Campanian terrestrial succession in the Songliao Basin, northeastern China and its implication for long-period behavior of the

- Solar System. *Palaeogeogr. Palaeoclimatol. Palaeoecol.* 385, 55–70.
<https://doi.org/10.1016/j.palaeo.2012.09.004>
- Yilmaz, Ö., 2001. Seismic Data Analysis: Processing, Inversion, and Interpretation of Seismic Data. Society of Exploration Geophysicists. <https://doi.org/10.1190/1.9781560801580>
- Yin, Q., 2013. Insolation-induced mid-Brunhes transition in Southern Ocean ventilation and deep-ocean temperature. *Nature* 494, 222–225. <https://doi.org/10.1038/nature11790>
- Yokoyama, Y., Esat, T.M., Thompson, W.G., Thomas, A.L., Webster, J.M., Miyairi, Y., Sawada, C., Aze, T., Matsuzaki, H., Okuno, J., Fallon, S., Braga, J.-C., Humblet, M., Iryu, Y., Potts, D.C., Fujita, K., Suzuki, A., Kan, H., 2018. Rapid glaciation and a two-step sea level plunge into the Last Glacial Maximum. *Nature* 559, 603–607.
<https://doi.org/10.1038/s41586-018-0335-4>
- Yokoyama, Y., Lambeck, K., De Deckker, P., Johnston, P., Fifield, L.K., 2000. Timing of the Last Glacial Maximum from observed sea-level minima. *Nature* 406, 713–716.
<https://doi.org/10.1038/35021035>
- Zeebe, R.E., Lourens, L.J., 2022. Geologically constrained astronomical solutions for the Cenozoic era. *Earth Planet. Sci. Lett.* 592, 117595.
<https://doi.org/10.1016/j.epsl.2022.117595>
- Zeebe, R.E., Lourens, L.J., 2019. Solar System chaos and the Paleocene–Eocene boundary age constrained by geology and astronomy. *Science* 365, 926–929.
<https://doi.org/10.1126/science.aax0612>
- Zhang, D., Msadek, R., McPhaden, M.J., Delworth, T., 2011. Multidecadal variability of the North Brazil Current and its connection to the Atlantic meridional overturning circulation. *J. Geophys. Res.* 116, C04012. <https://doi.org/10.1029/2010JC006812>
- Zhang, R., Delworth, T.L., 2005. Simulated Tropical Response to a Substantial Weakening of the Atlantic Thermohaline Circulation. *J. Clim.* 18, 1853–1860.
<https://doi.org/10.1175/JCLI3460.1>
- Zhang, Y., Chiessi, C.M., Mulitza, S., Zabel, M., Trindade, R.I.F., Hollanda, M.H.B.M., Dantas, E.L., Govin, A., Tiedemann, R., Wefer, G., 2015. Origin of increased terrigenous supply to the NE South American continental margin during Heinrich Stadial 1 and the Younger Dryas. *Earth Planet. Sci. Lett.* 432, 493–500.
<https://doi.org/10.1016/j.epsl.2015.09.054>
- Zhisheng, A., Kutzbach, J.E., Prell, W.L., Porter, S.C., 2001. Evolution of Asian monsoons and phased uplift of the Himalaya–Tibetan plateau since Late Miocene times. *Nature* 411, 62–66. <https://doi.org/10.1038/35075035>

- Zhu, M., Graham, S., Pang, X., McHargue, T., 2010. Characteristics of migrating submarine canyons from the middle Miocene to present: Implications for paleoceanographic circulation, northern South China Sea. *Mar. Pet. Geol.* 27, 307–319.
<https://doi.org/10.1016/j.marpetgeo.2009.05.005>
- Zühlke, R., 2004. Integrated cyclostratigraphy of a model Mesozoic carbonate platform—the Latemar (Middle Triassic, Italy).

Titre : Évolution du plateau continental externe de la Marge Équatoriale Brésilienne depuis 4 Ma : Impact des sédiments silicoclastiques Amazoniens, des changements eustatiques contrôlés par les paramètres orbitaux, de la subsidence, et des courants océanographiques

Mots clés : Marge Équatoriale Brésilienne, Bassin Offshore de l'Amazone, cyclostratigraphie, sismique et stratigraphie séquentielle, géomorphologie, Great Amazon Reef System (GARS)

Résumé : Cette thèse étudie l'effet du climat sur les sédiments amazoniens le long de la marge équatoriale brésilienne durant les derniers 3,7 à 4,1 millions d'années. Utilisant une approche multidisciplinaire incluant cyclostratigraphie, stratigraphie séquentielle et géomorphologie, l'étude pallie les manques significatifs de chronostratigraphie du Plio-Pléistocène grâce à des données Gamma-Ray issues de forages. L'analyse de données sismiques 3D a permis d'identifier neuf séquences sismiques liées à des cycles d'excentricité de 405 000 ans. L'étude géomorphologique révèle diverses structures côtières sur le plateau externe et des constructions carbonatées type barrière-récifal jusqu'alors non détectées.

Nos résultats montrent un schéma cyclique tant dans l'architecture sédimentaire que dans les morphologies côtières. Le littoral atteint le plateau externe tous les 405 000 ans, favorisé par une faible excentricité orbitale terrestre induisant d'important bas niveaux marins. Depuis environ 2,5 Ma, l'amplification des glaciations de l'hémisphère Nord modifie le courant du Nord-Brésil, favorisant le développement de récifs lors du début des déglaciations. La transition du mid-Pléistocène influencent particulièrement la taille des unités sismiques. Tandis que la transition du mid-Brunhes impacte la croissance des carbonates, et la géométrie des dépôts sédimentaire passant de majoritairement progradant à agradant.

Title: Shelf Edge Evolution of the Brazilian Equatorial Margin since 4 Ma: Impact of Amazonian Siliciclastic Sediments, Orbitally Controlled Sea-Level Changes, Subsidence, and Oceanographic Currents

Keywords: Brazilian Equatorial Margin, Offshore Amazon Basin, cyclostratigraphy, seismic and sequence stratigraphy, geomorphology, Great Amazon Reef System (GARS)

Abstract: This PhD thesis investigates the influence of climate on the architecture and morphology of Amazonian sediments along the Brazilian Equatorial Margin over the last 3.7-4.1 million years. Using a multidisciplinary approach that incorporates cyclostratigraphy, sequence stratigraphy, and geomorphology, the study primarily fills substantial gaps in the chronostratigraphy of the Plio-Pleistocene series through Gamma-Ray borehole data. Examination of 3D seismic data yields the identification of nine seismic sequences, each associated with 405-kyr eccentricity cycles. Geomorphological evaluation reveals a variety of coastal structures on the outer shelf and show previously undetected, expansive carbonate build-ups.

Synthesis of these findings demonstrates that both sedimentary architecture and coastal morphologies display a cyclic pattern. The coastline extends to the outer shelf in 405-kyr intervals, facilitated by low Earth orbital eccentricity that facilitates significant sea-level lowstand. Since 2.5 Ma, the intensification of Northern Hemisphere glaciations alters the North Brazil Current, thereby enabling reef development during initial transgressive phases over 405-kyr cycles. Additionally, the Mid-Pleistocene Transition impacts the size of seismic units and markedly alters sediment deposition patterns. Finally, the Mid-Brunhes Transition enhances carbonate accumulation and switches the depositional pattern from progradation to aggradation.